CURRENT RESEARCH IN

ENGINEERING

MARCH 2023

Editors

Assoc. Prof. Dr. Selahattin BARDAK

Assoc. Prof. Dr. Ümit AYATA

gece kitaplığı

İmtiyaz Sahibi / Publisher • Yaşar Hız
Genel Yayın Yönetmeni / Editor in Chief • Eda Altunel
Kapak & İç Tasarım / Cover & Interior Design • Gece Kitaplığı
Editörler / Edıtors • Assoc. Prof. Dr. Selahattin BARDAK
Assoc. Prof. Dr. Ümit AYATA
Birinci Basım / First Edition • © Mart 2023
ISBN • 978-625-430-720-1

Gece Kitaplığı / Gece Publishing
Türkiye Adres / Turkey Address: Kızılay Mah. Fevzi Çakmak 1. Sokak Ümit Apt. No: 22/A Çankaya / Ankara / TR
Telefon / Phone: +90 312 384 80 40
web: www.gecekitapligi.com
e-mail: gecekitapligi@gmail.com

Baskı & Cilt / Printing & Volume
Sertifika / Certificate No: 47083

Current Research in Engineering

March 2023

Editors

Assoc. Prof. Dr. Selahattin BARDAK
Assoc. Prof. Dr. Ümit AYATA

CONTENTS

Chapter 1

PHOSPHORUS RECOVERY BY CHEMICAL EXTRACTION FROM DIFFERENT TYPES OF AIR POLLUTION CONTROL ASHES OF SLUDGE INCINERATORS[1]

Ezgi KARABACAK[2]

Güray SALIHOĞLU[3]

Nezih Kamil SALIHOĞLU[4]

1 This work has been produced as part of MSc thesis study by Ezgi Karabacak: Karabacak, E., 2021. Recovery of phosphorus from sewage sludge incineration ashes (Arıtma çamuru yakma fırını küllerinden fosfor geri kazanımı), MSc Thesis (in Turkish)- Ezgi Karabacak (ORCID: 0000-0003-2196-803X), Bursa Uludağ University/ Institute of Science/Environmental Engineering Science Division, 22 January 2021. Supervisor: Prof. Dr. Güray Salihoğlu (ORCID: 0000-0003-0714-048X).

2 Env. Eng. MSc. Ezgi Karabacak, Environmental Engineering Department, Faculty of Engineering, Bursa Uludag University, ORCID: 0000-0003-2196-803X

3 Prof. Dr. Güray Salihoğlu, Environmental Engineering Department, Faculty of Engineering, Bursa Uludag University, ORCID: 0000-0003-0714-048X

4 Prof. Dr. Nezih Kamil Salihoğlu, Environmental Engineering Department, Faculty of Engineering, Bursa Uludag University, ORCID: 0000-0002-7730-776X

1. Introduction

Phosphorus is the eleventh element in the lithosphere with an average concentration of 1180 ppm and is a limited resource (Biswas, Inoue, Harada, Ohto, & Kawakita, 2009; Oelkers & Valsami-Jones, 2008; Shiba & Ntuli, 2017; Smil, 2000). As a component of DNA, RNA, ATP, and ADP (Filippelli, 2011; Oelkers & Valsami-Jones, 2008; Shiba & Ntuli, 2017) it plays a significant role in physiological and biochemical processes (Cooper et al., 2018). It is non-renewable (Adam, Peplinski, Michaelis, Kley, & Simon, 2009; Biswas et al., 2009; R. Li, Zhao, Li, Wang, & Zhu, 2015) and irreplaceable (Bindraban, Dimkpa, & Pandey, 2020; Smil, 2000). Since it is a limiting factor for plant growth (Cornel & Schaum, 2009; R. Li et al., 2015), fertilizers containing phosphorus are used in agricultural applications (Egle, Rechberger, Krampe, & Zessner, 2016; Lim & Kim, 2017; Smil, 2000) for seed formation, plant growth, and sustaining crop yields (Smil, 2000; van Vuuren, Bouwman, & Beusen, 2010). Phosphate rocks are used in various sectors, primarily for fertilizer manufacturing (Gorazda, Tarko, Kominko, Worek, & Nowak, 2019). Besides, detergents, animal feed, food additives, and other chemicals are the sectors in which phosphorus is used (Brunner, 2010; Cieślik & Konieczka, 2017; Gorazda et al., 2019; van Vuuren et al., 2010).

The global phosphate reserves are estimated to be 69000 million tons (USGS, 2020). Significant reserves are found in Morocco & Western Sahara (50000 Mt), followed by China (3200 Mt) and Algeria (2200 Mt) (USGS, 2020). Total phosphate production in the world, which is 249 million tons, constitutes 0.36% of the world's total reserves (USGS, 2020). The major countries which produce phosphate from rocks are China (144 Mt), Morocco&Western Sahara (34.8 Mt), the United States (25.8 Mt), and Russia (14 Mt) (USGS, 2020). China is the world's top producer of phosphate, with a percentage of 57.8% (USGS, 2020). Turkey's phosphate rock reserve is around 70 million tons and is located in the district of Mazidagi in Mardin (ETI, 2021). The capacity of the phosphate enrichment plant, which is in the same district, is 1.75 million tons/year (ETI, 2021). In 2020, Turkey's phosphate export was 1.4 tons, while the import was 1.1 million tons (MTA, 2020).

Increasing demand for phosphorus (Xue et al., 2019) and its limited availability depending on the geographical location (USGS, 2020) increased the interest in phosphorus recovery. Many researchers investigated potential resources of phosphorus recovery, such as wastewater (Egle et al., 2016), municipal solid waste incineration fly ash (Gao, Fedje, & Strömvall, 2015; Kalmykova & Karlfeldt Fedje, 2013), pig manure (Azuara, Kersten, & Kootstra, 2013; Szögi, Vanotti, & Hunt, 2015) and dairy manure (Jin, Hu, & Wen, 2009). In recent years, sewage sludge has drawn attention as

an alternative source of phosphorus (Selçuk Kuşçu & Çelik, 2019; Shiba & Ntuli, 2017).

Sewage sludge has a high amount of phosphorus (Liang et al., 2019; Liu, Iordan, Cherubini, Hu, & Fu, 2021), but it also contains large amounts of heavy metals (Cieślik & Konieczka, 2017; Marani, Braguglia, Mininni, & Maccioni, 2003). Mass (70%) and volume (90%) reduction are the main advantages of incineration (Kosson, van der Sloot, & Eighmy, 1996; Liang et al., 2019; Liu et al., 2021) in sewage sludge management. The phosphorus in the sludge is converted into oxide form during the incineration at 800-900 ^{o}C (Cieślik & Konieczka, 2017; Shane Donatello & Cheeseman, 2013); then cooled in the flue gas control system and appeared as phosphate (P_2O_5) in the sewage sludge ash (SSA) (Cieślik & Konieczka, 2017). The P_2O_5 content of SSA is reported to range between 8.9% and 25.7% (Adam et al., 2009; Coutand, Cyr, & Clastres, 2006; Franz, 2008; J. Li et al., 2018; Stark, Plaza, & Hultman, 2006; Wang, Li, Tang, Fang, & Poon, 2018; Xu, He, Gu, Wang, & Shao, 2012).

Several researchers investigated phosphorus recovery to make use of the phosphorus in the SSA with various methods such as thermochemical treatment (Adam et al., 2009; Herzel, Krüger, Hermann, & Adam, 2016), electrodialytic process (Guedes, Couto, Ottosen, & Ribeiro, 2014), and wet chemical extraction (chemical extraction) (Abis, Calmano, & Kuchta, 2018; Biswas et al., 2009; Fang, Li, Guo, et al., 2018; Fang, Li, Donatello, et al., 2018; Gorazda et al., 2016). Acid, base, and chelating agents are used for phosphorus recovery from sewage sludge ashes by chemical extraction. Sodium hydroxide (NaOH) is used as a base (Biswas et al., 2009; Stark et al., 2006; Wang et al., 2018), sulfuric acid (H_2SO_4) (Abis et al., 2018; Biswas et al., 2009; Fang, Li, Guo, et al., 2018; Fang, Li, Donatello, et al., 2018; J. Li et al., 2018; Wang et al., 2018), hydrochloric acid (HCl) (Biswas et al., 2009; Stark et al., 2006), and nitric acid (HNO_3) (Abis et al., 2018; Fang, Li, Guo, et al., 2018; J. Li et al., 2018) as an inorganic acid, citric acid ($C_6H_8O_7$) (Abis et al., 2018; Fang, Li, Guo, et al., 2018; J. Li et al., 2018), oxalic acid ($C_2H_2O_4$) (Abis et al., 2018; Fang, Li, Guo, et al., 2018; J. Li et al., 2018), and lactic acid (Abis et al., 2018) as an organic acid, EDTA and EDTMP as a chelating agent (Fang, Li, Guo, et al., 2018; Fang, Li, Donatello, et al., 2018; J. Li et al., 2018). After the chemical extraction, the precipitation process is applied to obtain struvite (Xu et al., 2012) and calcium phosphate (Franz, 2008), which have a fertilizer potential. The methods used for phosphorus recovery from sewage sludge ashes are summarized in Table 1.

Table 1 *Phosphorus recovery methods from sewage sludge ashes*

Method	Reference	Principle	Effect
Chemical Extraction (Acid leaching)	(Stark et al., 2006)	Extraction with HCl Evaluation of the amount of phosphorus extracted	Phosphate release was 87% for 1 M HCl. In addition, heavy metals were dissolved.
Chemical Extraction (Base leaching)	(Stark et al., 2006)	Extraction with NaOH Evaluation of the amount of phosphorus extracted	Phosphate release was 70% for 1 M NaOH. The amount of extracted heavy metals in NaOH was lower than of HCl
Calcium Phosphate Precipitation	(Franz, 2008)	Extraction with H_2SO_4 Removal of heavy metals by ion exchange and sulfide precipitation Precipitation of calcium phosphate using lime water	Calcium phosphate fertilizer (high level of phosphorus and low level of heavy metals)
Struvite Precipitation	(Xu et al., 2012)	Extraction with HCl Removal of heavy metals using ion-exchange Addition of $MgCl_2 6H_2O$ and NH_4Cl Adjustment of Mg:N:P and pH	Struvite (High phosphorus bioavailability and low level of heavy metals)
Chemical Extraction (Chelating agent leaching)	(Li et al., 2018)	Extraction with chelating agents (EDTA and EDTMP) Evaluation of the amount of phosphorus extracted	Phosphorus release was around 25% for 0.05 M EDTA and 15% for 0.05 M EDTMP. Chelating agents extracted less heavy metal compared to acids.
Thermochemical Treatment	(Adam et al., 2009)	Mono-incineration of the sludge and mixing ash with chlorine donor ($MgCl_2$/$CaCl_2$) Separation of heavy metal chlorides from sewage sludge ash at 1000 °C	Raw material for phosphorus fertilizers (High phosphorus bioavailability, low heavy metal content)
Electrodialytic Process	(Guedes et al., 2014)	Extraction with H_2SO_4 Transport of phosphorus towards the anode Transport of heavy metals to the cathode	Phosphorus rich solution (low level of heavy metals)

Many studies investigated phosphorus recovery from SSA using the acid extraction method. However, a limited number of the studies (Pettersson, Åmand, & Steenari, 2008a, 2008b) differentiated the phosphorus recovery potential of SSA according to the air pollution control system (APCS) that they are trapped. Fly ashes originated from co-combustion of sewage sludge with wood were studied (Pettersson et al., 2008a, 2008b). The influence of the APCS on phosphorus extraction from ashes of incinerators devoted to only sewage sludges was investigated in this study. SSA samples were classified according to the unit they were formed (baghouse dust filters and multi-cyclones), and their differences in terms of phosphorus recovery using the acid extraction method were evaluated.

2. Materials and methods

2.1. Sewage sludge ashes

SSA samples were obtained from the sewage sludge incineration plant located in Bursa, Turkey. The wastewater treatment plant, where the sludge originated, is operated with a five-stage Bardenpho® process, and phosphorus-rich sewage sludge is produced as a result. Sewage sludge is dewatered by the centrifuge unit to 22-26% dry solids and transferred to the fluidized-bed incinerator. The temperature reaches 868 °C, and the sludge is converted into inert ash. Per annum, 103502 tons of sewage sludge are incinerated, and 6457 tons of SSA are generated.

The flue gas containing dust and particulates from the waste heat boiler passes through the multi-cyclone unit for treatment. Multi-cyclone unit collects particles larger than 4 μm and removes 75-85% of the total particulate matter. After the multi-cyclone unit, lime is injected to remove acidic compounds such as SO_2. Baghouse dust filters capture particles after the multi-cyclone unit and lime injection. A wet scrubber tower is used as the last stage of emission control. The SSA samples used in this study were obtained from the multi-cyclone unit (MC-Ash) and baghouse dust filter units (BF-Ash).

2.2. Experimental method

The first step of the experiments was to characterize the ashes used in this study. The acid extraction method was used to recover phosphorus from the ashes. After acid extraction, phosphorus analysis was carried out in the liquid phase. The residual solid phases of the samples were also analyzed. The experimental method used in this study is shown in Fig. 1.

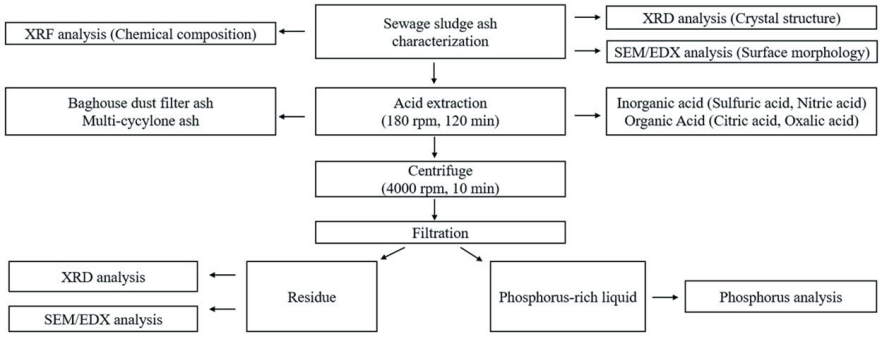

Fig. 1 *Experimental method*

The pH values of the ashes were measured in a 1:5 (mass/volume) ash/deionized water ratio using a pH meter (HANNA HI9811-5). Before analysis of XRD and SEM/EDX, both of the ashes and solid residues samples were oven-dried at 105 ° C for 24 hours and milled. The chemical compositions

of MC-Ash and BF-Ash were analyzed by X-ray fluorescence (XRF Thermoelectron-ARL 8660, Switzerland). The crystalline phases in the BF-Ash, MC-Ash, and residues were analyzed by an X-ray diffractometer (XRD, Bruker AXS, Discover, USA) by using CuKA radiation (λ = 1.54060 Å) obtained at 40kV and 40 mA. Peaks were identified with a 2θ step interval of 0.02° (5–80°).

The morphologies of BF-Ash, MC-Ash, and residues were analyzed using a scanning electron microscope with energy-dispersive X-ray spectroscopy (SEM/EDX, Carl Zeiss, Gemini 300, Australia) operated at 15 kV. BF-Ash, MC-Ash, and residues were gold coated with a vacuum-based coating instrument (Leica, EM ACE 600) before SEM/EDX analysis.

The influence of various acid (e.g. sulfuric acid, nitric acid, oxalic acid, citric acid) concentrations such as 0.1 mol/L, 0.2 mol/L, 0.5 mol/L, and 1 mol/L on the extraction efficiency of phosphorus were investigated. Along with the acid extraction, distilled water was also used to extract the BF-Ash and MC-Ash. The liquid-to-solid ratio was determined to be 20:1 (ml g^{-1}) in the experimental design as recommended by the literature (Fang, Li, Guo, et al., 2018). 40 ml acid solution was added to 2 g sewage sludge ash sample. Both of the ashes were mixed with six different acid solutions at 180 rpm in a horizontal shaker for two hours. After acid extraction, the mixture was transferred to a centrifuge tube and was centrifuged at 4000 rpm for 10 min (Fang, Li, Guo, et al., 2018). The leachates were then filtered through a 0.45 µm mixed cellulose esters membrane filter, so the solid and liquid phases were separated from each other. The extracted phosphorus was measured colorimetrically by the ascorbic acid method. In this method, ammonium molybdate and potassium antimonyl tartrate generate phosphomolybdic acid in acidic conditions, so the molybdenum blue color develops (Murphy & Riley, 1962). The molybdenum blue complex is measured at 882 nm (Murphy & Riley, 1962). Phosphorus determination was carried out using a UV-Vis spectrophotometer (HACH LANGE DR 5000). The extracted level of phosphorus and leached heavy metals from the ashes to the liquid phase was calculated according to the eq. (1) below (Fang, Li, Donatello, et al., 2018).

$$M\ (mg/g) = \frac{(C \times T \times V)}{M_o} \qquad (1)$$

In the eq. (1), M is the extracted level of phosphorus (mg/g), C is the concentration of the phosphorus in the liquid phase (mg/L); T is the dilution factor, V is the volume of the extract (L), and Mo is mass of the ash before extraction (g).

3. Results and discussion

3.1. Characterization of sewage sludge ashes

The chemical compositions and physical characterizations of BF-Ash and MC-Ash are presented in Table 2. The pH values of BF-Ash and MC-Ash were measured as 12.3 and 11.9, respectively. Both of the ashes were alkaline, but the pH value of BF-Ash was higher than that of the MC-Ash. This can be explained by lime injection after the multi-cyclone unit. Loss on ignition (LOI) is an indication of unburned carbon for sewage sludge ashes and is reported to generally be below 3 wt.% (Shane Donatello & Cheeseman, 2013). Lynn, Dhir, Ghataora, & West (2015) reported the average LOI value to be 3.5 in their review. The LOI levels for both ash samples in the present study, 3.22% and 1.51%, agree with the literature values. Blaine fineness levels of BF-Ash and MC-Ash were determined as 6090 and 2870 cm^2/g, respectively. The distributions of the oxides for both BF-Ash and MC-Ash were SiO_2>CaO>P_2O_5>Al_2O_3>Fe_2O_3>MgO>K_2O>SO_3>Na_2O>Cl. The main oxide compositions of BF-Ash and MC-Ash were SiO_2, CaO, P_2O_5, Al_2O_3, and Fe_2O_3. The main oxides in sewage sludge ash were reported as SiO2, Al2O3, and CaO in the literature (Lynn, Dhir, Ghataora, & West, 2015). As shown in Table 2, the main components of the BF-Ash and MC-Ash were similar to other studies (Adam et al., 2009; Coutand et al., 2006; Franz, 2008; J. Li et al., 2018; Wang et al., 2018; Xu et al., 2012).

Table 2 *Physical characterization and chemical compositions of ashes*

Parameter		Value								
		BF-Ash	MC-Ash	Franz (2008)	Li et al. (2018)	Xu et al. (2012)	Coutand et al. (2006)	Stark et al. (2006)	Wang et al. (2018)	Adam et al. (2009)
Physical Characterization	SG*	2.64	2.68	-	2.49	-	2.64	-	2.49	-
	LOI** (%)	3.22	1.51	-	0.99	-	5.5	-	0.99	-
	Blaine (cm^2/g)	6090	2870	-	-	-	6400	-	-	-
	pH	12.3	11.9	-	8.45	-	-	-	8.45	-

Chemical Composition (%)	P_2O_5	17.36	11.49	8.9	9.27	15.2	14.8	18.5	9.33	25.7
	SiO_2	27.59	38.5	18.2	31.15	49.1	34.2	-	33.90	19.6
	Al_2O_3	8.26	8.35	9.1	11.88	15.1	12.6	41.1	15.24	15.5
	Fe_2O_3	5.32	5.08	15.6	23.95	6.44	4.7	11.9	16.42	5.7
	CaO	19.6	16.86	22.8	9.73	7.77	20.6	6.91	7.45	18.5
	MgO	4.53	4.01	2.3	1.66	2.72	1.9	0.99	2.73	3.63
	SO_3	3.14	3.06	8.2	4.08	-	2.8	-	-	-
	Na_2O	1.67	1.63	5.5	2.42	1.52	1.0	-	6.96	0.98
	K_2O	3.7	3.16	0.5	3.53	2.83	1.7	-	2.74	2.05
	Cl	0.11	0.078	<0.1	0.24	-	-	-	-	-

*SG: Specific gravity, **LOI: Loss on ignition

The P_2O_5 levels of BF-Ash and MC-Ash were measured as 17.36% and 11.49%, respectively. As shown in Table 2, the P_2O_5 levels of both BF-Ash and MC-Ash fall within the range reported for the ash contents in the literature to be between 8.9% and 25.7%. A range of 5-40% is reported for the P_2O_5 content of phosphate rocks in the literature (S. Donatello, Tong, & Cheeseman, 2010), and the P_2O_5 contents of both ashes are also within this range. As shown in Fig. 2, the particle size distributions of BF-Ash and MC-Ash were different from each other. The average particle sizes of BF-Ash and MC-Ash were determined as 16.093 µm and 44.701 µm, respectively. BF-Ash had a finer particle size distribution compared to MC-Ash.

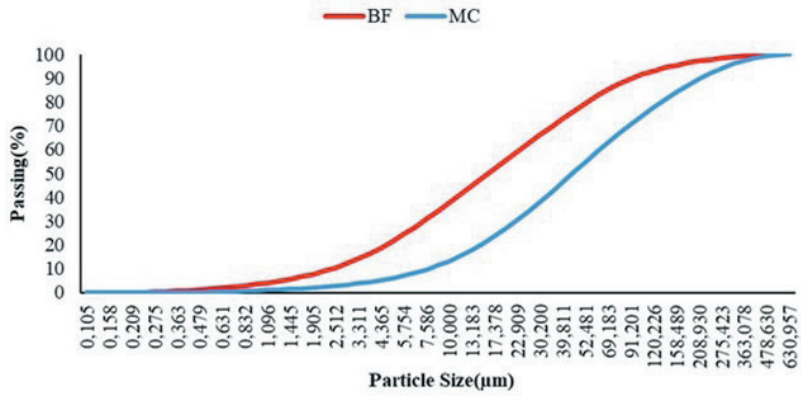

Fig. 2 *Particle size distribution of ashes*

Fig. 3 shows the morphology of BF-Ash and MC-Ash obtained by SEM micrographs (x300 magnifications). The SEM images of the ashes (Fig. 3) agreed with the particle size distribution (Fig. 2) that the BF-Ash was finer than the MC-Ash.

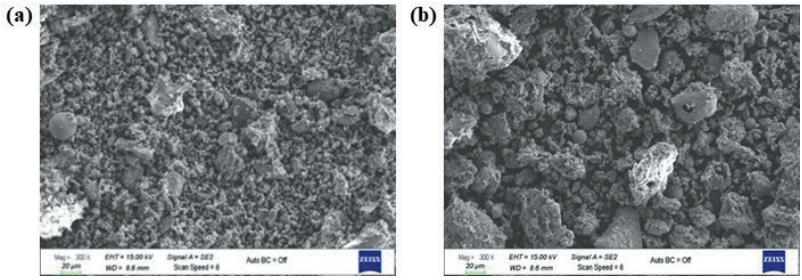

Fig. 3 *SEM images of sewage sludge ashes (300x) a) BF-Ash b) MC-Ash*

Both the BF-Ash and MC-Ash had a porous structure and many small irregular particles (Fig. 3). The MC-Ash exhibited smooth spherical particles (Fig. 3b). MC-Ash contained more agglomeration than BF-Ash. The SEM analysis showed that BF-Ash had thinner particles than MC-Ash. Many researchers (Anderson, 2002; Biswas et al., 2009; Coutand et al., 2006; J. Li et al., 2018) reported that SSA showed small particles, irregular particles, and agglomeration. The morphology of both the BF-Ash and MC-Ash agree with the literature. The SEM/EDX analysis of BF-Ash and MC-Ash are given in Fig. 4.

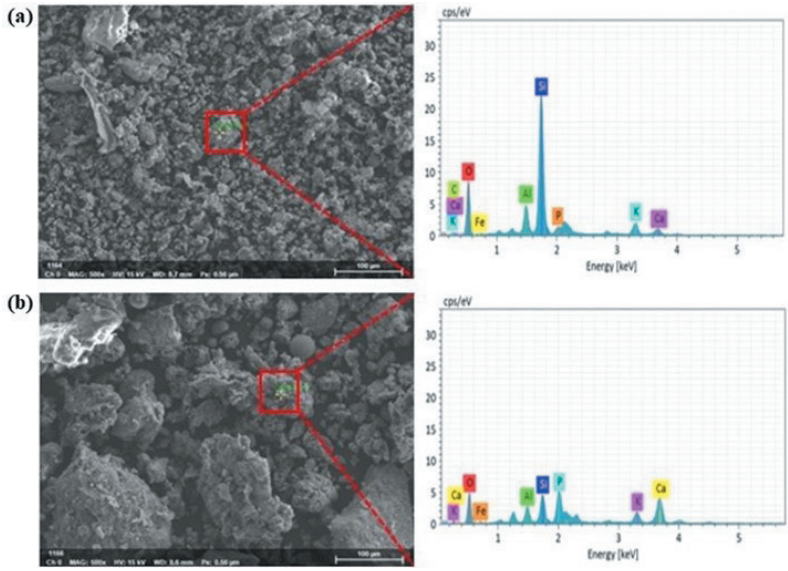

Fig. 4 *SEM/EDX analysis of sewage sludge ashes a) BF-Ash b) MC-Ash*

According to SEM/EDX results in Fig. 4a, the main elements of BF-Ash were oxygen (41.22%) and silicon (32.83%); carbon (5.93%), potassium (5.66%), aluminum (5.17%), calcium (4%), iron (3.53%), and phosphorus (1.66%) were present in smaller quantities. Silicon oxide (Fig. 4a) can be identified clearly. BF-Ash's SEM/EDX analysis supported the XRF analysis with high SiO_2 content (27.59%) (Table 2). J. Li et

al., (2018) also reported the presence of SiO_2 in sewage sludge ash. The SEM-EDX analysis of MC-Ash showed the presence of oxygen (44.11%), iron (22.08%), calcium (17.04%), phosphorus (8.08%), silicon (5.14%), potassium (2.25%), and aluminum (1.31%). Calcium and iron in Fig. 4b may be present as Fe_2O_3 or CaO forms; the chemical composition of MC-Ash analysis showed the existence of both iron oxide and calcium oxide (Table 2). The XRD analyses of BF-Ash and MC-Ash are shown in Fig. 5 and Fig. 6, respectively.

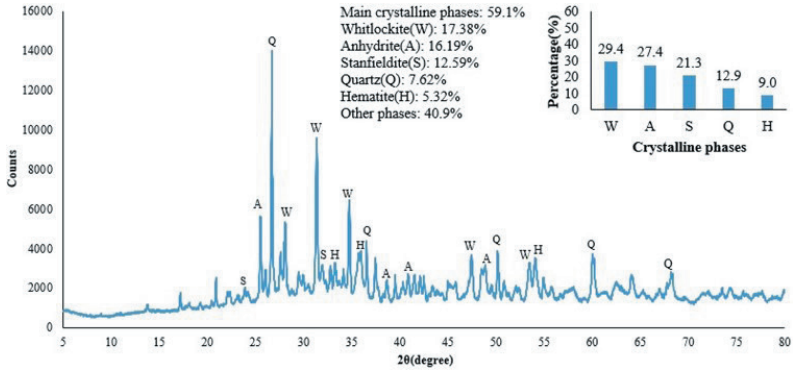

Fig. 5 *X-ray diffraction analysis results of BF-Ash*

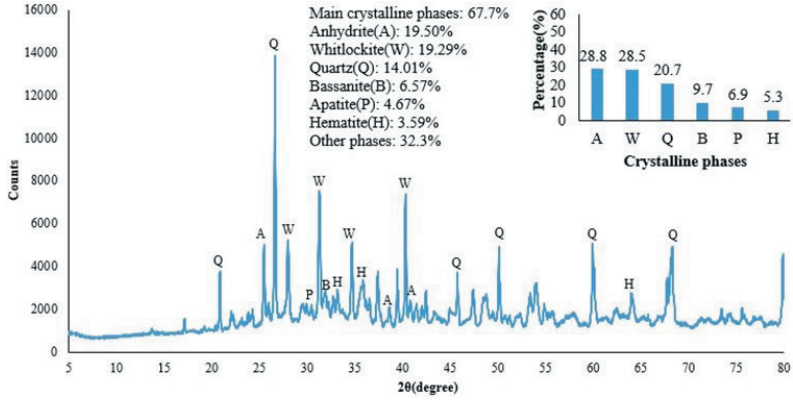

Fig. 6 *X-ray diffraction analysis results of MC-Ash*

As can be seen in Fig. 5, the ratio of the crystalline phases was 59.1%, and of the amorphous phases was 40.9% for BF-Ash. The crystalline phases contained in BF-Ash were: whitlockite 17.38% ($Ca_9(MgFe)(PO_4)_6PO_3OH$), 16.19% anhydrite ($CaSO_4$), 12.59% stanfieldite ($Mg_3C_3(PO_4)_4$), 7.62% quartz (SiO_2), and 5.32% hematite (Fe_2O_3). The ratio of crystalline phases was 67.7%, and of amorphous phases was 32.3% for MC-Ash (Fig. 6). The crystalline phases contained in MC-Ash were: 19.50% anhydrite ($CaSO_4$), 19.29% whitlockite ($Ca_9(MgFe)(PO_4)_6PO_3OH$), 14.01% quartz

(SiO_2), 6.57% bassanite ($CaSO_4.0.5H_2O$), 4.67% apatite ($Ca_5(PO_4)_3$), and 3.59% hematite (Fe_2O_3). Despite the presence of Al_2O_3 in BF-Ash and MC-Ash, $AlPO_4$ was not detected in the XRD analysis. XRD did not identify Al compounds in sewage sludge ashes; a possible reason may be their presence as amorphous aluminosilicate (Liang et al., 2019). According to the XRD analysis, the rate of crystalline phases in both ashes was higher than that of amorphous phases. In addition, the rate of crystalline phases of MC-Ash was higher than that of BF-Ash. Similar results were reported (Salihoglu & Mardani-Aghabaglou, 2021); the crystalline phases rate of MC-Ash (76.7%) was higher than that of BF-Ash (60.7%). On the other hand, several researchers (Chen, Li, & Poon, 2018; J. Li et al., 2018) reported that the ratios of amorphous phases of SSA were higher than that of the crystalline phases. The amorphous phases of SSA was reported to range between 35 and 75%. (Lynn et al., 2015). Franz (2008) reported that the major crystalline phases of SSA are quartz, calcium oxide, hydroxyapatite, hematite, and a low amount of iron oxide phosphate. Several researchers (S. Donatello, Tong, et al., 2010; Wang et al., 2018) reported that the major crystalline phases of SSA are quartz, hematite, and whitlockite. Fang, Li, Guo et al., (2018) reported that the major crystalline phases of SSA are anorthite, quartz, hematite, whitlockite, calcium silicate, and albite. J. Li et al., (2018) reported that the major crystalline phases of SSA are quartz, anorthite, whitlockite, hematite, and a low amount of berlinite ($AlPO_4$), and giniite ($Fe^{2+}Fe^{3+}{}_4(PO_4)_4(OH)_2.2(H_2O)$). Other researchers (Mahieux, Aubert, Cyr, Coutand, & Husson, 2010) reported the major crystalline phases to be whitlockite, quartz, gypsum ($CaSO_4.2H_2O$), feldspar, and a low amount of mica. The minerals in crystalline phases in this study's ash samples agree with the literature.

Whitlockite, berlinite, calcium phosphate, and stanfieldite are reported to be present in SSA as phosphate forms (Gorazda et al., 2016). BF-Ash (Fig. 5) contained crystalline peaks of whitlockite ($Ca_9(MgFe)(PO_4)_6PO_3OH$) (17.38%) and stanfieldite ($Mg_3C_3(PO_4)_4$) (12.59%) as phosphates, whereas MC-Ash (Fig. 6) exhibited the peaks of whitlockite ($Ca_9(MgFe)(PO_4)_6PO_3OH$) (19.29%) and apatite ($Ca_5(PO_4)_3$) (4.67%). XRD analysis results support that the P_2O_5 content of BF-Ash was higher than that of MC-Ash. As can be seen in Fig. 5 and Fig. 6, the crystalline peaks of phosphates of BF-Ash (29.97%) were higher than that of MC-Ash (23.96%).

3.2. Phosphorus extraction

The types of the acids used in this study, their concentrations, and the pH levels of the solutions before and after extraction are shown in Table 3. As shown in Table 3, the pH levels of the solutions before and after acid extraction decreased with the increase in the acid concentration, as

expected. J. Li et al., (2018) reported the initial pH values of the sulfuric acid, nitric acid, oxalic acid, and citric acid solutions as 0.89, 0.85, 1.01, and 1.70, respectively, for a concentration of 0.5 mol/L. In this study, the initial pH values of the sulfuric acid, nitric acid, oxalic acid, and citric acid solutions were measured as 0.7, 0.8, 1.3, and 1.7, respectively, for a concentration of 0.5 mol/L. After acid extraction, the pH levels were reported as 1.14, 0.97, 1.03, and 2.55 for sulfuric acid, nitric acid, oxalic acid, and citric acid solutions, respectively, for 0.5 mol/L concentrations by J. Li et al., (2018). The increases in the pH levels when ashes were introduced to the acid solutions in this study were higher than the increase reported by J. Li et al., (2018). This could be explained by the higher alkalinity of both BF-Ash (pH=12.3), and MC-Ash (pH=11.9) compared to that reported by J. Li et al., (2018) (pH=8.45).

Table 3 *Types of the acids used in this study and the pH levels of the solutions before and after extraction*

Leaching Acid		Concentration (mol/L)	pH		
			Before Extraction	After Extraction	
				BF-Ash	MC-Ash
Inorganic Acids	Sulfuric Acid (H_2SO_4)	0.1	1.2	6.5	8.6
		0.2	0.9	3.9	6
		0.5	0.7	1.2	1.1
		1.0	0.6	0.9	0.7
	Nitric Acid (HNO_3)	0.1	1.2	8.5	11
		0.2	1	5.9	7.7
		0.5	0.8	2.5	4.4
		1	0.5	0.8	0.6
Organic Acids	Oxalic Acid ($C_2H_2O_4$)	0.1	1.5	6.1	7.1
		0.2	1.3	3.9	3.8
		0.5	1.3	1.5	1.4
		1	1.1	1.3	1.2
	Citric Acid ($C_6H_8O_7$)	0.1	2.2	4.5	4.1
		0.2	1.7	3.6	3.9
		0.5	1.7	2.9	3.1
		1	1.5	2.4	2.6

The phosphorus levels extracted from ashes are shown in Fig. 7 and Fig. 8 for BF-Ash and MC-Ash, respectively.

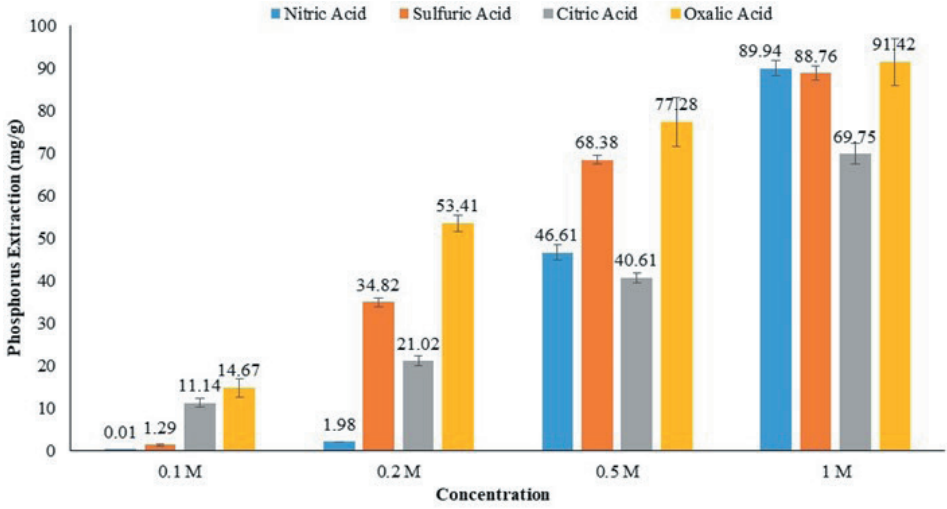

Fig. 7 *The levels of phosphorus extracted from BF-Ash by using different types of acids in different concentrations*

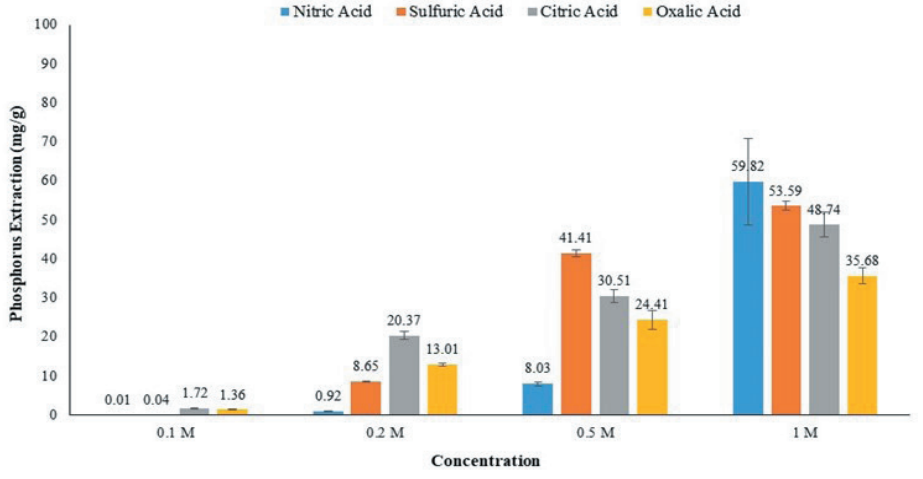

Fig. 8 *The levels of phosphorus extracted from MC-Ash by using different types of acids in different concentrations*

When sewage sludge ashes were treated with inorganic acids (0.1 mol/L), the phosphorus level extracted from BF-Ash was measured as 0.01 mg/g in nitric acid and 1.29 mg/g in sulfuric acid. The phosphorus level extracted from MC-Ash was 0.01 mg/g in nitric acid and 0.04 in sulfuric acid. For organic acids (0.1 mol/L), the phosphorus extracted level from BF-Ash was 11.14 mg/g in citric acid and 14.67 mg/g in oxalic acid, whereas the phosphorus extracted level from MC-Ash was 1.72 mg/g in citric acid and 1.36 mg/g in oxalic acid. Organic acids were more effective than inorganic acids at low concentrations of acid solutions. A similar trend was

reported by Fang, Li, Guo, et al., (2018); phosphorus levels extracted from SSA was 2 mg/g in nitric acid solution with a concentration of 0.1 mol/L, ~7 mg/g in sulfuric acid solution, ~12 mg/g in oxalic acid solution, and ~18 mg/g in citric acid solution. As shown in Fig. 8, the phosphorus level extracted from the MC-Ash was close to zero at a concentration of 0.1 M for inorganic acids. Increasing the acid concentration increased phosphorus extracted from both BF-Ash (Fig. 7) and MC-Ash (Fig. 8), especially for nitric acid, which is in agreement with the literature (Fang, Li, Guo, et al., 2018). Fang, Li, Guo, et al., (2018) reported that the extracted phosphorus level increased to 36 mg/g from 2 mg/g as the nitric acid concentration increased to 0.5 M from 0.1 M.

Extracted phosphorus levels from BF-Ash ranged between 1.29-88.76 mg/g in sulfuric acid solutions with different molarities, and 0.01-89.94 mg/g in nitric acid solutions (Fig. 7). Phosphorus levels from MC-Ash ranged between 0.04-53.9 mg/g in sulfuric acid solutions with different molarities, and 0.01-59.82 mg/g in nitric acid solutions (Fig. 8). When MC-Ash was treated with inorganic acids at 1 mol/L concentration, the phosphorus levels were measured as 59.82 mg/g and 53.59 mg/g in nitric acid and sulfuric acid solutions, respectively. However, sulfuric acid was clearly more effective than nitric acid at 0.2 mol/L and 0.5 mol/L for MC-Ash. When inorganic acids were compared, sulfuric acid had higher phosphorus releasing capacity than nitric acid for BF-Ash. Several researchers (Fang, Li, Guo, et al., 2018; J. Li et al., 2018) reported similar results where sulfuric acid was more effective than nitric acid. This can be explained that sulfuric acid has double H^+ ions at the same concentration compared to nitric acid (J. Li et al., 2018).

When organic acids were considered, the phosphorus levels from BF-Ash ranged between 14.67 mg/g-91.42 mg/g and 11.14 mg/g-69.75 mg/g for oxalic acid and citric acid, respectively (Fig. 7). Oxalic acid was found to be more effective compared to citric acid in terms of phosphorus extraction from BF-Ash. The level of extracted phosphorus from BF-Ash was 28% in 0.2 mol/L citric acid and 70% in 0.2 mol/L oxalic acid solution. Fang, Li, Guo, et al., (2018) reported similar results, where oxalic acid solution of 0.2 mol/L was more effective (>95%) than citric acid solution (approximately 80%). Abis et al., (2018) reported oxalic acid to be the most effective acid, followed by sulfuric acid for their research with 0.4 mol/L solutions of oxalic acid, sulfuric acid, citric acid, and lactic acid. The extraction results of BF-Ash agree with the literature (Abis et al., 2018); however, MC-Ash extraction yielded a different ordinance where citric acid was more effective than oxalic acid. Phosphorus from MC-Ash ranged between 1.36 and 35.68 mg/g in oxalic acid and 1.72 and 48.74 mg/g in citric acid (Fig. 8).

In this study, phosphorus could not be extracted from BF-Ash and MC-Ash with distilled water. Xu et al., (2012) reported that phosphorus extraction was less than 0.2% when distilled water was used. Wang et al., (2018) reported that phosphorus extraction was close to zero when distilled water was used. Several researchers (Adam et al., 2009; Wang et al., 2018) reported that phosphorus compounds in sewage sludge ashes were water-insoluble.

More phosphorus was released from BF-Ash than MC-Ash. Gorazda et al., (2016) reported that phosphorus extraction was more effective when sewage sludge ash had a high P/Ca mass ratio. According to XRF analysis (Table 2), the P/Ca ratio was determined at 0.54 for BF-Ash and 0.42 for MC-Ash, which agrees with Gorazda et al., (2016). The finer particle size of BF-Ash may have facilitated the extraction providing a larger surface area than that of MC-Ash and resulting in more phosphorus extraction.

3.3. Phase distribution and microstructure of the residues after acid extraction

XRD analyzes and SEM images of BF-Ash residues and MC-Ash residues produced after extraction at 0.5 mol/L concentration were examined to infer the effect of acid extraction on the microstructure. SEM images (x1000 magnifications) of the residues produced after extraction with BF-Ash are given in Fig. 9.

Compared to the SEM images of the untreated BF-Ash (Fig. 9a), the large and irregular plate-like pieces were not observed in BF-Ash residues after acid extraction. After extraction by both inorganic acid (Fig. 9b) and organic acid (Fig. 9c and Fig. 9d), the BF-Ash particles were broken down into smaller particles. The BF-Ash residue treated by sulfuric acid presented small particles, rod-like particles, and spheres particles (Fig. 9b). After extraction by organic acids (Fig. 9c and Fig. 9d), agglomeration of the BF-Ash particles was observed. BF-Ash residues treated by both oxalic acid and citric acid exhibited loose structures. J. Li et al., (2018) reported similar findings for oxalic acid treatment. As shown in Fig. 9d, the BF-Ash residue treated by citric acid presented a smooth spherical surface. The agglomeration was much more evident for organic acid treatments than inorganic acid treatment.

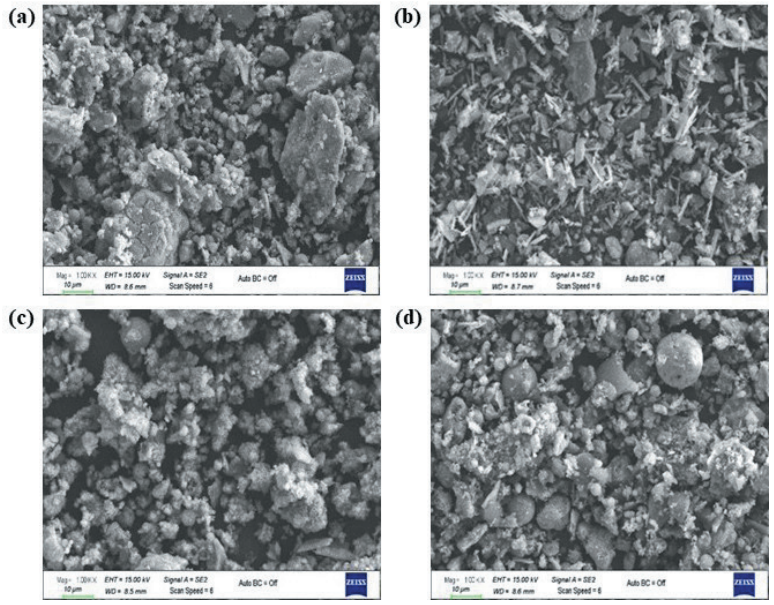

Fig. 9 *SEM images (x1000) of BF-Ash and residues a)BF-Ash b)Residue of sulfuric acid c)Residue of oxalic acid d)Residue of citric acid*

SEM image (x1000) of the residue produced after sulfuric acid extraction at 0,5 mol/L with MC-Ash is given in Fig. 10. Porous particles were not observed in MC-Ash residue after sulfuric acid extraction (Fig. 10b) compared to the untreated MC-Ash (Fig. 10a). After extraction by sulfuric acid, porous particles in MC-Ash were broken down into smaller particles, and rod-like particles were observed, as shown in Fig. 10b. MC-Ash residue (Fig. 10b) contained more agglomerates than the BF-Ash residue treated by sulfuric acid (Fig. 9b)

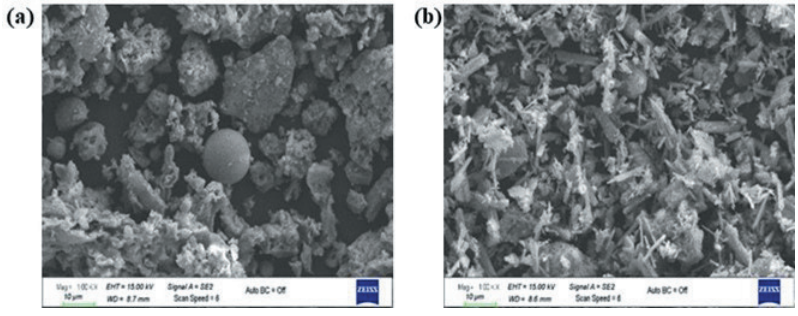

Fig. 10 *SEM images (x1000) of MC-Ash and residues a)MC-Ash b)Residue of sulfuric acid*

SEM images of the representative region of the solid residues are shown in Fig. 11, and their EDX analysis is given in Table 4. As shown in Table 4, the first sampling point (Fig. 11a) of BF-Ash residue treated

by sulfuric acid showed the presence of O (34.88%) and Fe (16.84%); the second sampling point (Fig. 11b) exhibited O (47.56%), and Si (32.17%), predominantly. The possible content for the first sampling point of BF-Ash residue treated by sulfuric acid for SEM/EDX analysis in Fig. 11 a could be Fe_2O_3. It was observed that SiO_2 (Fig. 4a) in BF-Ash, which has a large structure, was transformed into a smooth spherical surface in the BF-Ash residue treated by sulfuric acid (Fig. 11b).

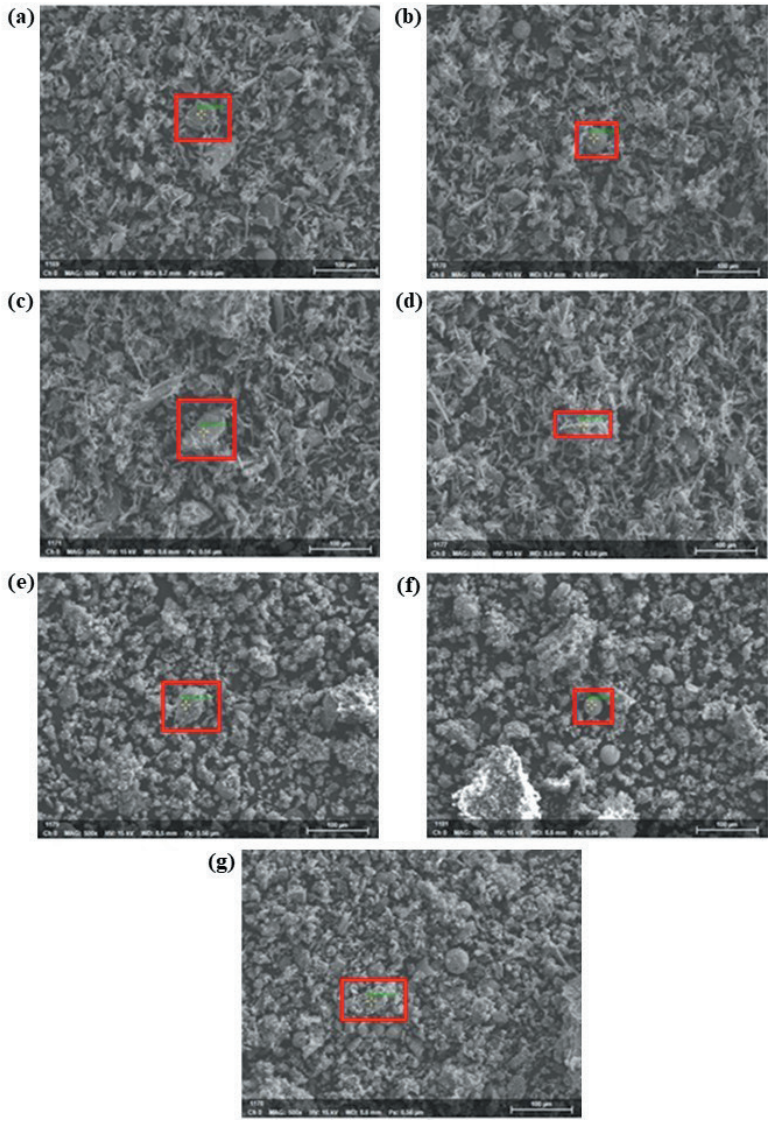

Fig. 11 *SEM/EDX images of solid residues a)Sulfuric Acid BF-Ash (FSP) b) Sulfuric Acid BF-Ash (SSP) c)Sulfuric Acid MC-Ash (FSP) d)Sulfuric Acid MC-Ash (SSP) e)Oxalic Acid BF-Ash (FSP) f)Oxalic Acid BF-Ash (SSP) g)Citric Acid BF-Ash, (*FSP: First sampling point, **SSP: Second sampling point)*

As given in Table 4, the first sampling point (Fig. 11c) of MC-Ash residue treated by sulfuric acid showed the presence of O (49.35%) and Si (21.94%), so the possible content for the residue in Fig. 11c could be SiO_2. The second sampling point (Fig. 11d) of MC-Ash residue treated by sulfuric acid exhibited O (56.99%), Ca (17.13%), and S (11.99%), predominantly. Therefore, the possible content for the rod-like particle in Fig. 11d could be $CaSO_4$. The research reported by J. Li et al., (2018) showed that $CaSO_4$ was determined in residue treated by sulfuric acid.

Table 4 shows that the first sampling point (Fig. 11e) of oxalic acid-treated residue contains the highest C level (15.61%) compared to all samples. This sample exhibited O (22.42%) and Ca (18.16%). Therefore, the possible content for the sample for SEM/EDX analysis in Fig. 11 e could be calcium oxalate. Several researchers (Liang et al., 2019, 2021) reported that EDS analysis of the sewage sludge ash residue treated by oxalic acid contained calcium oxalate hydrate crystal and calcium oxalate. The second sampling point (Fig. 11f) of BF-Ash residue treated by oxalic acid showed the presence of O (48.36%) and Si (16.93%), so the spherical particle in Fig. 11f could be SiO_2. J. Li et al., (2018) reported that SEM-EDS analysis of the residue after extraction with oxalic acid was found to be silicon oxide. The BF-Ash residue treated by citric acid (Fig. 11g) exhibited the O (41.63%), Fe (21.06%), and Si (16.63%), predominantly. Possible content for the residue in Fig. 11g could be Fe_2O_3 or SiO_2. The SEM/EDX analysis of residues treated by acids mostly included SiO_2 due to the high SiO_2 content of sewage sludge ash.

Table 4 *EDX analysis of residues after acid extraction*

Element (%)	Sulfuric Acid (BF-Ash) FSP*	Sulfuric Acid (BF-Ash) SSP**	Sulfuric Acid (MC-Ash) FSP*	Sulfuric Acid (MC-Ash) SSP*	Oxalic Acid (BF-Ash) FSP*	Oxalic Acid (BF-Ash) SSP*	Citric Acid (BF-Ash)
O	34.88	47.56	49.35	56.99	22.42	48.36	41.63
Fe	16.84	4.18	9	9.53	8.84	10.75	21.06
Ca	14.18	2.93	1.26	17.13	18.16	4.14	11.63
Si	14.36	32.17	21.94	4.34	21	16.93	16.63
Al	10.28	4.07	5.45	0.00	0.79	5.09	2.05
Cu	8.32	0.15	0.00	0.00	11.21	0.00	0.19
C	1.15	3.27	3.43	0.00	15.61	8.44	0.29
K	0.00	1.83	3.95	0.00	1.96	2.72	0.65
P	0.00	1.34	0.11	0.00	0.00	1.5	3.84
Mg	0.00	1.59	0.18	0.00	0.00	2.08	0.00
S	0.00	0.29	0.62	11.99	0.00	0.00	1.2

Ti	0.00	0.62	0.61	0.00	0.00	0.00	0.00
Zn	0.00	0.00	3.53	0.00	0.00	0.00	0.81
Na	0.00	0.00	0.57	0.00	0.00	0.00	0.00

*FSP: First sampling point, **SSP: Second sampling point

The XRD analysis of sewage sludge ash residues treated by acids and the distributions of their crystalline phases are shown in Fig. 12. As shown in Fig. 12a, the rates of crystalline and amorphous phases were 76.3% and 23.7%, respectively, for BF-Ash residue treated by sulfuric acid. The crystalline phases were: bassanite ($CaSO_4.0.5H_2O$) (45.7%), quartz (SiO_2) (11.22%), anhydrite ($CaSO_4$) (9.46%), hematite (Fe_2O_3) (6.49%), and aluminum phosphate ($AlPO_4$) (3.43%). For MC-Ash residue treated by sulfuric acid (Fig. 12b), the rate of crystalline and amorphous phases were 74.9% and 25.1%, respectively. The crystalline phases were: bassanite ($CaSO_4.0,5H_2O$) (31.16%), quartz (SiO_2) (20.45%), anhydrite ($CaSO_4$) (9.71%), anorthite ($CaAl_2Si_2O_8$) (5.39%), hematite (Fe_2O_3) (4.72%) and aluminum phosphate ($AlPO_4$) (3.45%). Both of the ashes contained whitlockite (calcium phosphate). However, their residues treated with sulfuric acid did not contain it. This could be explained by the release of whitlockite into the liquid phase. Liang et al., (2019) reported that minerals containing phosphorus were dissolved when sewage sludge ash was treated with sulfuric acid and also underlined the presence of quartz and hematite in the H_2SO_4 treated ash residue.

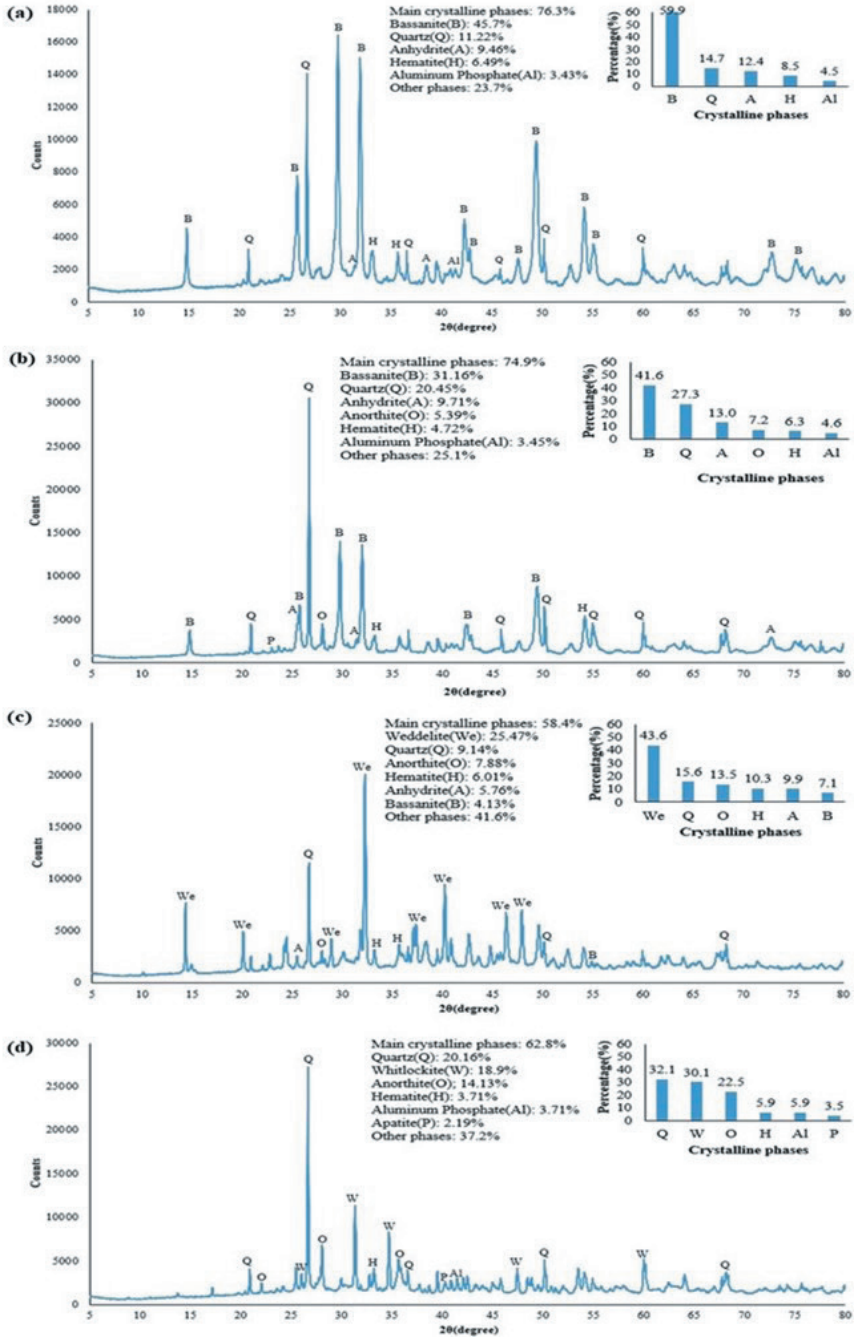

Fig. 12 *XRD analysis of residues after acid extraction a)Sulfuric acid BF-Ash b) Sulfuric Acid MC-Ash c)Oxalic acid BF-Ash d)Citric acid BF-Ash*

J. Li et al., (2018) reported the presence of quartz, bassanite, anorthite, and berlinite in residue treated by sulfuric acid. BF-Ash (Fig. 5) contained crystalline peaks of anhydrite ($CaSO_4$) (16.19%) as calcium sulfates, whereas in BF-Ash residue treated by sulfuric acid (Fig. 12a) detected the peaks of anhydrite ($CaSO_4$) (9.46%) and bassanite ($CaSO_4 \cdot 2H_2O$) (45.7%). $CaSO_4$ in BF-Ash transformed to aqueous form as basanite in the residue after sulfuric acid extraction. The MC-Ash residue treated by sulfuric acid (Fig. 12b) contained crystalline peaks of bassanite ($CaSO_4.0.5H_2O$) (31.16%) and anhydrite ($CaSO_4$) (9.71%) as calcium sulfates. The level of bassanite in the MC-Ash (Fig. 6) increased from 6.57% to 31.16% in the residue treated by sulfuric acid (Fig. 12b). Calcium sulfates might have transformed into the aqueous phase.

MC-Ash contained basanite before sulfuric acid extraction; however, BF-Ash did not contain it. Nevertheless, the bassanite level of BF-Ash residue treated by sulfuric acid (45.7%) was higher than that of MC-Ash residue (31.16%). XRD analysis of both the BF-Ash (Fig. 12a) and MC-Ash (Fig. 12b) residues treated by sulfuric acid presented a high basanite and $CaSO_4$ level. After sulfuric acid washing, calcium and phosphorus in whitlockite, a component of sewage sludge, dissolved, and $CaSO_4$ was observed in the ash residue in the literature (S. Donatello, Freeman-Pask, Tyrer, & Cheeseman, 2010).

The rates of crystalline and amorphous phases were 58.4% and 41.6%, respectively, for BF-Ash residue treated by oxalic acid (Fig. 12c). The main crystalline phases of BF-Ash residue were: weddellite ($CaC_2O_4.H_2O$) (25.47%), quartz (SiO_2) (9.14%), anorthite ($CaAl_2Si_2O_8$) (7.88%), hematite (Fe_2O_3) (6.01%), anhydrite ($CaSO_4$) (5.76%), and bassanite ($CaSO_4.0.5H_2O$) (4.13%). Weddellite was the main crystalline phase of BF-Ash oxalic acid residue with a level of 25.47%. Liang et al., (2021) that $CaC_2O_4.H_2O$ was found in ash residue treated by oxalic acid. J. Li et al., (2018) also reported that this residue contained calcium oxalate, hematite, and anorthite.

For BF-Ash residue treated by citric acid (Fig. 12d), the rates of crystalline and amorphous phases were found to be 62.8% and 37.2%, respectively. The crystalline phases were: quartz (SiO_2) (20.16%), whitlockite ($Ca_2.71Mg0.29(PO_4)_2$) (18.9%), anorthite ($CaAl_2Si_2O_8$) (14.13%), hematite (Fe_2O_3) (3.71%), aluminum phosphate ($AlPO_4$) (3.71%) and apatite ($Ca_5(PO_4)_3$) (2.19%). J. Li et al., (2018) reported the presence of quartz, hematite, and anorthite in the residue treated by citric acid. Whitlockite in BF-Ash was observed in the citric acid residue (Fig. 12d), although not observed in the sulfuric acid residue (Fig. 12a) and oxalic acid residue (Fig. 12c). Whitlockite may have dissolved by sulfuric acid and oxalic acid but not by citric acid. This result agrees with the phosphorus extraction data in Fig. 7. The level of extracted phosphorus from BF-Ash

in citric acid at a concentration of 0.5 mol/L was lower than the amount of phosphorus extracted in sulfuric acid and oxalic acid (Fig. 7).

The crystalline phases rates of untreated BF-Ash (Fig. 5) and BF-Ash residue treated by sulfuric acid (Fig. 12a) were 59.1% and 76.3%, respectively. On the other hand, the crystalline phases rates of untreated MC-Ash (Fig. 6) and MC-Ash residue treated by sulfuric acid (Fig. 12b) were 67.7% and 74.9%, respectively. The rates of crystalline phases of the residues were higher than those of the amorphous phases. The crystalline phases of both of the residues increased after sulfuric acid extraction. J. Li et al., (2018) reported a similar finding, where the rate of crystalline phases in the ash increased from 40.22% to 76.12% after extraction with sulfuric acid.

When organic acids were used to extract BF-Ash, the ratios of crystalline phase in residues were 58.4% (Fig. 12c) and 62.8% (Fig. 12d) for oxalic acid and citric acid treatments, respectively. J. Li et al., (2018) reported that the rates of crystalline phases were 87.67% and 85.33% for oxalic and citric acid-treated residues, respectively. The rates of crystalline phases did not significantly change with organic acid treatment. The increase in the crystalline phase was more noticeable when inorganic acid was used.

The hematite level in BF-Ash increased in BF-Ash residues, except for the residue treated by citric acid. When MC-Ash was extracted with sulfuric acid, the hematite level increased in MC-Ash residue. Fang, Li, Guo, et al., (2018) reported a similar finding, where the hematite level in the residue increased after the treatment of the ash by organic and inorganic acids.

4. Conclusions

This study investigated the phosphorus recovery potential of sewage sludge ashes originating from different air pollution control units. The P_2O_5 levels of BF-Ash and MC-Ash were found as high as 17.36% and 11.49%, respectively. BF-Ash contained more phosphorus than MC-Ash. The ratios of P_2O_5 contents of the ashes are similar to those of phosphate rocks. The average particle size of BF-Ash and MC-Ash was determined as 16,093 μm and 44,701 μm, respectively. BF-Ash had a finer particle size distribution than MC-Ash. The extracted phosphorus levels ranged between 0.01-91.42 mg/g and 0.01-59.82 mg/g for BF-Ash and MC-Ash, respectively. Phosphorus leaching from BF-Ash was higher than that from MC-Ash. The levels of the extracted phosphorus increased from both ash types as the acid concentration increased. Organic acids were more effective than inorganic acids in terms of phosphorus releasing, especially at low concentrations of acid solutions. When organic acids were considered, oxalic acid extracted more phosphorus than citric acid. Sulfuric acid was more effective than nitric acid among inorganic acids. Phosphorus could not be extracted from both ash types by using distilled water.

The rates of the crystalline and amorphous phases of BF-Ash were 59.1% and 40.9%, respectively. Crystalline and amorphous phases of MC-Ash were 67.7% and 32.3%, respectively. Sulfuric acid extraction of both ashes resulted in increases in the crystalline phases. The rates of crystalline phases of BF-Ash and MC-Ash residues were 76.3% and %74.9, respectively. The ratios of amorphous phases in BF-Ash and MC-Ash residues decreased from 40.9% and 32.3% to 23.7 and 25.1%, respectively, with the influence of sulfuric acid extraction. Changes in the crystalline phase ratios were not significant after organic acid extraction. The rate of crystalline phase of BF-Ash residue was 58.4% after oxalic acid extraction. BF-Ash extracted by using citric acid resulted in a crystalline phase rate of 62.8%.

Although both ashes contained whitlockite (calcium phosphate), their sulfuric acid residues did not include it. The phosphorus release into the liquid phase may explain this, so whitlockite did not remain in the residues. Whitlockite in BF-Ash was observed in the citric acid residue, although not in the sulfuric acid and oxalic acid residues. It can be inferred that whitlockite was dissolved by sulfuric acid and oxalic acid but not by citric acid. After acid extraction of BF-Ash, the agglomeration was much more evident for organic acids than inorganic acid (e.g., sulfuric acid). It was observed that the MC-Ash residue treated by sulfuric acid contained more agglomerates than the BF-Ash residue treated by sulfuric acid. The SEM/EDX and XRD analysis of BF-Ash residue treated with oxalic acid showed the presence of calcium oxalate.

Considering the high phosphate levels in the ashes and their solutions after acid leaching, it can be inferred that both ashes are promising as phosphorus resources. When both ashes were compared, BF-Ash was found to have a higher phosphorus recovery potential than MC-Ash.

Phosphorus recovery from sewage sludge ash is a sustainable waste management method. It supports the circular economy approach since utilizing sewage sludge ashes as a phosphorus source, which is a waste otherwise, would bring economic benefits.

Acknowledgment

This work was supported by The Scientific and Technological Research Council of Turkey (TUBITAK) -BIDEB 2210/C National MSc Scholarship Program in the Priority Fields in Science and Technology. Author Ezgi Karabacak has received scholarship under the above mentioned program. The authors would like to thank Bursa Cement Factory Co. Inc. and Bursa Water and Sewerage Administration (BUSKI) authorities and staff for their help in the analysis of sewage sludge ashes and other samples.

REFERENCES

Abis, M., Calmano, W., & Kuchta, K. (2018). Innovative technologies for phosphorus recovery from sewage sludge ash. *Detritus*, *1*, 23–29.

Adam, C., Peplinski, B., Michaelis, M., Kley, G., & Simon, F. G. (2009). Thermochemical treatment of sewage sludge ashes for phosphorus recovery. *Waste Management*, *29*(3), 1122–1128.

Anderson, M. (2002). Encouraging prospects for recycling incinerated sewage sludge ash (ISSA) into clay-based building products. *Journal of Chemical Technology & Biotechnology*, *77*(3), 352–360.

Azuara, M., Kersten, S. R. A., & Kootstra, A. M. J. (2013). Recycling phosphorus by fast pyrolysis of pig manure: Concentration and extraction of phosphorus combined with formation of value-added pyrolysis products. *Biomass and Bioenergy*, *49*, 171–180.

Bindraban, P. S., Dimkpa, C. O., & Pandey, R. (2020). Exploring phosphorus fertilizers and fertilization strategies for improved human and environmental health. *Biology and Fertility of Soils*, *56*(3), 299–317.

Biswas, B. K., Inoue, K., Harada, H., Ohto, K., & Kawakita, H. (2009). Leaching of phosphorus from incinerated sewage sludge ash by means of acid extraction followed by adsorption on orange waste gel. *Journal of Environmental Sciences*, *21*(12), 1753–1760.

Brunner, P. H. (2010). Substance Flow Analysis as a Decision Support Tool for Phosphorus Management. *Journal of Industrial Ecology*, *14*(6), 870–873.

Chen, Z., Li, J. S., & Poon, C. S. (2018). Combined use of sewage sludge ash and recycled glass cullet for the production of concrete blocks. *Journal of Cleaner Production*, *171*, 1447–1459.

Cieślik, B., & Konieczka, P. (2017). A review of phosphorus recovery methods at various steps of wastewater treatment and sewage sludge management. The concept of "no solid waste generation" and analytical methods. *Journal of Cleaner Production*, *142*, 1728–1740.

Cooper, J., Reed, E. Y., Hörtenhuber, S., Lindenthal, T., Løes, A. K., Mäder, P., … Möller, K. (2018). Phosphorus availability on many organically managed farms in Europe. *Nutrient Cycling in Agroecosystems*, *110*(2), 227–239.

Cornel, P., & Schaum, C. (2009). Phosphorus recovery from wastewater: Needs, technologies and costs. *Water Science and Technology*, *59*(6), 1069–1076.

Coutand, M., Cyr, M., & Clastres, P. (2006). Use of sewage sludge ash as mineral admixture in mortars. *Proceedings of Institution of Civil Engineers: Construction Materials*, *159*(4), 153–162.

Donatello, S., Freeman-Pask, A., Tyrer, M., & Cheeseman, C. R. (2010). Effect of milling and acid washing on the pozzolanic activity of incinerator sewage sludge ash. *Cement and Concrete Composites*, *32*(1), 54–61.

Donatello, S., Tong, D., & Cheeseman, C. R. (2010). Production of technical grade phosphoric acid from incinerator sewage sludge ash (ISSA). *Waste Management*, *30*(8–9), 1634–1642.

Donatello, Shane, & Cheeseman, C. R. (2013). Recycling and recovery routes for incinerated sewage sludge ash (ISSA): A review. *Waste Management*, *33*(11), 2328–2340.

Egle, L., Rechberger, H., Krampe, J., & Zessner, M. (2016). Phosphorus recovery from municipal wastewater: An integrated comparative technological, environmental and economic assessment of P recovery technologies. *Science of the Total Environment*, *571*, 522–542.

ETI. (2021). Mazidagi Phosphate Plant, ETI BAKIR. Retrieved 11 December 2021, from https://etibakir.com.tr/plants/mazidagi-phospate-plant/?lang=en

Fang, L., Li, J., Guo, M. Z., Cheeseman, C. R., Tsang, Daniel, C. W., Donatello, S., & Poon, C. S. (2018). Phosphorus recovery and leaching of trace elements from incinerated sewage sludge ash (ISSA). *Chemosphere*, *193*, 278–287.

Fang, L., Li, J. shan, Donatello, S., Cheeseman, C. R., Wang, Q., Poon, C. S., & Tsang, D. C. W. (2018). Recovery of phosphorus from incinerated sewage sludge ash by combined two-step extraction and selective precipitation. *Chemical Engineering Journal*, *348*, 74–83.

Filippelli, G. M. (2011). Phosphate rock formation and marine phosphorus geochemistry: The deep time perspective. *Chemosphere*, *84*(6), 759–766.

Franz, M. (2008). Phosphate fertilizer from sewage sludge ash (SSA). *Waste Management*, *28*(10), 1809–1818.

Gao, B., Fedje, K. K., & Strömvall, A.-M. (2015). Phosphorus Recovery from Sorted Municipal Solid Waste Incineration Ash. *The Journal of Solid Waste Technology and Management*, *41*(3), 249–261.

Gorazda, K., Tarko, B., Kominko, H., Worek, Z., & Nowak, A. K. (2019). *Phosphate industry in the balance of sustainable development and circular economy*. In *HERAKLION 2019 7th International Conference on Sustainable Solid Waste Management* (pp. 1–16).

Gorazda, K., Tarko, B., Wzorek, Z., Nowak, A. K., Kulczycka, J., & Henclik, A. (2016). Characteristic of wet method of phosphorus recovery from polish sewage sludge ash with. *Open Chemistry*, *14*(1), 37–45.

Guedes, P., Couto, N., Ottosen, L. M., & Ribeiro, A. B. (2014). Phosphorus recovery from sewage sludge ash through an electrodialytic process. *Waste Management*, *34*(5), 886–892.

Herzel, H., Krüger, O., Hermann, L., & Adam, C. (2016). Sewage sludge ash - A promising secondary phosphorus source for fertilizer production. *Science of the Total Environment*, *542*, 1136–1143.

Jin, Y., Hu, Z., & Wen, Z. (2009). Enhancing anaerobic digestibility and phospho-

rus recovery of dairy manure through microwave-based thermochemical pretreatment. *Water Research*, *43*(14), 3493–3502.

Kalmykova, Y., & Karlfeldt Fedje, K. (2013). Phosphorus recovery from municipal solid waste incineration fly ash. *Waste Management*, *33*(6), 1403–1410.

Kosson, D. S., van der Sloot, H. A., & Eighmy, T. T. (1996). An approach for estimation of contaminant release during utilization and disposal of municipal waste combustion residues. *Journal of Hazardous Materials*, *47*(1–3), 43–75.

Li, J., Chen, Z., Wang, Q., Fang, L., Xue, Q., Cheeseman, C. R., … Poon, C. S. (2018). Change in re-use value of incinerated sewage sludge ash due to chemical extraction of phosphorus. *Waste Management*, *74*, 404–412.

Li, R., Zhao, W., Li, Y., Wang, W., & Zhu, X. (2015). Heavy metal removal and speciation transformation through the calcination treatment of phosphorus-enriched sewage sludge ash. *Journal of Hazardous Materials*, *283*, 423–431.

Liang, S., Chen, H., Zeng, X., Li, Z., Yu, W., Xiao, K., … Yang, J. (2019). A comparison between sulfuric acid and oxalic acid leaching with subsequent puri fi cation and precipitation for phosphorus recovery from sewage sludge incineration ash. *Water Research*, *159*, 242–251.

Liang, S., Yang, L., Chen, H., Yu, W., Tao, S., Yuan, S., … Yang, J. (2021). Phosphorus recovery from incinerated sewage sludge ash (ISSA) and reutilization of residues for sludge pretreated by different conditioners. *Resources, Conservation and Recycling*, *169*, 105524.

Lim, B. H., & Kim, D. J. (2017). Selective acidic elution of Ca from sewage sludge ash for phosphorus recovery under pH control. *Journal of Industrial and Engineering Chemistry*, *46*, 62–67.

Liu, W., Iordan, C. M., Cherubini, F., Hu, X., & Fu, D. (2021). Environmental impacts assessment of wastewater treatment and sludge disposal systems under two sewage discharge standards: A case study in Kunshan, China. *Journal of Cleaner Production*, *287*, 125046.

Lynn, C. J., Dhir, R. K., Ghataora, G. S., & West, R. P. (2015). Sewage sludge ash characteristics and potential for use in concrete. *Construction and Building Materials*, *98*, 767–779.

Mahieux, P. Y., Aubert, J. E., Cyr, M., Coutand, M., & Husson, B. (2010). Quantitative mineralogical composition of complex mineral wastes - Contribution of the Rietveld method. *Waste Management*, *30*(3), 378–388.

Marani, D., Braguglia, C. M., Mininni, G., & Maccioni, F. (2003). Behaviour of Cd, Cr, Mn, Ni, Pb, and Zn in sewage sludge incineration by fluidised bed furnace. *Waste Management*, *23*(2), 117–124.

MTA. (2020). Mining foreign trade of Turkey in 2020. Mineral Research and Exploration General Directorate.

Murphy, J., & Riley, J. P. (1962). A modified single solution method for the determination of phosphate in natural waters. *Analytica Chimica Acta*, *27*, 31–36.

Oelkers, Eric. H., & Valsami-Jones, E. (2008). Phosphate Mineral Reactivity and Global Sustainability. *Elements*, *4*(2), 83–87.

Pettersson, A., Åmand, L.-E., & Steenari, B.-M. (2008a). Leaching of ashes from co-combustion of sewage sludge and wood—Part I: Recovery of phosphorus. *Biomass and Bioenergy*, *32*(3), 224–235.

Pettersson, A., Åmand, L.-E., & Steenari, B.-M. (2008b). Leaching of ashes from co-combustion of sewage sludge and wood—Part II: The mobility of metals during phosphorus extraction. *Biomass and Bioenergy*, *32*(3), 236–244.

Salihoglu, G., & Mardani-Aghabaglou, A. (2021). Characterization of sewage sludge incineration ashes from multi-cyclones and baghouse dust filters as possible cement substitutes. *Environmental Science and Pollution Research*, *28*(1), 645–663.

Selçuk Kuşçu, Ö., & Çelik, V. E. (2019). Recovery of Nitrogen And Phosphorus In Sewage Sludge by Pulsed Electrical Field Technique and Strüvite Production. *Pamukkale University Journal of Engineering Sciences*, *25*(6), 700–704.

Shiba, N. C., & Ntuli, F. (2017). Extraction and precipitation of phosphorus from sewage sludge. *Waste Management*, *60*, 191–200.

Smil, V. (2000). PHOSPHORUS IN THE ENVIRONMENT : Natural Flows and Human Interferences. *Annual Review of Energy and the Environment*, *25*(1), 53–88.

Stark, K., Plaza, E., & Hultman, B. (2006). Phosphorus release from ash, dried sludge and sludge residue from supercritical water oxidation by acid or base. *Chemosphere*, *62*(5), 827–832.

Szögi, A. A., Vanotti, M. B., & Hunt, P. G. (2015). Phosphorus recovery from pig manure solids prior to land application. *Journal of Environmental Management*, *157*, 1–7.

USGS. (2020). Mineral Commodity Summaries 2020-Phosphate Rock. U.S Geological Survey. Retrieved 6 February 2023, from https://pubs.usgs.gov/periodicals/mcs2020/mcs2020.pdf.

van Vuuren, D. P., Bouwman, A. F., & Beusen, A. H. W. (2010). Phosphorus demand for the 1970-2100 period: A scenario analysis of resource depletion. *Global Environmental Change*, *20*(3), 428–439.

Wang, Q., Li, J. shan, Tang, P., Fang, L., & Poon, C. S. (2018). Sustainable reclamation of phosphorus from incinerated sewage sludge ash as value-added struvite by chemical extraction, purification and crystallization. *Journal of Cleaner Production*, *181*, 717–725.

Xu, H., He, P., Gu, W., Wang, G., & Shao, L. (2012). Recovery of phosphorus as struvite from sewage sludge ash. *Journal of Environmental Sciences (China)*, *24*(8), 1533–1538.

Xue, Q., He, X., Sachs, S. D., Becker, G. C., Zhang, T., & Kruse, A. (2019). The current phosphate recycling situation in China and Germany: a comparative review. *Frontiers of Agricultural Science and Engineering*, *6*(4), 403–418.

Chapter 2

A SURVEY ON APPLICATION AREAS AND ADVANCED MATERIALS FOR BORON MINERALS

Fatma İrem ŞAHIN[1], Nil ACARALI[2]

1 Yildiz Technical University, Department of Chemical Engineering, Davutpasa Campus, 34220, Esenler-İstanbul, Türkiye.
2 Yildiz Technical University, Department of Chemical Engineering, Davutpasa Campus, 34220, Esenler-İstanbul, Türkiye.

1. INTRODUCTION

Boron, a semiconductor element between metal and nonmetal, was an important input to modern industry. It had low density, high melting and high evaporation temperature, mechanical features, and excellent neutron absorption capacity. Boron compounds with low volatility value without toxic gas release were environmentally friendly. It provided high technology product properties such as resistance to high temperatures and mechanical stress, specific electrical conductivity, chemical resistance, semi- or selective permeability to the materials. It was utilized in a variety of industries, including textiles, agriculture, detergent, refractory, ceramics, cement, glass, porcelain, aviation, and nuclear advancements, as minerals and compounds, as raw materials, semi-finished products, and end products. There were boron deposits concentrated in only a few regions on Earth, and 72% of their apparent reserves and 70% of the total reserves were in Turkey [1, 2].

2. BORON

Boron was represented in the periodic table by the notation B and was found in group 3A. It was not found as a free element in nature but existed in compounds with other elements. The element boron was a semi-metal and had semiconductor features. It could be used in a variety of industries due to the formation of compounds with varying properties with various metal or non-metallic elements. Appearance and structure of elemental boron was given in Figure 1 [3].

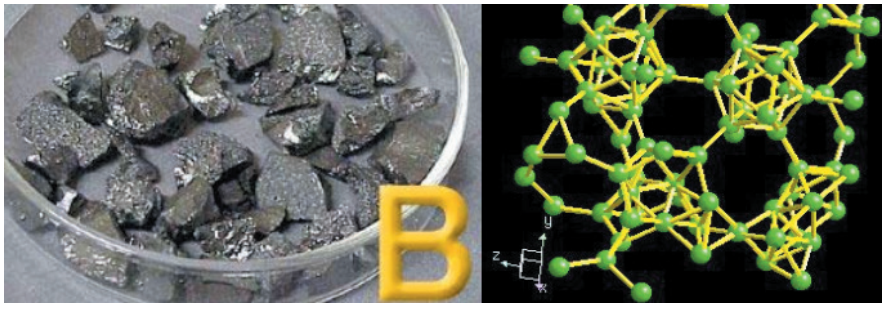

Figure 1. Appearance and structure of elemental boron [3]

Crystallized boron was like diamond in appearance and optical properties and was the hardest element after diamond. Amorphous boron reacted violently at micron scales, whereas crystalline boron reacted poorly. Boric acid was formed in reaction with mineral acids by generating a product with a slow or explosive effected based on the concentration and temperature [4-6].

Boron was used as a fire retardant and retardant due to its melting temperature of 2300°C or by adding in different proportions into materials

with this feature. Zinc borate, borax, ammonium fluoroborate products were fire-preventing, and they were a superior product as they could be used together with antimony trioxide, prolonging the rate of absorption of smoke, and suppressing even embers quickly [6, 7].

Since boron was prone to bond with oxygen, it formed many different oxygen compounds. These minerals had varying amounts of boron oxide in their formations. Boron containing minerals were shown in Figure 2 [7, 8].

Figure 2. Boron containing minerals (a) Borax (Tincal), (b) Ulexite, (c) Colemanite, (d) Kernite, (e) Probertite, (f) Pandermite [7, 8]

Many organic and inorganic boron compounds were obtained from the processing of boron minerals' main ingredients, borax, and boric acid. Borax (Tincal) ($Na_2B_4O_7.10H_2O$) was colourless and transparent. It could be found in pink, yellowish, and gray colours due to various impurities in its composition. It could decompose quickly and turned into tincalconite

by losing its water. Clays were found together with intercalated tincalconite and ulexite. It was found in the Eskişehir-Kırka deposit in Turkey. Ulexite ($NaCaB_5O_9.8H_2O$) was found in the form of massive, fibrous, and columnar. The pure one was white and was also found in gray hues. It was found together with hydroboracite, ulexite and probertite. It was located Kırka, Bigadiç and Emet in Turkey and Argentina in the world. Colemanite ($Ca_2B_6O_{11}.H_2O$) crystallized in the monoclinic system. It dissolved slowly in water, quickly dissolved in HCl. It was the most common among boron compounds. It was found as large, shiny, transparent crystals in ore cavities in clays. It was found in Emet, Bigadiç and Kestelek deposits in Turkey and USA in the world. Kernite ($Na_2B_4O_7.4H_2O$) was found as colourless, transparent white, elongated cluster crystals. It transformed into tincalconite under atmospheric conditions. It dissolved slowly in cold water. It was found in the deep parts of the Na-borate mass in Kırka, Turkey. In the world, it was found in Argentina and the USA. Probertite ($NaCaB_5O_9.5H_2O$) was off-white, light yellowish in colour and found in the form of radial and fibrous crystals. It was observed as a secondary mineral besides ulexite in the deposits. Pandermite ($Ca_2B_{10}O_{19}.7H_2O$) was white in colour and resembles limestone. It was observed in Sultançayırı and Bigadiç beds. It turned into colemanite and calcite. Hydroboracite ($CaMgB_6O_{11}.6H_2O$) occurred as randomly oriented and intersecting clusters of radial and needle-shaped crystals from a centre. It had a fibrous texture. It was found in white colour, sometimes in yellow or reddish colours depending on the impurities in it. It was found together with colemanite, ulexite, probertite, tunellite. It was mostly found in Emet Doğanlar İğdeköy area and Kestelek in Turkey [7, 8].

Boron was produced using specific techniques depending on the depth and physical makeup of the boron because production varies with location and depth. One of the most used methods in the world is the open pit method. It was the method of revealing the ore by removing the cover layer from the ore because of loosening the area where the ore was located close to the earth by drilling and blasting method. The closed caking pit method was used for ores that were difficult to extract with the open pit method. It was the process of extracting the ore by opening tunnels, it was a difficult and costly method. Solution mining method was used to extract boron minerals from the waters. It was the process of adding 5% HCl to the waterbed and waiting for a certain time, then pumping it to the surface and then adding lime to it. The ore preparation and enrichment method applied for each of the boron minerals included crushing, grinding, screening and classification processes depending on the general trend and demand in the market for the boron product to be produced, and showed similarities with the methods applied for other industrial raw materials [3, 9, 10].

3. BORON IN THE WORLD AND TURKEY

Human beings used boron mine for the first time 4000 years ago. Boron, which was utilized by many ancient civilizations for various purposes, in gold processing by Babylonians, Egyptians mummia, The Romans used glass in glass, and the ancient Greek and Romans used them for cleaning. Boron element was used in 875 for the first time in the construction of drugs. At the end of the 13th century, borax was brought to Europe from Tibet and was utilized as a brazing and glazing material at that time. Elemental boron was obtained in 1808 with a purity of not more than 50%, dark coloured and flammable. In 1895, boric oxide and magnesium were subjected to the reduction process to obtain elemental boron with a purity of about 86% and a high amount. The Moissan process formed the basis of today's commercial boron production [5, 11].

The important boron deposits and commercial boron reserves were mainly in Turkey, Russia, and USA in 3 different regions in the world. Turkey's share in the world's total boron reserves was more than 70%. These data showed that Turkey had the largest boron resources in the world. The importance and usage area of boron compounds, which had a wide variety of uses in the industry, had increased day by day. It was used as an indispensable element in more than 400 products. While only 10% of the boron ores produced in the world can be used directly, the remaining part of the ores was used to obtain boron refining products. World boron consumption generally tracked the trajectory of global economic growth [6]. Based on B_2O_3 world reserve amount was shown in Table 1 [12].

Table 1. Based on B_2O_3 world reserve amount [12]

Countries	Reserve Amount (Thousand Ton (Based on B_2O_3))	Distribution (%)
Turkey	956,000	73.6
Russia	100,000	7.7
USA	80,000	6.2
Peru	22,000	1.7
Argentina	9000	0.7
China	36,000	2.8
Bolivia	19,000	1.5
Chile	41,000	3.2
Kazakhstan	15,000	1.2
Serbia	21,000	1.6
Total	1,299,000	100

United States, Boron minerals and products in Western Europe and Japan were different. The most consumption in the United States was in the fiberglass production and insulation industry. In Western Europe, boron was consumed soap and detergent industry. The largest boron consumption took place in the textile and fiberglass industry in Japan. Mineral concentrates were used in some industries, while refined boron

products were utilized in others. In some cases, refined and concentrated boron products replaced each other according to convenience and price. The global distribution of boron reserves was shown in Figure 3 [13, 14].

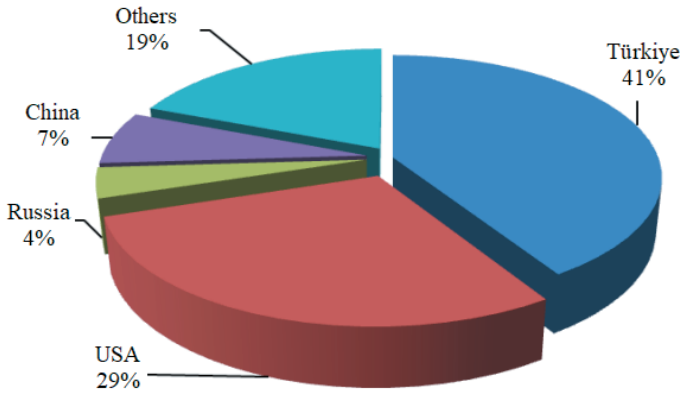

Figure 3. Distribution of world boron production by country [13]

Turkey had the world's largest and best quality boron reserves and, in parallel, became the country with the highest boron production in the world. The most abundant boron ores in Turkey in terms of reserves were tincal and colemanite Colemanite, a common calcium borate, was the dominant mineral in all borate deposits except Kırka. Ulexite and borax were important borate minerals [11]. Some places where boron was produced in the world was given in Figure 4 [1].

Figure 4. Some places where boron was produced in the world [1]

4. APPLICATION AREAS OF BORON MINERALS

Boron was mainly used in glass and fiberglass, ceramics and enamel, construction cement, metallurgy, health, agriculture, nuclear and defence industries. Boron products were utilized in plastics, industrial fiber

production, rubber and paper industry, heat-resistant glassware production, nuclear power plants, rocket fuels, hard steel production, enamel and porcelain glazes, pharmaceuticals, cosmetic industry, and photography. Boron, boron alloys, boron salts and organometallic boron complexes were both used as high-tech materials by adding them to other substances due to their lightness, resistance to stretching and resistance to chemical effects [8, 11]. The amount of boron consumed in various industries were shown in Figure 5 [15].

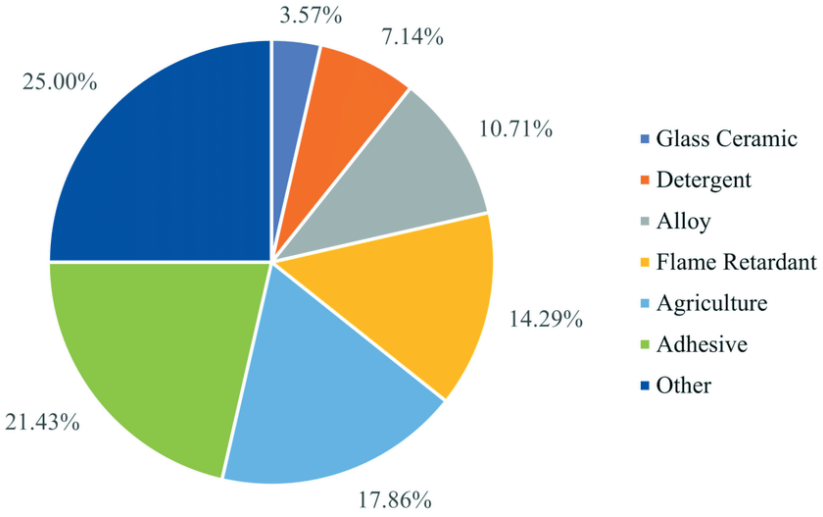

Figure 5. The amount of boron consumed in various industries [15]

In special glasses, boric acid was the most important raw material. It was used in its natural form such as refined juicy/thirsty borax, boric acid, or colemanite/borax. Boron participated in the glass products that were deemed necessary to insulate the heat as it increased its viscosity, surface hardness and durability when it joined the melted glass intermediate product. Boron leaned from heat to heat, quickly melted during glass manufacturing, and prevented the devitrification and increased its properties such as reflection, breaking and glare. Boron was protected the glass against acid and scratch [8].

In non-ferrous metal industry, borates used as a slag forming and melting accelerator due to their ability to form a smooth, sticky, protective and clean at high temperatures. It was used in electrolytic coating industry, nickel plating, hardening of tin, lead, copper, steel. Boron up to 50 ppm could gave steel the required hardness. For special purposes, the outer face of the steel could be hardened with boron. In this process, boron penetrated from the surface to form Fe_2B and FeB, which were more durable than carbon or nitride steel. This type of steel was used in the manufacture of moving parts that encountered water. The ability of

metal oxides to dissolved easily in boron at high temperatures made it more suitable to use boron instead of fluorite in the steel industry. In blast furnaces, borates reduced acidity and made refractories last longer. A boron compound known as a type of ceramics replaced zirconia crucibles in making crucibles used in metal melting, due to its greater durability. The low specific gravity and high strength of boron compounds increase the use of plastics and metals reinforced with fibers obtained from these compounds in various industries. For example, aircraft wings, helicopter propellers, high-rise buildings on narrow foundations, suspension bridges and similar structures were made by using plastic and metals supported by the type of boron fibers [13].

Boric acids and borates provided resistance to cellulosic substances and fever. The use of cellulosic insulation as a fever resistant substance led to an increase in boric acid. In Australia and the United States, the consumption in this branch increased quite rapidly. Boron compounds were used in plastics increasingly as preventive combustion [16].

In cleaning industry, borates took their place for about 100 years. Recent trials on laundry soap bars showed that borates significantly improved the cleaning effect and reduce soil re-deposition. This led to brighter, cleaner laundry. 10% of borax decahydrate was provided to soaps and detergents because of its germicidal and water softening influence, and about 10-20% sodium perborate was provided to powder detergents to rise its whitening effect. Borates proved to be extremely effective in stain removal. It also acted as a biostat that inhibited dye transfer, softens water, buffers alkali, improved surfactant performance and helped control to bacteria and fungi [9, 16].

In agricultural industry, boron was an essential micronutrient for the growth and development of plants. Boron was unique among the essential elements because it was the only non-ionized molecular element normally found in soil solution. It was understood that it affects flowering, pollen fertilization, active salt absorption, cell fertilization, hormone movement and activity. It gave the plants drought tolerance. It was also preferred in cases where weed removal or soil sterilization was required with compounds such as sodium chlorate and bromosol. When boron deficiency was observed in tuberous plants such as sugar beet, olive, coffee, tobacco and cotton, fertilizer supplement containing anhydrous borax and borax pentahydrate was applied [16, 17].

In ceramic and enamel industry, it was a widely used additive for glazing. It enabled the silica to melt easily and spread quickly on the surface. As the amount of boron increased, the glaze became harder, more durable, and shinier. It was also used in the enamel industry to increase

the brightness, hardness, and durability of enamels. Boron oxide, which reduced the viscosity and saturation temperature of the enamels, could be added up to 20%. Boron, which made it resistant to scratching, was added to ceramic glazes in the form of colemanite (3-24%) [17, 18].

In health, boron was used in the treatment of cancer, especially in the treatment of brain cancers, for selectively destroying sick cells and was preferred because of its minimal damage to healthy cells. It increased resistance in metabolism and helped to maintain mineral balance. It was utilized as a sterilization tool in eye inflammations, production of some ointments, nuclear medicine in the search for neutrons with boron [19].

In atomic reactors, stainless boron steel was preferred as neutron absorbing. Approximately each boron atom absorbed a neutron. It was used in atomic reactors in cooling pools and alarm. Boron hydrides showed the potential to be used as a fuel because it was a nature-compatible compound that could be used as a hydrogen carrier and reservoir. In addition, studies were carried out on boron hydrides, which were used in the reduction of toxic wastes and the synthesis of magnetic metal nanoparticles [17, 20].

In energy industry, it became an energy source used for the storage and production of hydrogen. Hydrogen could be produced from sodium borohydride and was a potential fuel for fuel cells. Boron became one of the key elements in the production of clean and environmentally friendly hydrogen energy, which could replace fuels such as oil and coal in the future [20, 21].

Apart from these usage areas, boron compounds were used in photography, pharmaceutical industry, weaving, casting and welding, paint and paper industry, delaying the solidification of gypsum and similar materials, plastic production, leather making, additive in drilling mud, rubber and latex industry, pH control and more, storage of solar energy, protection in solar cells, use of cell fuels in the energy sector, processors, current plates, semiconductors, vacuum tubes, dielectric materials, capacitors in the electricity sector [21].

5. ADVANCED TECHNOLOGY BORON COMPOUNDS

High-tech materials were defined as materials with high added value, requiring advanced technology and knowledge. The use of industrially advanced technology materials showed harmony with the development levels and economies of the countries. High-tech materials were composed of pure or very near pure oxides such as magnesium, aluminum, zirconium, beryllium oxide, and non-oxide ceramics such as silicon nitride, boron carbide, silicon carbide. Some boron compounds were used as an abrasive and luminescent, for cutting, sharpening, and

polishing metals and superalloys because of its high hardness. Boron compounds had a higher cutting rate and sustained heavy-duty capability than tungsten carbide. High-tech products had properties such as resistance to high temperatures, specific electrical conductivity, chemical resistance, resistance to mechanical and thermal stresses (cutting, drilling), biological compatibility, semi- or selective permeability, heat repelling and discharge, low expansion, and non-toxicity [22-24].

Boron fiber showed the feature of being the first fiber used in high-tech composite materials. The first production of boron fiber based on 1960s and it was referred to and used as the original high modulus fibers until the commercial production of carbon and/or graphite fibers. Boron fiber was defined as special yarns made of metallic boron. It was both lighter and had better mechanical properties than steel and aluminum. It was used in refractory coatings, electronic, polymer and metal matrix composites, because of its high hardness, lightness, tensile strength, and corrosion resistance. Commercially used boron fibers were obtained by vapor decomposition on a substrate. The use of boron fiber in the production of composite materials had not found much place in widespread industrial applications due to its quite intensive production and high cost of reinforcement material. It was the main component used in the construction of aircraft and rocket bodies in developing technology, and it entered the civil aviation field as well as it was mostly used in warplanes, and it was evaluated in automobile bodies for the purpose of absorbing energy especially during impact and absorbing the load that would be reflected on the driver. In space studies, the middle body of the space shuttle orbiter was made of boron fiber reinforced aluminum composite tubes as resulting in a 45% light weight compared to the use of aluminum in the initial design [22].

Developments in aerodynamics, high speed wing applications, high temperature resistant fuselage, low weight, high capacity and similar applications in the aircraft and aviation industry made widespread the use of composite materials. Boron-containing composite materials constituted a large part of the material used in the vehicles produced in the aviation industry. Boron fibers in plastics had a hardness/density ratio of 6 times that of aluminum and titanium. It combined high temperature resistance, flexibility, lightness, invisibility to radars, power, and ease of manufacture. It was utilized in compressor blades of jet engines, and rudders of airplanes. Some aircraft types by using high-tech materials containing boron were shown in Figure 6 [25].

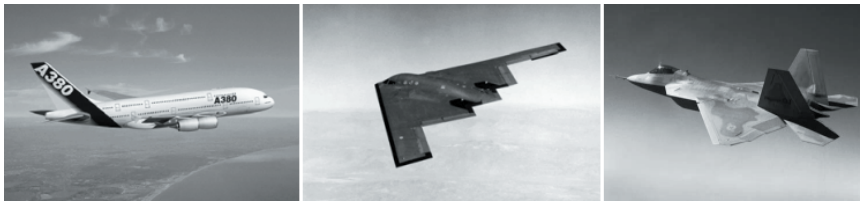

Figure 6. Some aircraft types by using high-tech materials containing boron [25]

After diamond and cubic boron nitride, boron carbide was the hardest and most durable material. Boron carbide could be produced using different boron source and production method. Pure boron carbide crystals had a slightly shiny appearance. Hot pressed boron carbide was used in abrasive parts, gaskets, making ceramic armoured surfaces. It was used as a thermocouple for measuring temperatures above 2000°C and in the production of abrasive materials due to its hardness. It was insensitive to chemical reactions and radiation. It was an important material used in the production of control rods in nuclear power plants due to its neutron absorbing feature [26-28].

The metal borides were binary compounds in a wide variety of stoichiometry and structure, numbering more than 200. There were also ternary and more complex borides, in which more than one metal was combined with boron, or the metal combined with both boron and another element such as carbon. For example, the electrical and thermal conductivity of zirconium diboride and titanium diboride were several times higher than that of their metals, and their melting points were 1000°C higher than the melting points of their metals. Rare earth hexaborides were among the materials with the best-known thermionic permeability [29].

In the studies, it was discovered that magnesium diboride could be the superconductor of the future. The fact that superconductivity occurred mostly near absolute zero, which was -273^0C, and expensive to achieve such a low temperature, made magnesium diboride, which had a much higher critical temperature, a cheap and efficient alternative. Since superconductors could carry very high current densities without causing any energy loss, they had many applications such as efficient energy transmission from power plants to cities, applications requiring strong magnets, storing large amounts of energy in the magnetic field, or preventing undesired heating in microelectronics [30].

6. CONCLUSION

Boron was a versatile and indispensable element with a wide range of applications due to the compounds. Boron was utilized in glass, ceramics, construction, metallurgy, health, agriculture, nuclear and defence

industries. Boron products with high added value and a significant role in industrial applications were increasing in harmony with technological innovations. As a result, studies showed that producing high-tech boron products would provide advantageous in future both in Turkey with high reserve ratios and in the world.

REFERENCES

[1] Helvacı, C. (2017). Borate deposits: An overview and future forecast with regard to mineral deposits. Journal of Boron, 2(2), 59–70.

[2] Ediz, N. & Özdağ, H. (2001). Boron minerals and its economics. Journal of Science and Technology of Dumlupınar University, (002), 133-151.

[3] Demir, C. (2006), Evaluation of boron minerals as an energy source. M.Sc. Thesis. Selçuk University. Graduate School of Applied and Natural Sciences, Konya.

[4] Türkmen, İ. (2018). Development and characterization of alternative boriding composition by different boron derivatives. Ph.D. Thesis. Manisa Celal Bayar University Graduate School of Applied and Natural Sciences, Manisa.

[5] Kıpçak, A. S. (2009). Investigation of the usability of some boron compounds in neutron armor. M.Sc. Thesis. Yıldız Technical University. Graduate School of Applied and Natural Sciences, İstanbul.

[6] Helvacı, C. (2015). General evaluation and future prediction of boron deposits. Journal of Mining and Earth Sciences, 47, 66-78.

[7] Ün, S. (2019). Boron and arsenic removal from Emet boron operations directorate boric acid plant espey area spring water with pilot scale membrane systems. M.Sc. Thesis. Eskişehir Osmangazi University. Graduate School of Applied and Natural Sciences, Eskişehir.

[8] Kochkodan, V., Darwish, N. B. & Hilal, N. (2015b). The chemistry of boron in water. Elsevier e-Books, 35–63. https://doi.org/10.1016/b978-0-444-63454-2.00002-2.

[9] Çiğdem, M. (2020). Statistical evaluation of the thermal determination process of p-PVC boron composites. M.Sc. Thesis. Uşak University. Graduate School of Applied and Natural Sciences, Uşak.

[10] Özkan, Ş. G., Çebî, H., Delice. S. & Doğan, M. (1997). Properties and mining of boron minerals. II. Industrial Raw Materials Symposium, 224- 228, İzmir.

[11] Samuk, T. F. (2015). The analysis of researches which studies derivatives of boron used in building materials. M.Sc. Thesis. İstanbul Technical University. Graduate School of Applied and Natural Sciences, İstanbul.

[12] Çolak, A., Laratte, B., Elevli, B. & Çoruh, S. (2022). Abiotic depletion of boron: an update characterization factors for CML 2002 and ReCiPe. Minerals, 12(4), 435, 1-16. https://doi.org/10.3390/min12040435.

[13] Akgül, Ö. (2010). Zinc borate from different boron minerals production. M.Sc. Thesis. Yıldız Technical University. Graduate School of Applied and Natural Sciences, İstanbul.

[14] Özkan, Ş. G., Tombal, T. D., Kurşun Ünver, İ. & Osmanlıoğlu, A. E. (2016).

Properties, production, uses of boron compounds and their importance in nuclear reactor technology. Journal of Boron, 1(2), 86-95.

[15] Liu, X., Xu, C., Chen, P., Li, K., Zhou, Q., Ye, M., Zhang, L. & Lu, Y. (2022). Advances in Technologies for Boron Removal from Water: A Comprehensive Review. International Journal of Environmental Research and Public Health, 19(17), 10671, 1-34. https://doi.org/10.3390/ijerph191710671.

[16] Zengin, A., Aka, B., Gençay, S. & Uzun, M. (2021). Boron and Industrial Applications. Europan Journal of Science and Technology, (46), 161-178. https://doi.org/10.31590/ejosat.919451.

[17] Ediz, N. & Özdağ, H. (2001). Boron minerals and economy, Dumlupınar University. Journal of the Graduate School of Natural and Applied Sciences, 2, 133-151.

[18] Candar Koçyiğit, G. (2018). Boron removal and recovery from industrial wastewater by using chemical coagulation and electrocoagulation methods. M.Sc. Thesis. Ankara University. Graduate School of Applied and Natural Sciences, Ankara.

[19] Yakıncı, Z. D. & Kök, M. (2016). Use of boron in healthcare. Journal of İnönü University Vocational School of Health Services, 4(1), 36–44.

[20] Meydan, E. (2019). Boron compounds with magnetic properties and their application areas in industry. Journal of Scientific Perspectives, 3(1), 11–20. https://doi.org/10.26900/jsp.3.002.

[21] Yenmez, N. (2011). The importance of boron minerals in Turkey as a strategic mine. Journal of Geography, 19, 59–94.

[22] Ertürk, S. (2012). System design in tungsten-cored boron fiber production by chemical vapor deposition. Ph.D. Thesis. İstanbul Technical University. Graduate School of Applied and Natural Sciences, İstanbul.

[23] Özkol, E. (2008). Production of Boron Nitride, M.Sc. Thesis. Middle East Technical University. Graduate School of Applied and Natural Sciences, Ankara.

[24] Güzel, G. (2006). Synthesis of some type of lithium and boron rich chemical compounds and analyzed theirs structural properties by x ray diffraction (XRD). M.Sc. Thesis. Balıkesir University. Graduate School of Applied and Natural Sciences, Balıkesir.

[25] Yiğitbaşioğlu, H. (2004). Boron an important ore for Turkey boron. Journal of Geographical Sciences, 2(2), 13-25. https://doi.org/10.1501/cogbil_0000000046.

[26] Atasoy, A. (2011). Effect of metallic aluminum powder addition in boron carbide production. 6th International Advanced Technologies Symposium (IATS'11), 555-558, Elazığ.

[27] Uzun, H. A. (2002). Abrasion and corrosion resistance of steels hardened by boronizing. M.Sc. Thesis. Süleyman Demirel University. Graduate School

of Applied and Natural Sciences, Isparta.

[28] Garrett, D. (1998). Borates: Handbook of deposits, processing, properties and use, 1st edition, San Diego Academic Press, 400-428.

[29] Koyuncu, U. (2009). Synthesis of some metal borides. M.Sc. Thesis. Bozok University. Graduate School of Applied and Natural Sciences, Yozgat.

[30] Yılmaz, A. (2002). Our panacea treasure Boron, Tübitak-Science and Technical Journal, 38-41.

Chapter 3

NON-THERMAL ALTERNATIVE METHODS IN THE DAIRY INDUSTRY

Murat Emre TERZİOĞLU[1], Sümeyra IŞIK[2], İhsan BAKIRCI[3]

1 Corresponding author: Murat Emre TERZİOĞLU, Asst. Dr., Atatürk University, Faculty of Agriculture, Department of Food Engineering, 25240, Erzurum, Türkiye, e-mail: murat.terzioglu@atauni.edu.tr, ORCID: https://orcid.org/0000-0001-6370-0694

2 Sümeyra IŞIK, Dr., Atatürk University, Faculty of Agriculture, Department of Food Engineering, 25240, Erzurum, Türkiye, e-mail: sumbakirci@hotmail.com, ORCID: https://orcid.org/0000-0002-7203-1207

3 İhsan BAKIRCI, Prof. Dr., Atatürk University, Faculty of Agriculture, Department of Food Engineering, 25240, Erzurum, Türkiye, e-mail: ibakirci@atauni.edu.tr ORCID: https://orcid.org/0000-0002-3744-3863

INTRODUCTION

Today, developments in food processing and production technologies have accelerated in line with the demands of consumers for high-quality, safe and natural foods. In addition to maintaining food safety, minimizing the loss of nutritional value from the production stage to the consumption stage is among the primary goals of food businesses (Coşkun Topuz and Boran, 2018). Milk is a food that is prone to spoilage and has a short shelf life with its rich nutrient content and high water activity that can be used in the development of microorganisms. In the dairy industry, the inactivation of microorganisms and enzymes is important for extending shelf life and ensuring food safety, and different heat treatments such as pasteurization or sterilization are used for this purpose (Shabbir et al., 2020). However, depending on the duration and temperature of the heat treatments applied, various losses may occur in the nutritional elements as well as the sensory properties of the products such as colour, taste, smell and aroma (Evrendilek, 2014). For this reason, in recent years, new techniques have been developed as an alternative to heat treatment for the production of safe, high quality and highly attractive milk and dairy products. For this purpose, many techniques have been developed such as the application of pulsed electric field (PEF), high hydrostatic pressure (HHP), ultraviolet (UV), ultrasound, cold plasma and supercritical carbon dioxide (SC-CO_2). The freshness of the products is preserved, the inactivation of unwanted enzymes and microorganisms is ensured, and the quality losses are reduced to minimum levels (Güven and Yıldız, 2016). Non-thermal preservation methods are shown in Figure 1.

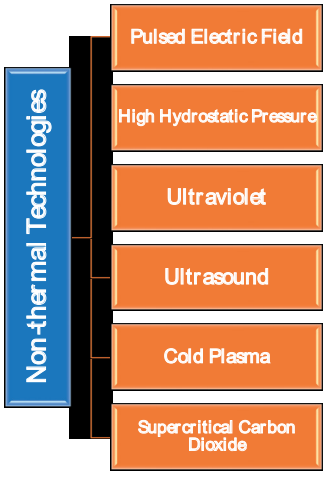

Figure 1. *Classification of non-thermal preservation methods*

Pulsed Electric Field (PEF)

It is reported that PEF has an important potential as an alternative to traditional heat treatments in the inactivation of pathogenic microorganisms and enzymes, especially in liquid foods such as milk (Shabbir et al., 2020). In this method, the food quality is preserved and the changes in the sensory and physical properties of the food are minimized due to the very small increase in the temperature of the food during the process (Patel et al., 2015). The PEF process is based on the application of short-term high-voltage electricity to the food placed between or passed through two electrodes (Buckow et al., 2014). In this method, the inactivation of microorganisms is carried out by applying an electric field of 10-80 kV/cm in micro or millisecond times (Syed et al., 2017). In the PEF method, charged particles cause a change in the electrical charge of the cell membrane, causing the pores to expand. Microorganism inactivation is provided by increasing the permeability of the cell membrane (Rashmi and Warrier, 2020). The efficiency level of the PEF method; The intensity of the electric field can vary depending on factors such as the number of stresses, the application time, the pH of the food, and the characteristics of microorganisms (Soltanzadeh et al., 2020). The working principle of the PEF method is shown in Figure 2.

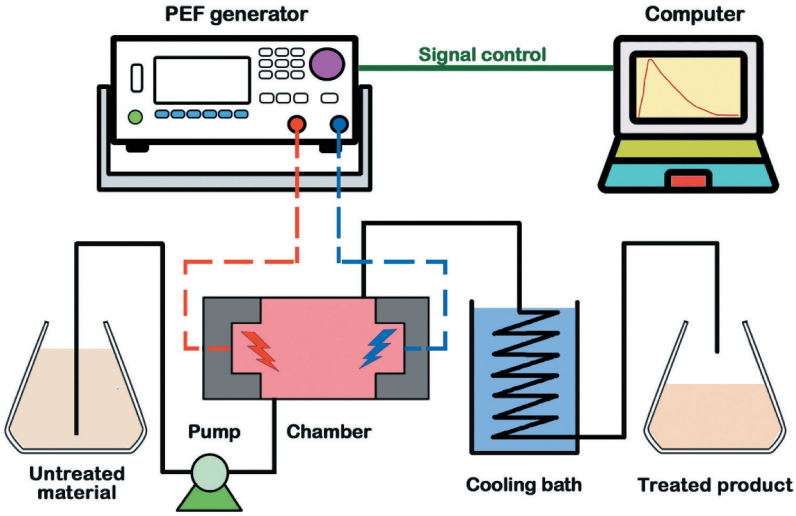

Figure 2. *Working principle of the PEF method (Soltanzadeh et al., 2020)*

Most of the studies on the application of the PEF method in dairy products such as milk and yoghurt, butter and cheese have focused on microbial inactivation. It has been reported in studies that this technique is effective in the inactivation of many pathogens such as *Bacillus cereus*, *Escherichia coli*, *Listeria innocua*, *Listeria monocytogenes*, *Pseudomonas fluorescens*, *Staphylococcus aureus* (Bermúdez-Aguirre et al., 2012;

Walter et al., 2016; Araújo et al., 2021). However, in various studies, it has been reported that the activities of enzymes such as lipase and alkaline phosphatase, which are important in dairy technology, can be reduced or completely inhibited by the PEF method (Bendicho et al., 2002; Castro et al., 2019; Yang et al., 2020a). It has been stated that the PEF method affects the casein coagulation, size and structure of casein micelles, as well as enzyme and microbial inactivation, and thus, it can provide a significant advantage in cheese production by showing positive effects on milk fermentation and clot hardness (Yangılar and Kabil, 2013; Rashmi and Warrier, 2020).

High Hydrostatic Pressure (HHP)

The HHP method, which is based on the principle of compressing the water around packaged or unpackaged foods with 100-1000 MPa pressure, is preferred more than other non-thermal methods (Oğuzhan, 2013). This method ensures the inactivation of enzymes and microorganisms by preserving the nutritional and sensory qualities of the foods to a large extent and also prevents the negative physical and chemical modifications that may occur in the structure of the foods since high temperature is not required (Aganovic et al., 2021). The inactivation effect of high pressure is explained by the Le Chatelier principle. Accordingly, when an external effect is made on the physical system in equilibrium, the system responds to this effect in order to restore the balance. As the volume decreases due to the increase in pressure, the density increases and therefore the equilibrium shifts to the side with the fewest moles. As a result, the chemical balance of the system changes (Liu et al., 2020). Based on this principle, the HHP method provides microorganism inhibition by destroying the cell membrane structure and deactivating the membrane permeability (Zhang et al., 2019). However, it has been reported that high pressure causes the denaturation of cell membrane proteins and inactivates enzymes (Aganovic et al., 2021). The effectiveness of inactivation in the HHP method; It can vary depending on the applied pressure, application time, temperature, microorganism resistance and the structure of the food (Zhang et al., 2019).

Many researchers have reported that *L. monocytogenes*, *E. coli*, *Enterobacteriaceae* and *S. typhimurium*, which can be found in milk, can be inactivated by the HHP method (Komora et al., 2020; Liu et al., 2020; Yang et al., 2020b). De Oliveira Alves and Pérez (2020) investigated the inactivation efficiency of the HHP method on different *L. monocytogenes* strains in cheese. The cheeses inoculated with 12 strains separately were subjected to 600 MPa pressure for different times (1, 3, 5 and 10 minutes). As a result of the procedure, they reported that the inactivation of *L. monocytogenes* varied between 1.25-6.49 log cfu/g, and the most effective

inactivation was achieved with the treatment applied under 600 MPa pressure for 5 minutes. In another study, it was stated that vegetative cell forms were more sensitive to high pressure than spores, and gram-negative bacteria were more sensitive than gram-positive ones (Zhang et al., 2019).

There are also various studies in which the HHP method and different methods (usually temperature) are combined for microbial inactivation. Chen and Hoover (2003) investigated the inactivation of *L. monocytogenes* in UHT milk at different temperatures (22°C, 40°C, 45°C and 50°C) and different pressure levels (400 and 500 MPa). They reported that the inactivation rate of *L. monocytogenes* increased with the use of temperature together with pressure, and a decrease of more than 8 logs was obtained with 500 MPa pressure at 50°C. The working principle of the combination of the HHP method and heat treatment is given in Figure 3.

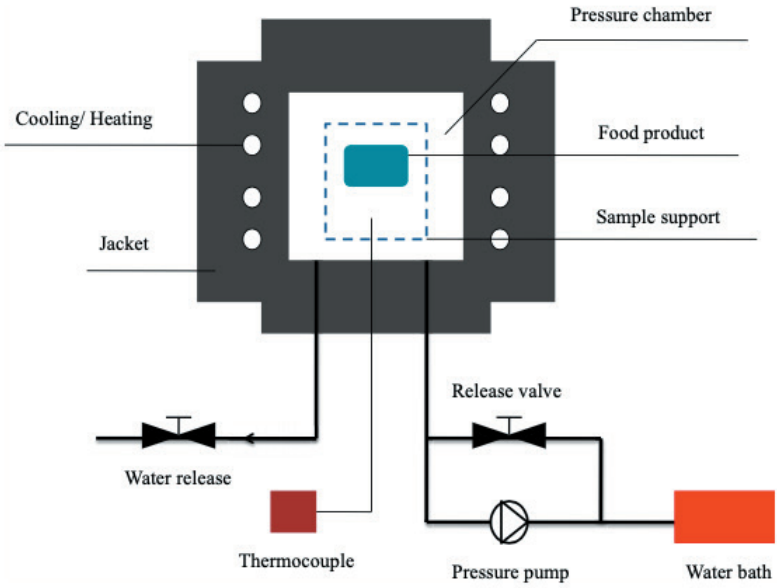

Figure 3. *Working principle of the combination of the HHP method and heat treatment (Zhang et al., 2019)*

The HHP method improves the structural properties of dairy products by providing various changes in the molecular structures of milk components as well as microbial inactivation. As a matter of fact, it has been reported that positive changes occur in casein micelles with the HHP method, β-lactoglobulin is denatured and crystallized in milk fat (Patel et al., 2015; Wang et al., 2016; Shabbir et al. 2020). With the HHP method, the coagulation time decreased and the yield increased in cheese production; In yoghurt, serum separation decreased, the viscosity increased, and

rheological and sensory properties improved; In butter, it has been stated in studies that the maturation time is shortened by the crystallization of the oil (Yangılar and Kabil, 2013; Swelam, 2018; Rashmi and Warrier, 2020; Shabbir et al., 2020; Tsevdou et al., 2020).

Ultraviolet (UV)

UV is a non-ionizing form of energy that lies between visible light and X-rays in the electromagnetic spectrum. UV, UV-A (315-400 nm), UV-B (280-315 nm), UV-C (200-280 nm) and vacuum-UV (100-200 nm) with wavelengths in the 100-400 nm range It is divided into four main classes, including (Delorme et al., 2020). Among them, it is stated that UV-C rays have germicidal properties in bacteria, yeasts, moulds and viruses (Guneser and Karagul Yuceer, 2012). It is stated that UV light inhibits DNA transcription and replication by photochemical changes in nucleic acids and proteins in the cell membrane, resulting in the inhibition of microorganisms (Matak et al., 2007).

UV method, which has an important potential in inhibiting microorganisms in solid and liquid foods, comes to the fore as an alternative to commercial heat treatments (Delorme et al., 2020). The effectiveness of the UV method; varies depending on many factors such as technical characteristics (wavelength of the beam, amount of the UV source, the physical arrangement of the UV source, etc.), biological factors (microorganism type, spore/vegetative form, etc.) and the structure of the food (optical properties, etc.) (Shabbir et al., 2020; Ricciardi et al., 2021). The working principle of the UV method is given in Figure 4.

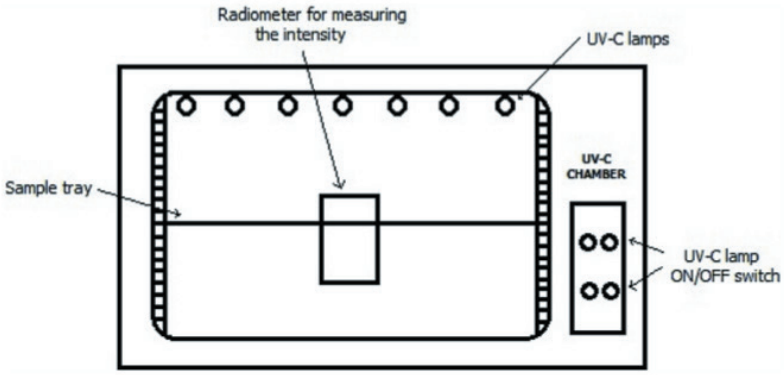

Figure 4. *Working principle of the UV method (Delorme et al., 2020)*

UV-C rays can be used in the sterilization of packaging materials as well as food and equipment surfaces that come into contact with food (Koca et al., 2018). Studies on the UV method in the dairy industry mostly focused

on the inhibition of pathogenic and saprophytic microorganisms in milk and the reduction of the surface microflora population in cheese (Bakri et al., 2018; Keklik et al., 2019; Ward et al., 2019; Hales and Bastarrachea, 2021). Ansari et al. (2019) evaluated the thermal inactivation efficiency of UV pretreatment on *B. subtilis* in skimmed and full-fat cow's milk and full-fat sheep's milk. UV-treated milk was heat treated at 110°C for 30 seconds. Researchers reported that the number of *B. subtilis* decreased by UV method by about 6 log cfu/mL in skimmed cow's milk, about 2.90 log cfu/ml in full-fat cow's milk and 1.1 log cfu/ml in full-fat sheep's milk. As a result, the researchers determined that the combination of the UV method with temperature could be an alternative to sterilization of milk at lower temperatures compared to the UHT method (135°C, 3 seconds). According to Keklik et al. (2020) investigated the effects of UV light applied to white cheese at different times (5, 15, 30, 45, and 60 seconds) and at different distances (5, 8 and 13 cm) on *S. aureus* and *E. coli* O157:H7. Accordingly, they reported that UV light (91.22 J/cm2) applied for 60 seconds from a distance of 8 cm provided approximately 1.31 and 2.20 log cfu/cm2 reduction in *S. aureus* and *E. coli* O157:H7 populations, respectively. They also stated that the UV method did not change the pH, lipid oxidation and moisture content of the cheese. In another study on cheddar cheese, the effect of UV light (0.32-9.63 kJ/m2) at different doses on physicochemical and sensory properties and mould inactivation was investigated. It was observed that 0.34, 0.69 and 2.49 log reductions were observed in the number of moulds in cheddar cheeses, which were exposed to UV light at doses of 0.32, 0.96 and 1.93 kJ/m2, respectively. In addition, it has been reported that there is no significant difference in composition and hardness values between UV-treated kashar cheeses and control group cheeses (Koca and Öztürk, 2020).

Ultrasound

In ultrasound application, bubbles are formed when sound waves pass through a liquid. After a while, when these bubbles reach the size that they cannot absorb the energy, inward explosions called cavitation occur and high temperature and pressure fluctuations are observed at that point (Açu et al., 2014). Sudden temperature and pressure changes cause some physical and chemical changes such as microflow, turbulence, microjet, shock waves and radical formation (Carrillo-Lopez et al., 2021). The cavitation formation in the ultrasound method is shown in Figure 5.

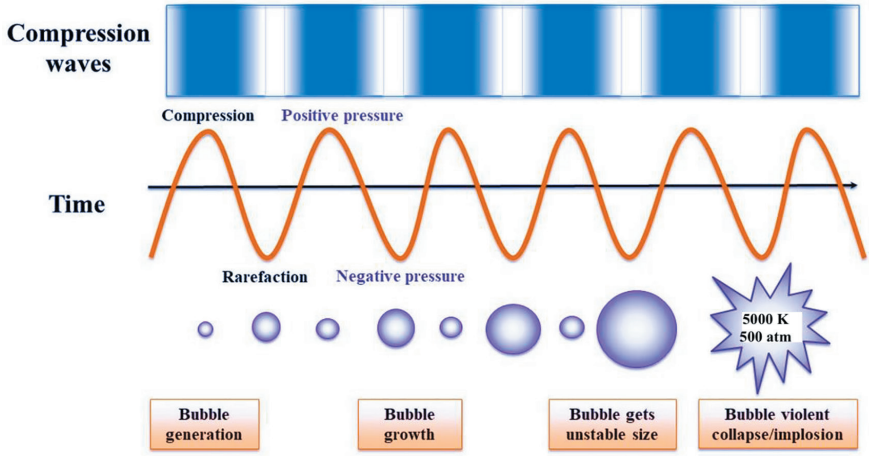

Figure 5. *Cavitation formation in ultrasound method (Carrillo-Lopez et al., 2021)*

Ultrasound technology is widely used around the world due to its harmless, low cost, fast, environmentally friendly and less energy requirement. This method has a wide application area in the food industry and has great potential in food processing techniques such as homogenization, emulsification, mixing, grinding, extraction, pasteurization, drying, filtration and crystallization (Rashmi and Warrier, 2020; Shabbir et al., 2020).

In milk technology, ultrasound application; It is applied for various purposes such as ultrafiltration of whey, homogenization of milk fat, shortening of fermentation time, shortening of ripening time in cheese, crystallization of lactose and microbial inactivation (Akdeniz and Akalın, 2020; Bhargava et al., 2021). In the literature, yoghurt (Körzendörfer and Hinrichs, 2019; Delgado et al., 2020), cheese (Carrillo-Lopez et al., 2020; Crespo et al., 2020) and ice cream (Jambrak et al., 2012; Aslan Türker and Dogan, 2021) on the physicochemical and textural properties of dairy products, there are many studies examining the effects of ultrasound application. However, some studies on the inactivation of microorganisms by ultrasound are also available in the literature (Bermúdez-Aguirre et al., 2009; Herceg et al., 2012; Cregenzán-Alberti et al., 2015; Li et al., 2019). It has been stated that microorganisms and enzymes are inactivated by the cavitation effect in ultrasound technology, thus increasing the quality of the products and extending the shelf life (Rashmi and Warrier, 2020). Bermúdez-Aguırre et al. (2011) investigated the inactivation of *L. innocua* in raw milk by thermosonication. The researchers reported a decrease of approximately 5 logs in the number of *L. innocua* 5 minutes after applying thermosensation (63°C, 24 kHz, 129 mW/mL), and a decrease of approximately 6 logs after 30 minutes. According to Tavsanli et al. (2021), on

the other hand, investigated the effect of ultrasound on pathogenic bacteria by applying ultrasound to raw goat milk under different conditions (100%, 50% and 10% amplitude, 20 kHz). They determined that the inactivation rate of *Brucella melitensis*, *S. typhimurium*, *E. coli*, *L. monocytogenes* and *S. aureus* was approximately 99% by ultrasound method.

Cold Plasma

The ionization of gases to plasma can be achieved by various methods such as thermal, electrical or laser. Properties of plasma; it is affected by various factors such as process parameters (pressure and temperature), gas used and its composition (oxygen, air, helium, argon or nitrogen) and power source (radio wave, corona discharge, dielectric discharges, microwave or plasma jet). The formation of reactive species is largely dependent on the gas used and the composition of the gas (Rashmi and Warrier, 2020; Rathod et al., 2021). The plasma production scheme is given in Figure 6.

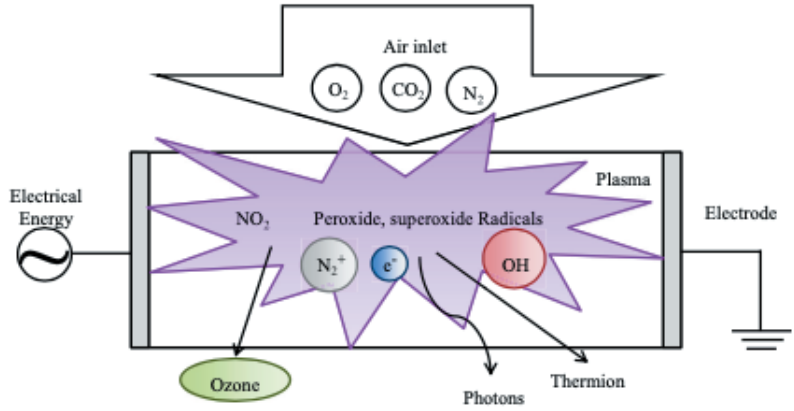

Figure 6. *Plasma production scheme (Mandal et al., 2018)*

Plasmas are divided into two, according to their thermodynamic properties, as hot plasma is produced at high temperatures (9000°C and above) and cold plasma is produced at atmospheric conditions (30-60°C) (Rathod et al., 2021). In hot plasma, there are basically many ions in the environment and very high energy levels are reached. Cold plasma, on the other hand, is used in various fields such as decontamination of contaminated surfaces, surface treatment, sterilization of medical instruments and ensuring food safety (Albayrak and Kılıç, 2020).

Cold plasma technology is one of the newest technologies for heat-sensitive foods (Annor, 2019), its low-temperature feature and high efficiency in microbial inactivation are among its most remarkable features (Shabbir et al., 2020). Microorganisms are inhibited in this method by three basic mechanisms: abrasion of cell surfaces caused by reactive species

formed during plasma production, DNA destruction as a result of the use of UV rays as an energy source, and detachment of compounds that can turn into gas as a result of the combustion of oxygen atoms (Albayrak and Kılıç, 2020). Since the penetration depth of plasma reagent species is limited, only surface decontamination of solid foods is provided (Mandal et al., 2018).

There are a limited number of studies examining microbial inactivation efficiency with cold plasma application in milk and dairy products. In the current studies in the literature, it has been reported that *E. coli*, *L. monocytogenes* and *Salmonella* in milk and cheese were successfully inactivated using cold plasma technology (Ruan et al., 2010; Gurol et al., 2012; Ott et al., 2022). Wan et al. (2021) subjected fresh cheese inoculated with *L. innocua* and *E. coli* to cold plasma treatment at different voltages (60 kV, 80 kV and 100 kV). Researchers stated that 100 kV energy application reduced the number of *L. innocua* and *E. coli* by 1.4 log cfu/g and 3.5 log cfu/g, respectively. Aguilar Uscanga et al. (2022) investigated the inactivation of *E. coli* ATCC 25922, *Salmonella* ATCC13076 and *S. aureus* ATCC 6538 microorganisms in traditional cheeses by cold plasma. They reported that by applying energy of 30 V to cheese at different intervals in the dielectric barrier discharge reactor (DBDR), they achieved a reduction of about 5 logs in these microorganisms and that plasma had an inhibiting effect on pathogens.

Super Critical Carbon Dioxide (SC-CO_2)

There is a supercritical region where liquids or gases exhibit low viscosity and surface tension, and high density and intermediate diffusion properties. Supercritical fluid application is related to the physical and chemical properties of the substance (Amaral et al., 2017). Various substances such as ammonia, ethylene and water are used in the supercritical fluid application, and carbon dioxide (CO_2) is the most preferred supercritical fluid (Zabot et al., 2015). Supercritical carbon dioxide (SC-CO_2); is used in different ways such as liquid carbon dioxide, dense phase carbon dioxide and high-pressure carbon dioxide (Hu et al., 2013).

In addition to its low acidity and high water activity, milk creates a suitable environment for the development of microorganisms such as *E. coli*, *Salmonella*, *Coxiella burnetii* and *L. monocytogenes* (Cappato et al., 2017). It has been reported that the temperature, pressure and time parameters of the SC-CO_2 method, as well as the cell cytoplasm and cell wall structure of the targeted microorganisms, are directly effective in providing microbial inactivation in milk. It has also been reported in studies that gram-negative bacteria are more sensitive than gram-positive

bacteria and vegetative cells are more sensitive than spores against the SC-CO_2 method (Bae et al., 2009; Calvo and Torres, 2010; Banana, 2013). The mechanism of action of the SC-CO_2 method on microorganisms is given in Figure 7.

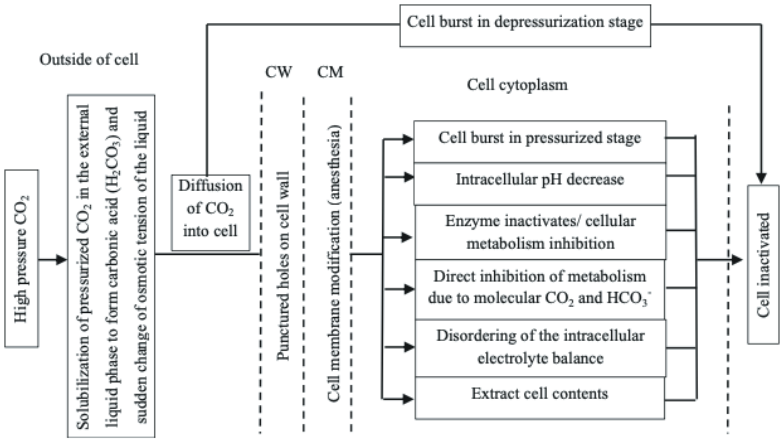

Figure 7. *The mechanism of action of the SC-CO_2 method on microorganisms (CW: cell wall, CM: cell membrane) (Efaq et al., 2015)*

In addition to microorganisms that cause deterioration in milk and dairy products, enzymatic activities also constitute an important risk factor in terms of shelf life and health. In order to protect consumer health, preserve the structure of milk and its products and extend the shelf life, unwanted microorganisms and some enzymes must be inactivated. The SC-CO_2 method can be preferred in order to inactivate enzymes and microorganisms in milk and dairy products, as well as to preserve their physical, chemical and sensory properties (Smigic et al., 2019).

Compared to the HHP method (average 50-1000 MPa), the SC-CO_2 method (average 10-20 MPa) uses lower pressures for enzymatic and microbial inactivation, resulting in lower processing costs and shorter processing times. In addition, with the SC-CO_2 method, mass transfer is realized at a higher rate, losses in terms of essential nutrients and sensory properties of foods, especially milk and dairy products, are kept at a minimum level, quality products are produced and the risk of chemical residues is eliminated (Khosravi-Darani, 2010; Ceni et al., 2016). Xu et al. (2011) reported that the SC-CO_2 method increased the particle size and protein density in whey protein isolation and provided a high-quality product. Vo et al. (2013) reported that the use of the SC-CO_2 method under 0.7 MPa pressure for 25 minutes completely inhibited *E. coli*, and the effectiveness of CO_2 in the inhibition of *E. coli* increased with the decrease in pH value. García-Cano et al. (2021) reported that the allergenic effect of

β-lactoglobulin in cow's milk, which causes allergies in some individuals, is reduced by incorporating the SC-CO_2 method into the process. On the other hand, Walter et al. (2021) revealed that the use of supercritical extracts in yoghurt production increases yoghurt's antioxidant properties and functionality without affecting physicochemical and sensory properties.

CONCLUSION

Traditional heat treatments used in milk and dairy products to inhibit enzymes and pathogenic microorganisms, as well as spore and vegetative forms of pathogenic microorganisms, cause losses in the nutritional values of these products and can also lead to various negativities in sensory properties such as color, taste, smell and aroma. Non-thermal alternative storage methods (PEF, HHP, UV, ultrasound, cold plasma and SC-CO_2 technologies) used to obtain products such as milk, yogurt, cheese, butter and ice cream with the desired microbial safety and quality, highly preserved naturalness and high economic value with minimum loss in nutritional values and sensory properties have an important potential as an alternative to heat treatments. These methods slow down the Maillard reaction in milk, provide denaturation of α-lactalbumin and β-lactoglobulin, reduce serum separation in yoghurt, increase viscosity and curd firmness, and increase ripening speed in butter and ice cream. In addition, these methods allow for an increase in the yield in cheese production and easily process the whey. It is thought that the use of non-thermal preservation methods, which have many advantages, in various food sectors, especially in the dairy industry, will increase significantly after extensive research and optimization studies.

REFERENCES

Açu, M., Yerlikaya, O., Kınık, Ö. (2014). Gıdalarda ısıl olmayan yeni teknikler ve mikroorganizmalar üzerine etkileri. Gıda ve Yem Bilimi-Teknolojisi, 14, 23-35.

Aganovic, K., Hertel, C., Vogel, R. F., Johne, R., Schlüter, O., Schwarzenbolz, U., Jäger, H., Holzhauser, T., Bergmair, J., Roth, A., Sevenich, R., Bandick, N., Kulling, S. E., Knorr, D., Engel, K. H., Heinz, V. (2021). Aspects of high hydrostatic pressure food processing: Perspectives on technology and food safety. Comprehensive Reviews in Food Science and Food Safety, 20(4), 3225-3266.

Aguilar Uscanga, B. R., Calderón Santoyo, M., Ragazzo Sánchez, J. A., Alemán Duarte, M. I., Pérez Montaño, J. A., Balcázar-López, E., Solís Pacheco, J. R. (2022). Effect of the application of cold plasma energy on the Inactivation of microorganisms, proteins, and lipids deterioration in Adobera Cheese. Journal of Food Quality, 2022.

Akdeniz, V., Akalın, A. S. (2020). Recent advances in dual effect of power ultrasound to microorganisms in dairy industry: activation or inactivation. Critical reviews in food science and nutrition, 62(4), 889-904.

Albayrak, A., Kılıç, G. B. (2020). Application of plasma technology in food processing. Turkish Journal of Agriculture-Food Science and Technology, 8(11), 2300-2306.

Amaral, G. V., Silva, E. K., Cavalcanti, R. N., Cappato, L. P., Guimaraes, J. T., Alvarenga, V. O., Esmerino, E. A., Portela, J. B., Sant' Ana, A. S., Freitas, M. Q., Silva, M. C., Raices, R. S. L., Meireles, M. A. A., Cruz, A. G. (2017). Dairy processing using supercritical carbon dioxide technology: Theoretical fundamentals, quality and safety aspects. Trends in Food Science & Technology, 64, 94-101.

Annor, G. A. (2019). Cold plasma effects on the nutritional, textural and sensory characteristics of fruits and vegetables, meat, and dairy products. In Effect of Emerging Processing Methods on the Food Quality (pp. 163-171). Springer, Cham.

Ansari, J. A., Ismail, M., Farid, M. (2019). Investigate the efficacy of UV pretreatment on thermal inactivation of *Bacillus subtilis* spores in different types of milk. Innovative Food Science & Emerging Technologies, 52, 387-393.

Araújo, M. A., Romão, A., Alves, M. R., & Fernandes, P. (2021). Inactivation of *Listeria monocitogenes* in milk by Pulsed Electric Field (PEF) and mild heating. https://hdl.handle.net/1822/75159

Aslan Türker, D., Dogan, M. (2021). Effects of ultrasound homogenization on the structural and sensorial attributes of ice cream: optimization with Taguchi and data envelopment analysis. Journal of Food Measurement and Characterization, 15(6), 4888-4898.

Bae, Y. Y., Lee, H. J., Kim, S. A., Rhee, M. S. (2009). Inactivation of *Alicyclobacillus acidoterrestris* spores in apple juice by supercritical carbon dioxide. International Journal of Food Microbiology, 136(1), 95-100.

Bakri, A., Hariono, B., Utami, M. M. D. (2018). Inactivation of bacteria *S. aureus* ATCC 25923 and *S. thyphimurium* ATCC 14 028 influence of UV-HPEF. In Journal of Physics: Conference Series (Vol. 953, No. 1, p. 012122). IOP Publishing.

Banana, A. A. S. (2013). Inactivation of pathogenic bacteria in human body fluids by steam autoclave, microwave and supercritical carbon dioxide. Ph.D. Thesis, Environmental Technology Division, School of Industrial Technology, UniversitiSains Malaysia (USM), Penang, Malaysia.

Bendicho, S., Estela, C., Giner, J., Barbosa-Cánovas, G. V., Martin, O. (2002). Effects of high intensity pulsed electric field and thermal treatments on a lipase from *Pseudomonas fluorescens*. Journal of Dairy Science, 85(1), 19-27.

Bermúdez-Aguirre, D., Mawson, R., Barbosa-Cánovas, G. V. (2011). Study of possible mechanisms of inactivation of *Listeria innocua* in thermo-sonicated milk using scanning electron microscopy and transmission electron microscopy. Journal of Food Processing and Preservation, 35(6), 767-777.

Bermúdez-Aguirre, D., Dunne, C. P., Barbosa-Cánovas, G. V. (2012). Effect of processing parameters on inactivation of *Bacillus cereus* spores in milk using pulsed electric fields. International Dairy Journal, 24, 13-21.

Bermúdez-Aguirre, D., Corradini, M. G., Mawson, R., Barbosa-Cánovas, G. V. (2009). Modeling the inactivation of *Listeria innocua* in raw whole milk treated under thermo-sonication. Innovative Food Science & Emerging Technologies, 10(2), 172-178.

Bhargava, N., Mor, R. S., Kumar, K., Sharanagat, V. S. (2021). Advances in application of ultrasound in food processing: A review. Ultrasonics sonochemistry, 70, 105293.

Buckow, R., Chandry, P. S., Ng, S. Y., McAuley, C. M., Swanson, B. G. (2014). Opportunities and challenges in pulsed electric field processing of dairy products. International Dairy Journal, 34(2), 199-212.

Calvo, L., Torres, E. (2010). Microbial inactivation of paprika using high-pressure CO_2. The Journal of Supercritical Fluids, 52(1), 134-141.

Cappato, L. P., Ferreira, M. V. S., Guimaraes, J. T., Portela, J. B., Costa, A. L. R., Freitas, M. Q., Cunha, R. L., Oliveira, C. A. F., Mercali, G. D., Marzack, L. D. F., Cruz, A. G. (2017). Ohmic heating in dairy processing: Relevant aspects for safety and quality. Trends in Food Science & Technology, 62, 104e112.

Carrillo-Lopez, L. M., Garcia-Galicia, I. A., Tirado-Gallegos, J. M., Sanchez-Vega, R., Huerta-Jimenez, M., Ashokkumar, M., Alarcon-Rojo, A. D. (2021). Recent advances in the application of ultrasound in dairy products: Effect

on functional, physical, chemical, microbiological and sensory properties. Ultrasonics Sonochemistry, 73, 105467.

Carrillo-Lopez, L. M., Juarez-Morales, M. G., Garcia-Galicia, I. A., Alarcon-Rojo, A. D., Huerta-Jimenez, M. (2020). The effect of high-intensity ultrasound on the physicochemical and microbiological properties of Mexican panela cheese. Foods, 9(3), 313.

Castro, A. J., Swanson, B. G., Barbosa-Cánovas, G. V., Zhang, Q. H. (2019). Pulsed electric field modification of milk alkaline phosphatase activity. In Pulsed electric fields in food processing (pp. 65-82). CRC Press.

Ceni, G., Silva, M. F., Valério Jr., C., Cansian, R. L., Oliveira, J. V., Rosa, C. D., Mazutt, M. A. (2016). Continuous inactivation of alkaline phosphatase and *Escherichia coli* in milk using compressed carbon dioxide as inactivating agent. Journal of CO2 Utilization, 13, 24e28.

Chen, H., Hoover, D. G. (2003). Modeling the combined effect of high hydrostatic pressure and mild heat on the inactivation kinetics of *Listeria monocytogenes* Scott A in whole milk. Innovative Food Science & Emerging Technologies, 4(1), 25-34.

Coşkun Topuz, F., Boran, G., 2018. Jelatin bazlı yenilebilir film ve kaplamalar. Akademik Gıda, 16 (3), 332-339.

Cregenzán-Alberti, O., Halpin, R. M., Whyte, P., Lyng, J. G., Noci, F. (2015). Study of the suitability of the central composite design to predict the inactivation kinetics by pulsed electric fields (PEF) in *Escherichia coli*, *Staphylococcus aureus* and *Pseudomonas fluorescens* in milk. Food and Bioproducts Processing, 95, 313-322.

Crespo, A., Martín, A., Ruiz-Moyano, S., Benito, M. J., Rufo, M., Paniagua, J. M., Jiménez, A. (2020). Application of ultrasound for quality control of Torta del Casar cheese ripening. Journal of Dairy Science, 103(10), 8808-8821.

De Oliveira Alves, A. C., Pérez, M. H. (2020). Study of the effect of high hydrostatic pressure in the decrease of *Listeria monocytogenes* in pasteurized mixed cheese. Brazilian Journal of Development, 6(5), 23242-23252.

Delgado, K., Vieira, C., Dammak, I., Frasão, B., Brígida, A., Costa, M., Conte-Junior, C. (2020). Different ultrasound exposure times influence the physicochemical and microbial quality properties in probiotic goat milk yogurt. Molecules, 25(20), 4638.

Delorme, M. M., Guimarães, J. T., Coutinho, N. M., Balthazar, C. F., Rocha, R. S., Silva, R., Margalho, L. P., Pimentel, T. C., Silva, M. C., Freitas, M. Q., Granato, D., Sant'Ana, A. S., Duart, M. C. K. H., Cruz, A. G. (2020). Ultraviolet radiation: An interesting technology to preserve quality and safety of milk and dairy foods. Trends in Food Science & Technology, 102, 146-154.

Efaq, A. N., Rahman, N. N. N. A., Nagao, H., Al-Gheethi, A. A., Shahadat, M., Kadir, M. O. A. (2015). Supercritical carbon dioxide as non-thermal al-

ternative technology for safe handling of clinical wastes. Environmental Processes, 2, 797-822.

Evrendilek, G. A. (2014). Non-thermal processing of milk and milk products for microbial safety. Dairy microbiology and biochemistry: recent developments, 322, 322-355.

García-Cano, I., Yeh, P. W., Rocha-Mendoza, D., Jiménez-Flores, R. (2021). Supercritical CO_2 treatment reduces the antigenicity of buttermilk β-lactoglobulin and its inflammatory response in Caco-2 cells. JDS communications, 2, 1-6.

Guneser, O., Karagul Yuceer, Y. (2012). Effect of ultraviolet light on water-and fat-soluble vitamins in cow and goat milk. Journal of Dairy Science, 95(11), 6230-6241.

Gurol, C., Ekinci, F. Y., Aslan, N., Korachi, M. (2012). Low temperature plasma for decontamination of *E. coli* in milk. International Journal of Food Microbiology, 157(1), 1-5.

Güven, E., Yıldız, H. (2016). Isıl olmayan yeni gıda muhafaza tekniklerinin sanayi uygulamaları-2. Gıda, 41(4), 243-250.

Hales, B. R., Bastarrachea, L. J. (2021). Microbial inactivation on a processed cheese surface by UV-A light. ACS Food Science & Technology, 1(3), 347-353.

Herceg, Z., Režek Jambrak, A., Lelas, V., Mededovic Thagard, S. (2012). The effect of high intensity ultrasound treatment on the amount of *Staphylococcus aureus* and *Escherichia coli* in milk. Food Technology and Biotechnology, 50(1), 46-52.

Hu, W., Zhou, L., Xu, Z., Zhang, Y., Liao, X. (2013). Enzyme Inactivation in food processing using high pressure carbon dioxide technology. Critical Reviews in Food Science and Nutrition, 53, 145e161.

Jambrak, A. R., Lerda, D., Mirčeta, R., Šimunek, M., Lelas, V., Chemat, F., Herceg, Z., Batur, V. (2012). Experimental design and optimization of ultrasound treatment: Functional and physical properties of sonicated ice cream model mixtures. Food Processing & Technology, 3(3), 1000145.

Keklik, N. M., Elik, A., Salgin, U., Demirci, A., Koçer, G. (2019). Inactivation of *Staphylococcus aureus* and *Escherichia coli* O157: H7 on fresh kashar cheese with pulsed ultraviolet light. Food Science and Technology International, 25(8), 680-691.

Keklik, N. M., Elik, A., Salgın, U., Demirci, A., Kocer, G. (2020). Surface decontamination of white cheese by pulsed UV light treatment. Journal of Food Safety and Food Qualıty-Archıv Fur Lebensmıttelhygıene, 71(4), 86-92.

Khosravi-Darani, K. (2010). Research activities on supercritical fluid science in food biotechnology. Critical Reviews in Food Science and Nutrition, 50, 479e488.

Koca, N., Öztürk, M. (2020). Application of batch system ultraviolet light on the surface of kashar cheese, a kind of pasta-filata cheese: Effects on mould inactivation, lipid oxidation, colour, hardness and sensory properties. Journal of Dairy Research, 87(4), 493-497.

Koca, N., Saatli, T. E., Urgu, M. (2018). Gıda sanayisinde ultraviyole ışığın yüzey uygulamaları. Akademik Gıda, 16(1), 88-100.

Komora, N., Maciel, C., Pinto, C. A., Ferreira, V., Brandão, T. R. S., Saraiva, J. M. A., Castro, S. M., Teixeira, P. (2020). Non-thermal approach to *Listeria monocytogenes* inactivation in milk: The combined effect of high pressure, pediocin PA-1 and bacteriophage P100. Food Microbiology, 86, 103315.

Körzendörfer, A., Hinrichs, J. (2019). Manufacture of high-protein yogurt without generating acid whey–impact of the final pH and the application of power ultrasound on texture properties. International Dairy Journal, 99, 104541.

Li, J., Wang, J., Zhao, X., Wang, W., Liu, D., Chen, S., Ye, X., Ding, T. (2019). Inactivation of *Staphylococcus aureus* and *Escherichia coli* in milk by different processing sequences of ultrasound and heat. Journal of Food Safety, 39(2), e12614.

Liu, G., Carøe, C., Qin, Z., Munk, D. M., Crafack, M., Petersen, M. A., Ahrné, L. (2020). Comparative study on quality of whole milk processed by high hydrostatic pressure or thermal pasteurization treatment. LWT, 127, 109370.

Mandal, R., Singh, A., Singh, A. P. (2018). Recent developments in cold plasma decontamination technology in the food industry. Trends in Food Science & Technology, 80, 93-103.

Matak, K. E., Sumner, S. S., Duncan, S. E., Hovingh, E., Worobo, R. W., Hackney, C. R., Pierson, M. D. (2007). Effects of ultraviolet irradiation on chemical and sensory properties of goat milk. Journal of Dairy Science, 90(7), 3178-3186.

Oğuzhan, P. (2013). Yüksek hidrostatik basınç teknolojisinin gıda endüstrisinde kullanımı. Erzincan Üniversitesi Fen Bilimleri Enstitüsü Dergisi, 6(2), 205-219.

Ott, L. C., Jochum, J., Burrough, L., Clark, S., Keener, K., Mellata, M. (2022). High voltage atmospheric cold plasma inactivation of *Listeria monocytogenes* in fresh Queso Fresco cheese. Food Microbiology, 105, 104007.

Patel, H. A., Carroll, T., Kelly, A. L. (2015). Potential applications of nonthermal processing technologies in the dairy industry. Dairy Processing and Quality Assurance, 528-551.

Rashmi, K. G., Warrier, A. S. (2020). Non-thermal processing of dairy foods. In Dairy Processing: Advanced Research to Applications (pp. 25-49). Springer, Singapore.

Rathod, N. B., Kahar, S. P., Ranveer, R. C., Annapure, U. S. (2021). Cold plasma an emerging nonthermal technology for milk and milk products: A review. International Journal of Dairy Technology, 74(4), 615-626.

Ricciardi, F. E., Plazzotta, S., Conte, A., Manzocco, L. (2021). Effect of pulsed light on microbial inactivation, sensory properties and protein structure of fresh ricotta cheese. LWT, 139, 110556.

Ruan, R., Deng, S., Cheng, Y. (2010). Concentrated high intensity electric field (CHIEF) pasteurization of milk. Midwest Dairy Foods Research Center, 2010, 183-188.

Shabbir, M. A., Ahmed, H., Maan, A. A., Rehman, A., Afraz, M. T., Iqbal, M. W., Khan, I. M., Amir, R. M., Ashraf, W., Khan, M. R., Aadil, R. M. (2020). Effect of non-thermal processing techniques on pathogenic and spoilage microorganisms of milk and milk products. Food Science and Technology, 41, 279-294.

Smigic, N., Djekic, I., Tomic, N., Udovicki, B., Rajkovic, A. (2019). The potential of foods treated with supercritical carbon dioxide (sc-CO2) as novel foods. British Food Journal, 121 (3), 815-834.

Soltanzadeh, M., Peighambardoust, S. H., Gullon, P., Hesari, J., Gullón, B., Alirezalu, K., Lorenzo, J. (2020). Quality aspects and safety of pulsed electric field (PEF) processing on dairy products: A comprehensive review. Food Reviews International, 1-22.

Swelam, S. (2018). Composition and quality of soft cheese made from milk treated with high hydrostatic pressure. Journal of Food and Dairy Sciences, 9(1), 37-40.

Syed, Q. A., Ishaq, A., Rahman, U. U., Aslam, S., Shukat, R. (2017). Pulsed electric field technology in food preservation: a review. Journal of Nutritional Health & Food Engineering, 6(6), 168-172.

Tavsanli, H., Aydin, M., Ede, Z. A., Cibik, R. (2021). Influence of ultrasound application on the microbiota of raw goat milk and some food pathogens including *Brucella melitensis*. Food Science and Technology International, 28(7), 634-640.

Tsevdou, M., Ouli-Rousi, M., Soukoulis, C., Taoukis, P. (2020). Impact of high-pressure process on probiotics: Viability kinetics and evaluation of the quality characteristics of probiotic yoghurt. Foods, 9(3), 360.

Vo, H. T., Imai, T., Teek, J., Sekine, M., Kanno, A., Le, A. V., Higuchi, T., Phummala, K., Yamamoto, K. (2013). Comparison of disinfection effect of pressurized gases of CO_2, N_2O, and N_2 on *Escherichia coli*. Water Research, 47(13), 4286-4293.

Walter, L., Knight, G., Ng, S. Y., Buckow, R. (2016). Kinetic models for pulsed electric field and thermal inactivation of *Escherichia coli* and *Pseudomonas fluorescens* in whole milk. International Dairy Journal, 57, 7-14.

Walter, M., Brzozowski, B., Adamczak, M. (2021). Effect of supercritical extract from black poplar and basket willow on the quality of natural and probiotic drinkable yogurt. Animals, 11(10), 2997.

Wan, Z., Misra, N. N., Li, G., Keener, K. M. (2021). High voltage atmospheric cold plasma treatment of *Listeria innocua* and *Escherichia coli* K-12 on queso fresco (fresh cheese). LWT, 146, 111406.

Wang, C. Y., Huang, H. W., Hsu, C. P., Yang, B. B. (2016). Recent advances in food processing using high hydrostatic pressure technology. Critical Reviews in Food Science and Nutrition, 56(4), 527-540.

Ward, D. M., Patras, A., Kilonzo-Nthenge, A., Yannam, S. K., Pan, C., Xiao, H., Sasges, M. (2019). UV-C treatment on the safety of skim milk: Effect on microbial inactivation and cytotoxicity evaluation. Journal of Food Process Engineering, 42(4), e12944.

Xu, D., Yuan, F., Jiang, J., Wang, X., Hou, Z., Gao, Y. (2011). Structural and conformational modification of whey proteins induced by supercritical carbon dioxide. Innovative Food Science and Emerging Technologies, 12, 32-37.

Yang, S., Liu, G., Munk, D. M. E., Qin, Z., Petersen, M. A., Cardoso, D. R., Otte, J., Ahrné, L. (2020b). Cycled high hydrostatic pressure processing of whole and skimmed milk: Effects on physicochemical properties. Innovative Food Science & Emerging Technologies, 63, 102378.

Yang, S., Suwal, S., Andersen, U., Otte, J., Ahrné, L. (2020a). Effects of pulsed electric field on fat globule structure, lipase activity, and fatty acid composition in raw milk and milk with different fat globule sizes. Innovative Food Science & Emerging Technologies, 102548

Yangılar, F., Kabil, E. (2013). Süt ve süt ürünlerinde bazı ısıl olmayan mikrobiyal inaktivasyon yöntemleri. Uludağ Üniversitesi Ziraat Fakültesi Dergisi, 27(1), 97-108.

Zabot, G. L., Moraes, M. N., Carvalho, P. I. N., Meireles, M. A. A. (2015). New proposal for extracting rosemary compounds: Process intensification and economic evaluation. Industrial Crops and Products, 77, 758e771.

Zhang, Z. H., Wang, L. H., Zeng, X. A., Han, Z., Brennan, C. S. (2019). Non-thermal technologies and its current and future application in the food industry: a review. International Journal of Food Science & Technology, 54(1), 1-13.

Chapter 4

MAJOR PROBLEMS ABOUT MEMBRANE FOULING IN MEMBRANE BIOREACTORS (MBRS) AND THE EFFECT OF FOULANT ON MEMBRANE: A MINI-REVIEW

Enes ÖZGENÇ[1], Emine KELEŞ[2]

1 Lect., Trakya University, Vocational School of Health Services, Environmental Health Program, Edirne, Turkey. enesozgenc@trakya.edu.tr, ORCID: 0000-0003-0878-6418

2 Lect. Dr., Trakya University, Faculty of Architecture, Department of Landscape Architecture, Edirne, Turkey. eminekeles@trakya.edu.tr, ORCID:0000-0003-0084-9525

INTRODUCTION

Water scarcity at the global level is one of the main challenges faced in many places across the world (Baghbanzadeh et al. 2017; Wang et al. 2017; Cao, Wang and Chen 2019; Kahil et al. 2019; Lim et al. 2019). Owing to fast urbanization and industrialization, water requirements are ever-increasing (Arbués, García-Valiñas and Villanúa 2010; Kappel et al. 2014; Goswami et al. 2018). Even though the contamination of existing water resources which co-exists together with global climate change (Goswami et al. 2018) and non-climatic drivers, drought, solid waste leachate, intensive agricultural activities, and industrial utilization (Wang et al. 2016) erosion, inadequate infrastructure (Medeiros et al. 2017) has substantially augmented the requirements for clean freshwater resources (Bai et al. 2015), it is worsened by sources of water pollution such as sewage apart from the discharge of untreated domestic and industrial waste (Dharminder et al. 2019), municipal (Zhang et al. 2020), agricultural (Mohajeri et al. 2020), landfill, leaking underground storage tank (Rodrıguez et al. 2004), stormwater. Therefore, safe, clean, and desirable drinking waters free from existing microplastics (Shen et al. 2020), coliform bacteria, viruses, pathogenic microorganisms (Bagheri and Mirbagheri 2018; Wang et al. 2019), residual particles, organic micropollutants (Goswami et al. 2018; Di Marcantonio et al. 2020; Wang et al. 2021) and convenient sanitation have historically been a primary issue for all the world (Sillanpää et al. 2018).

To meet the progressive demand for freshwater resources and to produce treated wastewater with high-quality standards, membrane bioreactors (MBRs) are a reliable and promising technology that attract significantly attention as perhaps the fastest growing technology among treatment applications that may differ depending on wastewater characteristics, discharge limits, the method to be applied and treatment cost (Lee, Kang and Shin 2003; Guo, Ngo and Li 2012; Fortunato et al. 2016; Wong et al. 2016; Aslam et al. 2017; Lim et al. 2019; Ng et al. 2020). MBRs are different from conventional activated sludge systems since MBRs have small reactor volume, high MLSS concentrations and high volumetric loading, less waste activated sludge formation, no odor problems arising from the final settling ponds, the system being more stable against fluctuations in the influent organic loads, no sludge bulking and rising problems, ease of operation of the system, less space requirement, no need for a disinfection unit, high effluent quality (Meng et al. 2009; Guo et al. 2012; Lin et al. 2014; Besha et al. 2017; Bagheri and Mirbagheri 2018; Lim et al. 2019). In contrast to the advantages and popularity of MBRs in wastewater treatment, the principal concern related to this technology is the control of membrane fouling (Lin et al. 2020). Membrane substitutes for the major restriction to membrane process operation (Bagheri and

Mirbagheri 2018) and considerably decreases membrane performances and lifespan (Rosenberger et al. 2006; Meng et al. 2009; Jegatheesan et al. 2016). These restrictions can be occurred by bulking sludge (Pan et al. 2010), increase in transmembrane pressure (TMP), increase in MLSS, increase in F/M rate, increase in EPS (Pan et al. 2010) and SMP (Shi et al. 2018), decrease in permeate flux (Jegatheesan et al. 2016), decrease in SRT and HRT, sub-critical flux value (Zhang et al. 2006; Rosenberger et al. 2006; Meng et al. 2009; Bagheri and Mirbagheri 2018). This may be proved by the ever-increasing academic research related to membrane fouling in MBRs (Lin et al. 2020). Recently, significant several articles about this issue have been published. Fig. 1 shows the chronological variations of SCI articles regarding membrane fouling and MBRs. Almost whole of these studies have been conducted on different focus points. For this reason, it is necessary to compare and sum up the literature findings on membrane fouling in MBRs, especially in recent years. Therefore, the objectives of this article are to emphasize the primary problems under different circumstances in various membrane applications and to provide some advice to enhance the performance of MBR by alleviating membrane fouling depending on past and current academic findings.

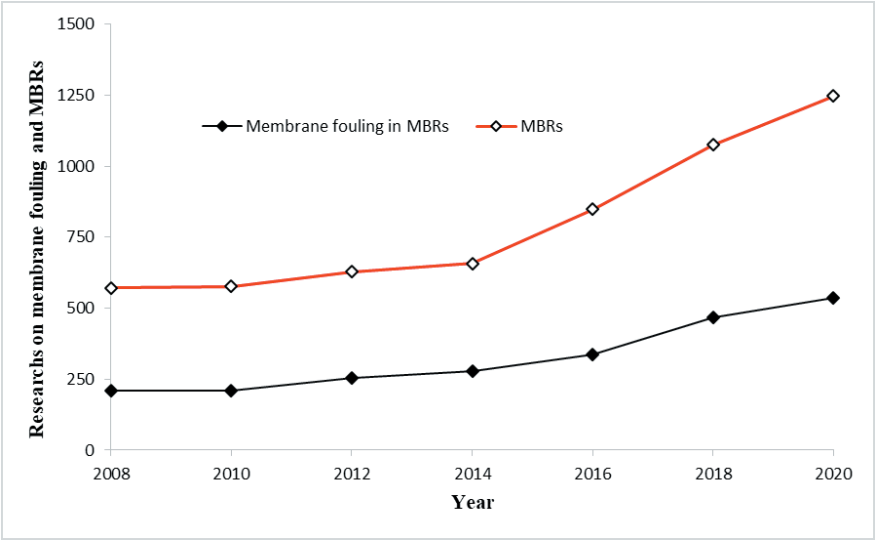

Figure 1. *The diagram shows the yearly academic research on MBR fouling and MBRs.*

Basics of membrane fouling in MBRs

Membrane fouling is a great barrier that affects water infiltration and the dissolved matter transport through the membrane (She et al. 2016), causing go worse fundamental membrane performance (Goh et al. 2018). This fouling occurred in membranes limits the amount of permeability of

the membrane. That is, it causes a decrease in the clean water output treated per unit membrane area. Membrane fouling features under sub-critical flux operation in MBRs have been investigated by many researchers (Wang et al. 2008; He et al. 2017; Borea et al. 2018; Nguyen et al. 2019; Banti et al. 2020). Membrane fouling in MBRs may be referred to as extracellular polymeric material (EPS) (Lin et al. 2014), soluble microbial products (SMP) (Teng et al. 2020), colloidal substances (Banti et al. 2020), dissolved organic matter (DOM) (Chon et al. 2020), organic and inorganic substances (Her et al. 2008), sludge flocs (Aslam et al. 2017) and biopolymer parts (Yin et al. 2020b). As shown in Table 1, factors contributing to membrane fouling can be divided into three major categories including operating conditions, biomass characteristics, and membrane properties.

Table 1. *Factors affecting membrane fouling in MBRs (Bagheri and Mirbagheri 2018).*

Operating conditions	Biomass characteristics	Membrane properties
Configuration	MLSS	Material
Cross-flow velocity	EPSs	Configuration
Aeration	SMPs	Hydrophobicity
Hydraulic retention time	Particle size distribution	Surface porosity
Sludge retention time	Floc structure	Pore size
Organic loading rate	Microbial community	Pore size distribution
DO	Dissolved matter	Molecular weight cut-off
TMP		
Permeate flux		
Temperature		
Influent composition		

As schematically illustrated in Fig. 2, the steps of membrane fouling are adsorption, pore-clogging, gel-layer formation, and cake-layer formation caused by interactions between the particles and the membrane surface (Meng et al. 2009; Lin et al. 2020).

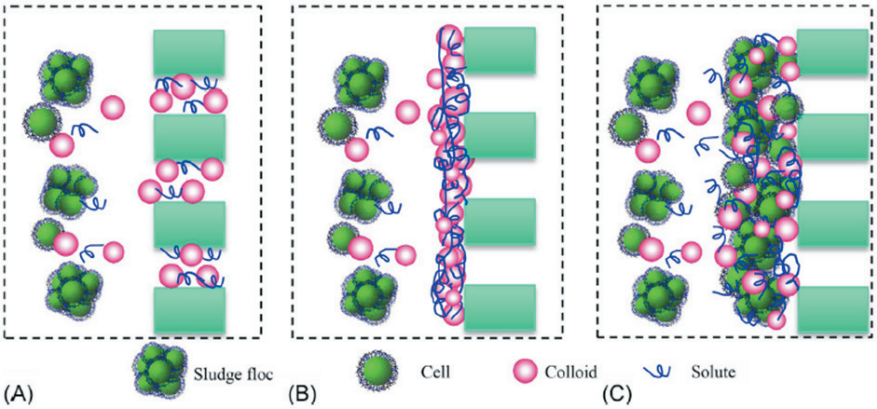

Figure 2. *The formation of membrane fouling in MBRs: (A) pore-clogging, (B) gel-layer composition, and (C) cake-layer composition in MBRs (Lin et al. 2020).*

The place where it occurs pollution in MBRs is divided into three as concentration polarization (Li et al. 2019), internal pollution, and external pollution (Zuthi et al. 2017). Concentration polarization causes resistance to fluid flow by increasing osmotic pressure, causing often means flux decline (Giacobbo et al. 2018). Internal fouling takes place by storage and adsorption of micro-molecules. External fouling is known as the formation of biofilm and storage of macromolecules, colloids, and particles on the membrane surface (Zuthi et al. 2017). As shown in Fig. 2, blocking of average pore sizes by contaminants of the membrane refer to pore-clogging because of the restriction of membrane pores ending up with tiny particles reaching into pore walls, while cake formation results from macromolecules such as DOMs, EPS, and SMP which are big pollutant particles and it occurs outside the membrane surface by increasing hydraulic resistance (Meng et al. 2007; Zheng et al. 2018). Also, the gel layer on the membrane surface occurs due to solidifying of dissolvable and colloidal microbial products (DCMPs), causing highly severe membrane fouling in MBRs (Chen et al. 2019). But, the ultimate layer that happened on the membrane surface may be eliminated by air scouring or the turbulence resulting from cross-flow (Iorhemen, Hamza and Tay 2016).

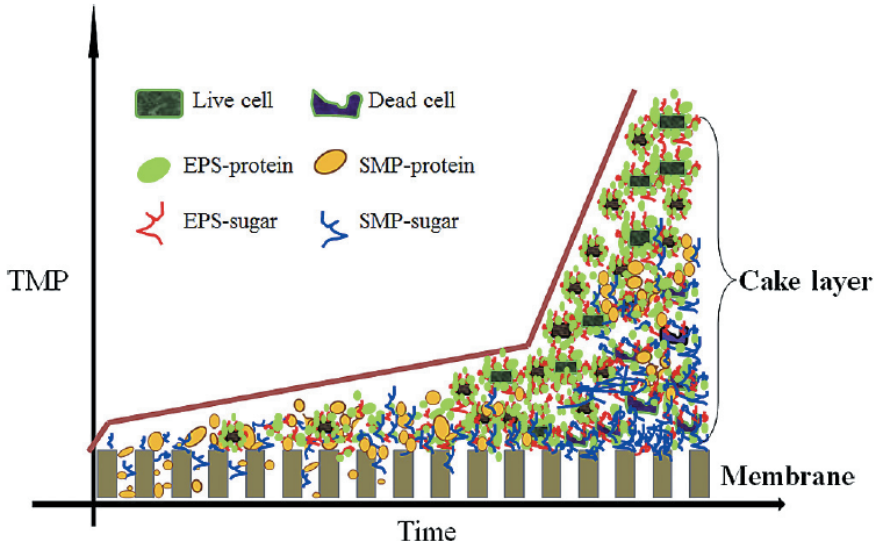

Figure 3. *Effect of contaminants such as EPS, SMP, living, and dead cells on TMP pressure time-varying (Meng et al. 2017).*

TMP has three phase profiles: a sharp increase in TMP, a gradual rise in TMP, and a sudden rapid increase in TMP (Jiang et al. 2018; Lin et al. 2020). (Zheng et al. 2018) reported that membrane filtration at low TMP may decrease fouling and concentration polarization when it has a lower flux, also (Zhang, Ding and Technology 2015) reported that higher TMP can promote driving force and therefore enhance flux and eliminate blocking fouling. Furthermore, (Rios et al. 2011) observed TMP merely had an effect on permeability, and higher TMP had hardly any effect on increasing microfiltration performance because of fouling effects. So, choosing of TMP convenient for membrane filtration is necessary (Luo et al. 2013). During operational conditions, at fixed TMP, infiltrate flux decreases with membrane fouling, causing the increase in TMP. TMP may also increase with decreasing HRT, which can cause enhancement growth of biomass and accumulation of SMP and an increase in sludge viscosity and EPS concentration, and higher MLSS concentration stemmed from longer SRT (Huang, Ong and Ng 2011). To sum up, as shown in Fig. 3, increase in TMP bring about the blocking of membrane pores, surpass critical flux value, accumulation of particle residuals, changes in the cake layer form, and changes of flux due to severe membrane fouling (Cinar et al. 2016; Skinner et al. 2018; Zhao et al. 2020; Schiffer et al. 2020). During MBRs operation, the features of membrane foulants change depending on time. EPS formation is regarding growth and substrate utilization. So, the rise of the organic loading rate or F/M rate will cause the formation of more bound EPS (Meng et al. 2009). In addition, aeration which provides dissolved oxygen in MBR is an important operating parameter for the

decrease in biofilm formation (Lee et al. 2009). Being inactive or dead of cells may be related to existing oxygen concentration. Cells in the deeper of the biofilm can die since anoxic or anaerobic conditions may develop (Hastuti, Medawaty and Pamekas 2011), causing the accumulation of considerable biopolymers and other cell degradation products. Yet, the live cells on the surface of the biofilm can support and boost the biodegradation of the deposited biopolymers (Meng et al. 2017). EPS can be also significantly affected by SRT which is one of the most important operating parameters affecting MBRs performance. As SRT increased, that is, as the biomass stays for a longer time in the system it causes a decrease in EPS concentration and TMP while lower SRT, which leads to the metabolism to quicker growth causes a rise in EPS concentration, and both increase the produced amounts of proteins and polysaccharides at the cake layer level and changes the fine structure of these extracellular molecules in the MBR, which brings about rise in membrane fouling and decrease in membrane performance (Silva et al. 2016). So, too short and long SRT could negatively affect membrane performance and result in extreme membrane fouling. (Hasan, Elektorowicz and Oleszkiewicz 2012) stated that TMP was influenced by the soluble carbohydrates (EPSc) and soluble proteins (EPSp) and EPSp contributed to membrane fouling more than EPSc. SMP have also strong relation with TMP which has three phase profiles; and causes significantly membrane fouling in MBRs (Shi et al. 2018). (Mahendran et al. 2011) also stated that proteins and polysaccharides are predominant contaminants existing on the membrane surface during MBR operation but the polysaccharides are more steady biofouling and more resistant to removal by oxidizing agents such as sodium hypochlorite. Moreover, the biofouling of membranes in MBRs is due to the emergence of abundant bacterial species on membranes. Though the major responsibility for this biofouling is high-abundance species that dominated the biofilm community (Zhang et al. 2018), since the accumulation of some low-abundance colonizers on the membrane can trigger the formation of biofilm, they are harmful to membrane filtration. So, during membrane fouling control must be concentrated on removal of some low-abundance bacteria rather than the high-abundance bacteria (Zhang et al. 2018; Xu et al. 2019).

Biofouling

One of the most significant operational problems in membrane practices, biofouling refers to microorganism's adhesion and cell growth and proliferation on the membrane surface, which has created a significant apprehension during membrane filtration operation and biofouling bring to a decrease in the performance of MBRs because of EPS and SMP deposition (Kampouris et al. 2018). Biofouling has been known as a contributing factor

to >45% of whole membrane fouling and it is an important problem for membrane separation processes such as microfiltration and ultrafiltration in that microbial flocks are larger than membrane pores (Kimura, Tanaka and Watanabe 2014; Bucs et al. 2018). Microorganisms such as Mycobacterium, Flavobacterium, Pseudomonas, Bacillus, Cytophaga, and Lactobacillus tend to increase by forming a biofilm that consists primarily of microbial cells and EPS. EPS can change in chemical and physical features, but include primarily polysaccharides, proteins, glycoproteins, lipoproteins, and other macromolecules of microbial origin (Matin et al. 2011; Guo et al. 2012; Goh et al. 2018). Even though the physical features of the biofilm are mostly specified by the EPSs, the physiological features are specified by the bacterial cells (Matin et al. 2011). EPSs which are linked to biofouling emergence consist of a multilayer of living, inactive, and dead microorganisms. The formation of EPSs is significant because it both keeps off nutrients from the environment to survive of bacteria and maintains a stable arrangement of a microbial consortium composed of distinct species (Matin et al. 2011). Also, other important factors related to the biofouling of membrane in MBRs are MLSS, OLR or F/M ratio, HRT, SRT, dissolved oxygen concentration (DOC), salinity, cations in feedwater, nutrients, and temperature (Guo et al. 2012). Biofilm formation together with the effect of these factors may take place in three stages; bacteria attachment, reproduction, and detachment phase (Ramsey and Whiteley 2004; Noori et al. 2019) as illustrated in Fig. 4. The first step comprises the preconditioning of the membrane surface with organic macromolecules and inorganic compounds (Liu and Mi 2014; BinAhmed et al. 2018). It has been stated that this conditioning increases the attachment of cells to the surface (Matin et al. 2011; Suwarno et al. 2016). After, the adsorption of these matters create a surface that is enriched in nutrient and convenient in terms of bacteria adhesion (Ronen et al. 2015; Goh et al. 2018). The bacteria attachment stage can be affected by several factors. These factors may be membrane characteristics, microbial properties, and operational conditions (Jiang, Li and Ladewig 2017). The next stage consists of clustering the attached cells and the formation of microcolonies (Johnson 2008). In this stage, cells start to generate exopolymers, grow and reproduce by consuming nutrients (Melo and Flemming 2010; Matin et al. 2011; Bjarnsholt 2013; Khatoon et al. 2018). During the cell reproduction process, EPS which includes components polysaccharides, nucleic acids, proteins, lipids, and other biopolymers is continually being produced and it may make biofilm structure more powerful (Matin et al. 2011; Toyofuku et al. 2016). In the last stage of biofilm formation, cells leave from mature biofilm owing to both lack of nutrients and an increase in population density. After, cells provide biofilm formation on new sites for further multiplication (Rochex and Lebeault 2007; Matin et al. 2011; Kim and Lee 2016; Jiang et al. 2017; Armbruster and Parsek 2018; Goh et al. 2018).

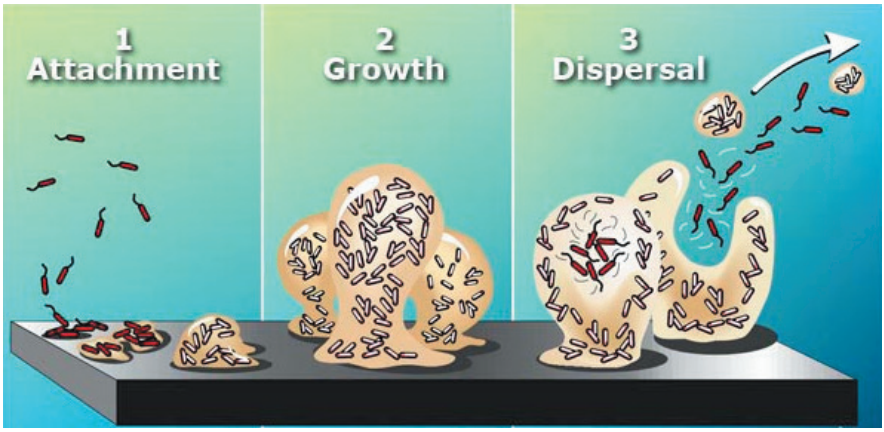

Figure 4. *Biofilm formation steps on the membrane surface.*

The Biofilms Hypertextbook: Introduction to Biofilms Alfred B. Cunningham, John E. Lennox, and Rockford J. Ross, Eds. 2001–2008.

(Bucs et al. 2018) stated that biofouling may not be avoided, so control strategies must focus on decreased or delayed impact of deposited biofilm on performance, delayed biofilm formation, and removal of biofilm by developed cleaning strategies. To determine fouling on the membrane surface may be useful applications such as cell scanning electron microscopy (SEM), CLSM, atomic force microscopy (AFM) (Miyamoto et al. 2019), direct observation through the membrane (DOTM) (Yachnin, Ramon and Technology 2017), energy dispersive X-ray spectroscopy (EDX), fourier transform infrared (FT-IR) spectroscopy, confocal laser scanning microscopy (CLSM), zeta potential, optical profilometer and contact angle, and flux modeling (Kaya et al. 2019). (Kaya et al. 2019) used flat-sheet and hollow-fiber membranes. They stated that the cake layer on the flat-sheet membrane occurred much more than that on the hollow-fiber membrane and also the thickness of the cake layer on the flat-sheet membrane was influentially decreased technique of physical stripping. However, because of irreversible fouling on the membrane, they reported that these techniques for the hollow-fiber membrane were more effective. In recent research, it has been observed that flux and sludge flocks also have an effect on biofouling. As regarding these factors, (Christensen et al. 2018) stated that the fastest flux fall happened in the solute fraction because of the formation of irreversible fouling, which then this fraction contained foulants smaller than the membrane pore diameter (0.2 μm) and stated that the existence of sludge flocs decreased formation of an external fouling layer and concentration of foulant because this can be due to surface erosion or more turbulence close to the membrane surface by sludge flocs. For this reason, membrane fouling, concentrations of solutes and colloids should be kept low, but the concentration of sludge flocs high (Iorhemen,

Hamza and Tay 2017). In addition to applications, (Maliszewska and Czapka 2020), for the removal of biofoulant on the surface of membranes, in dielectric barrier discharge (DBD) plasma technology for 3–10 min, which equates to a plasma dose of 13–42 J cm^{-2} performed removal of biological cells from the membrane surface. This study has shown that the removal of biofouling on the membrane surface is very effective and the biofouling removal relies on the membrane type and the exposure time to non-thermal plasma. Moreover, to enhance membrane performance, a recent study also revealed that membrane material modified like the addition of polyvinylpyrrolidone (PVP), UV irradiation, and thermal annealing allowed less foulant deposition on the membrane surface and the initial flux of modified membrane increased up to 200% by comparison with unmodified membrane, indicating that the modified membrane has perfect stability in term of permeate flux and rejection performance and has formed less foulant deposition on the membrane surface (Kusworo et al. 2020). Admittedly, these technologies and applications could be an important part of removing the biofouling of membranes. However, the improvement of more convenient strategies to control membrane biofouling in MBRs still requires a better understanding of features and behaviors of biofilm (Kochkodan and Hilal 2015; Bucs et al. 2018).

Organic Fouling

Organic fouling and inorganic scaling are major obstacles that substantially limit the performance of the membrane, that is, cause flux decline and a rise in transmembrane pressure and it is difficult to eliminate owing to their complex structure (Antony et al. 2011; Quay et al. 2018). Organic foulants in MBRs are known as alginate, octanoic acid, humic acids, hydrophilic carbohydrates, EPS, aquatic humic substances, bovine serum albumin, natural organic matter (NOM), transparent exopolymer particles (TEP), biopolymers, proteinaceous compounds (Jiang et al. 2017). Yet, bovine serum albumin (BSA), alginate, and humic acid among organic foulants have become the focus of interest in research areas. Also, other substantial factors affecting organic fouling are feedwater composition, foulant-surface, and foulant–foulant interplay (Mi and Elimelech 2010). (Wang and Li 2008) researched to evaluate the accumulation of biopolymer deposits in MBRs and its effect on membrane fouling. To research membrane fouling used a laboratory-scale submerged membrane bioreactor (SMBR) with a hollow-fiber membrane module under diverse operational conditions. The conclusion of their work demonstrated that the sludge supernatant inside the SMBR had higher organic ingredients than the MBR effluent. Analyzes in the SMBR system show that biopolymer clusters (BPC) are larger in size than soluble microbial products (SMP). The findings of their experiment show that BPC is an important foulant

and have a substantial effect on membrane fouling and also a private form of organic matter that is created by the adsorption and affinity clustering of mainly SMP within the sludge layer deposited on the membrane surface. The deposition of BPC bring about a fouling layer on the membrane surface, and so causing a serious problem such as resulting in irreversible fouling and reversible fouling (Yan et al. 2021). Therefore, it is inevitable to remove BPCs because of membrane fouling effects. Characterization of the fouling membrane can make through solid state 13C-nuclear magnetic resonance (NMR) spectroscopy, high performance size-exclusion chromatography (HP-SEC) (Meng et al. 2009), physicochemical analyses including SEM, excitation-emission matrix (EEM), aggregate size, zeta potential and fourier transform infrared (FTIR). FTIR analyses show that membrane fouling happens due to organic foulants such as polysaccharide-like, protein-like and humic substances, thereby indicating the existence of ALG, BSA, and HA foulants on the membrane (Nguyen et al. 2020). Aggregation extent provides a profound analysis of distinct fouling behavior by determining the features of fouling (Banti et al. 2018). The aggregation and the form of the particles can be confirmed by the Small-angle X-ray scattering method (SAXS) (Abdelrasoul et al. 2017). Solidstate 13C-nuclear magnetic resonance (NMR) spectroscopy which is a strong analytical tool for inquiry of the characteristics of organic matters revealed that the nature of the membrane foulants changes rely on F/M but a high F/M rate will make foulants more proteinaceous (Kimura et al. 2005). Scanning Electron Microscope (SEM) is used both to specify the aggregation of bacteria and their end-products forming a thick biofilm on the membrane surface (Flimban et al. 2020) and to compare the foulant coverage and morphology on the membranes (Freire-Gormaly and Bilton 2019). High-performance size-exclusion chromatography (HP-SEC) is a well-demonstrated and easily available technique that defines distributions of apparent molecular weight (AMW) (Liu et al. 2016). EEM is a strong and helpful tool not only for the rapid and sensitive characterization of DOM in MBR but for monitoring pollutant transformation and membrane fouling also (Yu et al. 2020). Zeta potentials can give beneficial knowledge about internal and external fouling characterization because membrane zeta potential is in part as a result of the existence of foulant materials on its surface and also it gives information related to surface electrical features in a certain physicochemical setting (Rouquié et al. 2020). Lately, in order to insight into the composition of organic as fouling on the membrane surface, (Motsa, Mamba and Verliefde 2018) used a thin-film composite (TFC) FO membrane. They used alginate, BSA, humic acid, and octanoic acid as model foulant in order to represent carbohydrates, proteins, humic substances, and fatty acids. Although humic acid and octanoic acid have no significant effect on permeate flux loss, alginate and BSA and their

mixtures have caused substantially total flux loss. The addition of humic acid to the BSA and alginate mixture further worsened existing membrane fouling. They also stated that foulants like carbohydrates, proteins, and polysaccharides on the membrane surface increase flux loss. Furthermore, their study finds out the effect of organic foulants on membrane fouling layer structure and severe permeate flux loss (Nguyen et al. 2020). For this reason, to mitigate membrane fouling that can derive from the effect of such organic foulants, (Li et al. 2020) used UV/H_2O_2 and UV/PS that are pre-treatment processes for the UF process and reported that UV/H_2O_2 and UV/PS strikingly reduced all the organic micro-pollutants (OMPs) by more than 80%. In another study, (Yin et al. 2020b) stated that O_3/SUF system influentially prevented irreversible membrane fouling, and also the application of O_3 may decrease the stickiness of the surface of organic pollutants and thus this application is advantageous to remove the pollutants clustered on the membrane surface by chemical backwashing. Similarly, (Yin et al. 2020a) used pre-ozonation before membrane filtration to mitigation of membrane fouling from biopolymers and they selected bovine serum albumin (BSA) and sodium alginate (SA) as representatives of protein and polysaccharides, respectively. The results showed the reduction of organic fouling on the membrane surface was restricted at an ozone dose of 0.05 mg O_3/mg DOC but during an ozone dose higher than 0.10 mg O_3/mg DOC, pre-ozonation influentially increased the permeate flux and reduced the irreversible fouling as well as decreased the clustered of BSA and SA on the membrane and the adhesive force between BSA or SA and membrane surface. In summary, these studies made related to membrane fouling verify that SMP and EPS compounds, which are the major causes of organic pollution on the membrane surface, have too important an effect on the formation of membrane pollution. However, it has been observed that organic fouling of membranes caused by biopolymers may still be mitigated influentially by pre-ozonation.

Inorganic Scaling

The inorganic scaling that happened by the precipitation and crystallization processes is due to the accumulation of calcium, magnesium, carbonate, sulfate, and phosphorus on the membrane surface (Goh et al. 2018). The major components causing inorganic scaling are inorganic salts, containing $CaSO_4$, $CaCO_3$, SiO_2, and $BaSO_4$ (Wang 2005) and matters including cations and anions such as Ca_2^+, Mg_2^+, Fe_3^+, Al_3^+, SO_4^{2-}, PO_4^{3-}, CO_3^{2-}, OH^-, etc. (Wang et al. 2014). The negatively charged membrane surface charge can also cause inorganic fouling due to reacting with the negatively charged membrane surfaces of some cations such as Ca_2^+ and Al_3^+ in the mixed liquor-suspended solids (Iorhemen et al. 2016). Membrane scaling precipitation occurs under process conditions leading

to the formation of oversaturation because of its association with soluble salts. These scalants adversely affect membrane performance by reducing permeate flow as a result of adhesion to the membrane surface, thereby blocking the membrane pores. Bulk crystallization refers to crystal particles constituted in the bulk phase via homogeneous crystallization and then deposit on the membrane surface as particles (Pääkkönen et al. 2009; Shirazi, Lin and Chen 2010). The most substantial extent of fouling from bulk crystallization occurs at intermediate cross-flow velocity and higher pressure (Lee and Lee 2000). Surface crystallization generates solid crystals directly on the membrane surface. Scala formation occurring on the membrane surface is also as a result of the lateral growth of crystals formed on the active regions of the membrane (Shirazi et al. 2010). (Lee and Lee 2000) also suggested that it decreased with an increase in flux velocity, though the fouling from surface crystallization boosted with a rise in operating pressure. Especially in high pressure membrane systems, concentration polarization is known that the principal factor increasing salt concentration at the membrane surface, thereby causing particle deposition (Tang et al. 2010; Goh et al. 2018; Hejase and Tarabara 2021). Factors affecting scale formation be connected with the composition and temperature of feed water, water chemistry, operating conditions, membrane morphology, and hydrodynamic characteristics of the membrane (Touati et al. 2020). The most common control strategies used to mitigate inorganic scaling are pretreatment technologies, membrane monitoring and cleaning, surface modification, and novel membrane materials (Jiang et al. 2017). The basic phases of inorganic scaling are illustrated in Fig. 5 (Touati et al. 2020).

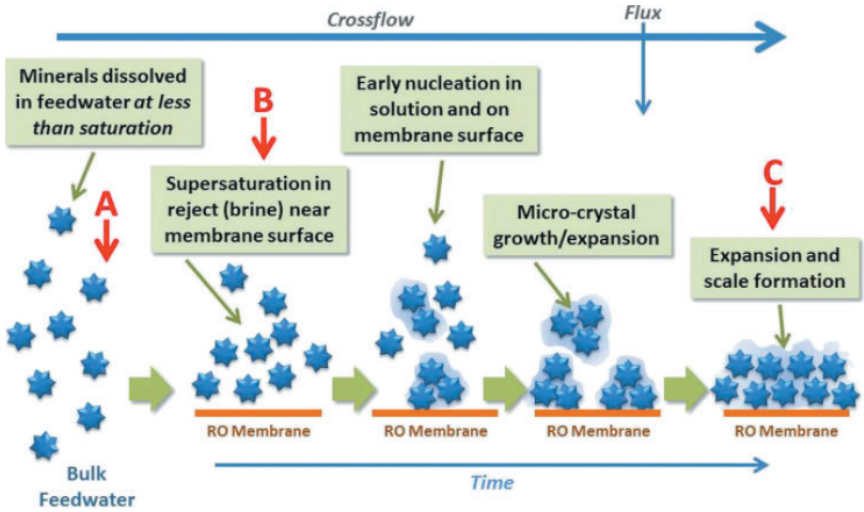

Figure 5. *Schematic illustration of the critical steps in scale formation onto the RO membrane surface over time (Touati et al. 2020).*

One of the most important factors is the nucleation process by which the free or dissolved ions or molecules amass and coordinate to set up new structures (Goh et al. 2018; Al-Ghamdi, Alhadidi and Ghaffour 2019; Touati et al. 2020), thereby causing membrane surface deposited with the inorganic scales that causes a rise in permeate flux decline and blocks membrane pores. Hence, it has been stated that membrane cleaning isn't appropriate through only physical activities such as relaxation and backwashing because of the limited ability to eliminate scaling and other foulants (see Fig. 5) (Weerasekara, Choo and Lee 2014). Therefore, removing inorganic scaling or reducing its effect must be concentrated on developing mitigation and preventive measures and promoting membrane performance (Ashfaq et al. 2020). Experimental studies have indicated that inorganic scaling can be eliminated both by pre-treatment of feedwater and chemical cleaning. The major chemical types and some of the often-used chemical agents to remove membrane fouling are shown in Table 2. As related to such membrane fouling problems, (Huang et al. 2019) operated two identical lab-scale MBRs. These are control MBR (Co-MBR) and a developed MBR dosed with ferric hydroxide (Fe-MBR). In their experiment, they observed that membrane fouling was reduced by 35% with the addition of iron. They stated that iron addition results in a rise in biomass floc extent, a decrease in the bacteria population related to biofilm formation, an increase in bacteria activity, and a decrease in of concentrations of DOMs and SMP, which contributes to positive impacts on membrane fouling mitigation. In addition, usage of antiscalants which are phosphonate-based and acrylic acid-based or pH adjustment may prevent scale formation on membranes, thereby leading to a lower permeate flux decrease, less calcium scale deposition on membrane surfaces, and an increase in the membrane lifetime (Lee et al. 2020; Yu et al. 2020).

Table 2. *Some of the applied chemical agents to remove membrane fouling and their mechanism of cleaning (Bagheri and Mirbagheri 2018).*

Chemical type	Mostly used agents	Mechanism of cleaning	Target foulants
Acids	Nitric, hydrochloric, oxalic and phosphoric acids	Solubilization and neutralization	Inorganic foulants
Bases	Sodium hydroxide	Hydrolysis, solubilization and saponification	Organic foulants
Oxidants	Sodium hypochlorite	Oxidation and disinfection	Organic and biological foulants
Surfactants and chelates	Sodium dodecyl sulfate and ethylene diamine tetraacetic acid	Hydrophilic/hydrophobic interactions and Chelation	Organic foulants associated with metal ions
New agents	Rhamnolipids and free nitrous acid	Solubilization, disinfection and hydrophilic/ hydrophobic interactions	Inorganic/organic and biological foulants

The scaling inhibiting technique by such antiscalants is that deposition of mineral ions in the solution by complexation can be prevented by antiscalants and by keeping microcrystals in the aqueous suspension, it further reduces their accumulation and growth on the membrane surface (Liu, Xu and Das 2019). Recently, (Quay et al. 2018) have revealed that silica which is one of the most prevalent inorganic scalants is considerably difficult to eliminate from the membrane surface but most notably commercially existing antiscalants which break the crystallization process of scale formation are ineffective in removing silica scale. So, silica scaling limiting high water recovery in RO has become a tough problem faced in membrane desalination. As related to this problem, to eliminate silica and sulfate from influent water, (German et al. 2019) used self-regenerating reversible ion exchange-membrane (RIX-M) processes by using an adjustable anion exchange mixture. They reported that RIX-M showed up as a new pre-treatment technique to maintain membranes from sulfate and silica fouling without dosing anti-scalants. They also used hybrid ion exchangers and/or HIX-NanoZr and observed especially more at pH 7.4 of removal of silica by zirconium oxide nanoparticles dispersed within ion exchangers. Moreover, additional of alginic acid after silica fouling has formed can eliminate silica scale from the membrane and restore permeate flux due to complexation between silica and carboxylic acid functional groups on the manuronic and guluronic acids in alginate (Higgin, Howe and Mayer 2010). These findings point out that inorganic scaling has become increasingly important in MBRs. For this reason, future research must concentrate on designing and optimizing novel membranes, exploring novel antiscalants and developing their usage areas, evaluating their positive and negative effects, and improving pretreatment techniques. Accordingly, performing these applications will lead to a significant increase in membrane efficiency and performance.

CONCLUSIONS

Lately, significant developments in membrane desalination technologies are mainly focused on decreasing membrane fouling in MBRs. In this article, membrane fouling in MBRs has been classified into biofouling, organic fouling, and inorganic scaling, and also the methods by which these foulants can be removed have been stated based on past and current studies. However, novel strategies in membrane modifications in addition to approaches with regard to other fouling control to mitigate and control membrane fouling have great importance. Therefore, by making membrane modifications under different conditions, fouling effects must be also focused on studying. Although better to understand membrane fouling, to develop appropriate pre-treatment processes to reduce the fouling effect, to provide better membrane treatability, and to produce acceptable wastewater quality are major objectives, the current strategies and more novel strategies still need to be further searched.

REFERENCES

Abdelrasoul, A., H. Doan, A. Lohi & C.-H. J. J. o. E. S. Cheng (2017) The influence of aggregation of latex particles on membrane fouling attachments & ultrafiltration performance in ultrafiltration of latex contaminated water and wastewater. 52**,** 118-129.

Al-Ghamdi, M. A., A. Alhadidi & N. J. W. r. Ghaffour (2019) Membrane backwash cleaning using CO2 nucleation. 165**,** 114985.

Antony, A., J. H. Low, S. Gray, A. E. Childress, P. Le-Clech & G. J. J. o. m. s. Leslie (2011) Scale formation and control in high pressure membrane water treatment systems: A review. 383**,** 1-16.

Arbués, F., M. Á. García-Valiñas & I. J. W. r. m. Villanúa (2010) Urban water demand for service and industrial use: The case of Zaragoza. 24**,** 4033-4048.

Armbruster, C. R. & M. R. J. P. o. t. N. A. o. S. Parsek (2018) New insight into the early stages of biofilm formation. 115**,** 4317-4319.

Ashfaq, M. Y., M. A. Al-Ghouti, D. A. Da'na, H. Qiblawey & N. J. S. o. T. T. E. Zouari (2020) Investigating the effect of temperature on calcium sulfate scaling of reverse osmosis membranes using FTIR, SEM-EDX and multivariate analysis. 703**,** 134726.

Aslam, M., A. Charfi, G. Lesage, M. Heran & J. J. C. E. J. Kim (2017) Membrane bioreactors for wastewater treatment: a review of mechanical cleaning by scouring agents to control membrane fouling. 307**,** 897-913.

Baghbanzadeh, M., D. Rana, C. Q. Lan & T. J. A. E. Matsuura (2017) Zero thermal input membrane distillation, a zero-waste and sustainable solution for freshwater shortage. 187**,** 910-928.

Bagheri, M. & S. A. J. B. T. Mirbagheri (2018) Critical review of fouling mitigation strategies in membrane bioreactors treating water and wastewater. 258**,** 318-334.

Bai, J., Q. Zhao, Q. Lu, J. Wang & K. R. J. J. o. H. Reddy (2015) Effects of freshwater input on trace element pollution in salt marsh soils of a typical coastal estuary, China. 520**,** 186-192.

Banti, D., M. Mitrakas, G. Fytianos, A. Tsali & P. J. M. Samaras (2020) Combined Effect of Colloids and SMP on Membrane Fouling in MBRs. 10**,** 118.

Banti, D. C., P. Samaras, C. Tsioptsias, A. Zouboulis, M. J. S. Mitrakas & P. Technology (2018) Mechanism of SMP aggregation within the pores of hydrophilic and hydrophobic MBR membranes and aggregates detachment. 202**,** 119-129.

Besha, A. T., A. Y. Gebreyohannes, R. A. Tufa, D. N. Bekele, E. Curcio & L. J. J. o. e. c. e. Giorno (2017) Removal of emerging micropollutants by activated sludge process and membrane bioreactors and the effects of micropollutants on membrane fouling: A review. 5**,** 2395-2414.

BinAhmed, S., A. Hasane, Z. Wang, A. Mansurov, S. J. E. s. Romero-Vargas Castrillón & technology (2018) Bacterial adhesion to ultrafiltration membranes: role of hydrophilicity, natural organic matter, and cell-surface macromolecules. 52**,** 162-172.

Bjarnsholt, T. J. A. (2013) The role of bacterial biofilms in chronic infections. 121**,** 1-58.

Borea, L., V. Naddeo, M. S. Shalaby, T. Zarra, V. Belgiorno, H. Abdalla & A. M. J. U. Shaban (2018) Wastewater treatment by membrane ultrafiltration enhanced with ultrasound: Effect of membrane flux and ultrasonic frequency. 83**,** 42-47.

Bucs, S. S., N. Farhat, J. C. Kruithof, C. Picioreanu, M. C. van Loosdrecht & J. S. J. D. Vrouwenvelder (2018) Review on strategies for biofouling mitigation in spiral wound membrane systems. 434**,** 189-197.

Cao, T., S. Wang & B. J. E. P. Chen (2019) Water shortage risk transferred through interprovincial trade in Northeast China. 158**,** 3865-3871.

Chen, Y., J. Teng, L. Shen, G. Yu, R. Li, Y. Xu, F. Wang, B.-Q. Liao & H. J. B. t. Lin (2019) Novel insights into membrane fouling caused by gel layer in a membrane bioreactor: Effects of hydrogen bonding. 276**,** 219-225.

Chon, K., N. Jeong, H. Rho, J.-Y. Nam, E. Jwa & J. J. D. Cho (2020) Fouling characteristics of dissolved organic matter in fresh water and seawater compartments of reverse electrodialysis under natural water conditions. 496**,** 114478.

Christensen, M. L., W. Niessen, N. B. Sørensen, S. H. Hansen, M. K. Jørgensen, P. H. J. S. Nielsen & P. Technology (2018) Sludge fractionation as a method to study and predict fouling in MBR systems. 194**,** 329-337.

Cinar, O., A. Kizilet, O. Isik, A. Ćemanović & M. Akif. 2016. A review on dynamic membrane bioreactors: comparison of membrane bioreactors and different support materials, transmembrane pressure. In *Proceedings of International Conference on Engineering and Natural Sciences*, 2505-2513.

Dharminder, R. K. S., V. Kumar, A. K. Devedee, M. Mruthyunjaya & R. J. I. Bhardwaj (2019) The clean water: The basic need of human and agriculture. 7**,** 1994-1998.

Di Marcantonio, C., C. Bertelkamp, N. van Bel, T. E. Pronk, P. H. Timmers, P. van der Wielen & A. M. J. C. Brunner (2020) Organic micropollutant removal in full-scale rapid sand filters used for drinking water treatment in The Netherlands and Belgium. 260**,** 127630.

Flimban, S. G., S. H. Hassan, M. M. Rahman & S.-E. J. i. j. o. h. e. Oh (2020) The effect of Nafion membrane fouling on the power generation of a microbial fuel cell. 45**,** 13643-13651.

Fortunato, L., S. Jeong, Y. Wang, A. R. Behzad & T. J. B. t. Leiknes (2016) Integrated approach to characterize fouling on a flat sheet membrane gravity

driven submerged membrane bioreactor. 222**,** 335-343.

Freire-Gormaly, M. & A. J. J. o. M. S. Bilton (2019) Impact of intermittent operation on reverse osmosis membrane fouling for brackish groundwater desalination systems. 583**,** 220-230.

German, M. S., H. Dong, A. Schevets, R. C. Smith & A. K. J. D. SenGupta (2019) Field validation of self-regenerating reversible ion exchange-membrane (RIX-M) process to prevent sulfate and silica fouling. 469**,** 114093.

Giacobbo, A., A. Moura Bernardes, M. J. Filipe Rosa & M. N. J. M. De Pinho (2018) Concentration polarization in ultrafiltration/nanofiltration for the recovery of polyphenols from winery wastewaters. 8**,** 46.

Goh, P., W. Lau, M. Othman & A. J. D. Ismail (2018) Membrane fouling in desalination and its mitigation strategies. 425**,** 130-155.

Goswami, L., R. V. Kumar, S. N. Borah, N. A. Manikandan, K. Pakshirajan & G. J. J. o. w. p. e. Pugazhenthi (2018) Membrane bioreactor and integrated membrane bioreactor systems for micropollutant removal from wastewater: a review. 26**,** 314-328.

Guo, W., H.-H. Ngo & J. J. B. t. Li (2012) A mini-review on membrane fouling. 122**,** 27-34.

Hasan, S. W., M. Elektorowicz & J. A. J. B. t. Oleszkiewicz (2012) Correlations between trans-membrane pressure (TMP) and sludge properties in submerged membrane electro-bioreactor (SMEBR) and conventional membrane bioreactor (MBR). 120**,** 199-205.

Hastuti, E., I. Medawaty & R. J. J. o. A. S. i. E. S. Pamekas (2011) APPLICATION OF DOMESTIC WASTEWATER TREATMENT USING FIXED BED BIOFILM AND MEMBRAN BIOREACTOR FOR WATER REUSE IN URBAN HOUSING AREA. 6.

He, Z., D. J. Miller, S. Kasemset, D. R. Paul & B. D. J. J. o. m. s. Freeman (2017) The effect of permeate flux on membrane fouling during microfiltration of oily water. 525**,** 25-34.

Hejase, C. A. & V. V. J. J. o. M. S. Tarabara (2021) Nanofiltration of saline oil-water emulsions: Combined and individual effects of salt concentration polarization and fouling by oil. 617**,** 118607.

Her, N., G. Amy, J. Chung, J. Yoon & Y. J. C. Yoon (2008) Characterizing dissolved organic matter and evaluating associated nanofiltration membrane fouling. 70**,** 495-502.

Higgin, R., K. J. Howe & T. M. J. D. Mayer (2010) Synergistic behavior between silica and alginate: Novel approach for removing silica scale from RO membranes. 250**,** 76-81.

Huang, S., X. Shi, X. Bi, L. Y. Lee & H. Y. J. B. T. Ng (2019) Effect of ferric hydroxide on membrane fouling in membrane bioreactor treating pharmaceutical wastewater. 292**,** 121852.

Huang, Z., S. L. Ong & H. Y. J. W. r. Ng (2011) Submerged anaerobic membrane bioreactor for low-strength wastewater treatment: effect of HRT and SRT on treatment performance and membrane fouling. 45**,** 705-713.

Iorhemen, O. T., R. A. Hamza & J. H. J. B. t. Tay (2017) Membrane fouling control in membrane bioreactors (MBRs) using granular materials. 240**,** 9-24.

Iorhemen, O. T., R. A. Hamza & J. H. J. M. Tay (2016) Membrane bioreactor (MBR) technology for wastewater treatment and reclamation: membrane fouling. 6**,** 33.

Jegatheesan, V., B. K. Pramanik, J. Chen, D. Navaratna, C.-Y. Chang & L. J. B. t. Shu (2016) Treatment of textile wastewater with membrane bioreactor: a critical review. 204**,** 202-212.

Jiang, S., Y. Li & B. P. J. S. o. t. T. E. Ladewig (2017) A review of reverse osmosis membrane fouling and control strategies. 595**,** 567-583.

Jiang, S., Y. Zhang, F. Zhao, Z. Yu, X. Zhou & H. J. A. r. Chu (2018) Impact of transmembrane pressure (TMP) on membrane fouling in microalgae harvesting with a uniform shearing vibration membrane system. 35**,** 613-623.

Johnson, L. R. J. J. o. t. b. (2008) Microcolony and biofilm formation as a survival strategy for bacteria. 251**,** 24-34.

Kahil, T., J. Albiac, G. Fischer, M. Strokal, S. Tramberend, P. Greve, T. Tang, P. Burek, R. Burtscher & Y. J. C. O. i. E. S. Wada (2019) A nexus modeling framework for assessing water scarcity solutions. 40**,** 72-80.

Kampouris, I. D., P. D. Karayannakidis, D. C. Banti, D. Sakoula, D. Konstantinidis, M. Yiangou & P. E. J. W. r. Samaras (2018) Evaluation of a novel quorum quenching strain for MBR biofouling mitigation. 143**,** 56-65.

Kappel, C., A. J. Kemperman, H. Temmink, A. Zwijnenburg, H. Rijnaarts & K. J. J. o. m. s. Nijmeijer (2014) Impacts of NF concentrate recirculation on membrane performance in an integrated MBR and NF membrane process for wastewater treatment. 453**,** 359-368.

Kaya, Y., A. M. Bacaksiz, H. Bayrak, I. Vergili, Z. B. Gönder, H. Hasar & G. J. J. o. W. P. E. Yilmaz (2019) Investigation of membrane fouling in an anaerobic membrane bioreactor (AnMBR) treating pharmaceutical wastewater. 31**,** 100822.

Khatoon, Z., C. D. McTiernan, E. J. Suuronen, T.-F. Mah & E. I. J. H. Alarcon (2018) Bacterial biofilm formation on implantable devices and approaches to its treatment and prevention. 4**,** e01067.

Kim, S.-K. & J.-H. J. J. o. m. Lee (2016) Biofilm dispersion in Pseudomonas aeruginosa. 54**,** 71-85.

Kimura, K., K. Tanaka & Y. J. W. R. Watanabe (2014) Microfiltration of different surface waters with/without coagulation: Clear correlations between membrane fouling and hydrophilic biopolymers. 49**,** 434-443.

Kimura, K., N. Yamato, H. Yamamura, Y. J. E. s. Watanabe & technology (2005)

Membrane fouling in pilot-scale membrane bioreactors (MBRs) treating municipal wastewater. 39**,** 6293-6299.

Kochkodan, V. & N. J. D. Hilal (2015) A comprehensive review on surface modified polymer membranes for biofouling mitigation. 356**,** 187-207.

Kusworo, T. D., W. Widayat, D. P. Utomo, Y. H. S. Pratama & R. A. V. J. R. E. Arianti (2020) Performance evaluation of modified nanohybrid membrane polyethersulfone-nano ZnO (PES-nano ZnO) using three combination effect of PVP, irradiation of ultraviolet and thermal for biodiesel purification. 148**,** 935-945.

Lee, H.-J., M. A. Halali, T. Baker, S. Sarathy, C.-F. J. S. de Lannoy & P. Technology (2020) A comparative study of RO membrane scale inhibitors in wastewater reclamation: Antiscalants versus pH adjustment. 240**,** 116549.

Lee, S. & C.-H. J. W. R. Lee (2000) Effect of operating conditions on CaSO4 scale formation mechanism in nanofiltration for water softening. 34**,** 3854-3866.

Lee, W.-N., W.-S. Cheong, K.-M. Yeon, B.-K. Hwang & C.-H. J. J. o. M. S. Lee (2009) Correlation between local TMP distribution and bio-cake porosity on the membrane in a submerged MBR. 332**,** 50-55.

Lee, W., S. Kang & H. J. J. o. m. s. Shin (2003) Sludge characteristics and their contribution to microfiltration in submerged membrane bioreactors. 216**,** 217-227.

Li, M., Q. Wen, Z. Chen, Y. Tang & B. J. C. Yang (2020) Comparison of ozonation and UV based oxidation as pre-treatment process for ultrafiltration in wastewater reuse: Simultaneous water risks reduction and membrane fouling mitigation. 244**,** 125449.

Li, W., X. Su, A. Palazzolo & S. J. J. o. m. s. Ahmed (2019) Numerical modeling of concentration polarization and inorganic fouling growth in the pressure-driven membrane filtration process. 569**,** 71-82.

Lim, S., D. S. Han, N. Pathak, N. Akther, S. Phuntsho, H. Park & H. K. J. B. t. Shon (2019) Efficient fouling control using outer-selective hollow fiber thin-film composite membranes for osmotic membrane bioreactor applications. 282**,** 9-17.

Lin, H., G. Yu, L. Shen, R. Li, Y. J. C. D. i. B. Xu & Bioengineering (2020) Advanced membrane bioreactor fouling control and prevention strategies. 209-224.

Lin, H., M. Zhang, F. Wang, F. Meng, B.-Q. Liao, H. Hong, J. Chen & W. J. J. o. M. s. Gao (2014) A critical review of extracellular polymeric substances (EPSs) in membrane bioreactors: characteristics, roles in membrane fouling and control strategies. 460**,** 110-125.

Liu, C., P. Li, X. Tang, G. V. J. E. S. Korshin & P. Research (2016) Ozonation effects on emerging micropollutants and effluent organic matter in wastewater: characterization using changes of three-dimensional HP-SEC

and EEM fluorescence data. 23**,** 20567-20579.

Liu, Q., G.-R. Xu & R. J. D. Das (2019) Inorganic scaling in reverse osmosis (RO) desalination: Mechanisms, monitoring, and inhibition strategies. 468**,** 114065.

Liu, Y. & B. J. J. o. M. S. Mi (2014) Effects of organic macromolecular conditioning on gypsum scaling of forward osmosis membranes. 450**,** 153-161.

Luo, J., Z. Zhu, L. Ding, O. Bals, Y. Wan, M. Y. Jaffrin & E. J. J. o. M. S. Vorobiev (2013) Flux behavior in clarification of chicory juice by high-shear membrane filtration: evidence for threshold flux. 435**,** 120-129.

Mahendran, B., H. Lin, B. Liao & S. N. J. J. o. E. E. Liss (2011) Surface properties of biofouled membranes from a submerged anaerobic membrane bioreactor after cleaning. 137**,** 504-513.

Maliszewska, I. & T. J. E. Czapka (2020) Biofouling removal from membranes using nonthermal plasma. 13**,** 4318.

Matin, A., Z. Khan, S. Zaidi & M. J. D. Boyce (2011) Biofouling in reverse osmosis membranes for seawater desalination: phenomena and prevention. 281**,** 1-16.

Medeiros, A. S., P. Wood, S. D. Wesche, M. Bakaic & J. F. J. R. E. C. Peters (2017) Water security for northern peoples: review of threats to Arctic freshwater systems in Nunavut, Canada. 17**,** 635-647.

Melo, L. F. & H.-C. Flemming (2010) 18 Mechanistic Aspects of Heat Exchanger and Membrane Biofouling and Prevention.

Meng, F., S.-R. Chae, A. Drews, M. Kraume, H.-S. Shin & F. J. W. r. Yang (2009) Recent advances in membrane bioreactors (MBRs): membrane fouling and membrane material. 43**,** 1489-1512.

Meng, F., H. Zhang, F. Yang, L. J. E. s. Liu & technology (2007) Characterization of cake layer in submerged membrane bioreactor. 41**,** 4065-4070.

Meng, F., S. Zhang, Y. Oh, Z. Zhou, H.-S. Shin & S.-R. J. W. r. Chae (2017) Fouling in membrane bioreactors: an updated review. 114**,** 151-180.

Mi, B. & M. J. J. o. m. s. Elimelech (2010) Organic fouling of forward osmosis membranes: Fouling reversibility and cleaning without chemical reagents. 348**,** 337-345.

Miyamoto, K., D. Ikeshima, T. Furutani, H. Xiao, A. Yonezu, X. J. S. T. M. Chen & Properties (2019) On the surface hydrophilization of a blended polysulfone membrane: atomic force microscopy measurement and molecular dynamics simulation. 7**,** 035003.

Mohajeri, P., C. M. Smith, H. W. Chau & N. J. J. o. W. P. E. Lehto (2020) Powdered ALLODUST/ALLOCHAR Augmented Single Batch Aerobic Reactor (SiBAR) for High Concentration Phosphorous Removal from Agricultural Wastewater. 36**,** 101301.

Motsa, M. M., B. B. Mamba & A. R. J. J. o. W. P. E. Verliefde (2018) Forward osmosis membrane performance during simulated wastewater reclamation: Fouling mechanisms and fouling layer properties. 23**,** 109-118.

Ng, T., M. He, B. Xu, C. Wang & H. Ng. 2020. Fundamentals of aerobic membrane bioreactors. In *Current Developments in Biotechnology and Bioengineering*, 25-44. Elsevier.

Nguyen, T.-T., S. Kook, C. Lee, R. W. Field & I. S. J. J. o. m. s. Kim (2019) Critical flux-based membrane fouling control of forward osmosis: Behavior, sustainability, and reversibility. 570**,** 380-393.

Nguyen, T.-T., C. Lee, R. W. Field & I. S. J. J. o. M. S. Kim (2020) Insight into organic fouling behavior in polyamide thin-film composite forward osmosis membrane: Critical flux and its impact on the economics of water reclamation. 606**,** 118118.

Noori, M. T., M. Ghangrekar, C. Mukherjee & B. J. B. a. Min (2019) Biofouling effects on the performance of microbial fuel cells and recent advances in biotechnological and chemical strategies for mitigation. 37**,** 107420.

Pääkkönen, T. M., M. Riihimäki, E. Puhakka, E. Muurinen, C. J. Simonson & R. L. Keiski. 2009. Crystallization fouling of CaCO3-effect of bulk precipitation on mass deposition on the heat transfer surface. In *Proceedings of International Conference on Heat Exchanger Fouling and Cleaning VII, Austria*, 209-216.

Pan, J. R., Y.-C. Su, C. Huang & H.-C. J. J. o. m. S. Lee (2010) Effect of sludge characteristics on membrane fouling in membrane bioreactors. 349**,** 287-294.

Quay, A. N., T. Tong, S. M. Hashmi, Y. Zhou, S. Zhao, M. J. E. s. Elimelech & technology (2018) Combined organic fouling and inorganic scaling in reverse osmosis: role of protein–silica interactions. 52**,** 9145-9153.

Ramsey, M. M. & M. J. M. m. Whiteley (2004) Pseudomonas aeruginosa attachment and biofilm development in dynamic environments. 53**,** 1075-1087.

Rios, S. D., E. Clavero, J. Salvadó, X. Farriol, C. J. I. Torras & e. c. research (2011) Dynamic microfiltration in microalgae harvesting for biodiesel production. 50**,** 2455-2460.

Rochex, A. & J.-M. J. W. r. Lebeault (2007) Effects of nutrients on biofilm formation and detachment of a Pseudomonas putida strain isolated from a paper machine. 41**,** 2885-2892.

Rodrıguez, J., L. Castrillon, E. Maranon, H. Sastre & E. J. W. R. Fernandez (2004) Removal of non-biodegradable organic matter from landfill leachates by adsorption. 38**,** 3297-3303.

Ronen, A., W. Duan, I. Wheeldon, S. Walker, D. J. E. s. Jassby & technology (2015) Microbial attachment inhibition through low-voltage electrochemical reactions on electrically conducting membranes. 49**,** 12741-12750.

Rosenberger, S., C. Laabs, B. Lesjean, R. Gnirss, G. Amy, M. Jekel & J.-C. J. W. r. Schrotter (2006) Impact of colloidal and soluble organic material on membrane performance in membrane bioreactors for municipal wastewater treatment. 40**,** 710-720.

Rouquié, C., S. Liu, M. Rabiller-Baudry, A. Riaublanc, M. Frappart, E. Couallier & A. J. J. o. M. S. Szymczyk (2020) Electrokinetic leakage as a tool to probe internal fouling in MF and UF membranes. 599**,** 117707.

Schiffer, S., M. Hartinger, A. Matyssek, U. J. S. Kulozik & P. Technology (2020) On the reversibility of deposit formation in low temperature milk microfiltration with ceramic membranes depending on mode of adjustment of transmembrane pressure and wall shear stress. 247**,** 116962.

She, Q., R. Wang, A. G. Fane & C. Y. J. J. o. M. S. Tang (2016) Membrane fouling in osmotically driven membrane processes: A review. 499**,** 201-233.

Shen, M., B. Song, Y. Zhu, G. Zeng, Y. Zhang, Y. Yang, X. Wen, M. Chen & H. J. C. Yi (2020) Removal of microplastics via drinking water treatment: Current knowledge and future directions. 251**,** 126612.

Shi, Y., J. Huang, G. Zeng, Y. Gu, Y. Hu, B. Tang, J. Zhou, Y. Yang, L. J. R. i. E. S. Shi & Bio/Technology (2018) Evaluation of soluble microbial products (SMP) on membrane fouling in membrane bioreactors (MBRs) at the fractional and overall level: a review. 17**,** 71-85.

Shirazi, S., C.-J. Lin & D. J. D. Chen (2010) Inorganic fouling of pressure-driven membrane processes—A critical review. 250**,** 236-248.

Sillanpää, M., M. C. Ncibi, A. Matilainen & M. J. C. Vepsäläinen (2018) Removal of natural organic matter in drinking water treatment by coagulation: A comprehensive review. 190**,** 54-71.

Silva, A. F., S. Antunes, A. Saunders, F. Freitas, A. Vieira, C. F. Galinha, P. H. Nielsen, M. T. B. Crespo, G. J. A. m. Carvalho & biotechnology (2016) Impact of sludge retention time on the fine composition of the microbial community and extracellular polymeric substances in a membrane bioreactor. 100**,** 8507-8521.

Skinner, S. J., A. D. Stickland, P. J. J. C. E. Scales & Technology (2018) Predicting transmembrane pressure rise from biofouling layer compressibility and permeability. 41**,** 51-60.

Suwarno, S. R., S. Hanada, T. H. Chong, S. Goto, M. Henmi & A. J. D. Fane (2016) The effect of different surface conditioning layers on bacterial adhesion on reverse osmosis membranes. 387**,** 1-13.

Tang, C. Y., Q. She, W. C. Lay, R. Wang & A. G. J. J. o. m. s. Fane (2010) Coupled effects of internal concentration polarization and fouling on flux behavior of forward osmosis membranes during humic acid filtration. 354**,** 123-133.

Teng, J., L. Shen, Y. Xu, Y. Chen, X.-L. Wu, Y. He, J. Chen & H. J. C. Lin (2020) Effects of molecular weight distribution of soluble microbial products

(SMPs) on membrane fouling in a membrane bioreactor (MBR): Novel mechanistic insights. 248**,** 126013.

Touati, K., H. S. Usman, T. Chen, N. Anwar, M. R. Choudhury & M. S. Rahaman. 2020. Inorganic Scaling in Desalination Systems. In *Corrosion and Fouling Control in Desalination Industry*, 251-268. Springer.

Toyofuku, M., T. Inaba, T. Kiyokawa, N. Obana, Y. Yawata, N. J. B. Nomura, biotechnology, & biochemistry (2016) Environmental factors that shape biofilm formation. 80**,** 7-12.

Wang, B., G. Huang, L. Liu, W. Li, Y. J. J. o. W. R. P. Xie & Management (2016) Integrated planning of urban water resources and water pollution control management: Case of Urumqi, China. 142**,** 05016001.

Wang, H., J. Xu, W. Tang, H. Li, S. Xia, J. Zhao, W. Zhang & Y. J. S. Yang (2019) Removal efficacy of opportunistic pathogens and bacterial community dynamics in two drinking water treatment trains. 15**,** 1804436.

Wang, J., D. de Ridder, A. van der Wal, N. B. J. C. R. i. E. S. Sutton & Technology (2021) Harnessing biodegradation potential of rapid sand filtration for organic micropollutant removal from drinking water: A review. 51**,** 2086-2118.

Wang, J., Y. Li, J. Huang, T. Yan & T. J. G. F. S. Sun (2017) Growing water scarcity, food security and government responses in China. 14**,** 9-17.

Wang, X.-M. & X.-Y. J. W. r. Li (2008) Accumulation of biopolymer clusters in a submerged membrane bioreactor and its effect on membrane fouling. 42**,** 855-862.

Wang, Y. 2005. *Composite fouling of calcium sulfate and calcium carbonate in a dynamic seawater reverse osmosis unit*. University of New South Wales Sydney, Australia.

Wang, Z., J. Ma, C. Y. Tang, K. Kimura, Q. Wang & X. J. J. o. m. s. Han (2014) Membrane cleaning in membrane bioreactors: a review. 468**,** 276-307.

Wang, Z., Z. Wu, X. Yin & L. J. J. o. M. S. Tian (2008) Membrane fouling in a submerged membrane bioreactor (MBR) under sub-critical flux operation: membrane foulant and gel layer characterization. 325**,** 238-244.

Weerasekara, N. A., K.-H. Choo & C.-H. J. W. r. Lee (2014) Hybridization of physical cleaning and quorum quenching to minimize membrane biofouling and energy consumption in a membrane bioreactor. 67**,** 1-10.

Wong, L. Y., C. A. Ng, M. J. Bashir, C. K. Cheah, K. L. Khoo, Y. C. J. D. Ching & W. Treatment (2016) Membrane bioreactor performance improvement by adding adsorbent and coagulant: a comparative study. 57**,** 13433-13439.

Xu, R., Z. Yu, S. Zhang & F. J. W. r. Meng (2019) Bacterial assembly in the bio-cake of membrane bioreactors: stochastic vs. deterministic processes. 157**,** 535-545.

Yachnin, E., G. Z. J. S. S. Ramon & Technology (2017) Direct observation of

macromolecular deposition on a nanofiltration membrane. 52**,** 258-265.

Yan, Z., F. Qu, H. Liang, H. Yu, H. Pang, H. Rong, G. Fan & B. J. J. o. M. S. Van der Bruggen (2021) Effect of biopolymers and humic substances on gypsum scaling and membrane wetting during membrane distillation. 617**,** 118638.

Yin, Z., T. Wen, Y. Li, A. Li & C. J. J. o. M. S. Long (2020a) Alleviating reverse osmosis membrane fouling caused by biopolymers using pre-ozonation. 595**,** 117546.

Yin, Z., T. Wen, Y. Li, A. Li & C. J. W. r. Long (2020b) Pre-ozonation for the mitigation of reverse osmosis (RO) membrane fouling by biopolymer: the roles of Ca2+ and Mg2+. 171**,** 115437.

Yu, W., D. Song, W. Chen & H. J. W. R. Yang (2020) Antiscalants in RO membrane scaling control. 183**,** 115985.

Zhang, J., H. C. Chua, J. Zhou & A. J. J. o. m. s. Fane (2006) Factors affecting the membrane performance in submerged membrane bioreactors. 284**,** 54-66.

Zhang, S., Z. Zhou, Y. Li & F. J. C. Meng (2018) Deciphering the core fouling-causing microbiota in a membrane bioreactor: low abundance but important roles. 195**,** 108-118.

Zhang, W., L. J. S. Ding & P. Technology (2015) Investigation of membrane fouling mechanisms using blocking models in the case of shear-enhanced ultrafiltration. 141**,** 160-169.

Zhang, X., M. Qi, L. Chen, T. Wu, W. Zhang, X. Wang, Y. J. E. Tong, Coastal & S. Science (2020) Recent change in nutrient discharge from municipal wastewater in China's coastal cities and implication for nutrient balance in the nearshore waters. 242**,** 106856.

Zhao, Y., R. Kitajima, N. Shirasaki, Y. Matsui & T. J. W. r. Matsushita (2020) Precoating membranes with submicron super-fine powdered activated carbon after coagulation prevents transmembrane pressure rise: Straining and high adsorption capacity effects. 177**,** 115757.

Zheng, Y., W. Zhang, B. Tang, J. Ding & Z. J. B. t. Zhang (2018) Membrane fouling mechanism of biofilm-membrane bioreactor (BF-MBR): Pore blocking model and membrane cleaning. 250**,** 398-405.

Zuthi, M. F. R., W. Guo, H. H. Ngo, D. L. Nghiem, F. I. Hai, S. Xia, J. Li, J. Li & Y. J. B. t. Liu (2017) New and practical mathematical model of membrane fouling in an aerobic submerged membrane bioreactor. 238**,** 86-94.

Chapter 5

THE EFFECTS OF AUTOMOTIVE-RELATED BIODIESEL AND DIESEL FUEL USAGE ON CO_2 EMISSIONS IN TURKEY: CURRENT STATUS AND FUTURE VISION

Muhammet BÜYÜKOĞLU[1], İlhan Volkan ÖNER[2]

1 Mak.Müh., Atatürk University, Graduate Scholl of Natural and Applied Sciences, Erzurum, TÜRKİYE, ORCID:0009-0007-5286-7545, muhammetbyk228@gmail.com

2 Dr.Öğr.Üyesi, Atatürk University, Faculty of Engineering, Department of Mechanical Engineering, Erzurum, TÜRKİYE, ivoner@atauni.edu.tr, ORCID: 0000-0003-3065-0189

1. Introduction

Energy is one of the essential elements of humanity and forms the basis of the economies of countries (Qiul et al., 2011). The increasing global population has resulted in a proportional increase in the demand for energy compared to previous years (Nematulla, 2020). Approximately 80% of the energy sources used in the world are derived from fossil fuels. Natural gas accounts for 10%, while oil accounts for 20% and the remaining percentage is made up of coal (Panwar et al., 2011). As the global population increases, it is predicted that the reserves of fossil fuels will decrease significantly over the next century due to the consumption of these resources to meet the growing energy demand (Stigka et al., 2014). Therefore, countries are increasingly turning towards alternative energy sources to meet their increasing energy demands. Among alternative energy sources, biomass energy is of great importance compared to other sources. Biomass energy includes animal and plant sources (Kralova & Sjöblom, 2010). Table 1 shows energy sources. Biodiesel is a subcategory of renewable energy, which is a type of biomass energy. Biodiesel is an alternative fuel type produced from animal and vegetable oils. The most significant feature that distinguishes biodiesel from other alternative fuel types is that its production is easier and less costly (Özdemir & Mutlubaş, 2016).

Table 1. *Energy Resources (K. Kaya & Koç, 2015)*

Renewable energy sources	Traditional Energy Sources
Solar energy	
Wind power	Fossil Fuels
Geothermal energy	Nuclear Energy Resources
Hydraulic Energy	
Biomass Energy(Biodiesel)	

The use of fossil fuels results in harmful emissions that cause environmental pollution and many negative effects. Studies have shown that if no alternative energy sources are adopted, the use of fossil fuels will decrease significantly by 2030 and environmental pollution will increase significantly (PWC, 2021). Therefore, renewable and environmentally friendly energy sources should be adopted worldwide, and support should be provided to facilitate their adoption (Akdoğan & Kovancılar, 2022). In Turkey, approximately 75% of the country's total energy is imported (Uysal et al., 2015).

In today's world, the best alternative fuel types compared to fossil fuels are biodiesel and ethanol. The fact that our country is an agricultural country shows that biodiesel production cannot be ignored. Biodiesel production from vegetable oils is more expensive than diesel fuel. However,

the fact that biodiesel can also be produced from waste vegetable oils reduces the cost to some extent. In our country, approximately 300000 tons of waste oil is generated every year, and if these oils are used for biodiesel production, it could provide our country with a gain of 480 million TL. With the use of biodiesel produced, the amount of CO_2 emissions released into the atmosphere compared to diesel fuel will be reduced by 900000 tons (Alptekin, 2005).

Biodiesel is an alternative renewable fuel type that can be produced from animal and vegetable oils through the transesterification method. Chemically, it consists of long-chain fatty acid mono alkyl esters. The word itself indicates that it is a biologically derived diesel fuel. The use of biodiesel was first demonstrated by Rudolph Diesel in 1898 at the World Exhibition held in Paris, where he operated a diesel engine with peanut oil (Bilgili et al., 2019).

2. Biodiesel as Fuel

Studies have been conducted to reduce the viscosity of animal and vegetable oils for the production of biodiesel, which can be used in a diesel engine without any modifications. The method of biodiesel production can be classified into two main categories: thermal method and chemical method, as shown in Table 2 (Scott et al., 2010). In the thermal method, preheating is performed to reduce the viscosity of the oils. However, due to some problems encountered when applying the thermal method in a moving diesel engine, the chemical method is more commonly preferred (Aksoy, 2010).

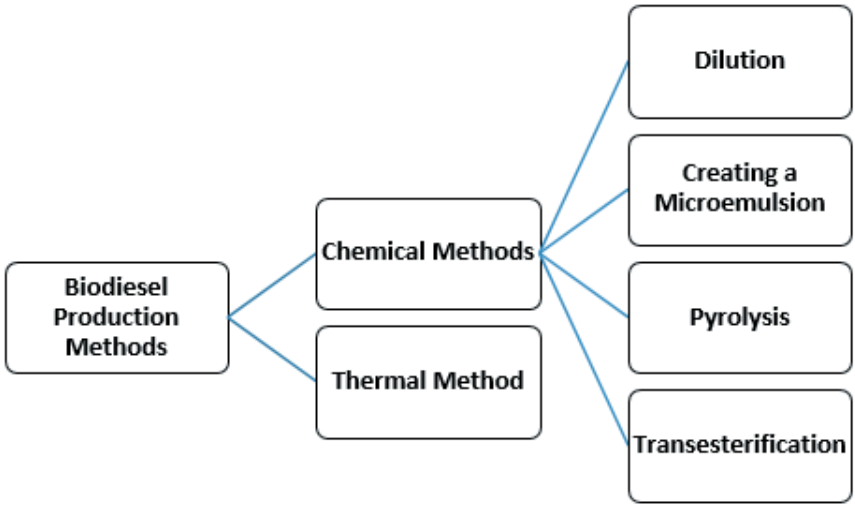

Figure 1. *Biodiesel Production Methods*

The most commonly used method among the biodiesel production methods shown in Figure 1 is the transesterification method. This method involves the formation of oil esters and glycerin as a result of the oil molecule reacting with alcohol and a catalyst (C. Kaya, 2006). For this reaction to occur, the molar ratio of alcohol to oil must be at least 3/1 (Cheng et al., 2014). Methanol (CH_3OH), ethanol (C_2H_5OH), isopropyl alcohol (C_3H_7OH), and butyl alcohol (C_4H_9OH) can be used as alcohols in the reaction (Özer, 2014). Basic catalysts such as potassium hydroxide (KOH) and sodium hydroxide (NaOH) are used to speed up the reaction in transesterification.

Table 2. *Comparison of Biodiesel and Diesel Fuel Properties*

Fuel Properties	Unit	Limits	Biodiesel	Diesel
Closed Formula			$C_{19}H_{35.2}O_2$	$C_{12.226}H_{23.29}S_{0.0575}$
Molecular Weight	g/mol		296	120-320
Specific Gravity	kg/L	0.875-0.90	0.87-0.88	0.82-0.86
Kinematic Viscosity	mm^2/s	2-4.5	4.3	2.5-3.5
Cetane number		49-…	>55	49-55
Flash point	°C	55-…	>100	>55
The amount of water	mg/kg	…-200	<300	<200

According to Table 2, it is understood that there are not significant differences between the properties of biodiesel and diesel fuel. Biodiesel's higher flash point compared to diesel fuel provides advantages in terms of being more reliable for transportation and storage. The aim of mixing biodiesel and diesel fuel is to improve the properties of diesel fuel. The biodiesel-diesel fuel blend is intended to reduce harmful emissions resulting from combustion compared to diesel fuel (Choedkiatsakul et al., 2015). The composition of the biodiesel-diesel fuel blends prepared is shown in Table 3.

Table 3. *Display of biodiesel-diesel fuel blends and blend percentages*

Nu.	Sample name	Biodiesel (%)	Diesel (%)
1	B100	100	0
2	B80	80	20
3	B60	60	40
4	B40	40	60
5	B20	20	80

2.1. Methods of Biodiesel Production

Chemical methods of biodiesel production are divided into four: dilution, microemulsion formation, pyrolysis, and transesterification.

2.1.1. Dilution Method

The dilution method involves mixing waste vegetable oils with diesel fuel or a solvent to reduce their viscosity and decrease the ratio of diesel fuel. Biodiesel fuel ratios in diesel fuel are 20%, 30%, 40%, 50%, and 80%. Sunflower and peanut oil are mostly used in the dilution method (Eryılmaz, 2014).

2.1.2. Microemulsion Formation Method

The microemulsion method is a colloidal solution created by the mixture of two immiscible liquids, either ionic or non-ionic. Similar fuels to alternative diesel fuel can be produced using this method. Aliphatic alcohols (MeOH) are used as the organic substance in this method (Acharya et al., 2015).

2.1.3. Pyrolysis Method

Pyrolysis is the process of converting high molecular structures into low-level molecular structures at extremely high temperatures. The pyrolysis method can be done in two ways. The first method involves heating vegetable oil in a closed container to break down the molecules. The second and most commonly used method involves the distillation process to break down waste oil and vegetable oil. Biodiesel produced by the second method is more similar to diesel fuel characteristics (Gedikaslan, 2020).

2.1.4. Transesterification Method

The transesterification method involves the reaction of vegetable oil with an alcohol and a basic catalyst to form glycerin and fatty acid esters, i.e., biodiesel. This is the most commonly used method among chemical production methods. The transesterification method's scheme is shown in Figure 2.

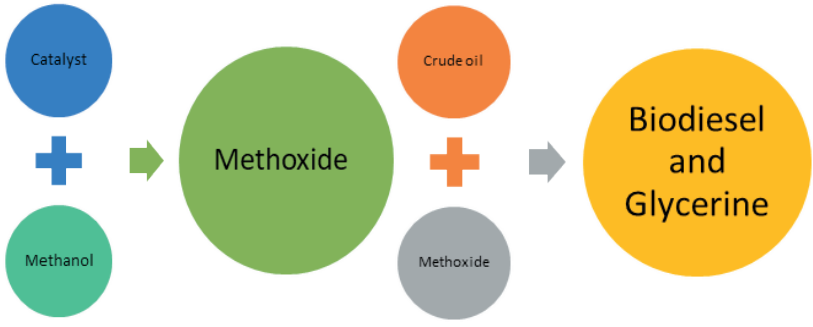

Figure 2. *Biodiesel Production by Transesterification Method*

The first step of the transesterification process involves mixing a catalyst and alcohol in a container. Afterwards, the raw oil is heated up

to 55°C and then put into a reactor where the catalyst-alcohol mixture is poured in and the mixing process is carried out. After the reaction time, biodiesel and glycerin are produced. Due to the difference in density, biodiesel stays on top while glycerin settles at the bottom and is drained out. Then, to remove any remaining glycerin in biodiesel, it is washed with warm water once or twice (Fukuda et al., 2001).

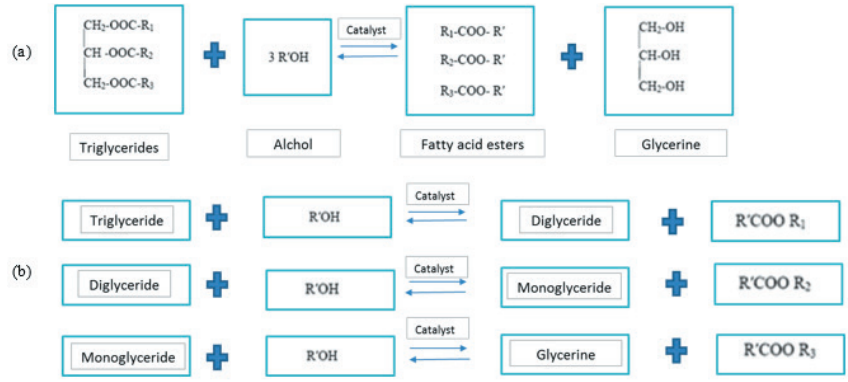

Figure 3. *Transesterification of Triglycerides with Alcohol (a) General Equation, (b) Reversible Step Reactions*

The reaction steps of the transesterification process are shown in Figure 3. Initially, triglycerides are converted into diglycerides, then diglycerides are converted into monoglycerides, and finally, monoglycerides are converted into glycerol (Fukuda et al., 2001).

2.2. Emissions from Biodiesel

Biodiesel is a renewable alternative to diesel that can be used directly in any diesel engine without the need for any modifications. Its properties are very similar to diesel fuel, allowing it to be blended with diesel fuel in predetermined ratios. The most commonly used blend is the B20 fuel blend, which contains 20% biodiesel. The use of biodiesel in compression ignition engines as a biofuel type enables the reduction of pollutant emissions, especially atmospheric CO_2 emissions. The change in emissions released into the atmosphere by using biodiesel as fuel is shown in Figure 4. As can be seen, the emissions released as a result of the combustion of biodiesel in a compression ignition engine, except for NO_x emissions, are lower.

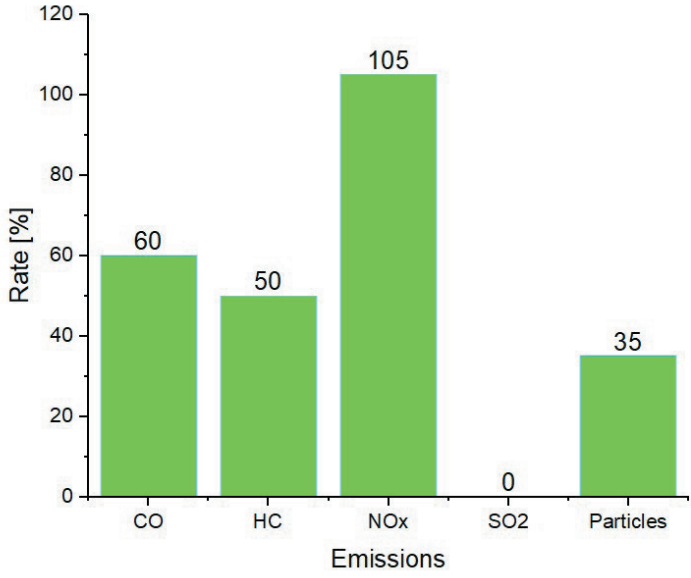

Figure 4. *Combustion emission levels of biodiesel*

In diesel engines, CO emissions when burning biodiesel are 40-50% lower than those of conventional diesel fuels. This is due to the presence of oxygen molecules in methyl or ethyl esters of biodiesel, which helps to achieve complete combustion. Additionally, for the same reasons, particulate matter emissions (PM) are reduced by 35% to 45% compared to diesel (Cormick, 2006). The amount of unburned hydrocarbons is also reduced due to the complete combustion reaction that occurs. The carbon-hydrogen and oxygen chains present in biodiesel esters also contribute to the formation of CO_2 and water, which differs from the amounts produced by diesel fuel (Szybist et al., 2007).

The use of biodiesel increases NO_x emissions by approximately 5%. Improved combustion reactions lead to higher temperatures in the combustion chamber when using biodiesel, which results in higher levels of NO_x formation. However, the low sulfur content of biodiesel fuel allows for the use of different NO_x control technologies than those used with traditional diesel fuel systems, preventing the release of NO_x emissions (A. Agarwal, 2007).

In compression-ignition engines, emissions resulting from burning biodiesel can be recycled through photosynthesis. When biodiesel is burned, CO_2 is released into the atmosphere and is later recycled by plants. As a result, biodiesel can help reduce global warming (Rodionova et al., 2017). Figure 5 shows the changes in carbon emissions caused by varying biodiesel blend ratios.

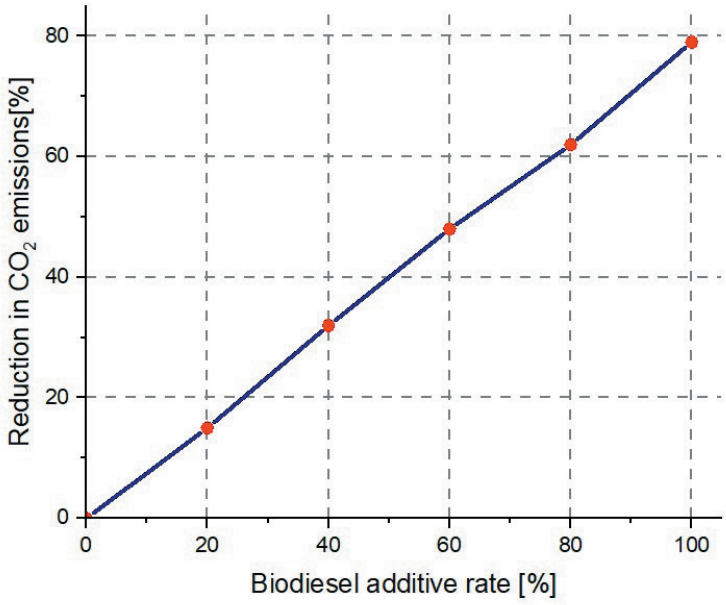

Figure 5. *Impact of biodiesel blend levels on CO_2 emissions (A. K. Agarwal, 2007).*

2.3. Toxicity in Internal Combustion Engines

In internal combustion engines, nitrogen oxide (NO) and carbon monoxide (CO) gases released as a result of burning fuel are toxic compounds. Incomplete combustion due to insufficient air causes an increase in carbon monoxide formation.

Oxygen, nitrogen, hydrogen, carbon dioxide, and water vapor released from the exhaust to the atmosphere are non-toxic emissions. Emissions that belong to the toxic substance group are hydrocarbons (C_xH_y), nitrogen oxides (NO_x), sulfur dioxide (SO_2), carbon monoxide (CO), solid particles, and aldehydes (A. K. Agarwal, 2007).

On average, a car emits between 0.6 and 1.7 kg/h of CO, while a truck emits between 1.5 and 2.8 kg/h of CO. Burning 1 kg of diesel fuel in a diesel engine generates approximately 80-100 grams of toxic compounds (Coronado et al., 2009).

3.Material and Method

In this study, total CO_2 emissions were calculated taking into account the number of vehicles and average mileage parameters in Turkey between 2015 and 2019. Comparisons were made based on the amount of reduction in CO_2 emissions resulting from the use of pure biodiesel (B100), B2, B5, and B20 blends, compared to the calculated CO_2 emission values when

using diesel fuel (D100), as reported in the literature. Finally, CO_2 emission predictions were made for future years in the automotive sector in Turkey, considering the use of B5, B20, and B100 blends.

3.1. CO_2 Emissions According to Fuels and Combustion Equations

The amount of CO_2 released into the atmosphere is one of the most important parameters in combustion processes, as it is one of the responsible gases for the formation of the greenhouse effect.

3.1.1. Diesel

The general formula of diesel fuel is $C_{12}H_{26}$. The density of the fuel is 0.864 t/m^3. The combustion of 528 g of diesel fuel results in the release of 170 g of CO_2. Therefore, 2683 tons of CO_2 is generated per m^3 of diesel fuel (Coronado et al., 2009).

$$1C_{12}H_{26} + 18.5O_2 + 69.56N_2 \rightarrow 12CO_2 + 13H_2O + 69.56N_2 \quad (1)$$

3.1.2. Biodiesel Production from Soybeans

The density of biodiesel produced from soybeans via transesterification with methanol is 0.878 t/m^3 (Coronado et al., 2009). The molecular weight of the methyl esters released from soybeans is 292.2 g/gmol. Upon stoichiometric combustion with air, 100 g of biodiesel releases 282.45 g of CO_2 emissions. Therefore, the combustion of 1 m^3 of soybean oil methyl esters results in the release of 2.48 tons of CO_2.

$$0.04437A + 0.01675B + 0.08432C + 0.1766D + 0.0205E + 9.037O_2 + 33.98N_2 \rightarrow 6.42CO_2 + 5.92H_2O + 33.98N_2 \quad (2)$$

A: $C_{15}H_{31}CO_2CH_3$

B: $C_{17}H_{35}CO_2CH_3$

C: $C_{17}H_{33}CO_2CH_3$

D: $CH_3(CH_2)_4CH{=}CHCH_2CH{=}CH(CH_2)7CO_2CH$

E: $CH_3(CH_2CH{=}CH)_3(CH_2)7\ CO_2CH_3$

3.1.3. Production of Biodiesel from Used Cooking Oils

The mass composition of biodiesel obtained from cooking oils is 77.4% C, 12% H, 11.2% O, and 0.03% S. Burning 100 grams of biodiesel results in 283.8 grams of CO_2 emissions (Coronado et al., 2009). As a result, 113.88 m^3 of biodiesel leads to the release of 283.8 tons of CO_2.

$$6{,}45C + 12H + 0{,}00094S + 9{,}45O_2 + 35{,}54N_2 \rightarrow 6{,}45CO_2 + 6H_2O + 0{,}00094SO2 + 35{,}54N_2 \quad (3)$$

3.2. Emission Amounts from Vehicles

In Turkey, 86.5% of CO_2 emissions are caused by the combustion of fuels. The remaining percentage comes from emissions from oil refineries and other applications.

Figure 6 shows the sources of CO_2 emissions from fuel combustion in Turkey. According to TÜİK data, CO_2 emissions from fuel combustion between 2010 and 2019 ranged from 270 million tons to 348 million tons. CO_2 emissions from transportation, i.e., vehicle exhaust gases, ranged from 44 million tons to 80 million tons. This change represents an 81.8% increase. Based on this rate, if there is no increase in biodiesel fuel consumption in the coming years, CO_2 emissions in Turkey will reach even higher levels.

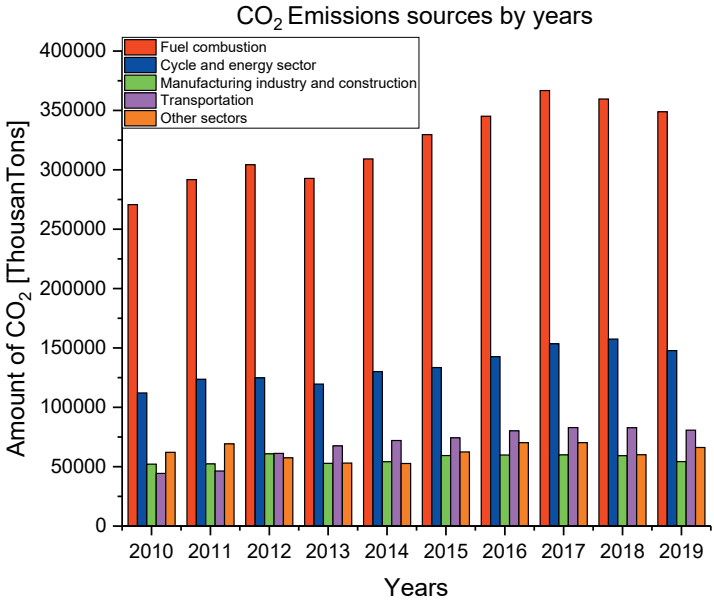

Figure 6. *Variation of CO_2 emission sources by years*

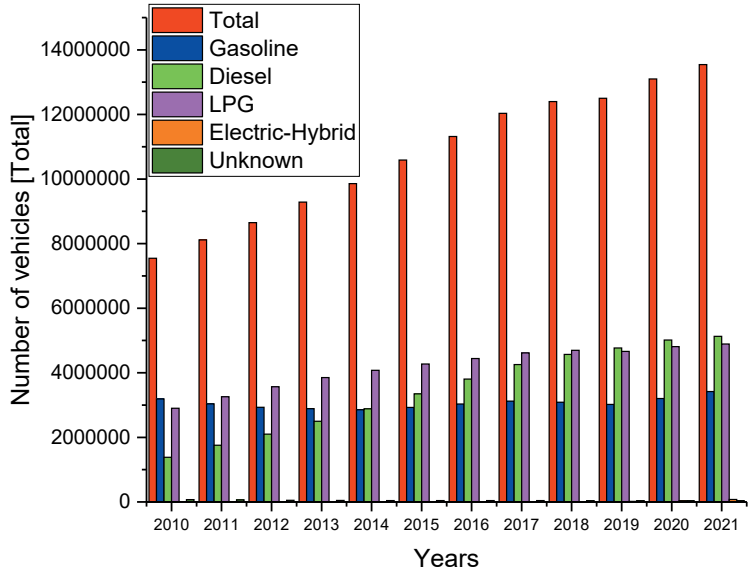

Figure 7. *Distribution of registered cars in Turkey by fuel type*

The biggest source of CO_2 emissions in Turkey is the burning of petroleum-based fuels. Therefore, the amount of CO_2 emissions from internal combustion engines in transportation is of great importance.

Figure 7 shows the distribution of registered vehicles in Turkey by fuel type. When Figure 7 is examined, it can be seen that the number of gasoline vehicles was 3191964 and 3417477 the number of diesel vehicles was between 1381631 and 5126831 and the number of LPG vehicles was between 2900034 and 4891707 from 2010 to 2021. When gasoline and diesel-fueled vehicles are compared between 2010 and 2021, the number of gasoline-fueled vehicles increased by 7.06%, while the number of diesel-fueled vehicles increased by 271.07%.

Table 4. *Total CO_2 Emission Values of Diesel Vehicles in Turkey (TÜİK, n.d.)*

		Years				
	Type of vehicle	**2015**	**2016**	**2017**	**2018**	**2019**
Number of vehicle	**Car**	3389573	3846623	4298729	4612847	4821325
	Truck	804319	825334	838718	845462	844481
	Van	3255299	3442483	3642625	3755580	3796919
Total kilometer (million km)	**Car**	55414	68240	77025	81604	87110
	Truck	33968	37745	42032	36178	37450
	Van	55192	61430	67969	63360	62884

Annual Average Kilometers (for 1 vehicle)	**Car**	16348	17740	17220	17691	16740
	Truck	42232	45735	50114	42791	44346
	Van	16954	17845	18659	16871	16562
Annual Total CO_2 Emission (tons)	**Car**	8921000	11000000	11900000	13130000	12900000
	Truck	15300000	17100000	19000000	16400000	16900000
	Van	21600000	24100000	26700000	24900000	24700000
	Total CO_2 Emissions	**45821000**	**52200000**	**57600000**	**54430000**	**54500000**

$$1C_{12}H_{26} + 18.5O_2 + 69.56N_2 \rightarrow 12CO_2 + 13H_2O + 69.56N_2 \qquad (4)$$

The CO_2 emission values for each diesel vehicle type have been calculated according to the combustion equation given above. The number of vehicles and annual average mileage numbers were taken from TÜİK data. For the diesel-powered automobile vehicle type, the annual average mileage for 2015 is 16348 km, as seen in Table 4. The average fuel consumption of a diesel-powered car is assumed to be 6 liters per 100 km. The density of diesel fuel is 0.864 ton/m^3. Using these values and the combustion equation above, approximately 51.84 g of fuel is consumed per kilometer. When 51.84 g of diesel fuel burns according to the combustion equation, 161.01 g of CO_2 emissions are produced. This result is the amount of emissions per kilometer emitted by one car. When multiplied by the average annual kilometers traveled, the annual CO_2 emission amount is 2.63 x 106 g/year. When the number of cars multiplies this result in 2015, an emission value of 8920000 tons of CO_2 is obtained. Similarly, for the years 2016-2019, the CO_2 emission values were calculated as 11000000, 11900000, 13130000 and 12900000 tons of CO_2, respectively, using the same calculations.

For the diesel-powered truck vehicle type, the annual average mileage for 2015 is 42232 km, as seen in Table 4. The average fuel consumption of a diesel-powered truck is assumed to be 17 liters per 100 km. The density of diesel fuel is 0.864 ton/m^3. Using these values and the combustion equation above, approximately 146.88 g of fuel is consumed per kilometer. When 146.88 g of diesel fuel burns according to the combustion equation, 453.45 g of CO_2 emissions are produced. This result is the amount of emissions per kilometer emitted by one truck. When multiplied by the average annual kilometers traveled, the annual CO_2 emission amount is 1.91 x 107 g/year. When this result is multiplied by the number of trucks in 2015, an emission value of 15 300 000 tons of CO_2 is obtained. Similarly, for the years 2016-2019, the CO_2 emission values were calculated as 17100000, 19000000, 16400000 and 16900000 tons of CO_2, respectively, using the same calculations. Similarly, for the diesel-powered van vehicle type, the annual average mileage for 2015 is 16954 km, as seen in Table 4. The average fuel consumption of a diesel-powered van is assumed to be 15

liters per 100 km. The density of diesel fuel is 0.864 ton/m^3. Using these values and the combustion equation above, approximately 129.6 g of fuel is consumed per kilometer. When 129.6 g of diesel fuel burns according to the combustion equation, 393.2 g of CO_2 emissions are produced. This result is the amount of emissions per kilometer emitted by one van. When multiplied by the average annual kilometers traveled, the annual CO_2 emission amount is 1.08 x 106 g/year. When this result is multiplied by the number of vans in 2015, an emission value of 2300000 tons of CO_2 is obtained. The CO_2 emission values have been calculated as 24100000, 26700000, 24900000 and 24700000 tons of CO_2.

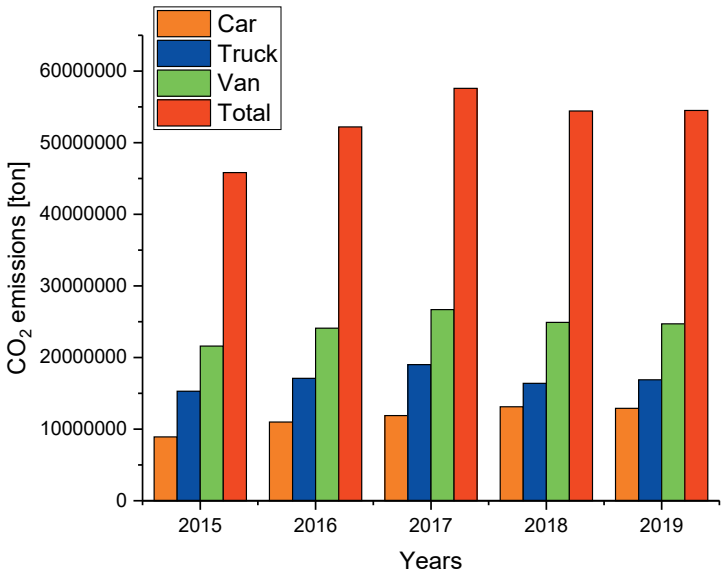

Figure 8. *Total CO_2 emission changes of diesel vehicles in Turkey between 2015-2019*

As seen in Figure 8 and according to the calculations, the increase in CO_2 emissions for car, truck, and van vehicle types between 2015-2019 is 44.61%, 10.45%, and 14.35%, respectively. Based on these results, it can be said that CO_2 emissions from vehicles will continue to increase in the future.

4. Results

4.1. Five-Year CO_2 Emissions from Diesel Vehicle Fleets in Turkey

The number and types of diesel vehicles in Turkey between 2015 and 2019 are listed in Table 4, taking into account the kilometers driven per year by Turkey's diesel fleets according to TÜİK data. (The average

number of kilometers driven per year for diesel vehicles, including vans and trucks in Turkey, was stated in previous sections.) When diesel fuel was used for average consumption throughout the given year (December 2015 - January 2019), CO_2 emissions reached 264 551 million tons of CO_2 over five years. Figures 9 and 10 show the changes in CO_2 emissions in tons for the data corresponding to the years 2015-2019 when 100% diesel fuel is used and when biodiesel blends are used. It can be seen that there is a significant decrease in CO_2 emissions as the percentage of biodiesel increases.

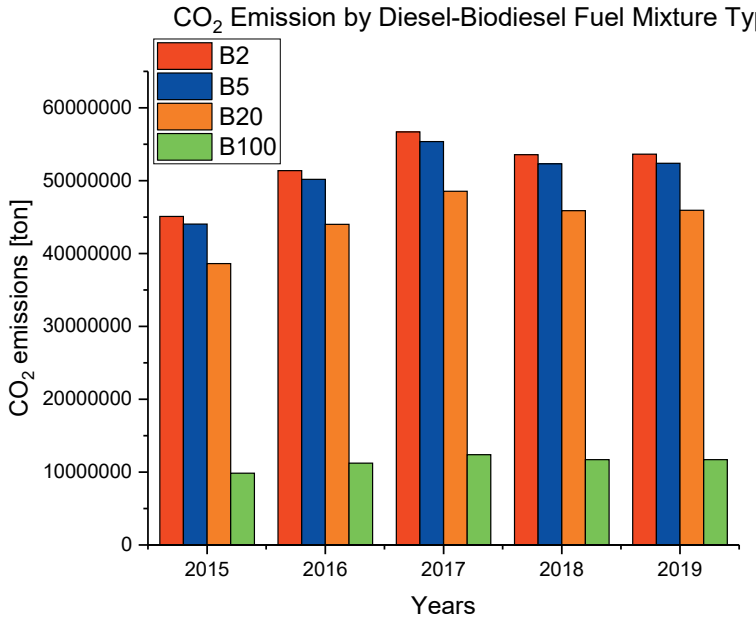

Figure 9. *Comparison of CO_2 emissions of diesel vehicles in Turkey between 2015-2019 when blends with biodiesel are used*

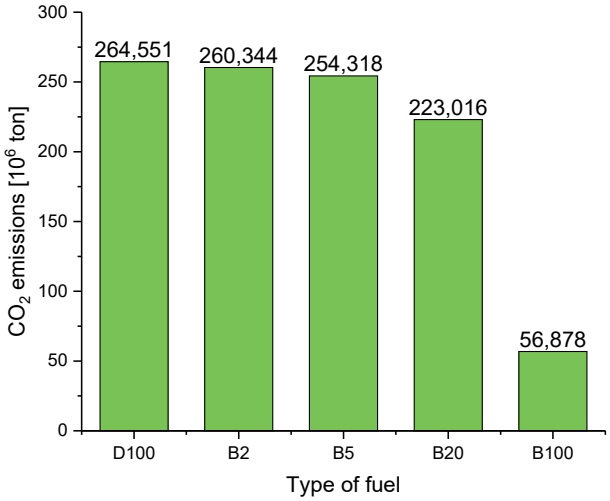

Figure 10. *Comparison of total CO_2 emissions of diesel vehicles in Turkey between 2015-2019 when mixtures with biodiesel are used*

The CO_2 emission value from diesel vehicles for the year 2019 has been calculated as 54.5 million tons of CO_2. If 2% (B2) biodiesel is used in diesel fuel, the emission amount will decrease to 53.63 million tons of CO_2, 5% (B5) biodiesel usage will decrease the emission amount to 52.39 million tons of CO_2, 20% (B20) biodiesel usage will decrease the emission amount to 45.94 million tons of CO_2, and using 100% (B100) biodiesel will decrease the emission amount to 11.71 million tons of CO_2.

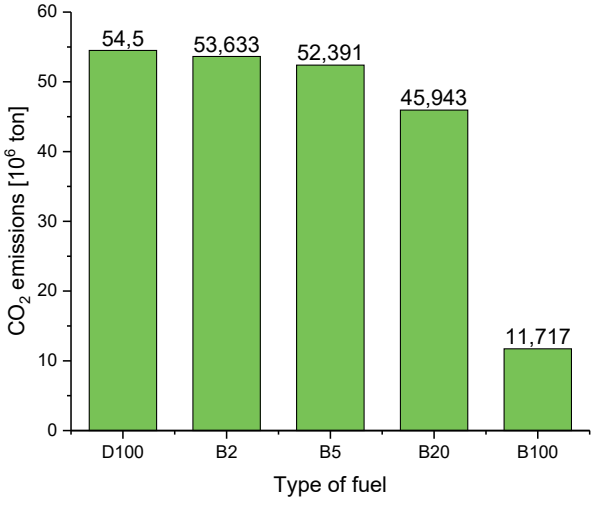

Figure 11. *CO_2 emission values of diesel vehicles in Turkey in 2019 when biodiesel and blends are used in their fuel*

As can be understood from Figure 10 and 11 and previous calculations, diesel fuel is the fuel that emits the highest amount of CO_2 into the atmosphere. Due to the oxygenated structure of biodiesel, it produces less unburned hydrocarbon and CO emissions as emissions. The advantage of using biodiesel is that the CO_2 emissions released can easily be synthesized by plants through photosynthesis. Therefore, when B100 biodiesel is used, emission levels decrease by approximately 78.49% compared to diesel fuel.

Between 2015 and 2019, the diesel vehicle fleet in Turkey increased by 213 534 vehicles, which led to CO_2 emissions reaching approximately 264.55 million tons during this period (December 2015 - January 2019). If B2 had been used in this diesel fleet between 2015-2019, CO_2 emissions would have decreased by 1.59%. CO_2 emissions would have decreased by 3.86% with B5 and by 15.70% with B20.

4.2. Projection of Total CO2 Emissions of Diesel Vehicles in Turkey in Future Years

Based on the CO_2 emission values calculated according to the number of vehicles between 2015 and 2019, the functions for the increase in the number of vehicles ($y = 7{,}70E\text{-}47e^{6{,}06E\text{-}02x}$) and total CO_2 emissions ($y = 54.949.000x - 110.677.320.000$) were determined, as shown in Figure 12. Using these functions, projections for the number of vehicles and CO_2 emission values in future years were calculated.

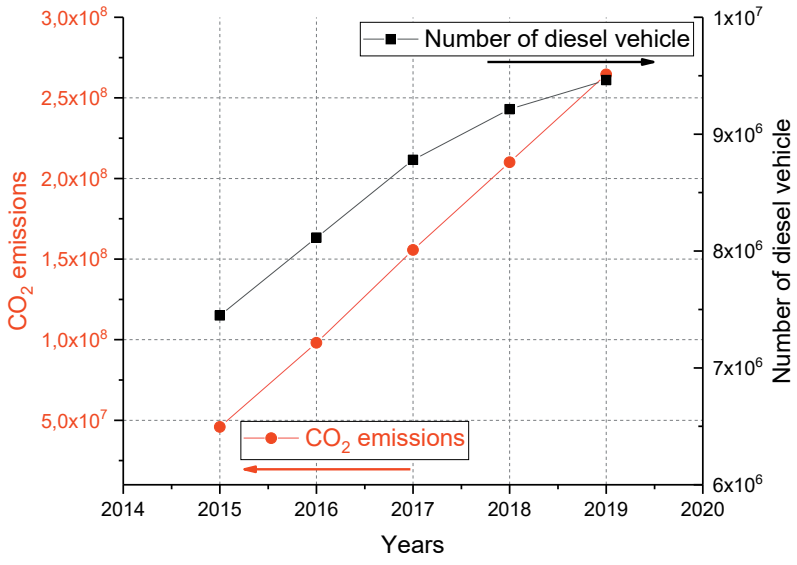

Figure 12. *The function and graph according to the number of vehicles and total CO_2 emission value between the years 2015-2019 in Turkey*

The increase in the Turkish diesel fleet from 2015 to 2019 was approximately 500000 vehicles per year. According to the calculated values, the expected CO_2 emissions from diesel vehicles in 2025 will be 594.4 million tons, in 2030 it will be 869.1 million tons, in 2035 it will be 1.143 billion tons, and in 2050 it will be 1.968 billion tons. Details regarding these projections are shown in Table 5.

Table 5. *Projection of Total CO_2 Emission Values of Diesel Vehicles in Turkey in the Future*

	2020	2025	2030	2035	2040	2045	2050
Number of Diesel Vehicles	10279843	13915085	18835850	25496737	34513101	46717905	63238671
Total CO_2 Emissions (ton)	319660000	594405000	869150000	1143895000	1418640000	1693385000	1968130000

Table 6. *Projection of Total CO_2 Emission Values of Diesel Vehicles in Turkey in Future Years in the Case of Using Biodiesel Mixture*

Years	ton CO_2 (10^6)-Diesel	ton CO_2 (10^6)-B5	ton CO_2 (10^6)-B20	ton CO_2 (10^6)-B100
2020	319.66	307.32	269.47	68.69
2025	594.4	571.45	501.07	127.73
2030	869.15	835.6	732.69	186.78
2035	1143.89	1099.00	964.29	245.82
2040	1418.64	1363.88	1195.91	304.86
2045	1693.38	1628.01	1427.51	363.9
2050	1968.13	1892.16	1659.13	422.95

When Table 6 is examined, it is seen that the estimated CO_2 emissions for 2025, 2035, and 2045 with B5 biodiesel use are 571.45 – 1099.00 and 1628.01 million tons, respectively. In the case of B20 biodiesel use, the estimated CO_2 emissions are 501.07 - 964.29 and 1427.51 million tons, respectively. The reduction estimates for B100 are 127.73 - 245.82 and 363.9 million tons, respectively. Figure 13 shows the possible change in CO_2 emission values between 2020-2050.

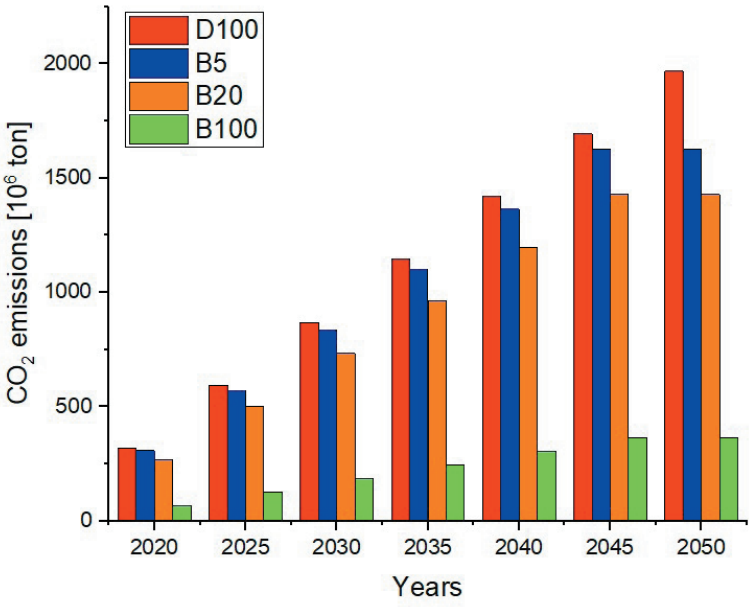

Figure 13. *The projection of the total CO_2 emission values of diesel vehicles in Turkey in the following years if biodiesel mixture is used*

REFERENCES

Acharya, B., Guru, P., & Dash, D. (2015). Tween-80–n-butanol/isobutanol–(Diesel+Kerosene)–Water microemulsions – Phase behavior and fuel applications. *Fuel*, *171*. https://doi.org/10.1016/j.fuel.2015.12.013

Agarwal, A. (2007). *İçten yanmalı motorlar için yakıt olarak biyoyakıtlar (alkoller ve biyodizel) uygulamaları* (pp. 233–271). Progress in Energy and Combustion Science.

Agarwal, A. K. (2007). Biofuels (alcohols and biodiesel) applications as fuels for internal combustion engines. *Progress in Energy and Combustion Science*, *33*(3), 233–271. https://doi.org/10.1016/j.pecs.2006.08.003

Akdoğan, İ., & Kovancılar, B. (2022). Avrupa Birliği ve Türkiye'de Çevre Dostu Yenilenebilir Enerji Politikalarının Teşvik Türleri Açısından Değerlendirilmesi. *Yönetim ve Ekonomi Dergisi*, *29*(1), 69–91. https://doi.org/10.18657/yonveek.1004872

Aksoy, L. (2010). *Alternatif Enerji Kaynağı Olarak Biyodizel ve Üretim Prosesleri*. *2010*(3), 45–52.

Alptekin, E. (2005). Biyodizel ve Türkiye'deki Durumu. *Kocaeli Üniversitesi Teknik Eđitim Fakültesi Dergisi*, 57–64.

Bilgili, M. E., Sevilmiş, U., Seydoşoğlu, S., Kahraman, Ş., & Sevilmiş, D. (2019). Keten Biyodizelinin Eldesi İle Özellikleri Ve Kullanım Alanları. *Ziraat Mühendisliği*, *367*, 36–53. https://doi.org/10.33724/zm.572710

Cheng, J., Huang, R., Li, T., Zhou, J., & Cen, K. (2014). Biodiesel from wet microalgae: Extraction with hexane after the microwave-assisted transesterification of lipids. *Bioresource Technology*, *170*, 69–75. https://doi.org/10.1016/j.biortech.2014.07.089

Choedkiatsakul, I., Ngaosuwan, K., Assabumrungrat, S., Mantegna, S., & Cravotto, G. (2015). Biodiesel production in a novel continuous flow microwave reactor. *Renewable Energy*, *83*, 25–29. https://doi.org/10.1016/j.renene.2015.04.012

Cormick, R. (2006). DOE / GO-102006-2358 Third Edition September 2006. *Biomass*, *3*(September).

Coronado, C. R., de Carvalho, J. A., & Silveira, J. L. (2009). Biodiesel CO_2 emissions: A comparison with the main fuels in the Brazilian market. *Fuel Processing Technology*, *90*(2), 204–211. https://doi.org/10.1016/j.fuproc.2008.09.006

Eryılmaz, T. (2014). Yozgat İli Şartlarında Yetiştirilen Aspir (Carthamus tinctorius L.) Dinçer Çeşidinden Üretilen Biyodizelin Yakıt Özelliklerinin Belirlenmesi. *Journal of Agricultural Faculty of Gaziosmanpasa University*, *31*(2014–1), 63–63. https://doi.org/10.13002/jafag703

Fukuda, H., Kondo, A., & Noda, H. (2001). Biodiesel fuel production by transesterification of oils. *Journal of Bioscience and Bioengineering*, *92*(5),

405–416. https://doi.org/10.1016/S1389-1723(01)80288-7

Gedikaslan, B. (2020). Atık Yemeklik Yağdan Biyodizel Üretiminde Bir Tepkimeli Damıtma Kolonunun Yapay Sinir Ağları ile Benzetimi. *Ankara Üniversitesi Yüksek Lisans Tezi*.

Kaya, C. (2006). Bitkisel Yağlardan Biyodizel Üretimi. *Dicle Üniversitesi Yüksek Lisans Tezi*.

Kaya, K., & Koç, E. (2015). Enerji Kaynakları-Yenilenebilir Enerji Durumu. *Mühendis ve Makina*, *56*(668), 36–47.

Kralova, I., & Sjöblom, J. (2010). Biofuels–Renewable Energy Sources: A Review. *Journal of Dispersion Science and Technology*, *31*(3), 409–425. https://doi.org/10.1080/01932690903119674

Nematulla, A. (2020). *Türkiye'nin Enerji Sorunu ve Alternatif Enerji Kaynağı Olarak Biyokütle Enerjisi: Bir Nedensellik Analizi*. 146–151. https://doi.org/10.47100/conference_physics/s4_22

Özdemir, Z., & Mutlubaş, H. (2016). *Biyodizel Üretim Yöntemleri ve Çevresel Etkileri*. *2*, 129–143.

Özer, S. (2014). Alkollerin İçten Yanmalı Motorlarda Alternatif Yakıt Olarak Kullanılması. *Uludağ Üniversitesi Mühendislik-Mimarlık Fakültesi Dergisi*, *19*(1), 97–114.

Panwar, N. L., Kaushik, S. C., & Kothari, S. (2011). Role of renewable energy sources in environmental protection: A review. *Renewable and Sustainable Energy Reviews*, *15*(3), 1513–1524. https://doi.org/10.1016/j.rser.2010.11.037

PWC. (2021). *Biyokütle ve Biyoenerji Sektörlerine Genel Bakış*.

Qiul, J., Fan, X., & Zou, H. (2011). Development of biodiesel from inedible feedstock through various production processes. Review. *Chemistry and Technology of Fuels and Oils*, *47*(2), 102–111. https://doi.org/10.1007/s10553-011-0266-3

Rodionova, M. A., Khrestianovskaia, M. V, & Kukolev, M. I. (2017). Primary energy sources of cogeneration units. *Construction of Unique Buildings and Structures*, *4*(55), 50–67. https://doi.org/10.18720/CUBS.55.4

Scott, S. A., Davey, M. P., Dennis, J. S., Horst, I., Howe, C. J., Lea-Smith, D. J., & Smith, A. G. (2010). Biodiesel from algae: Challenges and prospects. *Current Opinion in Biotechnology*, *21*(3), 277–286. https://doi.org/10.1016/j.copbio.2010.03.005

Stigka, E. K., Paravantis, J. A., & Mihalakakou, G. K. (2014). Social acceptance of renewable energy sources: A review of contingent valuation applications. In *Renewable and Sustainable Energy Reviews* (Vol. 32, pp. 100–106). Elsevier. https://doi.org/10.1016/j.rser.2013.12.026

Szybist, J. P., Song, J., Alam, M., & Boehman, A. L. (2007). Biodiesel combustion, emissions and emission control. *Fuel Processing Technology*, *88*(7),

679–691. https://doi.org/10.1016/j.fuproc.2006.12.008

TÜİK. (n.d.). *Türkiye'deki Dizel Araçların Toplam CO2 Emisyon Değerleri <https://data.tuik.gov.tr/Bulten/Index?p=Sera-Gazi-Emisyon-Istatistikleri-1990-2019-37196>(15 Kasım 2021).*

Uysal, D., YILMAZ, K., & Alparslan, T. T.-. (2015). Enerji İthalatı ve Cari Açık İlişkisi :Türkiye Örneği. *Dergipark.Org.Tr*, 63–78.

Chapter 6

RECENT DEVELOPMENTS IN COOLING OF PHOTOVOLTAIC SOLAR PANELS

Perihan ÇULUN[1], Sinem KILIÇKAP IŞIK[2]

1 Bingöl Üniversitesi, Mühendislik ve Mimarlık Fakültesi, Makine Mühendisliği Bölümü, **email:** pculun@bingol.edu.tr
2 Bingöl Üniversitesi, Mühendislik ve Mimarlık Fakültesi, Makine Mühendisliği Bölümü

PHOTOVOLTAIC SOLAR PANELS

Due to the rapid increase in the population and the inability of fossil energy sources to meet the energy demands, the trend towards renewable energy sources has accelerated. Fossil energy sources are preferred because they are insufficient and cause various air pollution. On the other hand, solar energy, wind energy, wave energy, geothermal energy etc. for the supply of necessary energy. The production limits of renewable energy sources need to be pushed. It is essential to carry out studies on the efficiency increase of all systems developed in this field.

Solar energy, which is one of the important sources of renewable energy, is at the forefront compared to other renewable energy sources in terms of both hot water supply and electrical energy production. The sun is the richest energy source in terms of co-existing with the existence of human beings and continuing its existence as long as human life continues, as well as the fact that the sun's rays coming to the earth in one hour have the power to meet the energy of the whole world for one year. Therefore, the investments to be made in this field will be more accurate. There is no doubt that there are many research studies on higher efficiency in solar hot water supply. However, in this study, electricity generation from solar energy (photovoltaic panels) will be emphasized. It is known that 1°C increase in panel surface temperature in Photovoltaic Panels(PV) adversely affects panel efficiency by 0.45% (Maatallah et al. 2019).

With this study, it is aimed to convey the latest developments in panel cooling technologies to increase the efficiency of photovoltaic solar cells. In this direction, first of all, cooling studies to increase the efficiency of photovoltaic solar cells are discussed respectively. It has been revealed by many studies that the cooling method with phase change materials, which is one of these cooling types, maximizes the efficiency (Rajvikram et. al. 2019). The PV/T cooling system and Phase Change Materials(PCM), which are the cooling types that increase the efficiency the most compared to other cooling types, are presented in more detail because they are the latest technology in this field.

COOLING of PHOTOVOLTAIC PANELS

The efficiency of a photovoltaic (PV) panel refers to the amount of solar energy converted into usable electrical energy. The parameters affecting the efficiency in photovoltaic panels are generally as follows (Wardowski and Akbarzadeh, 1996; Rodrigues et al., 2011; Kerem et al., 2020);

1. Solar radiation: The solar radiation or the amount of sunlight received by the panel directly affects the amount of electricity it can produce. Higher levels of solar radiation will lead to higher levels of

electricity production.

2. Temperature: The temperature of the PV panel is one of the most important factors affecting the efficiency. As the temperature of the panel increases, its efficiency decreases (Xu et al. 2020). This is because the electrical properties of the panel material change with temperature, resulting in a huge reduction in voltage and also efficiency.

3. Angle of incidence: The angle of impact of sunlight on the panel surface can also affect its efficiency. The most ideal angle of incidence of sunlight is the angle perpendicular to the surface of the panel. As the angle deviates from the vertical, the efficiency decreases.

4. Shading: Since the shading on the panel reduces the amount of solar radiation received by the panel, it also significantly reduces the panel efficiency.

5. Panel design and materials: The material used in panel construction and the design of the panel is another factor that affects its efficiency. Panels made from higher quality materials and more efficient designs can have higher efficiency.

6. Age and deterioration of the panel: PV panels may deteriorate over time due to environmental factors such as exposure to sunlight, temperature and humidity. This, in turn, can affect their productivity.

8. Inverter efficiency: Inverters convert the direct current power produced by PV panels into alternating current power that can be used in homes. The efficiency of the inverter in the PV system also affects the overall efficiency of the system.

The efficiency of photovoltaic panels is directly related to the panel type, weather conditions, the angle of incidence of the sun rays and the panel angle. While solar thermal systems efficiencies can rise up to 60%, it is known that panel efficiencies are generally very low, such as 5%–20% (Sharma et al., 2015; Dwivedi et al. 2020). However, 47% of solar radiation consists of visible rays that can be converted into electrical energy (Shastry and Arunachala, 2020). This means that it is possible to increase the panel efficiency up to approximately 50%. Panel efficiency is significantly affected by the panel material as well as the panel surface temperature. It is understood from the literature studies that the best efficiency is provided for the panel surface temperature value to be around 25°C (Shastry et al., 2020). It is stated that the efficiency decrease of 0.5% or 0.65% for 1°C temperature increasing at the panel surface temperature (Klugman et al. 2017). It has been experimentally determined that the surface temperature can range from 51.8°C to 88.2°C in a monocrystalline panel, depending on the region where the experiment is performed (Khanna et al. 2017). In

such a system, if the temperature is kept constant at 51°C, an efficiency loss of 20% will be prevented. On the other hand, it is understood that the efficiency increases significantly for 1°C temperature drop in regions with higher solar radiation. As a matter of fact, in a study conducted in a region where solar radiation is 901W/m^2, it is mentioned that 7.28% efficiency increase for a temperature drop of 4.7°C (Luo et al., 2017). This means a 1.6% increase in efficiency at a temperature drop of 1°C. In another similar study, it is mentioned that an efficiency increase of 7.3% is achieved with a temperature drop of 2.4°C in the region operating in the flux range of 100-1120W/m^2 (Indartono et al., 2016). Although the efficiency increases obtained are closely related to the physiology of the study, it is clear that the increase in efficiency corresponding to 1°C cooling is also related to the solar radiation of the working environment.

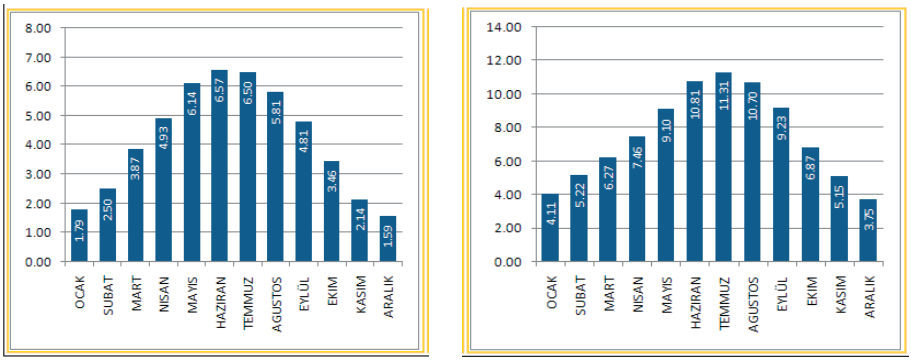

a) *b)*

Figure 1a. Global radiation values in Turkey, kWh/m^2-day, b) Global radiation values in Turkey, kWh/m^2-day (GEPA, 2023

In a country like Turkey, which receives significant solar radiation, even in January when the sun is at its weakest, the daily amount of solar radiation is 1.79kWh/m^2-day (Figure 1a). Considering that the sunshine duration in the relevant month is 4.1 hours (Figure 1b), the daily sunshine amount in January is 437W/m^2, and in June and July this value is 575W/m^2 (GEPA, 2023). It is known that cooling of the panel surface is of great importance if the amount of solar radiation per unit area is over 500W/m^2 (Wongwuttanasatian et al. 2020). As can be seen, the amount of solar radiation per unit area, even in January, when Turkey gets the least sunshine, is not to be underestimated. It is understood that panel cooling is essential in such countries.

Although the short circuit current (Isc) increases slightly with the increase of the panel surface temperature, it is known that the open circuit voltage (Voc) decreases significantly (Rezvanpour et al. 2020). Since the maximum power and efficiency of the panel is dependent on the open circuit

voltage and short circuit current, the net electricity production decreases significantly with temperature increase (Dwivedi et al., 2020; Shastry et al., 2020). For this reason, it is necessary to work on reducing the panel surface temperature in order to prevent the decrease of the panel efficiency or to increase the efficiency. Various active and passive cooling methods have been used in this field for years. The most commonly used ones are presented in Figure 2. In active cooling systems as can be seen from the figure, air, water, water-nanofluid mixture, refrigerant etc. subjected to forced transport. In the passive system, cooling systems using a natural convection fluid and PCM systems are widely used.

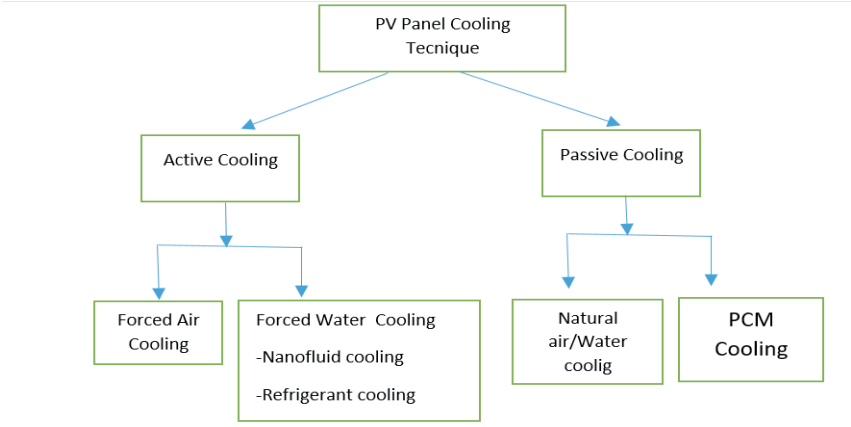

Figure 2. Commonly used PV cooling systems

The cooling systems given in Figure 2 can be summarized as water-based, air-based and PCM-based (Teo et al., 2012; Grubisic-Cabo et al., 2016; Kane et al. 2017; Kalaiselvan et al., 2018; Benato and Stoppate, 2019).) according to this;

1. Water-based cooling: In this method, excess heat is absorbed by the water circulating on the surface of the solar cells. Heated water transfers heat into a cooling medium such as air. It does this by passing through the heat exchanger. The cooled water is then circulated back to the panel. This method is a very effective method. However, it requires pumping power due to a continuous water supply.

2. Air-based cooling: In this method, the excess heat is tried to be removed with the air blown onto the surface of the solar cells. The air is blown naturally or by force by means of fans. It requires less maintenance than water-based cooling but is less effective.

3. Cooling with phase change material: In this method, a phase change material is used to absorb excess heat. This material, known as PCM, melts when it absorbs heat, and solidifies as it cools, releasing stored heat. It is a method that works very effectively thanks to a correctly

selected PCM.

In these cooling methods, water and air-based cooling can be seen as both active and passive cooling. Apart from these, cooling with thermoelectric and cooling with PCM material are used as passive cooling. As mentioned before, in active cooling, the panel is cooled by providing the flow of water or air fluid with a pump/compressor for cooling purposes (Figure 3a). In passive cooling, PCM material based on latent heat of evaporation or cooling with water evaporation, heat pipes, fins, etc. By increasing the heat transfer surface, cooling is achieved by conduction and convection without the use of electrical energy (Figure 3b). Recently, hybrid systems have emerged where both active and passive systems are used together. For example, in the same system, both active cooling with water and passive cooling with PCM material can be done. Or, in addition to PCM material, fins can be made, heat pipes, nanofluid addition, etc. More effective cooling methods using

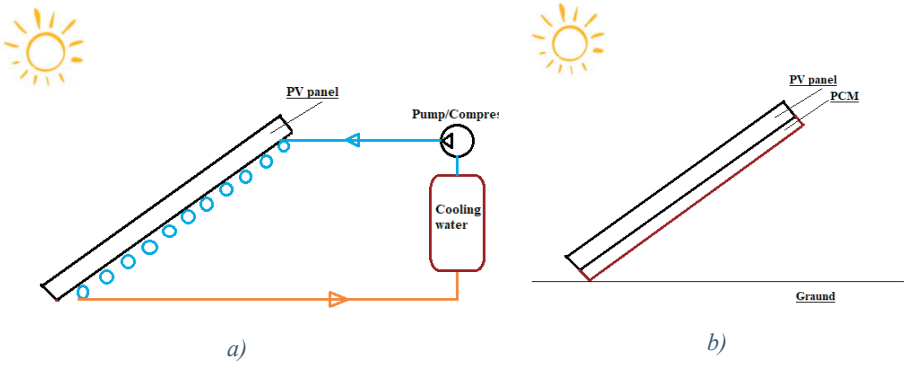

a) b)

Figure 3. a) Active cooling method, b) Passive cooling moethod

The choice of cooling method to be used in PV panels depends on several factors such as cost, availability of resources and performance requirements.

1. ACTIVE COOLING METHODS OF PHOTOVOLTAIC PANELS

Active cooling methods are one of the methods used to dissipate the excess heat generated during the operation of the panel in order to increase the efficiency and life of solar cells. Active cooling methods are used to increase panel efficiency and life, especially in hot climates. The cells in the photovoltaic panel absorb photons when exposed to sunlight and convert them into electrical energy. During this transformation, a significant part of the energy absorbed is converted into heat. This raises the temperature of the cells, reducing their performance. In active cooling methods, it can be in the form of spraying water on the PV panel surface, cooling with

impinging jets, cooling the surface by passing air or water through pipes or channels (Royne and Dey, 2007; Odehand and Behnia, 2009; Krauter, 2014; Ceylan et al. 2014). Providing more effective cooling by adding nanofluid to the main fluid used in active cooling is also among the studies investigated. In addition, if the heat removed from the PV panel is passed through the heat pump for heating a place or system, then a secondary fluid such as refrigerant flow can be used in the same system.

Both active and passive cooling systems have advantages and disadvantages compared to each other. Various advantages and disadvantages of active cooling methods used in photovoltaic panels compared to passive types are given in Table 1 (Siecker et al., 2017; Nižetić et al., 2018).

Table. 1. *Advantages and disadvantages of active cooling methods*

Advantages	Disadvantages
• **Panel efficiencies are increased:** With active cooling methods, higher power output and energy production from the PV system are provided. • **Their useful life is extended:** With this method, the temperatures of the panel cells are lowered, resulting in a longer life and less maintenance costs. • **Panel reliability is improved:** Active cooling methods can increase the reliability of the PV system as it prevents high temperatures that can cause cell damage.	• **Increased complexity:** Active cooling methods use additional equipment such as pump, heat exchanger and coolant, making the system more complex, which can increase the cost of installation and maintenance of the system. • **Energy consumption increases:** electrical energy is required for devices such as fans or pumps to be used in this method. This, in turn, can reduce the net energy output and efficiency of the system, as well as contribute to the system's energy consumption. • **Increased cost:** The cost of the system increases due to additional equipment and components.

1.1. Active Cooling Method with Water

The active cooling method with water in photovoltaic (PV) panels involves using water flow to remove excess heat from the solar panels (Figure 4). This method can significantly increase the efficiency and lifetime of PV panels in hot environments. Since water has a higher heat capacity than air, it can absorb more heat energy per unit volume, thus providing a more effective cooling environment. There are several methods for active water cooling in PV panels (Grubisic-Cabo et al., 2016; Zubeer et al., 2017; Kalaiselvan et al., 2018). These;

1. **Direct water cooling:** In this method, water in direct contact with the surface of the solar panels is used. The water, heated by excess heat, is passed through a heat exchanger to transfer its heat to a cooling medium such as air or another body of water. The cooled water is then circulated back to the panel. This method is effective, but requires a constant supply of water and a pump to circulate the water. Cooling with water spray and

burr jets can also be evaluated in this section (Awad et al. 2020). Figure 4b shows the cooling process with the impinging jet. In the water spray method, the panel can be on one side or both sides of the panel can be cooled. It is mentioned that by reducing the temperature of the cooling panel to 35°C by spraying water on the upper surface of the panel, an efficiency increase of up to 15% is achieved (Moharrema et al. 2013; Nizetic et al. 2016).

2. Indirect water cooling: In this method, the heat in the panel is transferred to a cooler using a heat exchanger and then circulated in the system. The heatsink, which absorbs the heat from the panels, is cooled by a cooling tower or other heat exchanger. It is then circulated back to the panel. This method is more cost effective but less efficient than direct water cooling.

3. Hybrid water cooling: It consists of combining direct and indirect water cooling methods for a more efficient cooling system. In this method, the hottest part of the panel is cooled directly with water, while the remainder is cooled using a heat exchanger cooling. It is more efficient than other methods.

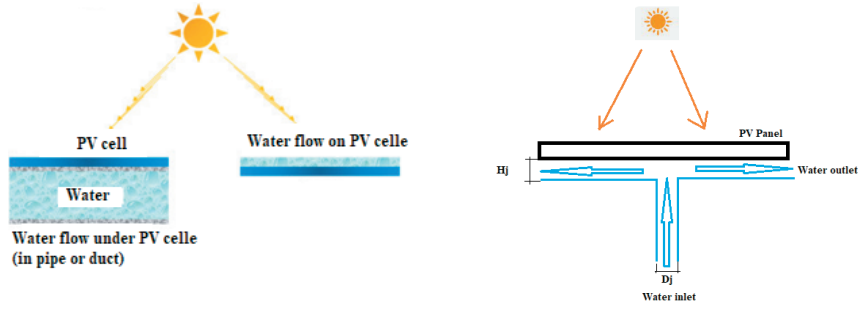

Figure 4. a) Water cooling method, b) Impact jet cooling (or water spray)

The advantages and disadvantages of active cooling methods with water in photovoltaic (PV) panels are as follows (Siecker et al., 2017; Nižetić et al., 2018);

Advantages:

1. Water provides higher efficiency and energy production as it has a higher heat capacity than air.

2. It can extend the life of PV cells and reduce maintenance costs as it will help to reduce the high temperatures that cause the performance and lifetime of the PV cells to decrease.

3. With this method, the panel cells are kept cooler and the reliability of the PV system is increased.

4. They require less maintenance than air cooling systems.

Disadvantages:

1. As additional components and equipment such as pumps, heat exchangers and coolant are used in water cooling systems, it causes an increase in the cost of the PV system.

2. Since water is used in this system, there is a risk of leakage that may damage the PV system or surrounding components. Proper maintenance and installation procedures are required to reduce the risk of leakage.

3. Electrical energy is required to operate the pump used in water cooling systems. This increases the overall energy consumption of the system.

12. Active cooling method with air

Air flow is used to dissipate the heat in the panel in active cooling methods with air (Figure 5). With this method, the efficiency and lifetime of the panels can be increased significantly. There are several methods for active air cooling in PV panels (Kalaiselvan et al., 2018; Siah Chehreh Ghadikolaei, 2021; Ghadikolaei , 2021; Sharaf et al., 2022). These;

1. Natural convection cooling: This method uses natural air flow to cool the panels. Air flows over the surface of the panel and heat is transferred from the solar cells to the air by convection. Heated air rises and creates a natural flow of air that helps dissipate heat.

2. Forced convection cooling: In this method, fans are used to circulate the air over the surface of the panels. Fans increase airflow which improves the rate of heat transfer from solar cells to air. Forced convection cooling is more efficient than natural convection cooling but requires electricity to power the fans.

3. Microchannel cooling: Microchannels are placed inside the PV panel to circulate the air over the surface of the solar cells. Air flows through channels made of a thermally conductive material and removes heat from solar cells through convection.

4. Jet impingement cooling: In this method, a high velocity air stream is directed to the surface of the solar cells. The airflow removes heat from the cells by forced convection. Jet impact cooling is an effective method. But high pressure air sources are required.

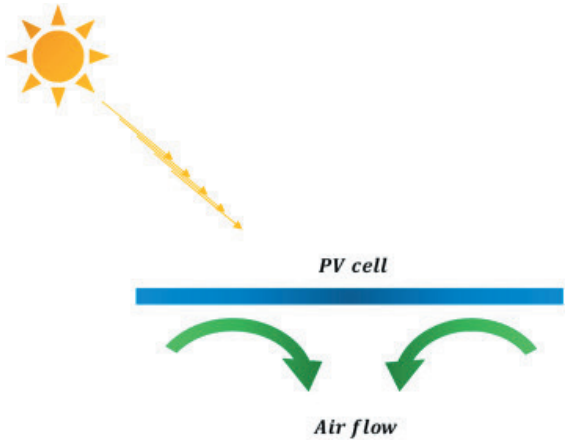

Figure 5. *Air cooling method (Siah Chehreh Ghadikolaei, 2021)*

Active cooling methods with air have advantages such as being efficient, extending the life of the panel as it reduces the temperature, and being a more cost-effective system because there are only fans and blowers in the system. However, in order for the fans used in these systems to work properly and efficiently, regular maintenance is required. In addition, noisy fans can cause noise pollution in residential areas. Electricity is also needed for the operation of fans and blowers. This increases energy consumption and cost. One of the main disadvantages is that active air cooling may not be effective at extremely high temperatures, as the temperature difference between ambient air and panel temperature may not be sufficient to provide adequate cooling. Studies show that the panel temperature can be reduced up to 40°C by using suitable open air ducts and fin structures in these systems (Dwivedi et al. 2020). Therefore, the suitability of active air cooling method depends on various factors such as location, temperature and the special needs of the PV system (Al-Amri and Mallick, 2013; Ghadikolaei , 2021).

As mentioned before, the main difference in active cooling method is that electrical energy is used for cooling. Pressurized water, air, nanofluid or refrigerant gases are also the main fluids used in this method (Yao et al. 2020). With this method, it is possible to increase the panel electrical efficiency significantly by reducing the panel temperatures effectively. However, the consumption of electrical energy used in the active cooling system is an undesirable situation. Because it reduces the total efficiency of the final system (photovoltaic panel + cooling system). According to the latest technological developments in this field, passive cooling systems will be preferred more because they are less costly, no additional energy expenditure, no operating maintenance costs or less.

1.3. PV/T Cooling Method

In PV/T systems, which can be called the latest technology of active cooling, the heat taken from the panel with the help of pressurized fluid can be used for heating with the help of another intermediate fluid. The heat obtained from such a system can be used to obtain domestic hot water, to heat an environment (heat pump) or to meet any heating needs in industrial institutions or to generate electricity with thermoelectricity. In Figure 6, the heat obtained from the PV/T panel heats the water in the water tank. In Figure 7, a house is heated by using the hot fluid obtained. However, this system will be used as an alternative system in systems where house heating or continuous heating is required. As a matter of fact, the hot fluid obtained from PV/T systems may be discontinuous in the winter season. PV/T systems are generally included in the class of active cooling systems. However, recently PCM materials have been used to increase the efficiency of such systems. This is the result of efforts to create more efficient systems by combining the advantages of active and passive systems. The main purpose here is to ensure that the heat obtained is stored in the PCM material and used for a longer period of time. In this way, it is ensured that the net efficiency of PV/T systems is increased.

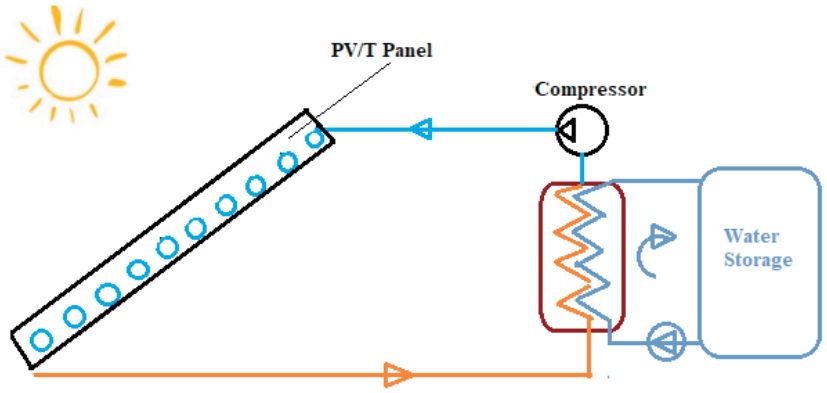

Şekil 6. PV/T sistemde sıcak su elde edilmesi

In PV/T systems, electrical energy efficiency has been increased with effective panel cooling compared to conventional PV panels. It is known that the sum of electrical and thermal efficiency in PV/T-PCM systems is generally 70%, although it has been stated that it reaches 90% in some studies (Xu et al. 2020). Recently, nano materials or nanofluids have been used to increase the efficiency of PV/T-PCM systems (Selimefendigil and Sirin, 2022). Thermal systems were obtained with the hot fluid obtained from the panel. Although there is unwanted pump or compressor power in

active cooling systems, they are much more advantageous in the long term (after the paybacperiod) compared to conventional PV panels.

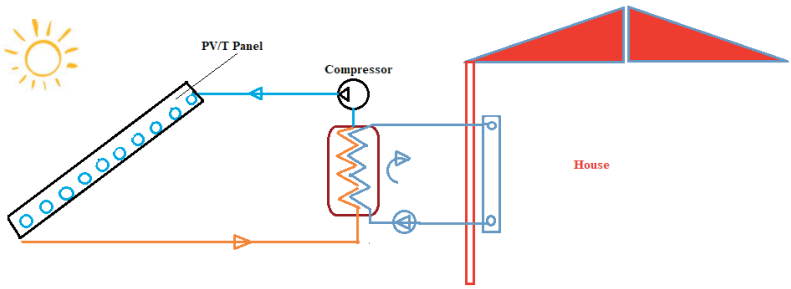

Şekil 7. PV/T sistemde evin ısıtılması

Existing studies point to the importance of thermodynamic analysis in PV/T systems. Studies indicate that the panel surface temperature causes an increase in entropy in PV or PV/T systems (Kandilli, 2019). However, when we look at the studies, there are very few studies especially in terms of second law analysis (Mataallah, 2019). From the studies conducted for PV and PV/T system, it is understood that the exergy efficiency obtained for the PV/T system is higher than that of PV. According to Serdarabadi et al. (2017) found an increase of up to 23% in exergy analysis compared to normal PV at the end of cooling using PV/T znO/Aqueous nanofluid and PCM. In this regard, for the further development of such systems, it will be possible to support interfluids with nanofluids together with sensitive thermodynamic analyzes, to increase the studies using various PCM materials for heat storage, and to use nanomaterials together with PCM materials.

2. PASSIVE COOLING METHODS IN PHOTOVOLTAIC PANELS

In this method, the panel surface is cooled by natural convection and transmission without the use of electrical energy. In the passive approach, heat is removed from the environment by convection and conduction without the need for any additional energy consumption such as heat emitters and heat pipes (Maleki et al. 2020). Since there is no additional energy expenditure in these cooling methods, the development of these methods is more essential than active methods. In the passive method, the natural convection fluid can be air or water, and it is also possible to provide better heat transfer by conduction. Previous studies have shown that when water is used as a natural convection fluid, an increase in efficiency is achieved up to 10.4%, on the other hand, if air is used as a fluid, it is understood that efficiency can be increased up to 7.5% (Chandrasekar et al. 2013; Popovici et al. 2016). However, in cases where water leakage that

may occur in passive cooling systems that will work with water adversely affects the electric current or efficiency, it is necessary to prevent the leakage of water to the panel. In case of using air fluid or PCM material, such a hazard cannot be mentioned. However, it should be noted that air is less effective than water. The advantages and disadvantages of passive cooling systems are presented in Table 2 in detail.

Table 2. *Advantages and disadvantages of passive cooling methods*

•**Advantages**	•**Disadvantages**
•**Panel efficiencies are increased**: Since there is no pump or compressor in the passive cooling system, it is possible that the net efficiency of the system is higher than the active cooling. •**Their useful life is extended:** Since the temperature of the panel cells is reduced, they have a longer life and less maintenance costs. In addition, since no corrosive substances such as water are used in the passive system, the system life is longer than the active cooling systems. •**Panel reliability is improved**: Passive cooling methods prevent high temperatures that can cause cell damage, increasing the reliability of the associated system. •**Easy applicability:** Since it has a simpler application, its applicability is higher than active systems. •**Maintenance and operating costs are less:** Since there are no moving mechanisms (pump or compressor) in the system, maintenance and modifications are easier and require less expense.	•If PCM material with suitable melting and freezing temperatures is not used, it is possible that the desired efficiency cannot be obtained. •If PCM material is used alone, it is possible to obtain lower electrical efficiency than the active system due to its low conductivity coefficient.

In PV panel passive cooling methods, there are basically three different types of cooling systems with wick structure, heat pipe and PCM material use (Maleki et al. 2020). In these cooling methods used to increase panel efficiency, the method that can be called the latest technology is cooling with phase change materials. This cooling method has a greater advantage over other passive methods in terms of both prolonging the life of the panel, being more reliable than water (not damaging the electric current on the panel), and not requiring pumping power and therefore no electricity consumption. It is known that various methods such as immersion in the dielectric medium, immersion of the panel in water, cooling with the air flow induced by buoyancy, cooling with the help of heat emitters, heat pipes, cooling with the evaporative technique are also used for passive cooling of PV panels. However, the most commonly used methods are cooling with natural convection water/air and PCM material, as previously classified in Figure 2. In this study, these cooling types are emphasized.

2.1. Passive Cooling Method with Natural Convection Air

Although it is one of the first cooling methods that used active cooling with air in PV panels, passive cooling with air was also used in most applications since it contains less mechanical parts, is more economical, and has lower operating and maintenance costs. Various heat emitters (fin structures), heat pipes, etc. are used in such cooling systems. It is possible to increase the effect of cooling with natural convection air by using structures. Figure 8 shows different fin structures in the natural convection air cooling system (Bilen et al. 2021).

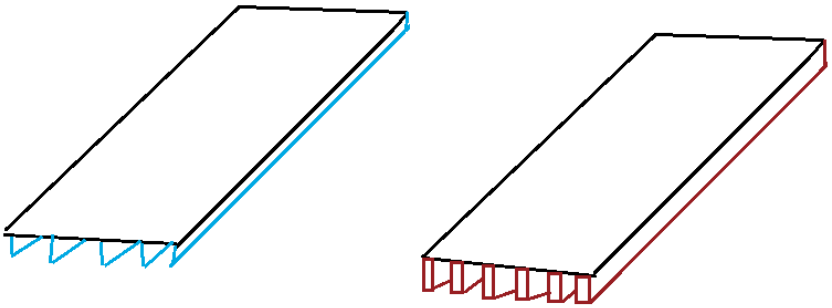

Figure 8. Effective natural convection air cooling with various fin structures

2.2. Passive Cooling Method with Natural Convection Water

Cooling with cotton wick and heat spreaders: With the help of cotton wicks, one end of which is immersed in the water reservoir, in the type of cooling with natural convection water, the relevant surface is cooled by allowing the water to travel to the PV panel and evaporate. By using various heat spreaders, faster cooling can be achieved in this method. This type of cooling can also be evaluated in the category of cooling with the technique of evaporation of water. In one of the sample studies conducted in the passive cooling method with water, the panel temperature value was 30%, 17% and 11% temperature decrease in the cooling made by using water, Al2O3/water, CuO/water in the cotton wicked capillary tube (Chandrasekar et al. 2013). In the aforementioned study, the other end of the cotton wick arranged spirally behind the PV panel was immersed in water. As a result of the latent heat released by the evaporation of the water walking on the wick, the panel surface is passively cooled. With the related study, it was stated that the PV panel temperature was reduced from 65°C to 45°C.

In the passive cooling system, which is made by using cotton wicks in the heat spreaders, the advantages of increasing the transmission coefficient of the heat emitters together with the latent heat of the steam of water are combined, thus reducing the surface temperature by 12% and increasing

the electricity production by 14% (Chandrasekar & Senthilkumar, 2015). The visual of the related study is given in Figure 9. As seen in the figure, U-profile aluminum heat spreader fins were used in order to accelerate the removal of heat from the environment in the cooling made by using the latent heat of evaporation of the water in the cotton wick. In this system, if it is used without cotton wicks, passive cooling can be done with the finned structure used. With the natural convection air movements hitting the wings, a passive air-operated cooling system is obtained

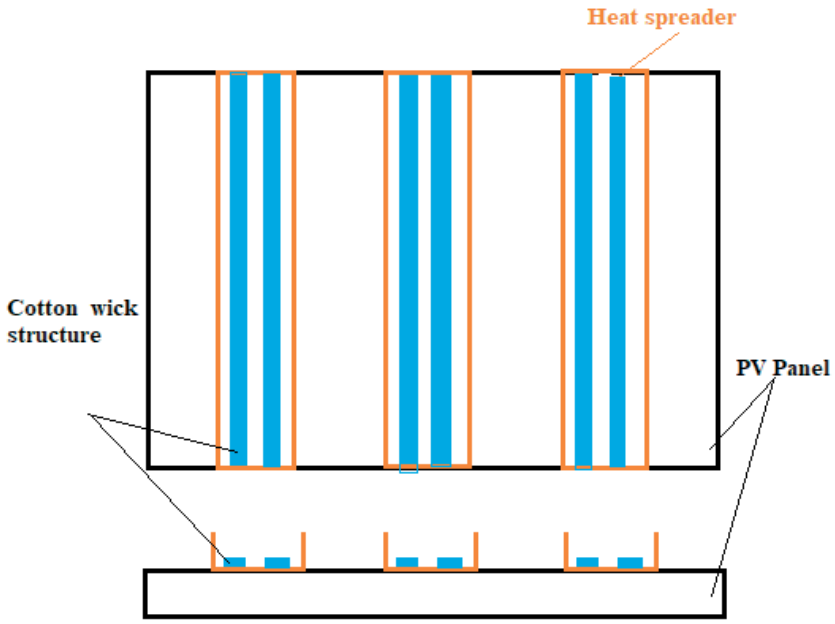

Figure 9. *Passive cooling with cotton wick and heat spreaders (Chandrasekar & Senthilkumar, 2015).*

Cooling of PV panels by submerged in water: It is one of the methods in which the panel surface temperature is passively cooled. Current studies in this area examine the cooling effects of the panel horizontally on the ground, horizontally while floating in water, and submerged (Kumar et al. 2020). According to this current study, the exergy loss of the panel on the ground was higher than the panel on the water surface and submerged in the water. The highest exergy efficiency was obtained in the submerged panel. In another study, where the panel is completely and partially submerged, it was observed that the electricity generation efficiency was higher in the fully immersed panel (Mathu et al. 2019). Similar investigations were made for different water conditions (Enaganti et al. 2020).2.3.

2.3. Passive Cooling Method with PCM Material

It is understood that passive cooling using phase change materials will be preferred more than other passive methods in terms of being less costly, no additional energy expenditure, no operating maintenance costs, and prolonging the panel life. The high heat storage capacity of PCM materials also encourages the effective use of these materials in thermal systems (Asgharian and Baniasadi, 2019). Research has been carried out on the low thermal conductivity coefficients, which is the only feature that is seen as a disadvantage in phase change materials. One of the current studies is the addition of nanomaterials to increase the thermal conductivity coefficients (Weinstein et al. 2008). Considering that the addition of nanomaterials increases the cost, less costly alternative studies are also being carried out. For example, various studies are carried out on passive cooling systems created by combining PCM material with materials with high thermal conductivity such as aluminum and copper in various combinations (Khanna et al. 2018). Figure 10 shows the passive cooling method using PCM material. The passive cooling method, which can serve as an example for the studies carried out with different thicknesses and different PCM material fillings on the back of the panel without using any blade type, is presented in Figure 10a. In Figure 10b, in order to eliminate the low transmission coefficient disadvantage of the PCM material and therefore to increase the heat transmission coefficient, fins with different shapes and produced from different materials with various heat transmission coefficients are used. In some studies, fins of different shapes and materials were placed between the PCM material, while in some studies, PCM material was filled between/inside the fins with different cross-sectional areas placed behind the PV panel. Along with such studies, reinforcement studies are also carried out with various nanofluids in order to increase the heat transfer coefficient .

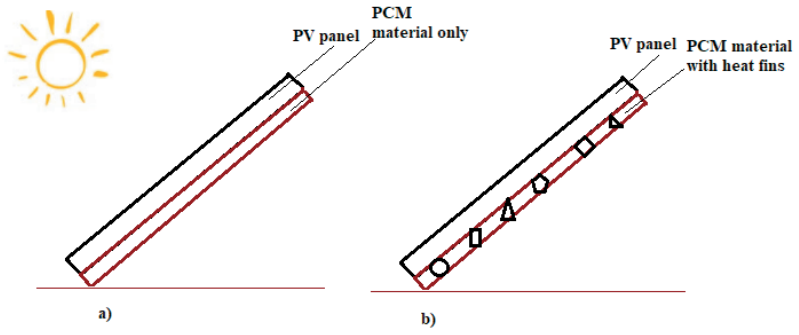

Figure 10. Passive cooling of PV panels with PCM material, a) cooling with PCM filling without using fins, b) fin placement in PCM filling in various shapes and materials

PCM materials used in this field are divided into three parts as organic, inorganic and eutectic. Organic materials have the advantage of being more resistant to corrosion and less costly than inorganic materials. On the other hand, the lower conductivity of organic materials compared to inorganic materials is one of the disadvantages of these materials. Organic PCM materials are generally known as paraffins and are expressed with the symbol RT. The number to the left of the RT expression symbolizes the melting and freezing point of the relevant material. For example, RT20 refers to organic paraffin PCM material with a melting and freezing point of 20°C. It is understood that organic PCMs work in the range of 10-45 ° C, inorganics at 30-60 ° C, and eutectics in the range of 25-65 ° C. In case of working in a low melting temperature environment such as 10-20°C, organic PCM is more likely to find eutectic PCM for high melting temperatures such as 60-70 (Yao et al. 2020).

In Table 3, some literature studies using PCM material in PV and PV/T systems and their brief results are presented. It has been determined that calcium chloride hexahydrate (CaCl2. 6H2O) is preferred because it is cheap in general cooling studies with PCM.

Table 3. *Some passive cooling studies using PCM material*

Hosseinzadeh et al. (2018)	They uses the PCM in nanofluid based PVT/ PCM	They demonstrated that the use of PCM in nanofluid based PVT/PCM system enhances the thermal output power of conventional PV/T
Yang et al. 2018	In the PV/T-PCM system Capric acid was used.	While providing a surface temperature drop of 15.8°C, 19% increase in electricity efficiency was achieved.
Abdelrahman et al. 2019	Different blade configurations are also used in the PV panel with RT35HC PCM material.	It was emphasized that the electrical efficiency increased from 20% t to 46.3%, so the PV efficiency increased significantly with PCM material.
Esfe et al. 2020	Cooling the PV/T with PCM -In case of cooling the PV/T with nanofluid -PVT-PCM system Cooling with uric acid, capric acid and nanofluid / nano-PCM (organic paraffin as PCM and SIC as nanoparticle)	increased the electrical efficiency between 15-23% compared to conventional PV. In the case of PV/T cooling passing the nanofluid through the direct, spiral and micro-channel, the efficiency increase was obtained as 20.5%, 37.6 and 27, respectively. The thermal efficiency was determined as 90%, 69.84% and 72%, respectively.
Yao et al. 2020	PCM heat storage based on PV/T panel	Meanwhile, the heating COP can reach 5.79 which is 70% higher than the conventional air conditioning system and the electrical, thermal, overall efficiencies are 17.77%, 55.76% and 75.49%, respectively.

Rezvanpour et al. 2020	PV-PCM(Calcium Chloride Hexahydrate)	Average temperature drop for November is 12C with 23.5% temperature drop; It dropped to 14C with 24.3% temperature drop for December. Maximum power output for November is 22.32%, while for Decemberwas 24.68%.

Due to the fact that the night is relatively cold compared to the day, the PCM material has to give off its internal heat and freeze during the night, and it must melt by absorbing heat from the high heat source (PV panel) with the effect of the increasing ambient temperature during the day. In this regard, when choosing PCM material, it should be noted that the freezing point of the area where the study will be carried out is at night temperature and below the ambient temperature in order to ensure that it melts during the day. In addition, it is necessary to adjust the amount of material well in order to ensure that the melting of the PCM material continues throughout the day and an effective cooling is provided throughout the day. Today, there are various studies that detect efficiency gains by using PCM material in PV panels and PVT panels (Maallah et al. 2019). It is known that non-toxic and non-hazardous organic PCM materials are generally preferred in studies conducted in this field (Kazemian et al. 2019, Kazemian et al. 2020. In addition to the efficiency increases with the use of PCM material in the PV panel, aluminum or copper blades with PCM material are used in various The electrical efficiency was increased by approximately 13% (Atkin & Farid, 2015). (2018) used nanofluid in the PV/T -PCM system and achieved an efficiency increase of 29.6%. According to Esfe et al. In his 2020 study, he mentions that cooling of the PVT with PCM increases the electrical efficiency by 15-23% compared to conventional PV. In the same study, it is mentioned that when the PVT is cooled with nanofluid, the efficiency increase is 20.5, 37.6 and 27, respectively, when the nanofluid is passed through the direct channel, spiral channel and micro channel.

CONCLUSIONS

It necessitates the active use of solar energy in order to meet the global energy demand without endangering human health. It is obvious that photovoltaic panels are the most utilized area from solar energy. On the other hand, the low yields of 15-20% make researches in this field valuable. An important research branch to increase this efficiency is the cooling of the panels. As a matter of fact, the increase in the panel surface temperature is one of the important reasons that reduces the efficiency. As a general evaluation of the cooling systems used in this sense;

1. The first cooling systems used were generally active cooling systems. It is the best cooling system to be used in using the heat in PV panels to meet the heat requirement of a system. However, in general, active

cooling methods used in PV panels have several benefits such as increased efficiency, extended panel life and reliability, as well as disadvantages such as becoming more complex, causing an increase in energy consumption and cost.

2. Passive cooling systems, developed as an alternative to active cooling systems, have started to be preferred more because they are less costly, no additional energy expenditure, no operating maintenance costs or less. It is understood that the most effective cooling among passive cooling types is provided by phase change materials. However, although phase change materials are the latest technology used to cool photovoltaic batteries and increase their efficiency, they also contain important issues that need to be researched and developed. As follows;

Phase change materials structurally have the disadvantage of low thermal conductivity coefficient. In this respect, every study to increase the thermal conductivity is important in terms of its application to photovoltaic panel cooling. As a matter of fact, it will be possible to increase panel efficiency in this direction. Currently, it is known that the transmission coefficient is increased by adding graphite nanofiber to the FDM material (Weinstein et al. 2008). However, it should be taken into account that the cost will increase as the nanomaterial ratio is increased.

3. In PV/T systems, which we call hybrid PV panels, which are thought to be more preferred in the future compared to the standard PV system, it is important to make the second law analysis of thermodynamics as a result of proper cooling. Because in PV/T systems, an increase in entropy occurs in parallel with the increase in surface temperature. However, it is understood from the existing studies that there are not enough studies in this field. In this respect, due attention should be paid to second law analyzes of second thermodynamics in order to establish more efficient systems.

REFERENCES

Al-Amri, F., & Mallick, T. K. (2013). Alleviating operating temperature of concentration solar cell by air active cooling and surface radiation. Applied Thermal Engineering, 59(1-2), 348-354.

Alami AH. Effects of evaporative cooling on efficiency of photovoltaic modules. Energy Convers Manag 2014;77:668e79.

Asgharian, H., Baniasadi, E., 2019. A review on modeling and simulation of solar energystorage systems based on phase change materials. J. Energy. Storage 21, 186–201.

Awad, M., Radwan, A., Abdelrehim, O., Emam, M., Shmroukh, A. N., & Ahmed, M. (2020). Performance evaluation of concentrator photovoltaic systems integrated with a new jet impingement-microchannel heat sink and heat spreader. Solar Energy, 199, 852-863.

Atkin, P., & Farid, M. M. (2015). Improving the efficiency of photovoltaic cells using PCM infused graphite and aluminium fins. Solar Energy, 114, 217-228.

Benato, A., & Stoppato, A. (2019). An experimental investigation of a novel low-cost photovoltaic panel active cooling system. Energies, 12(8), 1448.

BİLEN, K., Bilal, I. Ş. I. K., GEZER, S., & KIYIK, F. (2021). Hava soğutmalı fotovoltaik panellerde kanatçık tipinin soğutmaya etkisinin teorik olarak incelenmesi. Politeknik Dergisi, 1-1.

Brinkworth BJ, Sandberg M. Design procedure for cooling ducts to minimise efficiency loss due to temperature rise in PV arrays. Sol Energy 2006;80: 89e103.

Brinkworth BJ. Optimum depth for PV cooling ducts. Sol Energy 2006;80:

Chandrasekar, M., Suresh, S., & Senthilkumar, T. (2013). Passive cooling of standalone flat PV module with cotton wick structures. Energy Conversion and Management, 71, 43-50.

Ceylan I, Gurelb AE, Demircan H, Aksu B. Cooling of a photovoltaic module with temperature controlled solar collector. Energy Build 2014;72:96e101.

Chandrasekar, M., & Senthilkumar, T. (2015). Experimental demonstration of enhanced solar energy utilization in flat PV (photovoltaic) modules cooled by heat spreaders in conjunction with cotton wick structures. *Energy*, *90*, 1401-1410.

Diallo, T.M.O., Yu, M., Zhou, J., Zhao, X., Shittu, S., Li, G., Ji, J., Hardy, D., 2019. Energy performance analysis of a novel solar PVT loop heat pipe employing a microchannel heat pipe evaporator and a PCM triple heat exchanger. Energy 167, 866–888.

Enaganti, P. K., Nambi, S., Behera, H. K., Dwivedi, P. K., Kundu, S., Imamuddin, M., ... & Goel, S. (2019). Performance analysis of submerged polycrystalline photovoltaic cell in varying water conditions. IEEE Journal of Photovoltaics, 10(2), 531-538.

K.A. S Moharrama, H. Abd-Elhadyb, M.S. Kandila, A.H. El-Sherif, Enhancing the performance of photovoltaic panels by water cooling, Ain Shams Eng. J. 4 (2013) 869–877

Krauter S. Increased electrical yield via water flow over the front of photovoltaic panels. Sol Energy Mater Sol Cells 2004;82:131e7.

Kumar, N. M., Subramaniam, U., Mathew, M., Ajitha, A., & Almakhles, D. J. (2020). Exergy analysis of thin-film solar PV module in ground-mount, floating and submerged installation methods. *Case Studies in Thermal Engineering*, *21*, 100686.

Wang Y, Fang Z, Zhu L, Huang Q, Zhang Y, Zhang Z. The performance of silicon solar cells operated in liquids. Appl Energy 2009;86:1037e42.

Wu S, Xiong C. Passive cooling technology for photovoltaic panels for domestic houses. Int J Low Carbon Technol 2014;9:118e26.

Dwivedi, P., Sudhakar, K., Soni, A., Solomin, E., & Kirpichnikova, I. (2020). Advanced cooling techniques of PV modules: A state of art. Case studies in thermal engineering, 21, 100674.

GEPA: Türkiye güneş enerjisi potansiyel atlası, Erişim linki : https://gepa.enerji.gov.tr/MyCalculator/, Erişim tarihi: 16.02.2023

Ghadikolaei, S. S. C. (2021). Solar photovoltaic cells performance improvement by cooling technology: An overall review. International Journal of Hydrogen Energy, 46(18), 10939-10972.

Grubišić-Čabo, F., Nižetić, S., & Giuseppe Marco, T. (2016). Photovoltaic panels: A review of the cooling techniques. Transactions of FAMENA, 40(SI-1), 63-74.

H. Abdelrahman, M. Wahba, H. Refaey, M. Moawad, N. Berbish, Performance enhancement of photovoltaic cells by changing configuration and using PCM (RT35HC) with nanoparticles Al2O3, Sol. Energy 177 (2019) 665e671.

Hosseinzadeh, M., Sardarabadi, M., Passandideh-Fard, M., 2018. Energy and exergy analysis of nanofluid based photovoltaic thermal system integrated with phase change material. Energy 147, 636–647

Indartono, Y.S., Suwono, A., Pratama, F.Y., 2016. Improving photovoltaics performance by using yellow petroleum jelly as phase change material. Int. J. Low-Carbon Technol. 11 (3), 333–337.

Kandilli, C., 2019. A comparative study on the energetic-exergetic and economical performance of a photovoltaic thermal system (PVT). Res. Eng Struct. Mater. https://doi. org/10.17515/resm2019.90en0117.

Kane, A., Verma, V., & Singh, B. (2017). Optimization of thermoelectric cooling technology for an active cooling of photovoltaic panel. Renewable and Sustainable Energy Reviews, 75, 1295-1305. https://doi.org/10.1016/j.rser.2016.11.114

Kalaiselvan, S., Karthikeyan, V., Rajesh, G., Kumaran, A. S., Ramkiran, B., & Neelamegam, P. (2018, March). Solar PV active and passive cooling technologies-A review. In 2018 International conference on computation of power, energy, information and communication (ICCPEIC) (pp. 166-169). IEEE.

Kazemian, A., Salari, A., Hakkaki-Fard, A., Ma, T., 2019. Numerical investigation and parametric analysis of a photovoltaic thermal system integrated with phase change material. Appl. Energy 238, 734–746.

Kazemian, A., Taheri, A., Sardarabadi, A., Ma, T., Passandideh-Fard, M., & Peng, J. (2020). Energy, exergy and environmental analysis of glazed and unglazed PVT system integrated with phase change material: An experimental approach. Solar Energy, 201, 178-189.

Kerem, A., Mehmet, A. T. İ. K., & Bayram, A. (2020). Fotovoltaik (PV) panel sisteminde yüzey soğutma işleminin elektrik üretimine etkisinin deneysel incelenmesi. International Journal of Engineering Research and Development, 12(2), 565-578.

Khanna, S., Sundaram, S., Reddy, K. S., & Mallick, T. K. (2017). Performance analysis of perovskite and dye-sensitized solar cells under varying operating conditions and comparison with monocrystalline silicon cell. Applied Thermal Engineering, 127, 559-565.

Khanna, S., Reddy, K. S., & Mallick, T. K. (2018, September). Photovoltaic system integrated with phase change material for South West UK climate. In AIP Conference Proceedings (Vol. 2012, No. 1, p. 080007). AIP Publishing LLC.

Klugmann-Radziemska, E., & Wcisło-Kucharek, P. (2017). Photovoltaic module temperature stabilization with the use of phase change materials. Solar Energy, 150, 538-545.

Luo, Z., Huang, Z., Xie, N., Gao, X., Xu, T., Fang, Y., 2017. Numerical and experimental study on temperature control of solar panels with form-stable paraffin/expanded graphite composite PCM. Energy Convers. Manage. 149, 416–423.

Mazón-Hernández, R., García-Cascales, J. R., Vera-García, F., Káiser, A. S., & Zamora, B. (2013). Improving the electrical parameters of a photovoltaic panel by means of an induced or forced air stream. International Journal of Photoenergy, 2013.

Maatallah, T., Zachariah, R., & Al-Amri, F. G. (2019). Exergo-economic analysis of a serpentine flow type water based photovoltaic thermal system with phase change material (PVT-PCM/water). Solar Energy, 193, 195-204.

Madhu, B., Balasubramanian, E., Kabeel, A. E., Sathyamurthy, R., El-Agouz, E. S., & Muthu Manokar, A. (2019). Experimental investigation on the effect of photovoltaic panel partially and fully submerged in water. Heat Transfer—Asian Research, 48(5), 1709-1721.

Maleki, A., Haghighi, A., Assad, M. E. H., Mahariq, I., & Nazari, M. A. (2020). A review on the approaches employed for cooling PV cells. Solar Energy, 209, 170-185.

Nižetić, S., Čoko, D., Yadav, A., & Grubišić-Čabo, F. (2016). Water spray cooling technique applied on a photovoltaic panel: The performance response. Energy conversion and management, 108, 287-296.

Nižetić, S., Giama, E., & Papadopoulos, A. M. (2018). Comprehensive analysis and general economic-environmental evaluation of cooling techniques for photovoltaic panels, Part II: Active cooling techniques. Energy Conversion and Management, 155, 301-323.

Odehand S, Behnia M. Improving photovoltaic module efficiency using water cooling. Heat Transf Eng 2009;30(6):499e505.

Popovici, C. G., Hudişteanu, S. V., Mateescu, T. D., & Cherecheş, N. C. (2016). Efficiency improvement of photovoltaic panels by using air cooled heat sinks. Energy procedia, 85, 425-432.

Rajvikram, M., Leoponraj, S., Ramkumar, S., Akshaya, H., & Dheeraj, A. (2019). Experimental investigation on the abasement of operating temperature in solar photovoltaic panel using PCM and aluminium. Solar Energy, 188, 327-338.

Rezvanpour, M., Borooghani, D., Torabi, F., & Pazoki, M. (2020). Using CaCl2· 6H2O as a phase change material for thermo-regulation and enhancing photovoltaic panels' conversion efficiency: Experimental study and TRNSYS validation. Renewable Energy, 146, 1907-1921.

Rodrigues E., Melicio R., Mendes V. (2011). Simulation of a Solar Cell considering Single-Diode Equivalent Circuit Model, RE&PQJ, 1(9)

Royne A, Dey CJ. Design of a jet impingement cooling device for densely packed PV cells under high concentration. Sol Energy 2007;81:1014e24.

Sardarabadi, M., Passandideh-Fard, M., Maghrebi, M.-J., Ghazikhani, M., 2017. Experimental study of using both ZnO/water nanofluid and phase change material (PCM) in photovoltaic thermal systems. Sol. Energy Mater. Sol. Cells 161. https://doi. org/10.1016/j.solmat.2016.11.032.

Selimefendigil, F., & Şirin, C. (2022). Energy and exergy analysis of a hybrid photovoltaic/thermal-air collector modified with nano-enhanced latent heat thermal energy storage unit. Journal of Energy Storage, 45, 103467.

Sharma, S., Jain, K. K., & Sharma, A. (2015). Solar cells: in research and applications—a review. Materials Sciences and Applications, 6(12), 1145.

Shastry, D. M. C., & Arunachala, U. C. (2020). Thermal management of photovoltaic module with metal matrix embedded PCM. Journal of Energy Storage, 28, 101312.

Siah Chehreh Ghadikolaei, S. (2021). Solar photovoltaic cells performance improvement by cooling technology: An overall review. International Journal of Hydrogen Energy, 46(18), 10939-10972. https://doi.org/10.1016/j.ijhydene.2020.12.164

Siecker, J., Kusakana, K., & Numbi, E. B. (2017). A review of solar photovolta-

ic systems cooling technologies. Renewable and Sustainable Energy Reviews, 79, 192-203.

Sharaf, M., Yousef, M. S., & Huzayyin, A. S. (2022). Review of cooling techniques used to enhance the efficiency of photovoltaic power systems. Environmental Science and Pollution Research, 29(18), 26131-26159.

Slimani, M.E.A., Amirat, M., Kurucz, I., Bahria, S., Hamidat, A., Chaouch, W.B., 2017. A detailed thermal-electrical model of three photovoltaic/thermal (PV/T) hybrid air collectors and photovoltaic (PV) module: Comparative study under Algiers climatic conditions. Energy Convers. Manage. 133, 458–476.

Sopian, K., Yigit, K. S., Liu, H. T., Kakac, S., & Veziroglu, T. N. (1996). Performance analysis of photovoltaic thermal air heaters. Energy Conversion and management, 37(11), 1657-1670.

Solanki CS, Sangani CS, Gunashekar D, Antony G. Enhanced heat dissipation of V-trough PV modules for better performance. Sol Energy Mater Sol Cells 2008;92:1634e8.

Wardowski, T., & Akbarzadeh, A. (1996). Heat pipe-based cooling systems for photovoltaic cells under concentrated sorradiation. Applied Thermal Engineering, 16(1):

Weinstein, R. D., Kopec, T. C., Fleischer, A. S., D'Addio, E., & Bessel, C. A. (2008). The experimental exploration of embedding phase change materials with graphite nanofibers for the thermal management of electronics. Journal of Heat Transfer, 130(4).

Wongwuttanasatian, T., Sarikarin, T., & Suksri, A. J. S. E. (2020). Performance enhancement of a photovoltaic module by passive cooling using phase change material in a finned container heat sink. Solar Energy, 195, 47-53.

Teo, H., Lee, P., & Hawlader, M. (2012). An active cooling system for photovoltaic modules. Applied Energy, 90(1), 309-315. https://doi.org/10.1016/j.apenergy.2011.01.017

Xu, H., Zhang, C., Wang, N., Qu, Z., & Zhang, S. (2020). Experimental study on the performance of a solar photovoltaic/thermal system combined with phase change material. Solar Energy, 198, 202-211.

X. Yang, L. Sun, Y. Yuan, X. Zhao, X. Cao, Experimental investigation on performance comparison of PV/T-PCM system and PV/T system, Renew. Energy 119 (2018) 152e159.

Yao, J., Xu, H., Dai, Y., & Huang, M. (2020). Performance analysis of solar assisted heat pump coupled with build-in PCM heat storage based on PV/T panel. Solar Energy, 197, 279-291.

Zubeer, S. A., Mohammed, H. A., & Ilkan, M. (2017). A review of photovoltaic cells cooling techniques. In E3S web of conferences (Vol. 22, p. 00205). EDP Sciences.

Chapter 7

COMPARISON OF HORN ANTENNA DESIGNS WITH DIFFERENT SHAPES FOR GAIN MEASUREMENT AND CALIBRATION SYSTEMS

Serdal KARAHAN[1]

Ahmet Arif ULUSLU[2]

1 *Assistant Professor, İstanbul Üniversitesi-Cerrahpaşa, ORCID ID: 0000-0001-6534-137, karahan@iuc.edu.tr*

2 *Assistant Professor, İstanbul Üniversitesi-Cerrahpaşa, ORCID ID: 0000-0002-5580-1687, auluslu@iuc.edu.tr*

1- ANTENNAS

An antenna is the device used to transform electromagnetic waves into electrical signals (voltage and current) or electrical signals into electromagnetic waves. In 1888, antennas were used to demonstrate the presence of electromagnetic waves that Heinrich Hertz (1857–1894) and James Clerk Maxwell (1859–1894) had predicted. By positioning a dipole in front of a hertz parabolic reflector, he carried out this experiment. Typically, antennas are made up of one or more conductors. An electromagnetic field is produced when an antenna receives an alternating current from a source on the transmitter side, which causes the antenna to radiate using displacement currents. On the other side, this procedure is reversed in reception antennas. Communication is achieved when these electromagnetic waves cause a current to flow across the antenna surface. Incoming waves are focused on a single point using horn- or parabolic-shaped antennas. A directional antenna is the name for this kind of antenna. An omnidirectional antenna is one that emits or receives electromagnetic radiation equally from places in space that are equally distant from it. Figure 1 shows an illustration of an omnidirectional antenna's radiation pattern in a plane. The majority of antennas in use are directional, meaning that they work better in one direction than another for transmitting or receiving electromagnetic radiation. An illustration of the emission patterns of directional antennas is shown in Figures 1 and 2. The antenna is depicted in the diagrams below as the dot in the center of the circle.

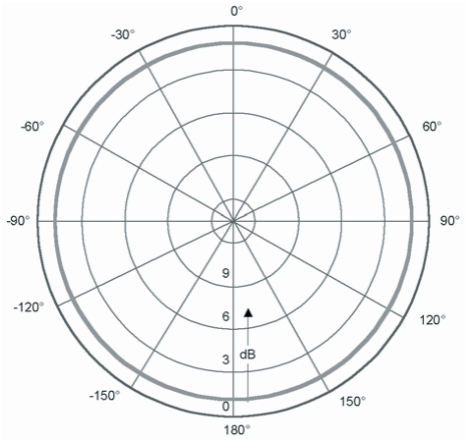

Figure 1 *Non-directional antenna radiation pattern*

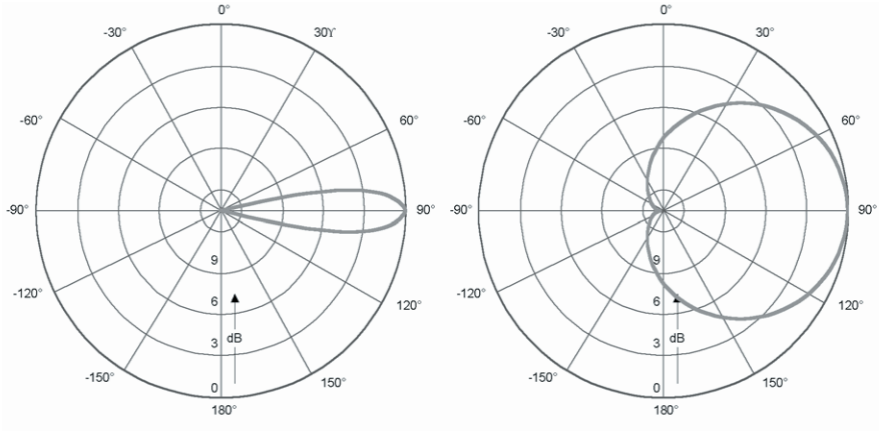

Figure 2 *Directional antenna radiation patterns*

The main function of antennas is to convert between the characteristic impedance of the radio frequency system and the free space impedance. An extremely crucial aspect of antennas is impedance matching of the antenna over the operational frequency band. Return loss (RL) or Voltage standing wave ratio (VSWR) are frequently used to describe the impedance matching quality. Simply put, using these two phrases is equivalent to using two distinct forms to convey the same impedance value.

The ideal scenario is for all power to be radiated back to the antenna without reflection, even if that is not achievable [1-3]. The literature contains studies that are comparable [4-5].

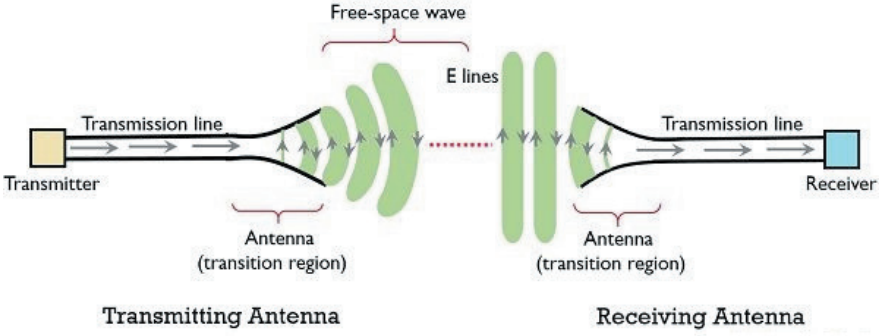

Figure 3 *Receiver and transmit antenna model*

1.1 Radiation Resistance and Efficiency

The antenna's radiant power is the amount of energy it emits as electromagnetic waves into space. Radiative resistance is the difference between the radiant power and the current passing through it that is determined by Ohm's law. The radiation resistor links the antenna's power with the current passing through it. It functions as a virtual resistor.

The losses at the input terminals are taken into consideration using the total antenna efficiency. There are two causes for these losses. The first are the reflections brought on by the transmission line and antenna being incompatible, and the second are the I^2R losses.

1.2 Radiation Pattern

The forms known as radiation patterns demonstrate how much power the antennas radiate in each direction. While the radiation diagram can be in any plane, it typically only addresses patterns that are horizontal or vertical. In directed antennas, the radiation diagram and definitions are as follows:

Main beam: The beam that is directed in the antenna's primary radiation direction.

Side flaps: Flaps that aren't desired around the primary beam

Posterior auricle: Auricle developed near the antenna's base.

Beam: Half power beam width (HPBW) is also the angle between the spots when the main beam's strength decreases to 3 dB.

1.3 Directivity and Antenna Gain

Two crucial factors, antenna gain and directivity, are determined by a specific reference antenna. All directions of radiation from a point source are equal. It is used as a reference and is known as an isotropic source. Antenna directivity is the capacity to radiate power equivalent to the power emitted by the isotropic source in a specific direction. For instance, a dipole antenna's radiation diagram has the form of a torus. In comparison to an isotropic antenna, the short dipole's directivity is 1.5 (1.75 dB), while the half-wave dipole's directivity is 1.64 (2.15 dB).

Directivity and antenna gain are synonymous in lossless antennas. However, with lossy antennas, the gain is determined by the directivity multiplied by the loss ratio (throughput). Analytical calculations can be used to determine the antenna directivity, but only measurements taken in relation to the reference antenna can determine the gain. The active surface is another variable that has a direct bearing on antenna gain. The capacity to transmit energy from electric fields in space to antenna terminals is referred to as an antenna active surface.

1.4 Polarization

The form of the electric field over time and how much radiation it emits in each direction are two definitions of polarization. When an antenna emits electromagnetic waves, the electric field during transmission is referred to as a vertically polarized wave if it is parallel to the ground and

a horizontally polarized wave if it is perpendicular. A structure known as an electromagnetic wave filter has the ability to only pass waves with the desired polarization and not those with the undesirable polarity. Particularly for directional antennas, polarization may frequently be anticipated from antenna structures. Side lobe polarization might be slightly different from main beam polarization. The polarization of radio antennas is determined by the configuration of the component of the antenna that emits the radiation. A vertically positioned omni-WIFI antenna, for instance, will mostly have vertical polarization. The sole exception to this rule is the extended waveguide, which becomes horizontally polarized if it is installed vertically. The majority of the time, the polarization is elliptical, which means that the polarization of the electromagnetic waves radiated from the antenna varies over time. Linear and circular polarization are two examples of exceptional situations. In linear polarization, the antenna makes it such that the electric field propagates in a certain direction, often vertical and horizontal polarization. The antenna continually modifies the electric field in circular polarization at all positions in relation to the ground. Circular polarization is produced by some antennas, including helical antennas. Circular polarization may be achieved, nevertheless, by feeding a linearly polarized antenna with two ports that have identical amplitudes and a 90° phase difference.

1.5 Voltage Standing Wave Ratio (VSWR)

It is the parameter that controls the amount of power that is radiating from the antenna. In a perfect world, all power sent would reach the load and be received by the receiver without any power being lost to radiation. Yet, in reality, this is never possible. The impedance mismatch between the waveguide and the supply causes a reflection. This reflection causes a loss in the power that the antenna will transmit. The highest voltage produced by the returned and sent voltage waves at the antenna input divided by the minimum voltage is known as the VSWR.

1.6 Near and Far Field

The term “near field” refers to the area immediately surrounding an antenna or other radiation source. The electric and magnetic field components do not exhibit plane wave characteristics in the near field. Measurements are challenging due to the complicated relationships in this area. Reactive energy builds up more. It is possible to approximate plane waves in the distant field. In terms of variables like frequency, antenna size, and other considerations, near and far field classifications are based on antenna type and interactions.

2- FREQUENCY BANDS

When categorizing electromagnetic waves using wavelengths as a guide, the microwave expression is employed for wavelengths varying in length between 1 cm and 1 m. When the appropriate frequency matching is determined using the formula for the speed of light, the wavelengths are the range between 300 MHz and 30 GHz. Table 1 provides a detailed illustration of the electromagnetic spectrum's frequency bands [6].

Table 1 *Frequency bands and usage areas*

Frequency Band	Describing	Where used
3 – 30 KHz	Very Low Frequency (VLF)	Directional and sonar (a method of detecting underwater objects with sound waves)
30 – 300 KHz	Low Frequency (LF)	Navigational help, radio navigation, and radio navigation
300 – 3000 KHz	Medium Frequency (MF)	AM radio, marine radio, communications with the Coast Guard, and navigation
3 – 30 MHz	High Frequency (HF)	fax, telephone, and telegraph Shortwave, public band, amateur radio, and global radio transmission
30 – 300 MHz	Very High Frequency (VHF)	Mobile communications include TV, FM broadcast, air traffic control, police, and taxi
300 – 3000 MHz	Ultrahigh Frequency (UHF)	TV, satellite connectivity, radar for monitoring, and a compass
3 – 30 GHz	Superhigh Frequency (SHF)	Satellite communications, land-based communications, microwave connectivity, and aircraft radar
30 – 300 GHz	Extremely High Frequency (EHF)	Experimental uses of radar

3- HORN ANTENNAS

One of the most popular microwave antennas is the horn antenna. The horn antenna, which was invented at the end of the 1800s but lost significance in the early 1900s, saw an upsurge in attention beginning in the 1930s and lasting into the Second World War. Since it resembles a horn, it gets its name from the English word "horn," which means "horn". In astronomy, satellite tracking, and satellite communication, horn antennas are frequently employed. A reflector or lens can also be used to boost the gain even more. The simplicity of production, adaptability, and high gain of a horn antenna are some of the crucial factors to consider. In essence, the mouth opening is separated into four sections by the electric field according to its structure. These structures include pyramids, Conical

Horns, E and H planes. Horn antennas spread by receiving their feed from a waveguide. A waveguide may often also propagate. Nevertheless, impedance mismatch is a serious drawback. Some of the wave is reflected back owing to impedance mismatch if it propagates into empty space without open-circuit termination.

3.1 E-plane Horn Antenna

An aperture antenna can be used to describe horn antennas. By conceptualizing the horn antenna as a radial waveguide, the fields at the horn antenna's mouth opening may be derived [7-8]. Cylindrical *TE* and *TM* wave functions that incorporate Henkel functions can be used to represent the fields in the horn antenna. This technique may be used to locate regions both inside the horn and in the mouth hole of the horn. Above the cutoff frequency, the *TE*10 mode is supported by the fields in the horn antenna's feed waveguide. During the horn's length, the aperture size grows. The lowest operational frequency is provided by *TE*10, the cutoff frequency.

3.2 H-Plane Horn Antenna Design

The magnetic field-plane of this construction is known as a horn antenna if the mouth opening of the rectangular waveguide grows in the direction of the magnetic field after the waveguide, while the other plane remains unchanged.

3.3 Pyramid Horn Antenna

The most common style of horn antenna is the pyramid horn construction. By enlarging the waveguide in both the magnetic and electric field directions, the horn structure is created. Since it makes advantage of the propagation properties of the E-plane and the H-plane together, it is known as a pyramid.

3.4 Conical Horn Antenna

Conical Horn antennas are yet another variety of horn. Conical Horn antennas are supplied in a different way than pyramid horn antennas, in the shape of a circular waveguide. The Conical Horn's radiation fields were originally investigated in [9]. The Conical Horn antenna's modes are specified in terms of Bessel functions and Legendre polynomials in spherical dimensions.

3.5 Customized Horn Antenna Structures

Many research has been conducted on horn antennas to lower overflow efficiency, reduce potential cross-polarization losses, and boost aperture efficiency in large reflectors. In microwave and radiometer applications, symmetrical patterns and high efficiency antennas are essential. While aperture efficiencies of 50 to 60 percent are attained with traditional horn

feeds, it has been shown that corrugated horn structures may achieve 75 to 80 percent efficiency. The diffraction brought on by the edges alters the shape of the posterior lobe area in the antenna pattern. This is particularly valid in areas where the horn's aperture is perpendicular to the electric field. Diffractions have detrimental propagation effects on the main and lateral lobes in addition to the posterior lobes. The horn antenna's walls have cavities carved out of them that provide identical boundary conditions in all polarization circumstances and shape the field distribution in the aperture in both planes. The scattering impact at the borders of the hole will be lessened by establishing the identical boundary conditions on the four walls. This produces a symmetrical pattern with roughly equal beam widths H and E for a square aperture. The walls of the H plane do not have grooves because there is little diffraction at the borders of the aperture in this plane. Another way to arrange the flutes is to create a slotted Conical Horn antenna. Many instances of literature are accessible [10–13].

4- STUDY CASE

In the study, return loss (S_{11}) for 5 different Horn antennas were obtained by simulating 3D radiation images in MATLAB, as well as typical radiation patterns.

4.1. Design Example 1: Horn antenna

Pyramidal Horn antenna with a typical gain of 15 dBi makes up the Horn object. The standard Horn antenna works in the 10 to 18 GHz X-Ku band. The hopper antenna feed is typically a WR-75 rectangular waveguide with a 15 GHz operating frequency. The schematic for the Horn antenna is given in Figure 4. In addition, the details of the design parameters are presented in Table 2. A simple Horn antenna with a center frequency of 15 GHz was designed and the results are shown in Figure 5, Figure 6 and Figure 7. The bandwidth of the designed antenna is between 13.5-17 GHz. A maximum of -30dB was observed in the S_{11} parameter. In addition, the maximum gain was found to be 15.5 dBi.

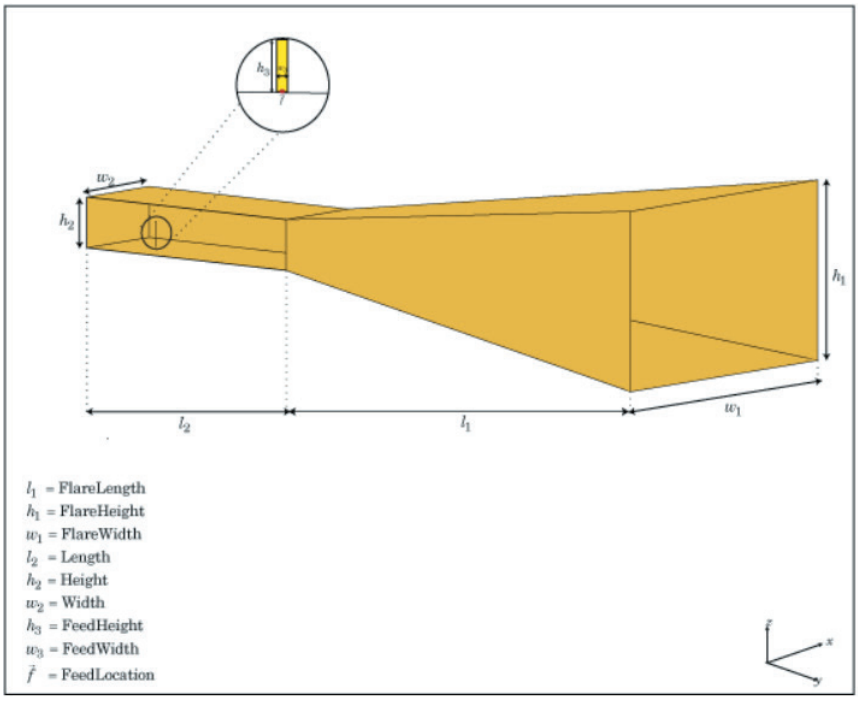

Figure 4 *Horn antenna*

Table 2 *Horn antenna design parameters*

Symbol	Parameter	Definition
FlareLength	Flare length of Horn	The horn's flashing length is given as a scalar in meters.
FlareWidth	Flare width of Horn	The horn's flare width is given as a scalar in meters.
FlareHeight	Flare height of Horn	The horn's glow height is given as a scalar in meters.
Length	Rectangular waveguide length	meter-long rectangular waveguide length represented in scalars.
Width	Rectangular waveguide width	Specified in scalars in meters, the width of a rectangular waveguide.
Height	Rectangular waveguide height	Height of a rectangular waveguide, measured in meters.
FeedHeight	Height of feed	In meters, the feed height is expressed as a scalar.
FeedWidth	Width of feed	In terms of meters, the feed width is provided as a scalar.

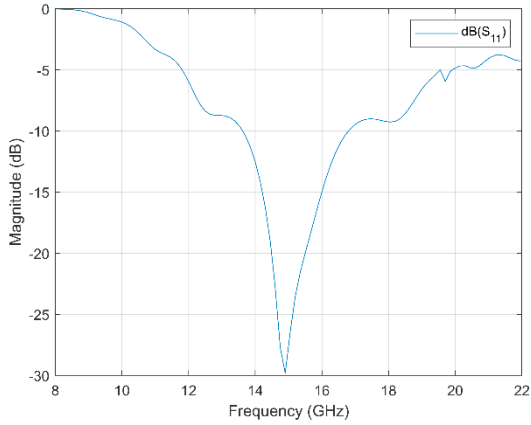

Figure 5 *Horn antenna S_{11} parameter*

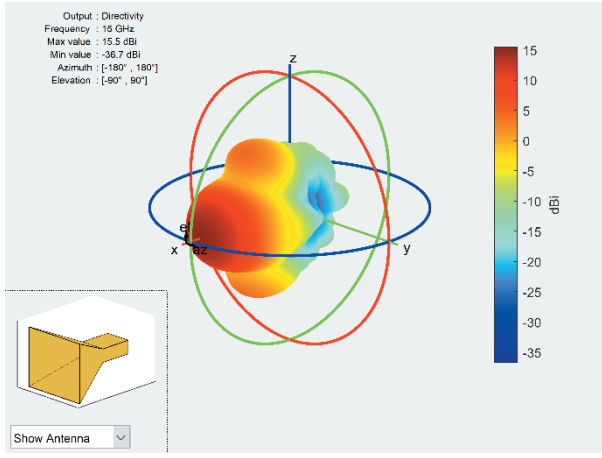

Figure 6 *Horn antenna 3D radiation pattern*

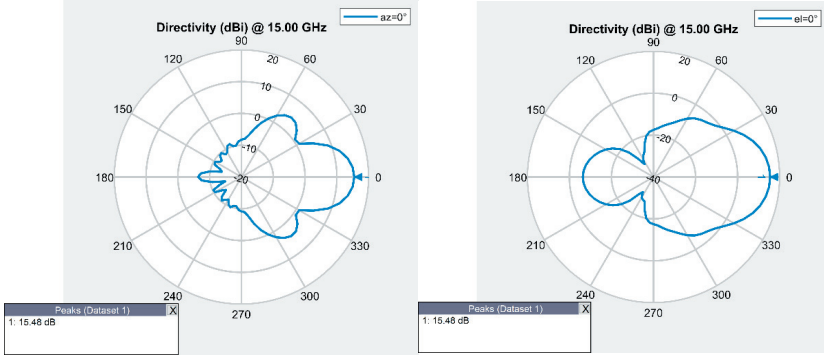

(a) *(b)*

Figure 7 *Horn antenna typical radiation pattern a) azimuth, b) elevation*

4.2. Design Example 2: Conical Horn antenna

To focus the radio waves into a beam, it forms a cone-shaped waveguide in this instance. A lot of huge radio astronomy observatories, satellite tracking devices, and communication dishes employ this type of horn as a feed element. Figure 8 shows the schematic for the Conical Horn antenna. Table 3 also includes information on the design parameters in detail. The results of designing a straightforward Conical Horn antenna with a core frequency of 15 GHz are depicted in Figures 9, 10, and 11. The planned antenna's bandwidth ranges from 13.3 to 17.6 GHz. The S_{11} parameter reached a high of -23dB. Moreover, 14.6 dBi was shown to be the maximum gain.

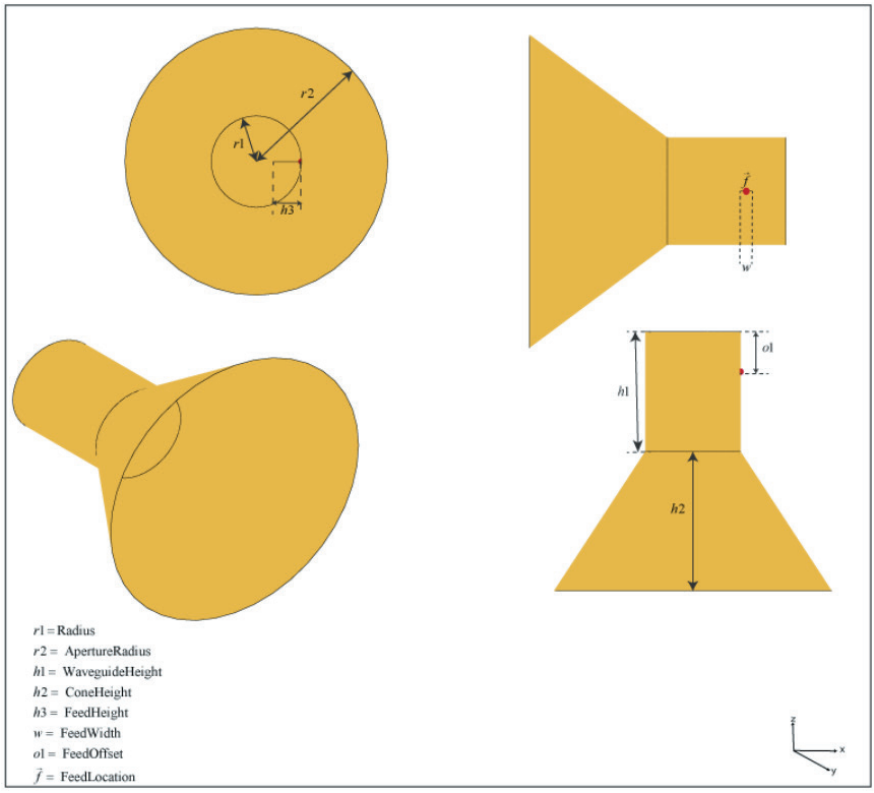

Figure 8 *Conical Horn antenna*

Table 3 *Conical Horn antenna design parameters*

Symbol	Parameter	Definition
Radius	Radius of waveguide	The waveguide's radius, expressed as a real-valued scalar in meters.
WaveguideHeight	Height of waveguide	a real-valued scalar representing the waveguide's height in meters.
FeedHeight	Height of feed	a real-valued scalar representing the height of the feed in meters.

FeedWidth	Width of feed	The feed's breadth, measured in meters, given as a real-valued scalar.
FeedOffset	Signed distance along y-axis	Real-valued scalars representing marked lengths along the y-axis expressed in meters.
ConeHeight	Height of cone	a real-valued scalar representing the cone's height in meters.
ApertureRadius	Radius of cone aperture	the real-valued scalar radius of the cone aperture, expressed in meters.

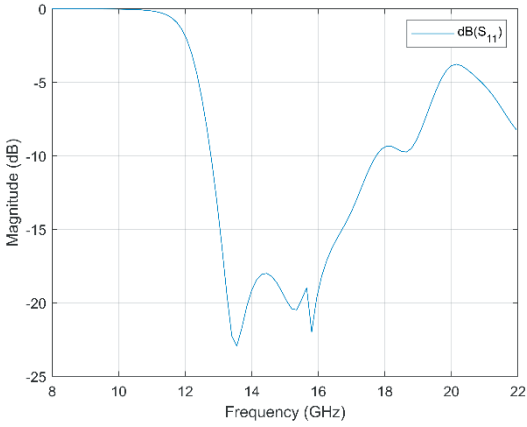

Figure 9 *Conical Horn antenna S_{11} parameter*

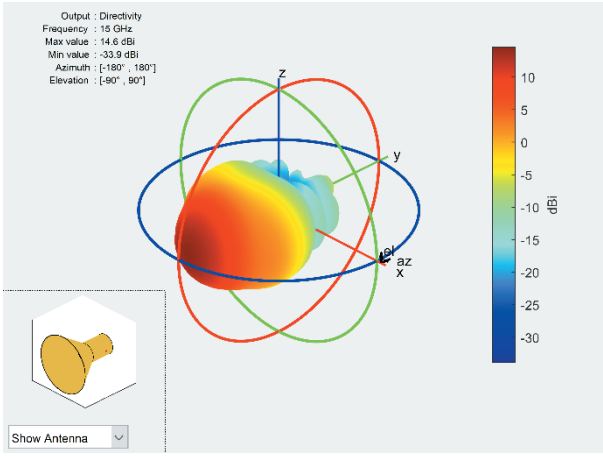

Figure 10 *Conical Horn antenna 3D radiation pattern*

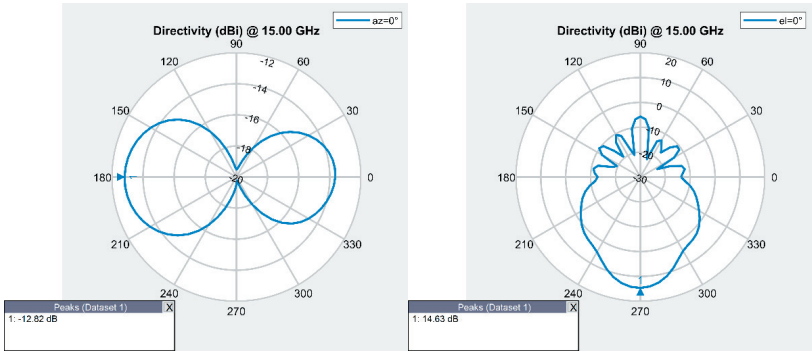

(a) *(b)*

Figure 11 *Conical Horn antenna typical radiation pattern a) azimuth, b) elevation*

4.3. Design Example 3: Conical Corrugated-Horn antenna

With grooves covering the interior surface of the cone, it creates a Conical Corrugated-Horn antenna in this situation. Because to their smaller side lobes and low cross-polarization level, these antennas are frequently employed as feed horns for dish reflector antennas. The schematic for the Conical Corrugated-Horn antenna is given in Figure 12. In addition, the details of the design parameters are presented in Table 4. A simple Conical Corrugated-Horn antenna with a center frequency of 15 GHz was designed and the results are shown in Figure 13, Figure 14 and Figure 15. The bandwidth of the designed antenna is between 14.2-15.1 GHz. A maximum of -13.8dB was observed in the S_{11} parameter. In addition, the maximum gain was found to be 17.8 dBi.

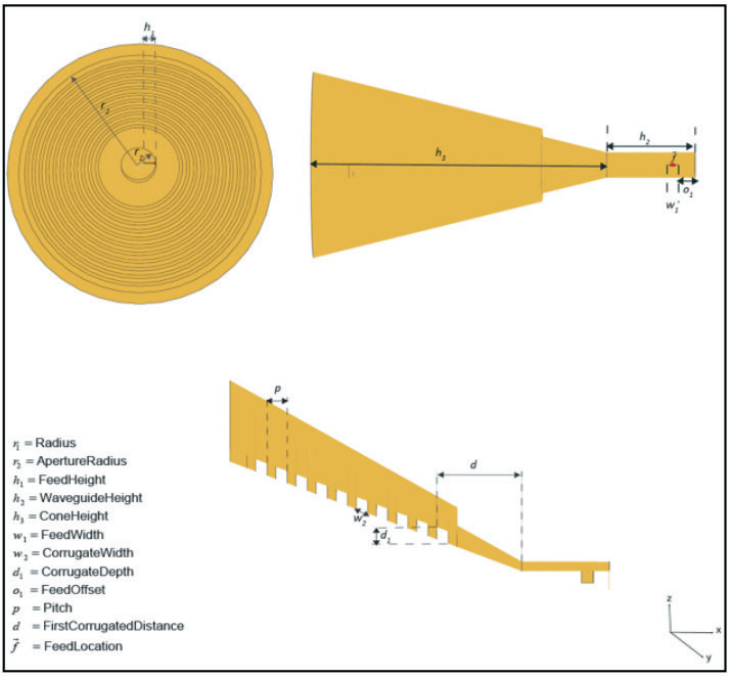

Figure 12 *Conical Corrugated-Horn antenna*

Table 4 *Conical Corrugated-Horn antenna design parameters*

Symbol	Parameter	Definition
Radius	Radius of waveguide	The waveguide's radius, expressed as a real-valued scalar in meters.
WaveguideHeight	Height of waveguide	a real-valued scalar representing the waveguide's height in meters.
FeedHeight	Height of feed	a real-valued scalar representing the height of the feed in meters.
FeedWidth	Width of feed	The feed's breadth, measured in meters, given as a real-valued scalar.
FeedOffset	Signed distance along y-axis	Y-axis feed sign distance, expressed as a real-valued scalar in meters.
ConeHeight	Height of cone	a real-valued scalar representing the cone's height in meters.
ApertureRadius	Radius of cone aperture	the real-valued scalar radius of the cone aperture, expressed in meters.
Pitch	Distance between two successive corrugations	The separation in meters between two adjacent grooves, expressed as a real-valued scalar.
FirstCorrugatedDistance	Distance of first corrugation from waveguide	The initial wave's separation from the waveguide, measured in meters using a real-valued scalar.
CorrugateWidth	Corrugation width	the real-valued scalar parameter representing the undulation breadth in meters.
CorrugateDepth	Corrugation depth	Specified as a real-valued scalar in meters, the depth of the groove.

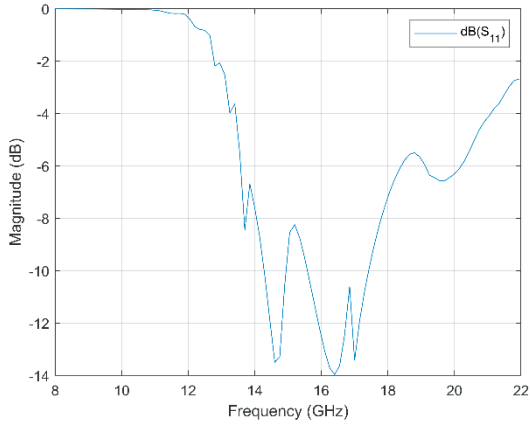

Figure 13 *Conical Corrugated-Horn antenna S_{11} parameter*

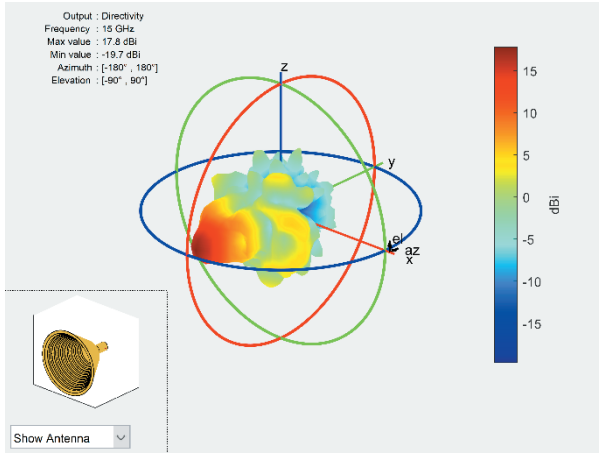

Figure 14 *Conical Corrugated-Horn antenna 3D radiation pattern*

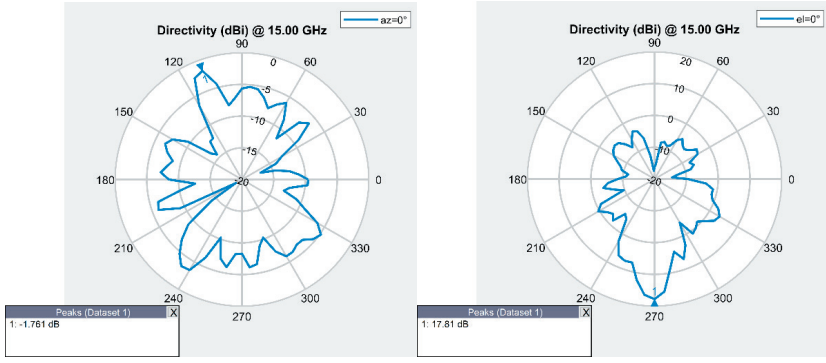

(a) *(b)*

Figure 15 *Typical radiation pattern of Conical Corrugated-Horn antenna a) azimuth, b) elevation*

4.4. Design Example 4: Rectangular Corrugated-Horn antenna

In this instance, a Rectangular Corrugated-Horn antenna with grooves on the flare's inner sides is created. These antennas are frequently employed in broadcast communications as a feed for reflector antennas because to their decreased spread, beam symmetry, and low side lobe level. Figure 16 shows the schematic for a Rectangular Corrugated-Horn antenna. Table 5 also includes information on the design parameters in detail. The results of designing a straightforward Conical Corrugated-Horn antenna with a central frequency of 15 GHz are depicted in Figures 17, 18, and 19. The planned antenna has a bandwidth of 14.5–15.5 GHz. The S_{11} parameter reached a high of -17dB. Moreover, 11.6 dBi was shown to be the maximum gain.

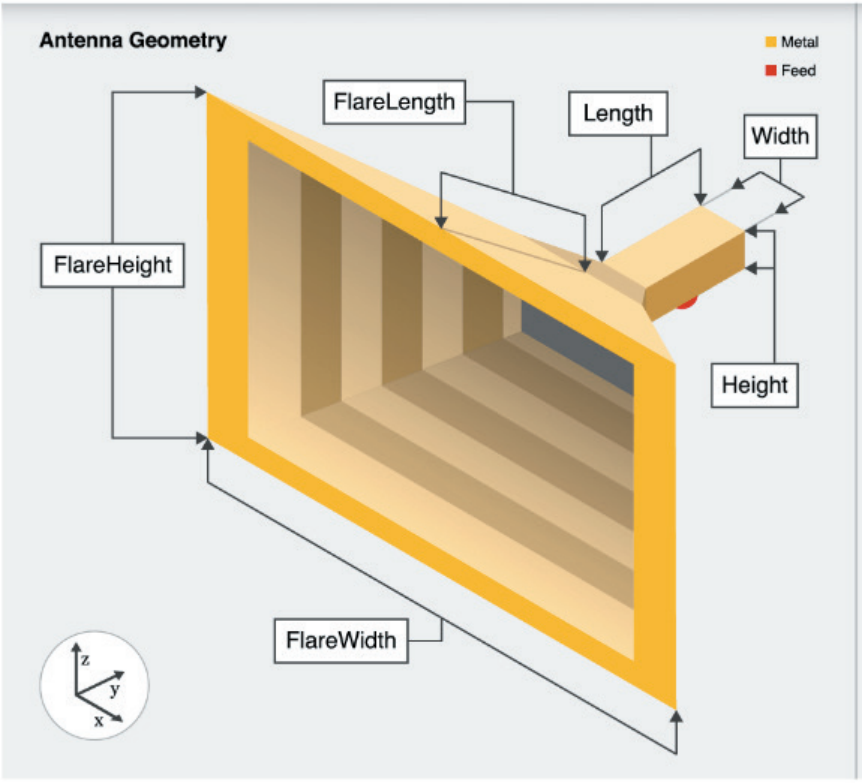

Figure 16 *Rectangular Corrugated-Horn antenna*

Table 5 *Rectangular Corrugated-Horn antenna design parameters*

Symbol	Parameter	Definition
FlareLength	Flare length of horn	The horn's flare length is given as a positive scalar in meters.
FlareWidth	Flare width of horn	The horn's flare width is given as a positive scalar in meters.
FlareHeight	Flare height of horn	The horn's flare height is given as a positive scalar in meters.
Length	Length of rectangular waveguide	a positive scalar representing the rectangular waveguide's length in meters.
Width	Width of rectangular waveguide	The positive scalar width of the rectangular waveguide, measured in meters.
Height	Height of rectangular waveguide	the positive scalar height of the rectangular waveguide stated in meters.

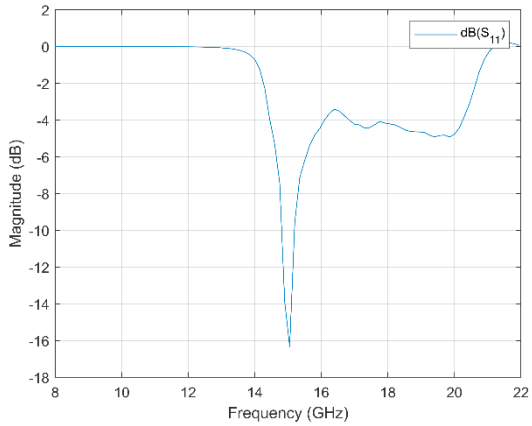

Figure 17 *Rectangular Corrugated-Horn antenna S_{11} parameter*

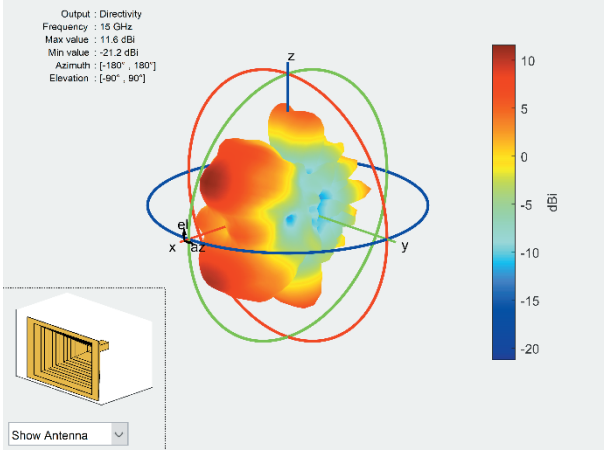

Figure 18 *Rectangular Corrugated-Horn antenna 3D radiation pattern*

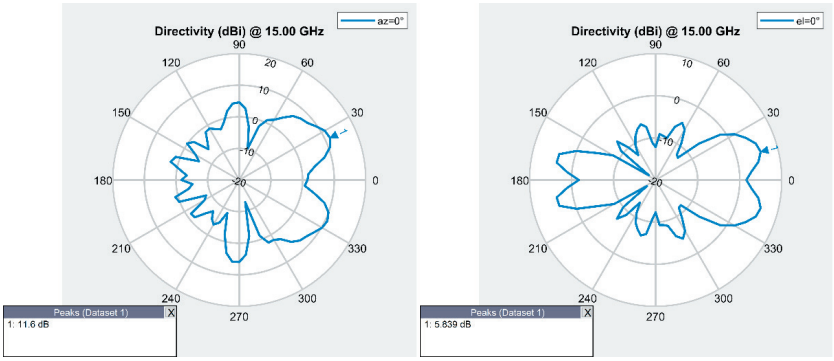

(a) *(b)*

Figure 19 *Typical radiation pattern of Rectangular Slot Horn antenna a) azimuth, b) elevation*

4.5. Design Example 5: Potter Horn

A discontinuous dual-mode Conical Horn antenna is the Potter Horn antenna. When low cross polarization, low side lobe, and beam symmetry are necessary, these antennas are employed in wireless applications. For frequency reuse, Potter Horns are commonly utilized in satellite communications. The schematic for the Potter Horn antenna is given in Figure 20. In addition, the details of the design parameters are presented in Table 6. A simple Conical Corrugated-Horn antenna with a center frequency of 15 GHz was designed and the results are shown in Figure 21, Figure 22 and Figure 23. The bandwidth of the designed antenna is between 14.2-16.6 GHz. A maximum of -15.8dB was observed in the S_{11} parameter. In addition, the maximum gain was found to be 11.9 dBi.

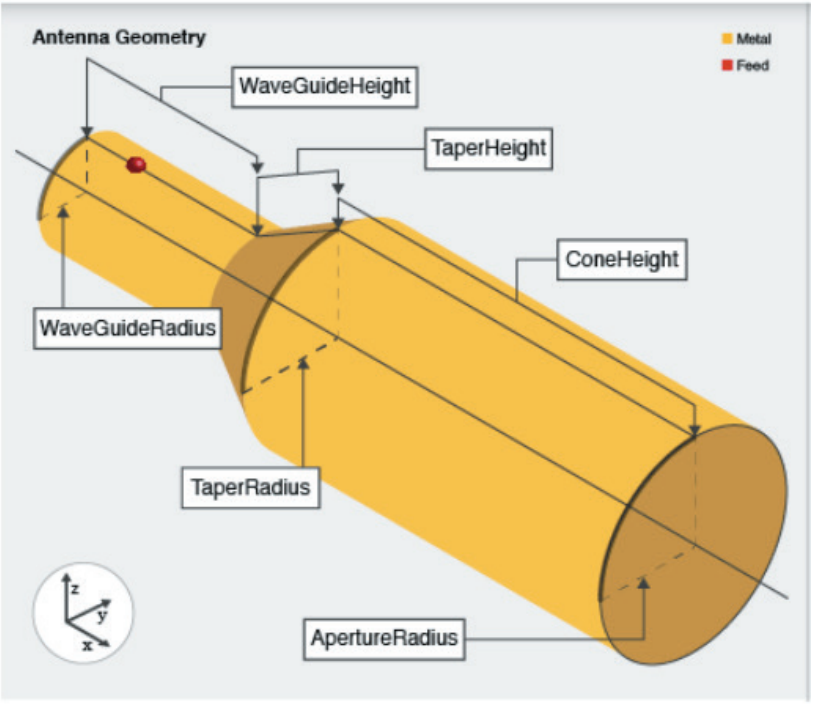

Figure 20 *Potter Horn antenna*

Table 6 *Potter Horn antenna design parameters*

Symbol	Parameter	Definition
Radius	Radius of circular waveguide	The positive scalar representation of the circular waveguide's radius in meters.
WaveguideHeight	Height of circular waveguide	the positive scalar height of the circular waveguide, measured in meters.
FeedHeight	Height of feed	The feed's height, given as a positive scalar, in meters.
FeedWidth	Width of feed	The feed's breadth is expressly set in meters.
FeedOffset	Signed distance along waveguide height	the real-valued scalar measurement of the indicated distance along the waveguide height in meters.
ConeHeight	Height of cone	a positive scalar representing the cone's height in meters.
ApertureRadius	Radius of cone aperture	The cone aperture's radius is given as a positive scalar in meters.
TaperRadius	Radius of taper	the positive scalar radius of the taper, measured in meters.
TaperHeight	Height of taper	The non-negative scalar representation of the taper's height in meters. To create a cascaded Potter Horn antenna, set TaperHeight to 0.

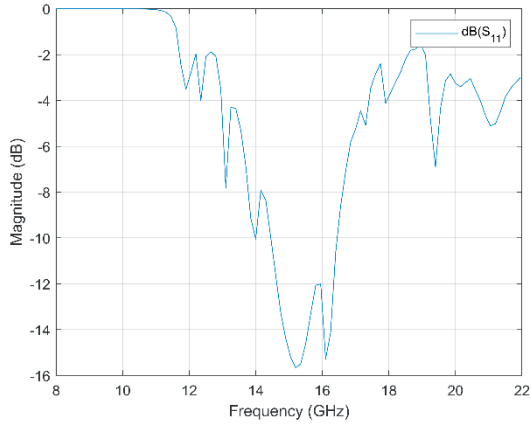

Figure 21 *Potter Horn antenna S_{11} parameter*

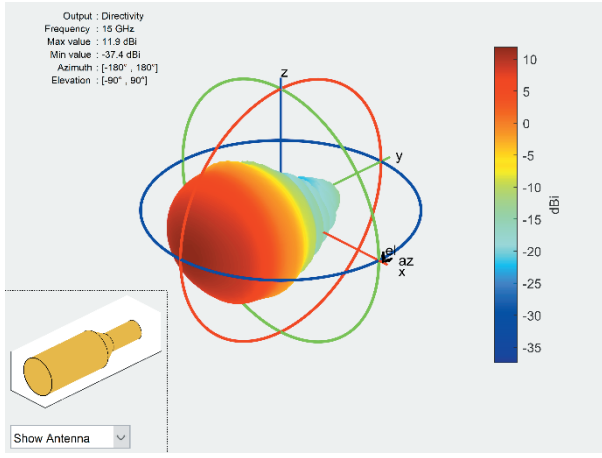

Figure 22 *Potter Horn antenna 3D radiation pattern*

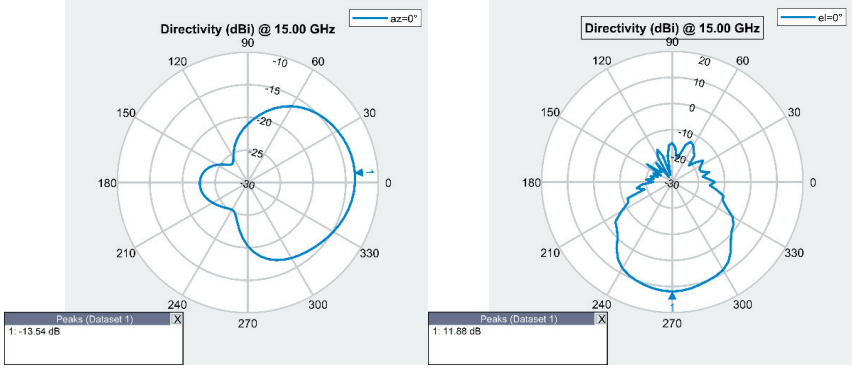

(a) *(b)*

Figure 23 *Typical radiation pattern of the Potter Horn antenna a) azimuth, b) elevation*

5- CONCLUSION

By looking at the data obtained from the study, changing the shape for horn antenna types affects the bandwidth and gain, especially the working band. If we compare the results of the study, the bandwidth of standard Horn antenna and Conical Horn antenna is wider than the others. The narrowest bandwidth was obtained for the Conical Corrugated-Horn antenna. A medium bandwidth was obtained in the Potter Horn antenna compared to other models. As it is known, return loss -10 dB and below is a valid value. Again, the lowest results were found for the S_{11} Horn antenna model. In addition, the largest S_{11} was obtained for the Rectangular Corrugated-Horn antenna. The highest gain was found for the Conical Corrugated-Horn antenna model. The lowest gain values were obtained for Rectangular Corrugated-Horn antenna and Potter Horn antenna models. In the light of all this information, if wide bandwidth is desired, the standard Horn antenna can be preferred. Conical Corrugated-Horn antenna model can be used for high gain and narrow bandwidth, Rectangular Corrugated-Horn antenna model can be used for low gain and narrow bandwidth. From this work, we can conclude what kind of results the Horn antenna models can give for the determined band.

REFERENCES

[1] C. A. Balanis, Antenna Theory –Jhon Wiley & Sons. Inc., 2005.

[2] Aysu Belen, Peyman Mahouti, Filiz Güneş, and Özlem Tari, "Gain Enhancement of a Traditional Horn Antenna using 3D Printed Square-Shaped Multi-layer Dielectric Lens for X-band Applications", ACES Journal, vol. 36, no. 2, ss. 132–138, Feb. 2021.

[3] Alper Çalışkan, "Geniş bantlı tem ve ridged horn anten dizisi tasarımı" Yıldız Teknik Üniversitesi, 2014.

[4] N. Keskin, S. Aksimsek, and N. Turker Tokan, "Wide-band gain enhancement of a pyramidal horn antenna with a 3D-printed epsilon-positive and epsilon-near-zero metamaterial lens," International Journal of Microwave and Wireless Technologies, vol. 13, no. 10, ss. 1015–1023, 2021.

[5] N. B. Alpaydın, P. Mahouti, F. Güneş "Design of Dielectric Lens Loaded Horn Antenna for Radar Applications" 1st International Conference on Innovations in Natural Science and Engineering, 3-6 Jan. 2018, Turkish Republic of Northern Cyprus.

[6] Johnson, R. C., Antenna Engineering Handbook, McGraw-Hill, Inc., New York, 1993

[7] R. F. Harrington, Time-Harmonic Electromagnetic Fields, McGraw-Hill, New York, 1961, ss. 208–213.

[8] C. A. Balanis Advanced Engineering Electromagnetics, John Wiley and Sons, New York, 1989.

[9] M. G. Schorr and F. J. Beck, Jr., "Electromagnetic Field of a Conical Horn," J. Appl. Phys., Böl. 21, ss. 795–801, Ağustos 1950.

[10] G. Kim, S. Kim, "Design and analysis of dual polarized broadband microstrip patch antenna for 5g mmwave antenna module on fr4 substrate," *IEEE Access*, vol. 9, pp. 64 306–64 316, 2021.

[11] P. Mahouti, M. A. Belen, N. Çalık, S. Koziel, "Computationally efficient surrogate-assisted design of pyramidal-shaped 3d reflectarray antennas," *IEEE Transactions on Antennas and Propagation*, 2022.

[12] Mallahzadeh, A.R., ve Karshenas, F., (2009). "Modified TEM Horn Antenna for Broadband Applications", Progress In Electromagnetics Research, PIER 90

[13] Scheers, B., Acheroy, M., ve Vorst, A.V., (2000). "Time-domain simulation and characterization of TEM horns using a normalized impulse response", IEE Proc. Microwave Antennas Propagation, 147:6:463-468.

Chapter 8

INVESTIGATION OF GROUND REACTION FORCES AND MOMENTS AFFECTING JOINTS OF FULL SCI AND HEALTHY INDIVIDUALS USING ANYBODY MUSCULOSKELETAL MODELING PROGRAM

Uğur FIDAN[1], İsmail ÇALIKUŞU[2]

1 Afyon Kocatepe University, Department of Biomedical Engineering, Afyon, Turkey (ORCID ID: 0000-0003- 0356-017X)
2 Nevsehir Hacıbektaş Veli Üniversitesi, Meslek Yüksek Okulu, Biyomedikal Cihaz Teknolojisi ,Nevşehir, Türkiye (ORCID: 0000-0002-6640-7917)

1. INTRODUCTION

Every year, more than 500,000 people suffer from various injuries, traffic accidents, etc., and are exposed to spinal cord injury (SCI) for reasons (Anjum et al., 2020). SCI is caused by disruption of neural transmission in the neural structure of the spinal cord, such as the medulla, medullary cone, and cauda equina (Yang et al., 2022). The disruption of this conduction may be due to mechanical impact, laseration, compression, transection, infection, or spinal cord degeneration (Yang et al., 2021). SCI is expressed in two ways as completed and incomplete SCI. In incomplete SCI patients, a weak EMG signal is obtained below the spinal cord injury area (Anderson et al., 2018). However, in patients with completed SCI, EMG signals are not observed below the spinal cord injury area, which causes deterioration in muscle and motor function functions. Impairment in these functions increases intestinal, urinary, musculoskeletal, neuronal, and cardiological disorders (Ong et al., 2020). Movement rescheduling is vital for these patients to restore functional independence and quality of life. Recently, robotic exoskeletons have been used to improve the quality of SCI patients in their daily lives and life functions. Gait training with these devices is seen to improve cardiorespiratory, urinary, musculoskeletal, neuronal, and somatosensory systems (Pinto et al., 2020).

Studies in the literature are AnyBody, OpenSim, etc. shows that musculoskeletal modeling programs are used in exoskeleton designs, which is a complex and difficult process. These modeling programs allow to examine the effects of realized designs on human muscles and joints. According to the findings obtained as a result of the examination, the most suitable exoskeleton systems for human ergonomics can be developed (Kim et al., 2018). When studies on this subject in the literature are examined, it is seen that the effects of the exoskeleton on muscle, joint, and ground reaction force are examined. For example, Ferrari et al. analysed the effects of the exoskeleton they designed with the OpenSim programs on the slow gait cycle. As a result of the analysis, it was observed that more time was spent in the double support phase of gait than in normal gait. (Ferrari et al., 2008). Zhu et al., on the other hand, used these programs to model the lower-extremity-powered exoskeleton (LEPE) and to measure the joint alignment between humans and LEPE [5]. In 2018, Fournier combined the ARKE lower extremity robot developed by Bionik Laboratories Inc. with the musculoskeletal system in the AnyBody programme. In this study, which does not include muscle activities and joint mechanics, the ground reaction forces that occur when the robot is operated at different speeds are examined. From the simulation results obtained, it has been proven that the lower gait of the exoskeleton creates a lower ground reaction force (Fournier et al., 2018). In 2020, Smith et al. analysed the effect of gait with

a lower exoskeleton and crutches on the upper extremity arm muscles and joints of a patient with SCI. As a result of the study, the use of crutches strains the elbow and shoulder muscles, posing a risk (Smith et al., 2020).

In this study, we explain how the exoskeleton designed in the Solidworks environment is transferred to the Anybody programme and how it is integrated into the whole body human model. The exoskeleton integrated into the body model was adapted to the gait of a normal and completed SCI person, and joint reaction force, moment, and ground reaction forces were analysed during this time.

2. MATERIAL AND METHODS

The human is the only creature that can stand and move with two legs. The gait cycle is the whole of the movements made to complete the movement of the heel of one foot to the ground for the first time to ensure the forward movement of the trunk and the movement of the same heel to the ground for the second time and to ensure that this process is continuous (Yavuzer, 2014). The gait cycle (Figure 1) takes place in two phases, the stance phase and the swing phase. As can be seen in Figure 1, the situation where the two feet touch the ground is called the double support phase, the situation where only the right foot touches is called the single stance phase and the situation where only the left foot touches is called the swing phase (Dugan & Bhat, 2005).

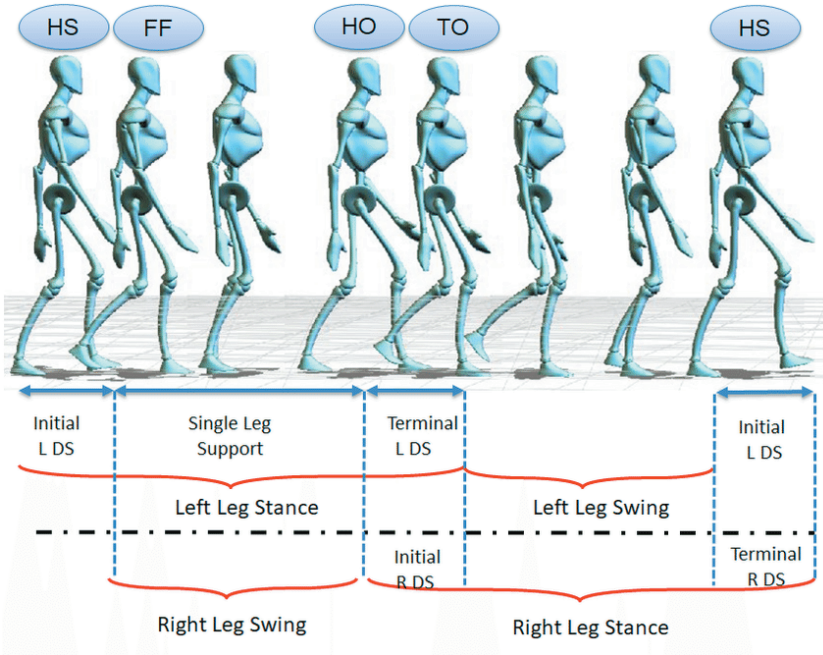

Figure 1. Human Gait Cycle Phases (Chalvatzaki et al., 2018).

2.1. Lower Extremity Exoskeleton Model

The lower extremity exoskeleton model consists of 3 parts in each leg as thigh, calf, and foot, and 7 parts in total, including the hip. Each part has 6 degrees of freedom. Carbon fibre from the Zoltex Panel was used in the construction of the exoskeleton. This material is inexpensive and offers high power-to-weight performance. Zoltex Panel carbon fiber has been chosen as one of the best solutions for an exoskeleton to be designed for SCI patients with its high performance, high strength, low weight, high stiffness, corrosion resistance, heat resistance (Hussain et al., 2021). The lower limb exoskeleton designed in the SolidWorks programme is shown in Figure 2.

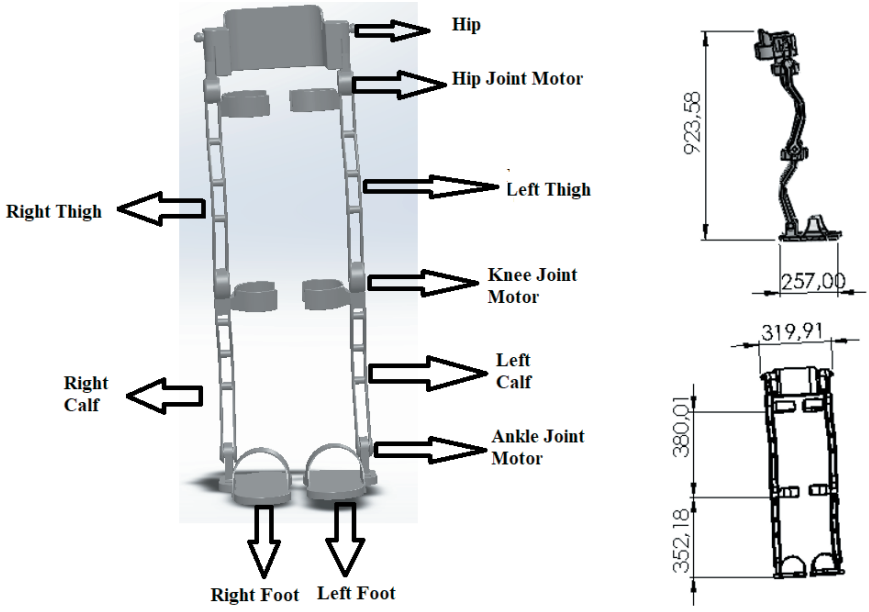

Figure 2. Lower limb exoskeleton designed with Zoltex Panel 33 material.

2.2 AnyBody Musculoskeletal Modelling Program

AnyBody musculoskeletal modeling program is a software developed by Denmark's Aalborg University to examine joint, muscle, ground reaction forces and moments and contact forces. The full human body model used in this program is derived from real cadaver studies. The loads falling on the joints and muscles can be simulated similar to the real human body. This programme has the feature of adjusting the desired height, weight and body parts (Rasmussen, 2019).

2.2.1. Human Musculoskeletal Model

The human musculoskeletal model was created using the full body model, which is a combination of lower extremity, upper extremity, head and body segments stored in AnyBody Managed Model Repository (AMMR) v.1.6.3. The model consists of 16 joints,804 muscleas and 25 parts. There are 140 and 159 muscles in each arm and leg, respectively, while there are 206 muscles in the trunk and head (Engelhardt et al., 2020). The programme can model the neck, sternoclavicular, glenohumeral, elbow, wrist, pelvis-thorax, hip, knee, and ankle joints (Trinler et al., 2019). In this study, the model in Figure 3, which has the anthropometric characteristics of a muscular person with a height of 1.75 cm and a weight of 75 kg, was used.

Figure 3. Human Musculoskeletal Model

In order to obtain the completed SCI human model (Figure 4), the muscles in the lower extremity were canceled in the AnyBody program, and she was allowed to walk with exoskeleton control (Smith, 2019). The effects of gait with an exoskeleton in SCI patients were analysed using the AnyBody program by analysing joint reaction forces, joint reaction moments, ground reaction forces and moments obtained from the SCI human model conducted over two gait cycles.

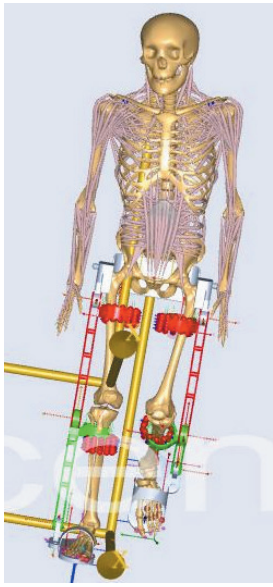

Figure 4. Full SCI human model

2.2.2 Joint reaction force and Moment

Muscles produce force and moment between joints during gait motion. In this study, 12 joint reaction forces and 6 joint reaction moments, which are effective in the hip, knee, and ankle, were determined in the gait cycle. The joint reaction forces and moments discussed in this study are as in Table 1.

Table 1

Joint reaction forces and Moments Calculated Using AnyBody Modeling System.

Joint Reaction Forces				**Joint Reaction Moments**	
Ankle Antero Posterior Force	Ankle ProximoDistal Force	Knee Lateral Joint Moment Force	Hip Antero Posterior Force	Ankle Plantar Flexion Joint Moment	Hip Abduction Joint Moment
Ankle Axial Moment Joint Force	Knee Antero Posterior Force	Knee Medio Lateral Joint Force	Hip Medio Lateral Joint Force	SubTalar Joint Eversion Moment	Hip External Rotation Joint Moment
Ankle Medio Lateral Joint Force	Knee Axial Moment Joint Force	Knee ProximoDistal Force	Hip ProximoDistal Force	Knee Flexion Joint Moment	Hip Flexion Joint Moment

2.3 Integration of Exoskeleton Design into AnyBody Program and Kinematic Analysis

Figure 5 shows what needs to be done to analyse the reaction forces and moments in the joints of SCI and healthy people during gait with exoskeletons. First of all, the exoskeleton design should be done in Solidworks 2016. The designed 3D CAD model is converted to Anyscript program file with AnyExp4Solidworks program patch. The hip, knee, and

ankle joint angles of the person gait on the RoboGait were obtained using the Kinovea Image processing programme and transferred to the AnyBody programme. In addition, whether there is a right angle or not, the whole body human model was added to the AnyBody program in the RoboGait program and the standing human model was first executed by entering the joint angles without exoskeleton. After the normal gait procedure was performed, the exoskeleton was allowed to walk with the same angles. After enabling the exoskeleton and the human model to walk, the human musculoskeletal model and the exoskeleton were integrated by adding contact points. Then, the whole human body model was run together with the exoskeleton. To simulate a patient with SCI, the lower extremity were excluded from the model. Then the joint reaction force, moment, and ground reaction force of SCI and a healthy person were compared.

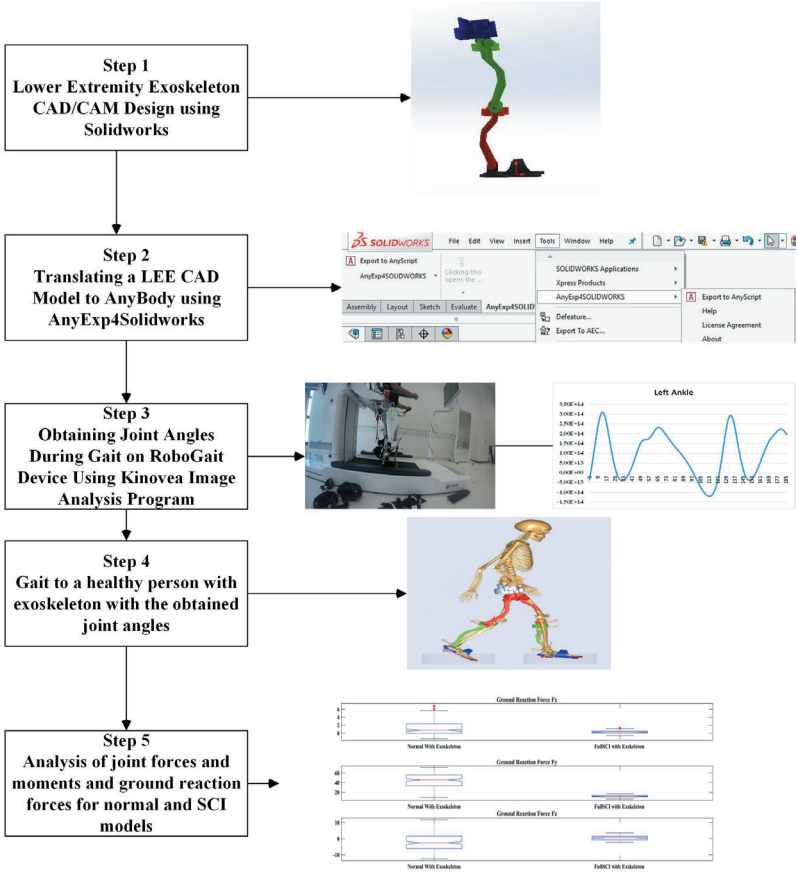

Figure 5. Integration of exoskeleton design into AnyBody Program and kinetic analysis.

3. RESULTS

In this study, a healthy human model and a full SCI human model with no lower extremity muscles were performed over two gait cycles. Joint reaction forces, joint reaction moments, ground reaction moments and ground reaction forces on healthy and SCI human muscle models during gait were investigated. In the study, a total of 12 joint reaction forces, including ankle, knee, and hip, were obtained by performing RoboGait Gait Orthosis with the angles obtained during 2 gait cycles. Joint reaction forces obtained for normal and SCI patients were compared with the plotbox as in Figure 6.

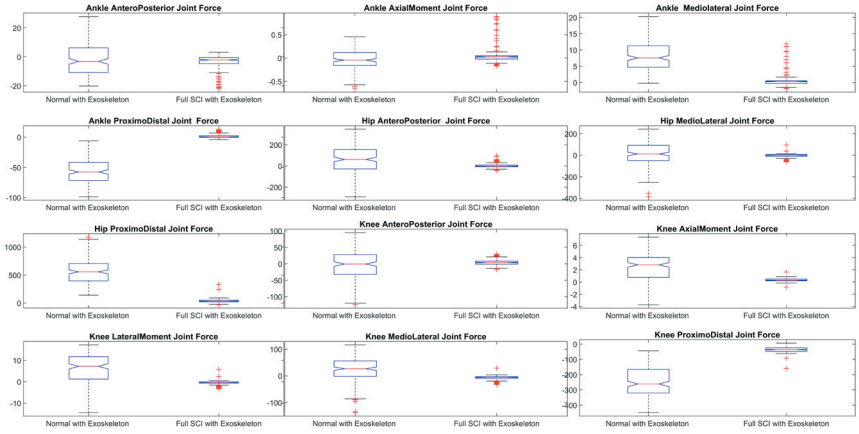

Figure 6. Joint reaction forces obtained during exokeleton gait of the normal and SCI model.

When the joint reaction forces of a normal person and a person with SCI were examined while gait with an exoskeleton, it was seen that normal human muscles exert an extra force on the joints. Therefore, the joint reaction forces of patients with SCI are lower than those of normal people. The highest joint reaction force was observed in the hip (proximo distal), while the lowest joint reaction force was observed in the axial moment force in the ankle. This shows that the force on the joints decreases from the trunk to the feet.

After examining the joint reaction forces, a total of 6 joint reaction moments (Figure 7) were obtained from the Model in AnyBody for Normal and SCI patients, three in the hip, one in the knee and two in the ankle.

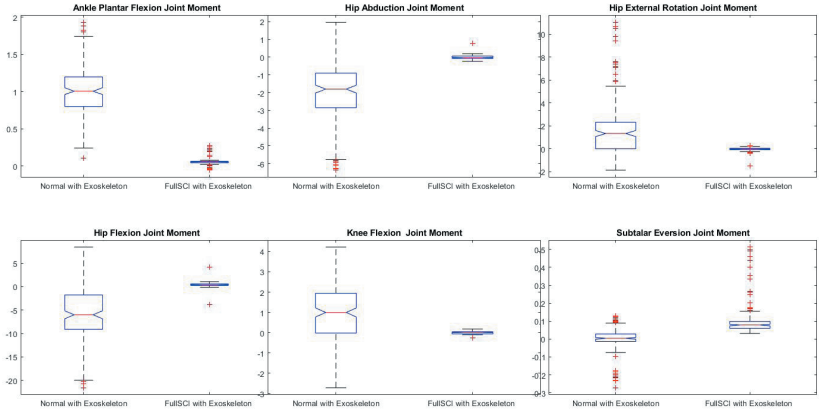

Figure 7. Joint reaction moments obtained during gait with the exoskeleton of the Normal and Full SCI model.

When the joint reaction moments in Figure 6 are examined, the joint moment force in all joints of the hip, knee, and ankle decreased except the eversion joint moment in the subtalar joint of the ankle. The reason for the increase in the subtalar eversion joint moment is that the exoskeleton creates an opposing force to the joint. After examining the joint forces and moments, the ground reaction force and moment, which are other factors affecting movement, are discussed. Here, ground reaction forces and moments in the x, y, and z directions in the coordinate system are discussed. The ground reaction forces were obtained for each of the three axes, as seen in Figure 8, by running the full SCI human model exoskeleton, with all muscles in the normal and lower extremities canceled, in the AnyBody program for two cycles.

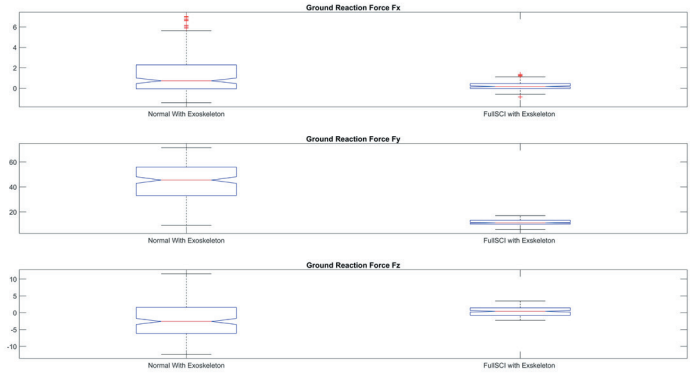

Figure 8. Ground reaction forces obtained for three different axes

When the ground reaction forces and moments are examined, it is seen that cancelling the muscles reduces the ground reaction force and moment. After examining the ground reaction forces, the ground reaction moments were obtained as in Figure 9 for two gait cycles.

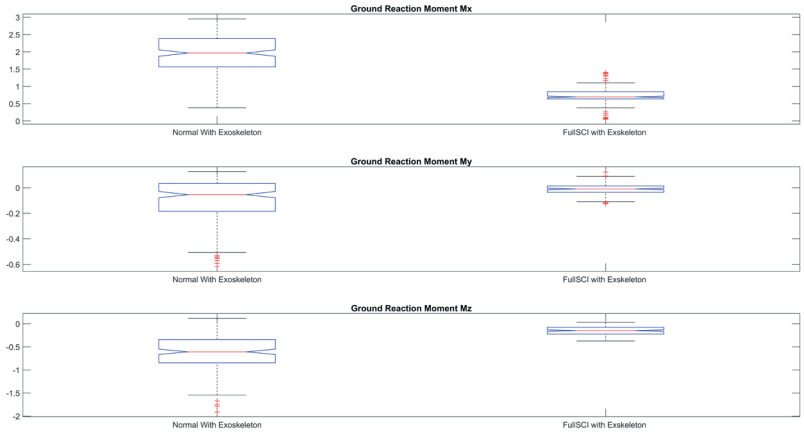

Figure 9. Ground reaction moments obtained for three different axes

4.DISCUSSION

Exoskeletons are used for the treatment of patients who have partially or completely lost their lower extremity gait functions due to paralysis, traffic accidents, and similar reasons. Joints and forces acting on the ground are important in the design of these devices. When studies in the literature are examined;

When performing the lower extremity gait analysis in the AnyBody Musculoskeletal System, only the profile of a healthy person was considered (Fournier et al., 2018; Smith, 2019).

- The analysis of the joint reaction force and ground reaction forces was ignored in model studies (Smith, 2019).

- In some studies, it has been observed that as the weight increases, the muscle signals and the force on the joint increase and the exoskeleton decreases it (Sohane & Agarwal, 2021).

- In the study by Fourier et al., ground reaction force was examined for the posture of patients with normal SCI and SCI, while joint strength was not examined (Fournier et al., 2018).

In this study, unlike the studies in the literature, the SCI model, whose muscles in the normal and lower extremities were canceled, was carried

out during two gait cycles. In the literature, Fourier et al. described the gait process cycle in only one cycle [9]. In this study, gait was obtained with the joint angles obtained from the real gait data, and the gait cycle was provided. In the execution process, gait angles suitable for the RoboGait gait cycle are discussed. Furthermore, the forces and moments were compared in the SCI model, which simulates a normal and full SCI patient, unlike in the literature. As a result of the comparison, it was seen that the use of the muscles increased the joint moment and joint strength, except for the foot subtalar eversion moment. The reason why it does not increase in subtalar eversion is thought to be due to the reverse movement of this joint during gait. Ground reaction forces and moments findings show that when the muscles are out of activity, the reaction forces and moments applied to the ground decrease. The reason for this is thought to be due to the disappearance of the force from the muscles towards the ground.

5. CONCLUSIONS

It is important to examine joint reaction force-moment, ground reaction force-moment for a lower extremity exoskeleton to be designed. In this study, 12 joint reaction forces and joint reaction forces were examined. Disabling muscles decreased the joint reaction force and moment on joints, except for the foot subtalar eversion moment of the foot. The findings show that the exoskeleton control systems should be designed considering the forces acting on the joints when designing the lower extremity exoskeleton.

REFERENCES

Anderson, M. A., O'Shea, T. M., Burda, J. E., Ao, Y., Barlatey, S. L., Bernstein, A. M., Kim, J. H., James, N. D., Rogers, A., & Kato, B. (2018). Required growth facilitators propel axon regeneration across complete spinal cord injury. *Nature*, *561*(7723), 396-400.

Anjum, A., Yazid, M. D. i., Fauzi Daud, M., Idris, J., Ng, A. M. H., Selvi Naicker, A., Ismail, O. H. R., Athi Kumar, R. K., & Lokanathan, Y. (2020). Spinal cord injury: pathophysiology, multimolecular interactions, and underlying recovery mechanisms. *International journal of molecular sciences*, *21*(20), 7533.

Chalvatzaki, G., Papageorgiou, X. S., Tzafestas, C. S., & Maragos, P. (2018). Augmented human state estimation using interacting multiple model particle filters with probabilistic data association. *IEEE Robotics and Automation Letters*, *3*(3), 1872-1879.

Dugan, S. A., & Bhat, K. P. (2005). Biomechanics and analysis of running gait. *Physical Medicine and Rehabilitation Clinics*, *16*(3), 603-621.

Engelhardt, L., Melzner, M., Havelkova, L., Fiala, P., Christen, P., Dendorfer, S., & Simon, U. (2020). A new musculoskeletal AnyBody™ detailed hand model. *Computer Methods in Biomechanics and Biomedical Engineering*, *24*(7), 777-787.

Ferrari, A., Benedetti, M. G., Pavan, E., Frigo, C., Bettinelli, D., Rabuffetti, M., Crenna, P., & Leardini, A. (2008). Quantitative comparison of five current protocols in gait analysis. *Gait & posture*, *28*(2), 207-216.

Fournier, B. N., Lemaire, E. D., Smith, A. J., & Doumit, M. (2018). Modeling and simulation of a lower extremity powered exoskeleton. *IEEE transactions on neural systems and rehabilitation engineering*, *26*(8), 1596-1603.

Hussain, F., Goecke, R., & Mohammadian, M. (2021). Exoskeleton robots for lower limb assistance: A review of materials, actuation, and manufacturing methods. *Proceedings of the Institution of Mechanical Engineers, Part H: Journal of Engineering in Medicine*, *235*(12), 1375-1385.

Kim, Y., Jung, Y., Choi, W., Lee, K., & Koo, S. (2018). Similarities and differences between musculoskeletal simulations of OpenSim and AnyBody modeling system. *Journal of Mechanical Science and Technology*, *32*(12), 6037-6044.

Ong, B., Wilson, J. R., & Henzel, M. K. (2020). Management of the patient with chronic spinal cord injury. *Medical Clinics*, *104*(2), 263-278.

Pinto, D., Garnier, M., Barbas, J., Chang, S.-H., Charlifue, S., Field-Fote, E., Furbish, C., Tefertiller, C., Mummidisetty, C. K., & Taylor, H. (2020). Budget impact analysis of robotic exoskeleton use for locomotor training following spinal cord injury in four SCI Model Systems. *Journal of neuroengineering and rehabilitation*, *17*(1), 1-13.

Rasmussen, J. (2019). The AnyBody modeling system. *DHM and Posturography*, 85-96.

Smith, A. J., Fournier, B. N., Nantel, J., & Lemaire, E. D. (2020). Estimating upper extremity joint loads of persons with spinal cord injury walking with a lower extremity powered exoskeleton and forearm crutches. *Journal of Biomechanics*, *107*, 109835.

Smith, A. J. J. (2019). *Modeling human dynamics for powered exoskeleton control* Université d'Ottawa/University of Ottawa].

Sohane, A., & Agarwal, R. (2021). Evaluation of 3D design lower limb exoskeleton on human musculoskeletal with various loads. *Expert Systems*, *38*(7), e12738.

Trinler, U., Schwameder, H., Baker, R., & Alexander, N. (2019). Muscle force estimation in clinical gait analysis using AnyBody and OpenSim. *Journal of Biomechanics*, *86*, 55-63.

Yang, J., Lee, J. Y., Kim, K. H., & Wang, K.-C. (2021). Disorders of secondary neurulation: mainly focused on pathoembryogenesis. *Journal of Korean Neurosurgical Society*, *64*(3), 386-405.

Yang, J., Lee, J. Y., Kim, K. H., Yang, H. J., & Wang, K.-C. (2022). Disorders of Secondary Neurulation: Suggestion of a New Classification According to Pathoembryogenesis. In *Advances and Technical Standards in Neurosurgery* (pp. 285-315). Springer.

Yavuzer, G. (2014). Yürüme analizi ve temel kavramlar. *Türk Ortopedi ve Travmatoloji Birliği Derneği Dergisi, İstanbul*, *13*, 304-308.

Chapter 9

HEAVY METAL LEACHING FROM SLUDGE INCINERATION ASHES: BEFORE AND AFTER PHOSPHORUS RECOVERY[1]

Ezgi KARABACAK[2]
Güray SALIHOĞLU[3]
Nezih Kamil SALIHOĞLU[4]

1 This work has been produced as part of MSc thesis study by Ezgi Karabacak: Karabacak, E., 2021. Recovery of phosphorus from sewage sludge incineration ashes (Arıtma çamuru yakma fırını küllerinden fosfor geri kazanımı), MSc Thesis (in Turkish)- Ezgi Karabacak (ORCID: 0000-0003-2196-803X), Bursa Uludağ University/ Institute of Science/Environmental Engineering Science Division, 22 January 2021. Supervisor: Prof. Dr. Güray Salihoğlu (ORCID: 0000-0003-0714-048X).

2 Env. Eng. MSc. Ezgi Karabacak, Environmental Engineering Department, Faculty of Engineering, Bursa Uludag University, ORCID: 0000-0003-2196-803X

3 Prof. Dr. Güray Salihoğlu, Environmental Engineering Department, Faculty of Engineering, Bursa Uludag University, ORCID: 0000-0003-0714-048X

4 Prof. Dr. Nezih Kamil Salihoğlu, Environmental Engineering Department, Faculty of Engineering, Bursa Uludag University, ORCID: 0000-0002-7730-776X

1. Introduction

Phosphorus is a critical element for living organism and irreplaceable for industrial sectors (Yu et al., 2022). Phosphate rocks, which are the raw materials of phosphorus, are limited resources (USGS, 2020). Phosphate rocks are used in various sectors, as shown in Fig. 1 (Gorazda, Tarko, Kominko, Worek, & Nowak, 2019). Agricultural application is the primary use of phosphorus (Brunner, 2010; Cieślik & Konieczka, 2017).

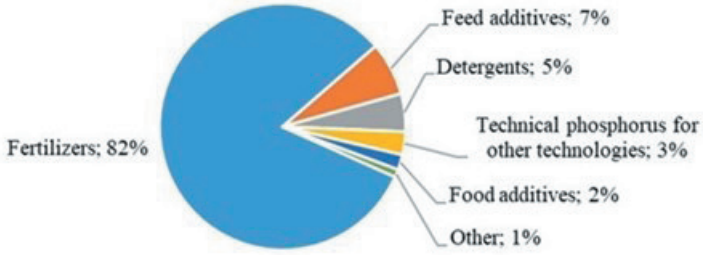

Fig. 1 *Phosphate rock usage by industrial sectors (Gorazda et al*

Phosphorus is a essential nutrient for plant growth (Chan, Liao, & Chiou, 2021). As food production and farming practices increase due to population growth (up to 10 billion by 2050) (Cieślik & Konieczka, 2017; Mogollón, Beusen, van Grinsven, Westhoek, & Bouwman, 2018), the demand for phosphorus fertilizer will naturally increase. Therefore, it is important to search for alternative sources of phosphorus such as sewage sludge and sewage sludge ash (SSA) containing high amounts of phosphorus.

Approximately 2.8 million tons of sewage sludge were disposed of in EU (European Union) countries in 2018 (EUROSTAT, 2021). 20.2% of the disposed sludge is reported to be applied to agricultural lands, 16.9% was used in compost and other applications, 13.7% was landfilled, and 26.7% was incinerated (EUROSTAT, 2021). In Turkey in 2018, 45.9% of the disposed sludge was landfilled, 49.4% was incinerated, 3.9% was used for agricultural applications (EUROSTAT, 2021). Several countries such as Poland, Sweden, Norway, Austria, Romania, Hungary, and Lithuania directly used sewage sludge as fertilizer to benefit from the phosphorus content according to recent EUROSTAT data for the year 2018 (EUROSTAT, 2021). Nevertheless, many countries limit the direct use of sewage sludge because of its potential effects on the environment and human health (Donatello & Cheeseman, 2013; Egle, Rechberger, Krampe, & Zessner, 2016; Marani, Braguglia, Mininni, & Maccioni, 2003).

Incineration is a widely used method in sewage sludge management. It is estimated that around 1.7 million tons of ash are generated per year from sludge incineration (Donatello & Cheeseman, 2013). The P_2O_5 content

of SSA is reported to range between 8.9% and 25.7% (Adam, Peplinski, Michaelis, Kley, & Simon, 2009; Coutand, Cyr, & Clastres, 2006; Franz, 2008; Li et al., 2018; Stark, Plaza, & Hultman, 2006; Wang, Li, Tang, Fang, & Poon, 2018; Xu, He, Gu, Wang, & Shao, 2012).

Several patented processes were developed for phosphorus recovery from SSA; their principles and products are given in Table 1. AshDec® process includes the thermochemical treatment of SSA produced from sewage sludge incineration (Hermann & Schaaf, 2019). In this process, heavy metals are removed from the SSA with thermochemical treatment (>900°C) using chloride sources such as $MgCl_2$ and $CaCl_2$ or sodium-based additives such as Na_2SO_4 and Na_2CO_3 (Egle et al., 2016; Hermann & Schaaf, 2019; Kabbe, 2015). SSA becomes a part of the final product with high bioavailability and low heavy metal levels (Egle et al., 2016). The phosphate is transformed into chlorapatite when using $CaCl_2$, whereas into calcium-magnesium-phosphates when using $MgCl_2$ (Hermann & Schaaf, 2019).

In the SEPHOS process, the pH-value is adjusted to 1.5 (Cieślik & Konieczka, 2017) by sulfuric acid for the extraction (Cornel & Schaum, 2009). The pH value is increased to <3.5 using NaOH in the next step, so $AlPO_4$ is precipitated (Cornel & Schaum, 2009). In the Advanced SEPHOS process, SEPHOS product ($AlPO_4$) is dissolved by the base adding, and calcium phosphate is precipitated by adding calcium (Cornel & Schaum, 2009).

In the BioCon process, SSA is extracted with sulfuric acid (Levlin, Löwén, Stark, & Hultman, 2002). In the next step, a cation exchanger is used to separate iron ions by HCl regeneration, then ferric chloride occurs (Levlin et al., 2002). $KHSO_4$ occurs in the anion exchanger, and phosphoric acid is the final product of BioCon process (Levlin et al., 2002). Stark & Hultman (2003) reported a recovery rate of 60%.

SSA is extracted with HCl in the PASCH process, and solvent extraction is used to extract heavy metals (Blöcher, Niewersch, & Melin, 2012). In the next step, phosphate is precipitated as MAP or calcium phosphate (Blöcher et al., 2012). Calcium phosphate is the final product of both the PASCH process and LeachPhos process (Egle et al., 2016).

Table 1 *Phosphorus recovery processes from SSA*

Process	Reference	Principle	Phosphorus	Product
AshDec®	(Hermann & Schaaf, 2019)	Thermochemical treatment (with $CaCl_2$/$MgCl_2$, /Na_2SO_4,/Na_2CO_3)	>%95 (Kabbe, 2015)	The product that can be used as fertilizer
SEPHOS	(Cornel & Schaum, 2009)	Chemical extraction (with H_2SO_4) $AlPO_4$ precipitation by ph adjustment	-	$AlPO_4$
Advanced SEPHOS	(Cornel & Schaum, 2009)	Chemical extraction (with H_2SO_4) Dissolved of SEPHOS product by the base adding Precipitation of calcium phosphate with adding calcium	-	Calcium phosphate
BioCon	(Levlin et al., 2002)	Chemical extraction (with H_2SO_4) Ion exchange	60% (Stark & Hultman, 2003)	H_3PO_4
PASCH	(Blöcher et al., 2012)	Chemical extraction (with HCl) Solvent extraction Phosphate precipitation	70-80% (Egle et al., 2016)	Calcium phosphate/ MAP
EcoPhos®	(Egle et al., 2016)	Chemical extraction (with acid) Ion exchange	95% Egle et al. (2016)	H_3PO_4
LeachPhos®	(Egle et al., 2016)	Chemical extraction (with acid) Leaching	70-80% (Egle et al., 2016)	Calcium phosphate
Mephrec®	(Scheidig et al., 2009)	Metallurgic melt-gassing	-	Slag (contain calcium phosphate)
Thermphos	(Egle et al., 2016)	Electrothermal process (Furnace at 1500 °C)	95% Egle et al. (2016)	P_4

The acidic wet chemical method is used for LeachPhos® and EcoPhos® (Egle et al., 2016). The phosphoric acid is the final product of the EcoPhos process and is a marketable material (Egle et al., 2016). In Mephrec® process, particular pure materials and the mixture of sewage sludge and ash are smelted using a shaft furnace (up to 2000 °C) (Scheidig, Schaaf, & Mallon, 2009). The liquid slag and liquid metallic phase are produced and tapped at 1450 °C (Scheidig et al., 2009). The slag, a product of Mephrec® process, contains calcium phosphate and low heavy metal levels (Scheidig et al., 2009).

Sewage sludge ash may contain high levels of heavy metals (Herzel, Krüger, Hermann, & Adam, 2016; Wang et al., 2018; Xu et al., 2012) that negatively affect plant growth and reach humans through plants and animals (Barbieri, 2016; Hossain, Piyatida, da Silva, & Fujita, 2012). The high levels of heavy metals in foods cause health risks for human

(Aladesanmi, Oroboade, Osisiogu, & Osewole, 2019).

Zinc (Zn), copper (Cu), nickel (Ni), and lead (Pb) are the heavy metals reported to generally limit agricultural applications (Stylianou et al., 2007). Lead can cause health problem such as damage of the nervous, skeletal, circulatory, enzymatic, endocrine, and immune systems (Zhang et al., 2012). Zinc can cause stomach cramps, nausea, vomiting, and disruption of the immune system (Zhang et al., 2012). Arsenic has toxic and carcinogenic effects (Singh, Kumar, & Sahu, 2007).

The wet chemical method has many advantages compared to other methods, such as high efficiency, low cost, and easy application (Abis, Calmano, & Kuchta, 2018; Donatello & Cheeseman, 2013; Li et al., 2018). However, heavy metal leaching from the SSA can be a problem. Therefore, heavy metal levels should be examined. Several studies investigated heavy metal leaching from SSAs using the acid extraction method. A limited number of the studies (Pettersson, Åmand, & Steenari, 2008a, 2008b) differentiated the heavy metal leaching of SSA according to the air pollution control system (APCS). In this study, SSA samples were classified according to the unit they were formed (baghouse dust filters and multi-cyclones), and their differences in terms of heavy metal leaching using the acid extraction method were evaluated.

2. Materials and methods

2.1 Materials

SSA samples used in this study were obtained from the sewage sludge incineration plant located in Bursa, Turkey. The wastewater treatment plant, where the sludge is originated from, is operated with five-stage Bardenpho® process for nitrogen and phosphorus removal and phosphorus-rich sewage sludge is produced as a result. Sewage sludge is dewatered by the centrifuge unit to 22-26% dry solids and transferred to the fluidized-bed incinerator.

The hot air of 588 °C given to the incinerator with the blowers fluidizes the sand bed. Sewage sludge is mixed with the hot sand and combustion air and is burned completely in five seconds. The temperature reaches at 868 °C, and the sludge is converted into inert ash. The flue gas is conveyed to the waste heat boiler to produce steam at 41 bar and 450 °C with 12 tons/hour capacity. The steam turbine is used to generate electricity with a power of 2500 kW/hour.

The flue gas containing dust and particulates from the waste heat boiler passes through the multi-cyclone unit for treatment. Multi-cyclone unit collects particles larger than 4 μm and removes 75-85% of the total particulate matter. After the multi-cyclone unit, lime is injected to remove

acidic compounds such as SO_2. Baghouse dust filters capture particles after the multi-cyclone unit and lime injection. A wet scrubber tower is used as the last stage of emission control. The flue gas is sent to the atmosphere with a 40-meter high stack. The flowchart of the BUSKI sludge incineration and energy production plant is shown in Fig. 2.

The P_2O_5 levels of BF-Ash and MC-Ash were determined as 17.36% and 11.49%, respectively.

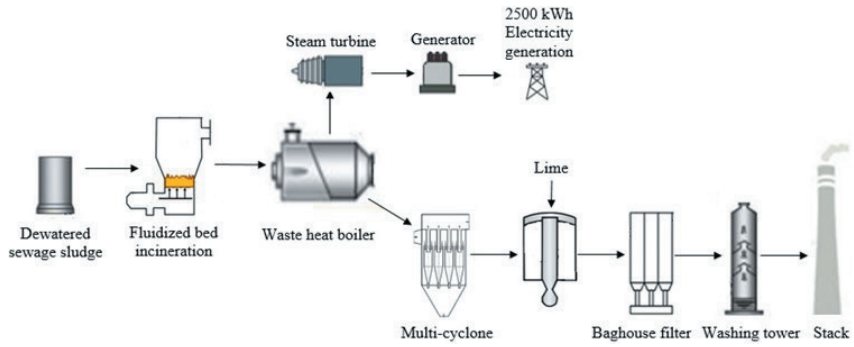

Fig. 2 *The flow chart of the sludge incineration and energy recovery plant*

2.2. Experimental method

The first step of the experiments was to heavy metal analysis of the ashes used in this study. Before this study, the acid extraction method was used to recover phosphorus from the ashes. The liquid-to-solid ratio was determined to be 20:1 (ml g^{-1}) (Fang, Li, Guo, et al., 2018). 40 ml acid solution was added to 2 g sewage sludge ash sample. Both of the ashes were mixed with acid solutions (sulfuric acid, nitric acid, oxalic acid, and citric acid) at 180 rpm in a horizontal shaker for two hours. After acid extraction, the mixture was transferred to a centrifuge tube and was centrifuged at 4000 rpm for 10 min (Fang, Li, Guo, et al., 2018). The leachates were then filtered through a 0.45 µm mixed cellulose esters membrane filter, so the solid and liquid phases were separated from each other. After acid extraction at different molarities (0.2 mol/L, 0.5 mol/L, and 1 mol/L) heavy metal analysis was carried out in the liquid phase. Phosphorus rich liquid phase was assessment according to Turkish Regulation (TR, 2018) and European Regulation (EU, 2019). The residual solid phases of the samples were also analyzed for heavy metal. The experimental method used in this study is shown in Fig. 3.

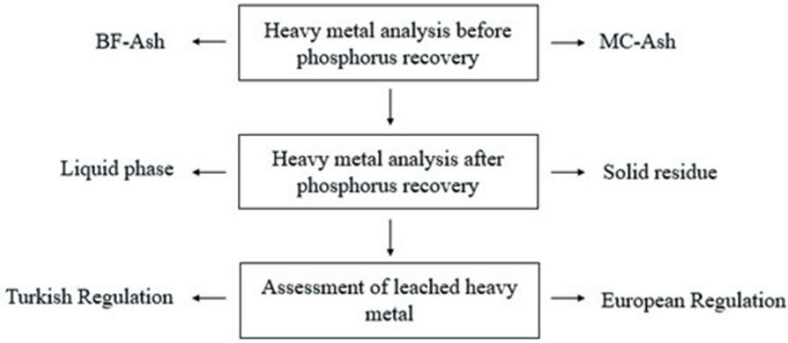

Fig. 3 *Experimental method*

Heavy metal analysis was performed by using inductively coupled plasma and optic emission spectrometry (AGILENT 5100 ICP-OES). Before ICP-OES analysis, microwave-assisted digestion was performed at 170±5°C for 30 min using an Anton Paar Multiwave PRO (Austria) according to the EPA 3015A method (EPA, 2007a) for liquid samples and 3051A method (EPA, 2007b) for solid samples.

The leached heavy metals from the ashes to the liquid phase was calculated according to the eq. (1) below (Fang, Li, Donatello, et al., 2018).

$$M\ (mg/g) = \frac{(C \times T \times V)}{M_o} \quad (1)$$

In the eq. (1), M is the leached heavy metals (mg/g), C is the concentration of heavy metals in the liquid phase (mg/L); T is the dilution factor, V is the volume of the extract (L), and M_o is mass of the ash before extraction (g).

3. Results and discussion

3.1. Heavy metal levels of SSAs

The amounts of heavy metals contained in the ashes and their limit values according to Turkish Regulation (TR, 2018) and European Regulation (EU, 2019) for fertilizers are shown in Table 2. The heavy metal limit values in both of the regulations are different from each other. The heavy metal levels in BF-Ash followed the sequence Zn (6637.08 mg/kg) > Cu (708.95 mg/kg) > Cr (606.81 mg/kg) > Ni (535.23 mg/kg) > Pb (183.98 mg/kg) > As (45.66 mg/kg) > Cd (4.12 mg/kg). The heavy metal levels followed the sequence Zn (4691.51 mg/kg) > Cu (469.95 mg/kg) > Cr (456.81 mg/kg) > Ni (359.85 mg/kg) > Pb (97.40 mg/kg) > As (22.68 mg/kg) > Cd (3.10 mg/kg) for MC-Ash. The order of abundance was similar in both ashes.

Table 2 *Heavy metal content of the ashes*

Parameter	BF-Ash	MC-Ash	Wang et al., 2018	Xu et al., 2012	Herzel et al., 2016	Gorazda et al., 2016	Turkish Regulation*	European Regulation**
Cu (mg/kg)	708.95	469.95	839	787.4	767	625	450	600
Ni (mg/kg)	535.23	359.85	85	53.8	73.3	168	120	50
Pb (mg/kg)	183.98	97.40	93	199.4	122.6	135	150	120
Zn (mg/kg)	6637.08	4691.51	2198	3318	2330	-	1100	1500
Cr (mg/kg)	606.81	456.81	-	89	159	917	350	2
Sn (mg/kg)	26.47	23.90	-	-	-	-	10	-
Cd (mg/kg)	4.12	3.10	-	-	2.1	26	3	P_2O_5<%5=3 P_2O_5=>%5=60
B (mg/kg)	231.45	158.37	-	-	-	-	-	-
Fe (mg/kg)	33577.57	24419.28	-	-	58500	-	-	-
Mn (mg/kg)	872.53	657.48	-	-	1190	-	-	-
Sb (mg/kg)	21.49	21.60	-	-	-	-	-	-
Ag (mg/kg)	4.79	3.36	-	-	-	-	-	-
Al (mg/kg)	38419.93	27826.21	-	-	67200	-	-	-
As (mg/kg)	45.66	22.68	107	-	11.1	3.29	-	40
Se (mg/kg)	3.79	2.12	-	-	-	-	-	-

*: Regulation on Organic, Mineral and Microbial Fertilizers Used in Agriculture in Turkey (TR, 2018)**: European Fertilising Products Regulation (EU) 2019/1009 (EU, 2019)

Sn is only evaluated for fertilizers of animal origin in Turkish Regulation (TR, 2018), whereas Cd is not evaluated for phosphorus fertilizers. Table 2 shows that the heavy metals in BF-Ash, such as copper (708.95 mg/kg), nickel (535.23 mg/kg), lead (183.98 mg/kg), zinc (6637.08 mg/kg), and chromium (606.81 mg/kg) exceeded the limits given by Turkish Fertilizer Regulation (TR, 2018). In addition, As (45.66 mg/g) exceeded the limit value, according to EU Regulation (EU, 2019). Copper (469.95 mg/kg), nickel (359.85 mg/kg), zinc (4691.51 mg/kg), and chromium (456.81 mg/kg) in MC-Ash exceeded the limits defined by Turkish Regulation (TR, 2018) and EU Regulation (EU, 2019).

The heavy metal levels of BF-Ash were higher than that of MC-Ash. As both of the ashes exceeded the legal limits, they cannot be directly used as fertilizer despite their high phosphorus content. The highest heavy metal level exceeding the legal limits was Zn. As also stated by several researchers (Adam et al., 2009; Wang et al., 2018; Xu et al., 2012) Zn was the most prominent heavy metal in SSA. Zn level was reported to be 2198 mg/kg by (Wang et al., 2018), 3318 mg/kg by (Xu et al., 2012), and 1540-2181 mg/kg by (Adam et al., 2009).

3.4. Heavy Metals Leaching

The heavy metals leached from ashes were evaluated according to Turkish (TR, 2018) and European Regulations (EU, 2019). The heavy metals were dissolved with acid extraction, similar to the literature findings (Lynn, Dhir, Ghataora, & West, 2015). The levels of heavy metals leached into the liquid phase after acid extractions from BF-Ash are shown in Fig. 4.

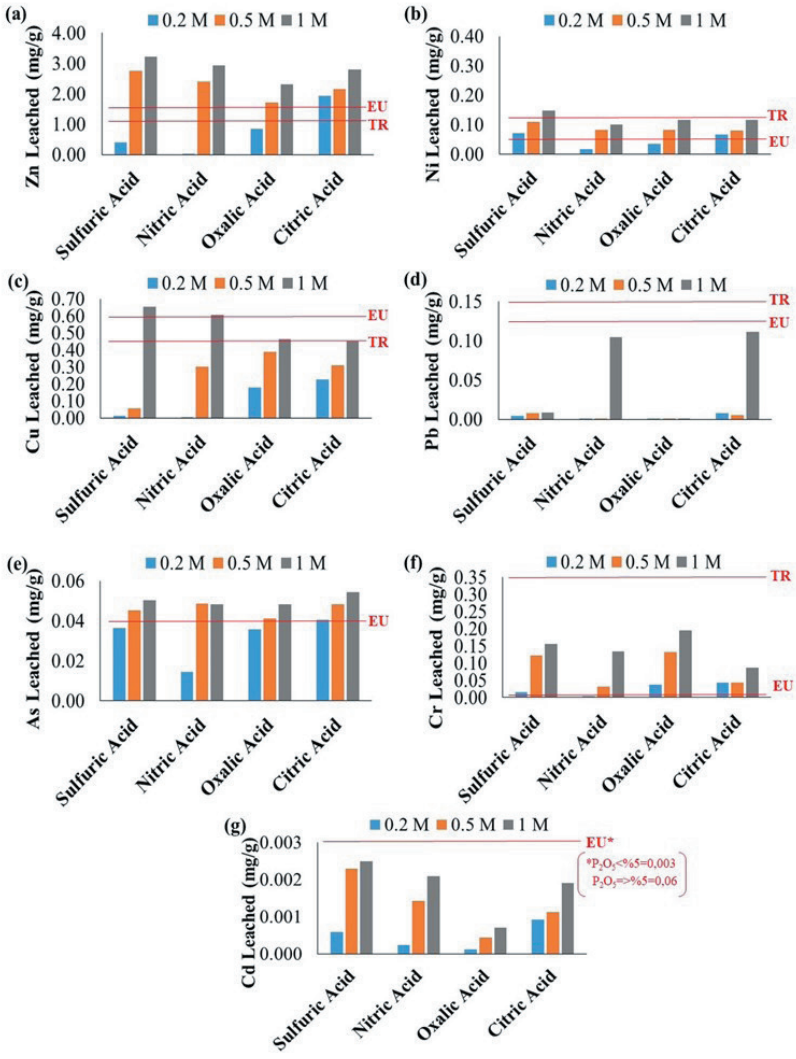

Fig. 4 *Leaching of heavy metals from BF-Ash a)Zn b)Ni c)Cu d)Pb e)As f)Cr g) Cd*

As shown in Fig. 4a, Zn levels leached from BF-Ash were measured to range between 0.38-3.21 mg/g in sulfuric acid solutions with different

molarities, 0.003-2.92 mg/g in nitric acid solutions, 0.84-2.30 mg/g in oxalic acid solutions, and 1.93-2.78 mg/g in citric acid solutions. The Zn limit value is 1.1 mg/g in the Turkish Regulation (TR, 2018) and 1.5 mg/g in the European Regulation (EU, 2019). Except for the 0.2 mol/L acid concentrations, Zn levels exceeded the legal Zn limits of both Turkish and EU Regulations. 1 mol/L sulfuric acid solution resulted in the highest Zn leaching level (3.21 mg/g) from BF-Ash (Fig. 4a). Ni levels leached from BF-Ash ranged between 0.07-0.15 mg/g in sulfuric acid solutions with different molarities (Fig. 4b). Ni leaching levels were between 0.01-0.10 mg/g in nitric acid solutions, 0.03-0.12 mg/g in oxalic acid solutions, and 0.06-0.11 mg/g in citric acid solutions. The Turkish Regulation's limit Ni value is 0.12 mg/g (TR, 2018). This value is 0.05 mg/g in the EU Regulation (EU, 2019). Ni leaching from BF-Ash (0.15 mg/g) exceeded the limits when 1 mol/L sulfuric acid was used.

Cu levels leached from BF-Ash ranged between 0.01-0.65 mg/g in sulfuric acid solutions with different molarities, 0.0004-0.60 mg/g in nitric acid solutions, 0.18-0.46 mg/g in oxalic acid solutions, and 0.23-0.45 mg/g in citric acid solutions (Fig. 4c). The limit levels for Cu are 0.45 mg/g and 0.6 mg/g in Turkish (TR, 2018) and EU Regulations (EU, 2019), respectively. Extraction with 1 mol/L sulfuric and nitric acids yielded leaching levels exceeding both legal limits.

Pb leaching from BF-Ash ranged between 0.004-0.01 mg/g in different concentrations of sulfuric acid solutions, 0.0002-0.10 mg/g in nitric acid solutions, and 0.01-0.11 mg/g in citric acid solutions (Fig. 4d). Pb did not leach when oxalic acid solutions were used for extraction. Pb leaching was close the zero except for 1 M nitric acid citric acid solutions. Pb legal limits of 0.15 mg/g and 0.12 mg/g in Turkish (TR, 2018) and European Regulations (EU, 2019) were not exceeded.

As leaching from BF-Ash ranged between 0.04-0.05 mg/g in sulfuric acid solutions, 0.01-0.05 mg/g in nitric acid solutions, 0.04-0.05 mg/g in oxalic acid solutions, and 0.04-0.05 mg/g in citric acid solutions (Fig. 4e). Sulfuric, nitric, citric, and oxalic acid solutions of 0.5 mol/L and 1 mol/L yielded As leaching exceeding the legal limit of 0.04 mg/g in the EU Regulation (EU, 2019). Turkish regulation does not contain a limit value for As.

Cr leaching ranged between 0.01-0.15 mg/g in sulfuric acid solutions, 0.0003-0.13 mg/g in nitric acid solutions, 0.04-0.19 mg/g in oxalic acid solutions, and 0.04-0.09 mg/g in citric acid solutions (Fig. 4f). There is a large difference between the Cr limits of Turkish and EU regulations; it is 0.35 mg/g in the Turkish Regulation (TR, 2018) and 0.002 mg/g in the EU Regulation (EU, 2019). The highest Cr leaching (0.19 mg/g) was found

in oxalic acid and sulfuric acid solutions (Fig. 4f). Cr leaching exceeded the limit of EU Regulation for all acid types and molarities, except for 0.2 mol/L sulfuric acid solution.

Cd leaching ranged between 0.001-0.002 mg/g in sulfuric acid solutions with different molarities, 0.0002-0.002 mg/g in nitric acid solutions, 0.0001-0.001 mg/g in oxalic acid solutions, and 0.001-0.002 mg/g in citric acid solutions (Fig. 4g). The limit value for Cd is 0.003 mg/g (P_2O_5<5) or 0.06 mg/g (P_2O_5>5) in the EU Regulation (EU, 2019). There is no limit value for Cd in the Turkish Regulation (TR, 2018). As shown in Fig. 4g, the Cd levels leached did not exceed the legal limit values of EU Regulation.

The heavy metals leached into the liquid phase after acid extractions from MC-Ash are shown in Fig. 5. Zn leaching from MC-Ash ranged between 0.62-3.29 mg/g in sulfuric acid solutions with different molarities, 0.001-3.34 mg/g in nitric acid solutions, 0.49-1.07 mg/g in oxalic acid solutions, and 1.96-2.95 mg/g in citric acid solutions (Fig. 5a). Zn leaching from MC-Ash exceeded the limit Zn value in sulfuric acid (0.5 mol/L and 1 mol/L), nitric acid (1 mol/L), and citric acid (0.2 mol/L, 0.5 mol/L, and 1 mol/L) for both Turkish and EU Regulation. For oxalic acid, Zn leaching did not exceed the limit values of both Turkish and EU Regulations. When oxalic acid was used, Zn leaching from BF-Ash (0.84-2.30 mg/g) was higher than leaching from the MC-Ash (0.49-1.07 mg/g). With citric acid, Zn leaching from MC-Ash (1.96-2.95 mg/g) was higher than leaching from the BF-Ash (1.93-2.78 mg/g).

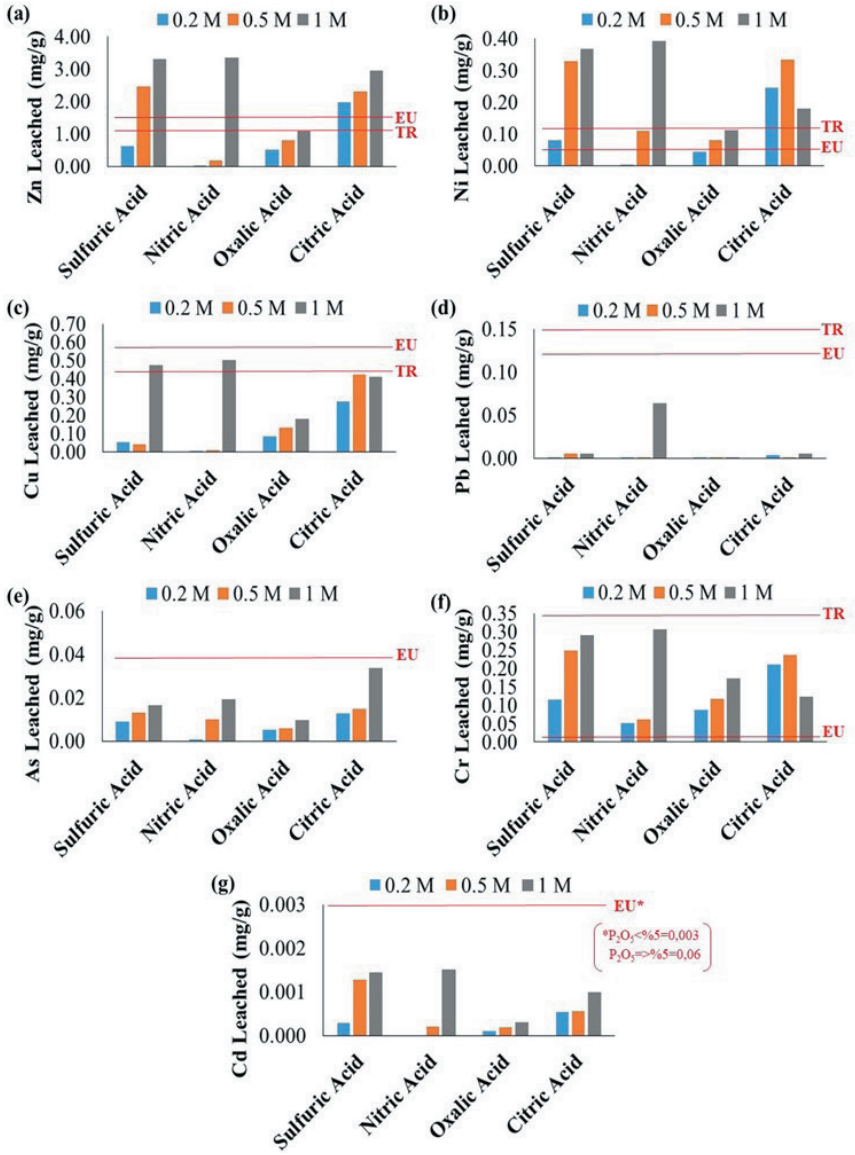

Fig. 5 *Leaching of heavy metals from MC-Ash a)Zn b)Ni c)Cu d)Pb e)As f)Cr g) Cd*

Ni leaching from MC-Ash ranged between 0.08-0.37 mg/g in sulfuric acid solutions, 0.003-0.39 mg/g in nitric acid solutions, 0.04-0.11 mg/g in oxalic acid solutions, and 0.18-0.33 mg/g in citric acid solutions (Fig. 5b). For oxalic acid, Ni leaching from MC-Ash did not exceed the Turkish limit.

As shown in Fig. 5c, Cu leaching from MC-Ash ranged between 0.05-0.47 mg/g in sulfuric acid solutions, 0.0002-0.50 mg/g in nitric acid solutions, 0.08-0.18 mg/g in oxalic acid solutions, and 0.27-0.42 mg/g in

citric acid solutions. Cu leaching from MC-Ash exceeded the limit of the Turkish Regulation for 1 mol/L sulfuric acid (0.47 mg/g) and 1 mol/L nitric acid (0.50 mg/g). The Cu leaching from BF-Ash was higher than leaching from MC-Ash.

Pb leaching from MC-Ash ranged between 0.0003-0.01 mg/g in sulfuric acid solutions, 0.0002-0.06 mg/g in nitric acid solutions, and 0.001-0.005 mg/g in citric acid solutions (Fig. 5d). Pb did not leach from oxalic acid solution. The highest leaching level of Pb was 0.06 mg/g at 1 mol/L nitric acid extraction.

As leaching from MC-Ash ranged between 0.01-0.02 mg/g in sulfuric acid solutions, 0.001-0.02 mg/g in nitric acid solutions, 0.005-0.01 mg/g in oxalic acid solutions, and 0.01-0.03 mg/g in citric acid solutions (Fig. 5e). As leaching levels did not exceed the EU limit. Cr leaching from MC-Ash ranged between 0.12-0.29 mg/g in sulfuric acid, 0.05-0.31 mg/g in nitric acid solutions, 0.09-0.17 mg/g in oxalic acid solutions, and 0.12-0.24 mg/g in citric acid solutions (Fig. 5f). Cr leaching was below the Turkish limit but above the EU limit.

Cd leaching from MC-Ash ranged between 0.0002-0.001 mg/g in sulfuric acid solutions, 0-0.002 mg/g in nitric acid solutions, 0.0001-0.0003 mg/g in oxalic acid solutions, and 0.0005-0.001 mg/g in citric acid solutions (Fig. 5g). Cd leaching levels were below the EU limit. The distribution of the heavy metals between the liquid phase and solid phase for BF-Ash extraction with acid concentrations of 0.2 mol/L, 0.5 mol/L, and 1 mol/L are shown in Fig. 6, Fig. 7, and Fig. 8, respectively.

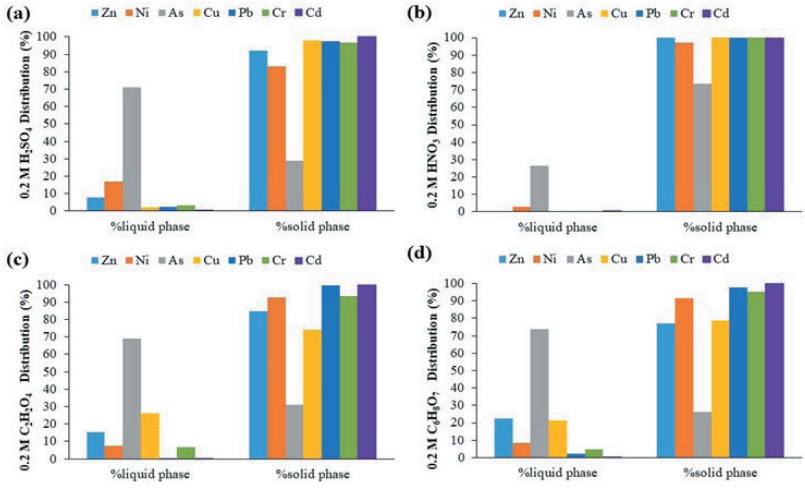

Fig. 6 *Distribution of heavy metals between the liquid and solid phase after 0.2 M acid extraction for BF-Ash a)Sulfuric acid b)Nitric acid c)Oxalic acid d)Citric acid*

As shown in Fig. 6, approximately 70% of As was found in the liquid phase with extractions by 0.2 mol/L sulfuric acid, oxalic acid, and citric acid solutions of BF-Ash. A high level of leaching of As draws attention despite the low acid concentration. After nitric acid extraction of BF-Ash at 0.2 mol/L of the acids, mostly 100% of heavy metals remained in the solid residue except for As (26.36% in the liquid phase) (Fig. 6b). As rate in the liquid phase increased from 26.36% (Fig. 6b) to 72.47% (Fig. 7b) for nitric acid with the increase in acid concentration (from 0.2 mol/L to 0.5 mol/L). As shown in Fig. 7, the rate of As (between 72.47% and 88%) leached from BF-Ash was the highest among all heavy metals for a concentration of 0.5 mol/L of all acids. For 1 M acid extraction, the rate of leached As from BF-Ash into the liquid phase was 89.32% for sulfuric acid (Fig. 8a), 89.56% for oxalic acid (Fig. 8c), 85.86% for citric acid (Fig. 8d), and 77.65% for nitric acid (Fig. 8b). According to the similar result reported by Fang, Li, Guo, et al., (2018), after acid extraction, almost all As in SSA was leached into the liquid phase, except for nitric acid (42%). The reason for the high level of arsenic leaching may be that the arsenic in the ash was in the form of non-silicate phases, and it was highly soluble (Fang, Li, Guo, et al., 2018).

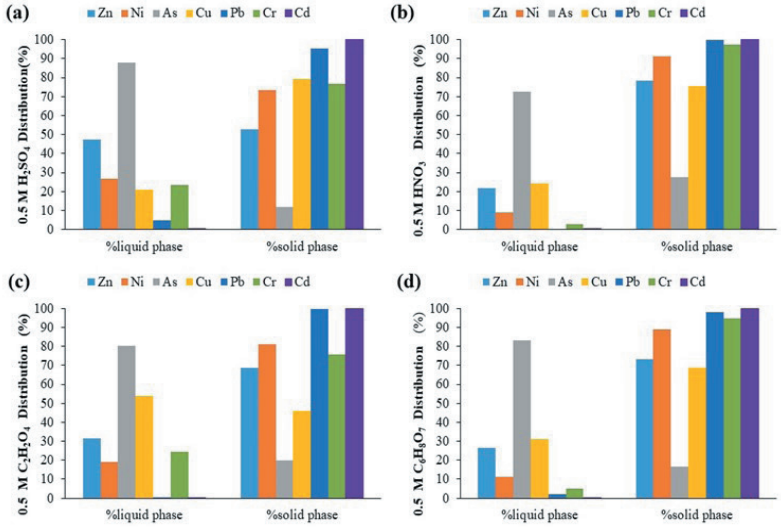

Fig. 7 *Distribution of heavy metals between the liquid and solid phase after 0.5 M acid extraction for BF-Ash a)Sulfuric acid b)Nitric acid c)Oxalic acid d)Citric acid*

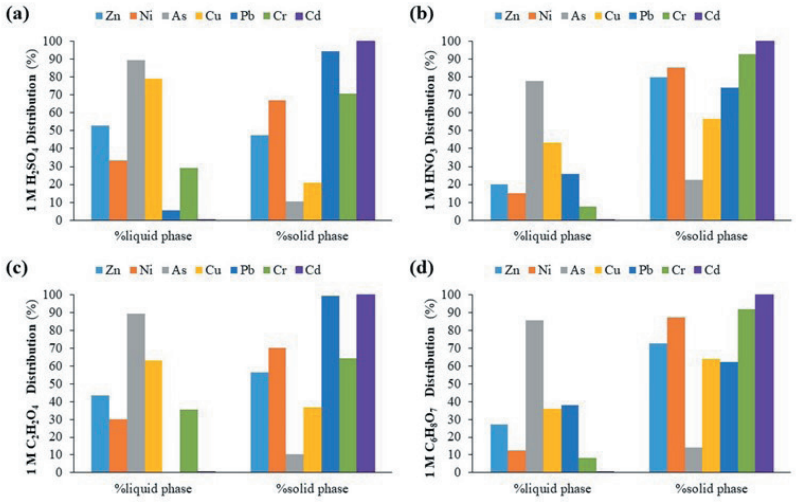

Fig. 8 *Distribution of heavy metals between the liquid and solid phase after 1 M acid extraction for BF-Ash a)Sulfuric acid b)Nitric acid c)Oxalic acid d)Citric acid*

Pb leaching from BF-Ash ranged between 0.32-2.64% (Fig. 6) at 0.2 mol/L acid concentration in the liquid phase, 0.19-4.73% (Fig. 7) at 0.5 mol/L acid concentration, 0.31-37.85% (Fig. 8) at 1 mol/L acid concentration. After BF-Ash was treated with acids with 0.2 and 0.5 mol/L concentration, almost 100% of Pb remained in the solid residue. However, the rate of leached Pb from BF-Ash in the 1 mol/L nitric acid and 1 mol/L citric acid solutions were 26.02% (Fig. 8b) and 37.85% (Fig. 8d), respectively. For BF-Ash, citric acid released more Pb than oxalic acid for organic acids, whereas nitric acid released more Pb than sulfuric acid for inorganic acid. Nitric acid and citric acid at a concentration of 1 mol/L caused the highest leaching of Pb from BF-Ash. Both inorganic acid and organic acid could not release the Pb in the BF-Ash. The tendency of Pb to remain in the solid phase was higher than in the liquid phase for all types of the acids and their varying concentrations, meaning that Pb has low solubility in BF-Ash. On the other hand, Fang, Li, Guo, et al., (2018) reported that oxalic acid (40%) caused the highest rate of Pb leached.

The rate of leached Ni from BF-Ash was found to be between 16.92% (Fig. 6a) and 33.22% (Fig. 8a) in the liquid phase for sulfuric acid extraction, 2.77% (Fig. 6b) and 14.98% (Fig. 8b) for nitric acid, 7.55% (Fig. 6c), and 29.87% (Fig. 8c) for oxalic acid, and 8.58% (Fig. 6d) and 12.54% (Fig. 8d) for citric acid. Sulfuric acid was the most efficient acid for Ni leaching from BF-Ash. Ni leaching into the liquid phase was lower than other metals.

The distribution of the heavy metals leached between the liquid phase and solid phase for concentrations of 0.2 mol/L, 0.5 mol/L, and 1 mol/L, after the treatment of MC-Ash with organic and inorganic acids are shown in Fig. 9, Fig. 10, and Fig. 11, respectively.

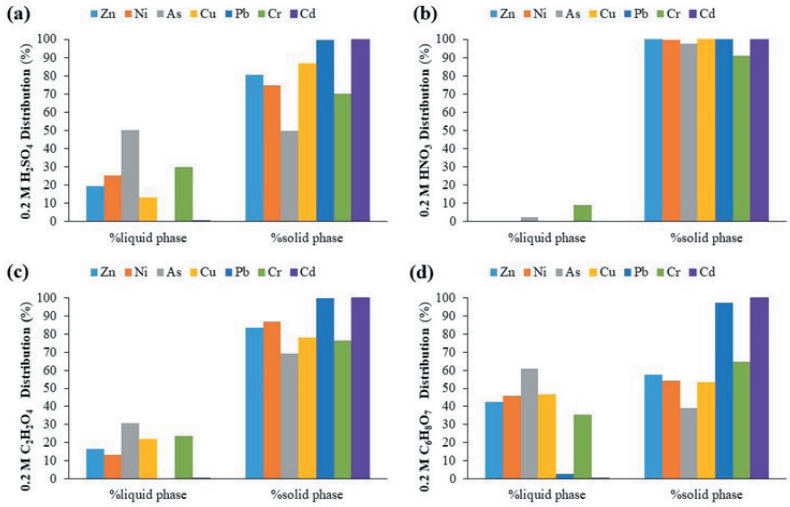

Fig. 9 *Distribution of heavy metals between the liquid and solid phase after 0.2 M acid extraction for MC-Ash a)Sulfuric acid b)Nitric acid c)Oxalic acid d) Citric acid*

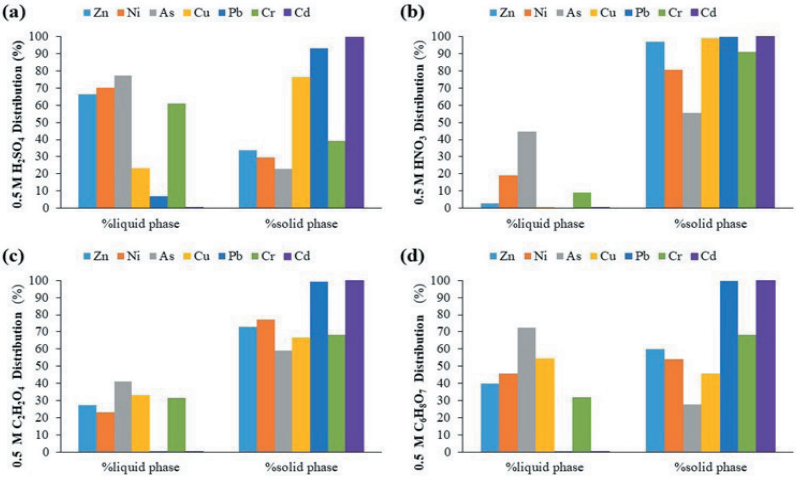

Fig. 10 *Distribution of heavy metals between the liquid and solid phase after 0.5 M acid extraction for MC-Ash a)Sulfuric acid b)Nitric acid c)Oxalic acid d) Citric acid*

Arsenic was the most leached heavy metal from MC-Ash into the liquid phase for all types of acids (Fig. 9, Fig. 10, and Fig. 11). For inorganic acid treatment of MC-Ash, sulfuric acid released more As than nitric acid

(except for 1 mol/L). For organic acid treatment of MC-Ash, citric acid released more As than oxalic acid did. For 0.2 M acid extraction, the leached As from MC-Ash into the liquid phase was 50.17% for sulfuric acid and 60.85% for citric acid. When nitric acid concentration was 0.2 mol/L, As remained mostly in the solid phase (97.44%) of MC-Ash. The rate of As leaching increased from 50.17% (Fig. 9a) to 78.58% (Fig. 11a) as sulfuric acid concentration increased from 0.2 to 1 mol/L. When MC-Ash was treated with citric acid, As leaching was between 60.85% (Fig. 9d) and 89.39% (Fig. 11d).

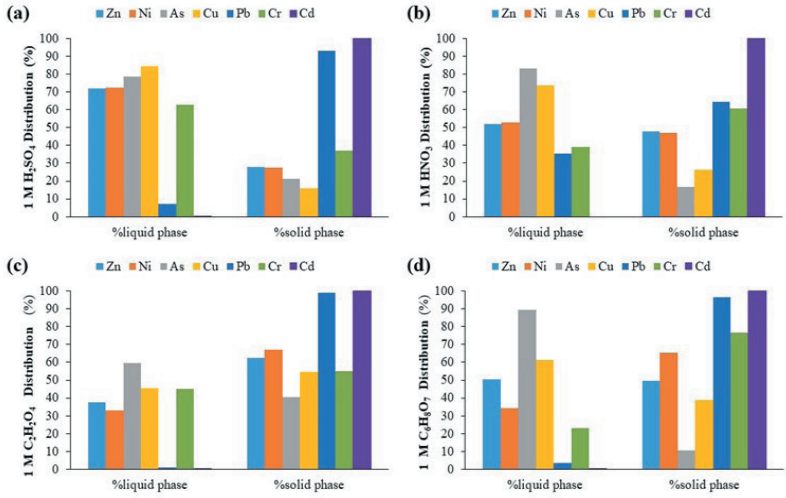

Fig. 11 *Distribution of heavy metals between the liquid and solid phase 1 M acid extraction for MC-Ash a)Sulfuric acid b)Nitric acid c)Oxalic acid d)Citric acid*

For 1 mol/L acid concentration, Pb leaching from MC-Ash was 35.36% (Fig. 11b) in nitric acid and 6.99% (Fig. 11a) in sulfuric acid solution. Almost all Pb remained in the solid phase, except for 1 mol/L nitric acid concentration. Similar to BF-Ash leaching results, Pb leaching from MC-Ash was almost negligible. Xu et al., (2012) reported a low Pb leaching when SSA was treated with HCl.

Almost all Cd remained in the solid phase with both organic and inorganic acid treatments of BF-Ash (Fig. 6, Fig. 7, and Fig. 8). MC-Ash leaching results showed a similar trend where Cd mostly remained in the solid phase (Fig. 9, Fig. 10, and Fig. 11). As Cd did not exceed the legal limit value Cd leaching does not restrict phosphorus recovery from both ashes.

With increasing acid concentration, Ni rates leached from MC-Ash into the liquid phase increased from 25.10% (Fig. 9a) to 72.54% (Fig. 11a)

for sulfuric acid, from 0.46% (Fig. 9b) to 52.95% (Fig. 11b) for nitric acid, from 13.01% (Fig. 9c) to 32.80% (Fig. 11c) for oxalic acid. With citric acid extraction, the rate of leached Ni from MC-Ash was 45.97% (Fig. 9d) and 34.40% (Fig. 11d) for 0.2 mol/L and 1 mol/L, respectively. Gorazda et al., (2016) reported that when using nitric acid, leached Ni level to the liquid phase from three different SSAs was around 10-30%. Sulfuric acid caused the most Ni releasing from MC-Ash. Ni mostly remained in the solid phase after MC-Ash was treated with acids, except for sulfuric acid. However, Ni leaching exceeded the legal limit for both of the ashes.

Cr leaching from MC-Ash with sulfuric acid extraction was 62.83% (Fig. 11a) for 1 mol/L and 60.79% (Fig. 10a) for 0.5 mol/L, so the Cr rate in the liquid phase was higher than in the solid phase. But, the Cr rate in the solid phase was higher than in the liquid phase for other acids. In BF-Ash extraction, Cr leaching rate was 23.22% (Fig. 7a) for 0.5 mol/L sulfuric acid, 29.15% (Fig. 8a) for 1 mol/L sulfuric acid, 24.28% (Fig. 7c) for 0.5 mol/L oxalic acid, and 35.56% (Fig. 8c) for 1 mol/L oxalic acid. Cr leaching from both of the ashes exceeded the EU limit. Gorazda et al., (2016) reported that after the 2.7 mol dm-3 nitric acid extraction from three different sludge ashes showed Cr leaching to be ~5-20% in the liquid phase.

After 0.2 mol/L acid extraction, the Zn rate in the liquid phase was between 0.02-42.54% (Fig. 9) and 0.04-22.72% (Fig. 6) for MC-Ash and BF-Ash, respectively. For low acid concentration, the Zn rate in the liquid phase for MC-Ash was higher than that of BF-Ash. Zn leaching from MC-Ash was 72.06% (Fig. 11a) in 1 mol/L sulfuric acid, 66.28% (Fig. 10a) in 0.5 mol/L sulfuric acid, 50.42% (Fig. 11d) in 1 mol/L citric acid, and 52.09% (Fig. 11b) in 1 mol/L nitric acid. Zn leaching rate ranged between 0.02-72.06% for MC-Ash, 0.04-52.75% for BF-Ash. Zn leaching from BF-Ash was 52.75% for 1 mol/L sulfuric acid (Fig. 8a). Li et al., (2018) reported that Zn leaching was ~37% for nitric acid at 0.5 mol/L, ~40% for sulfuric acid, 56.89% for oxalic acid, and ~25% for citric acid. Although most of the Zn remained in the solid phase, Zn leaching exceeded the limit of both Turkish and EU Regulations.

Cu leaching rate from BF-Ash was found to be 79.02% in 1 mol/L sulfuric acid (Fig. 8a), 63.05% in 1 mol/L oxalic acid (Fig. 8c), and 53.84% in 0.5 mol/L oxalic acid solutions (Fig. 7c). For BF-Ash, sulfuric acid was not effective in 0.2 mol/L and 0.5 mol/L, but was the most effective acid at 1 mol/L concentration for Cu releasing. Oxalic acid released more Cu than citric acid from BF-Ash. Cu leaching from MC-Ash was found to be 84.31% in 1 mol/L sulfuric acid (Fig. 11a), 73.78% in 1 mol/L nitric acid (Fig. 11b), 61.18% in 1 mol/L citric acid (Fig. 11d) and 54.39% in 0.5 mol/L citric acid (Fig. 10d). Citric acid was more effective in Cu leaching,

unlike BF-Ash. Gorazda et al., (2016) reported that Cu leaching from three different SSAs ranged between 40-65% when using nitric acid. Li et al., (2018) reported that after 0.5 mol/L acid extraction, Cu leaching was ~40% for sulfuric acid, ~37% for nitric acid, 65.77% for oxalic acid, and ~17% for citric acid. Xu et al., (2012) reported that when HCl was used, Cu leaching increased from 50% to 70% with the increase in acid concentration (0.1 mol/L-0.8 mol/L).

Fe leaching rates from the ashes after acid extraction is presented in Table 3.

Table 3 *Leaching of Fe from ashes*

Ash	mol/L	Sulfuric Acid	Nitric Acid	Oxalic Acid	Citric Acid
BF-Ash (%)	0.2	0.01	0.01	3.6	5.3
	0.5	23.09	3.09	29.7	14
	1	30.46	25.34	43.2	19.8
MC-Ash (%)	0.2	0.01	0.01	12.5	25.05
	0.5	49.2	0.01	24.69	10.7
	1	64.84	73.31	38.29	34.63

As shown in Table 3, Fe leaching from the ashes increased with the increasing acid concentration, except for citric acid extraction of MC-Ash. The Fe leaching rate was lower than 50%, except for at 1 mol/L sulfuric acid and nitric acid solutions. Fe remained mostly at the solid phase after acid extraction. Stark et al., (2016) reported that when HCl was used, Fe leaching rate was 0.3% for 0.25 M, 5.4% for 0.5 M, 6% for 1 M. Gorazda et al., (2016) reported that when 2.7 mol dm^{-3} nitric acid was used, the Fe leaching rate was ~9-14%. Iron is transformed to hematite during the sewage sludge incineration, and hematite is not dissolved in the base or strong acids (Gorazda et al., 2016; Stark et al., 2006); therefore, extracted Fe was at a low level.

4. Conclusions

This study investigated the phosphorus recovery potential of SSAs originating from different air pollution control units. Several conclusions derived from the study are as follows:

1. The heavy metal levels of both untreated BF-Ash and MC-Ash exceeded the legal limits of Turkish and European regulations. Therefore, both ashes cannot be directly used for agricultural applications.

2. The heavy metal leaching levels exceeded the legal limits after acid extraction of the ashes. Zn, Ni, and Cu from BF-Ash and MC-Ash exceeded the limits of Turkish Regulation. As and Cr levels were above the limits of EU Regulation.

3. High leaching levels of As even at low acid concentrations and low Pb leaching below regulations were marked. The Cd leaching was close to zero, and almost all Cd remained in the solid phase.

4. Fe remained mostly at the solid phase after acid extraction because hematite is not dissolved in the acids.

5. Before using the ashes or their acidic solutions in fertilizer production, the removal of heavy metals is a necessity. The phosphorus recovered from SSA may also find uses by industries other than the fertilizer sector; however, further research is needed for this kind of application.

Acknowledgment

This work was supported by The Scientific and Technological Research Council of Turkey (TUBITAK) -BIDEB 2210/C National MSc Scholarship Program in the Priority Fields in Science and Technology. Author Ezgi Karabacak has received scholarship under the above mentioned program. The authors would like to thank Bursa Cement Factory Co. Inc. and Bursa Water and Sewerage Administration (BUSKI) authorities and staff for their help in the analysis of SSAs and other samples.

REFERENCES

Abis, M., Calmano, W., & Kuchta, K. (2018). Innovative technologies for phosphorus recovery from sewage sludge ash. *Detritus*, *1*, 23–29.

Adam, C., Peplinski, B., Michaelis, M., Kley, G., & Simon, F. G. (2009). Thermochemical treatment of sewage sludge ashes for phosphorus recovery. *Waste Management*, *29*(3), 1122–1128.

Aladesanmi, O. T., Oroboade, J. G., Osisiogu, C. P., & Osewole, A. O. (2019). Bioaccumulation Factor of Selected Heavy Metals in Zea mays. *Journal of Health and Pollution*, *9*(24), 191207.

Barbieri, M. (2016). The Importance of Enrichment Factor (EF) and Geoaccumulation Index (Igeo) to Evaluate the Soil Contamination. *Journal of Geology & Geophysics*, *5*(1), 1–4.

Blöcher, C., Niewersch, C., & Melin, T. (2012). Phosphorus recovery from sewage sludge with a hybrid process of low pressure wet oxidation and nanofiltration. *Water Research*, *46*(6), 2009–2019.

Brunner, P. H. (2010). Substance Flow Analysis as a Decision Support Tool for Phosphorus Management. *Journal of Industrial Ecology*, *14*(6), 870–873.

Chan, C., Liao, Y.-Y., & Chiou, T.-J. (2021). The Impact of Phosphorus on Plant Immunity. *Plant and Cell Physiology*, *62*(4), 582–589.

Cieślik, B., & Konieczka, P. (2017). A review of phosphorus recovery methods at various steps of wastewater treatment and sewage sludge management. The concept of "no solid waste generation" and analytical methods. *Journal of Cleaner Production*, *142*, 1728–1740.

Cornel, P., & Schaum, C. (2009). Phosphorus recovery from wastewater: Needs, technologies and costs. *Water Science and Technology*, *59*(6), 1069–1076.

Coutand, M., Cyr, M., & Clastres, P. (2006). Use of sewage sludge ash as mineral admixture in mortars. *Proceedings of Institution of Civil Engineers: Construction Materials*, *159*(4), 153–162.

Donatello, S., & Cheeseman, C. R. (2013). Recycling and recovery routes for incinerated sewage sludge ash (ISSA): A review. *Waste Management*, *33*(11), 2328–2340.

Egle, L., Rechberger, H., Krampe, J., & Zessner, M. (2016). Phosphorus recovery from municipal wastewater: An integrated comparative technological, environmental and economic assessment of P recovery technologies. *Science of the Total Environment*, *571*, 522–542.

EPA. (2007a). U.S. EPA Method 3015A: Microwave Assisted Acid Digestion of Aqueous Samples and Extracts. Retrieved from https://www.epa.gov/esam/epa-method-3015a-microwave-assisted-acid-digestion-aqueous-samples-and-extracts

EPA. (2007b). U.S. EPA Method 3051A: Microwave Assisted Acid Digestion of

Sediments, Sludges, and Oils. Retrieved from https://www.epa.gov/esam/us-epa-method-3051a-microwave-assisted-acid-digestion-sediments-sludges-and-oils

EU. (2019). REGULATION (EU) 2019/1009 OF THE EUROPEAN PARLIAMENT AND OF THE COUNCIL of 5 June 2019 laying down rules on the making available on the market of EU fertilising products and amending Regulations (EC) No 1069/2009 and (EC) No 1107/2009 and repealing Regulation (EC) No 2003/2003. *Official Journal of the European Union Document 32019R1009*.

EUROSTAT. (2021). Sewage sludge production and disposal from urban wastewater. Retrieved 1 December 2021, from https://ec.europa.eu/eurostat/databrowser/view/TEN00030/default/table.

Fang, L., Li, J., Guo, M. Z., Cheeseman, C. R., Tsang, Daniel, C. W., Donatello, S., & Poon, C. S. (2018). Phosphorus recovery and leaching of trace elements from incinerated sewage sludge ash (ISSA). *Chemosphere*, *193*, 278–287.

Fang, L., Li, J. shan, Donatello, S., Cheeseman, C. R., Wang, Q., Poon, C. S., & Tsang, D. C. W. (2018). Recovery of phosphorus from incinerated sewage sludge ash by combined two-step extraction and selective precipitation. *Chemical Engineering Journal*, *348*, 74–83.

Franz, M. (2008). Phosphate fertilizer from sewage sludge ash (SSA). *Waste Management*, *28*(10), 1809–1818.

Gorazda, K., Tarko, B., Kominko, H., Worek, Z., & Nowak, A. K. (2019). *Phosphate industry in the balance of sustainable development and circular economy*. In *HERAKLION 2019 7th International Conference on Sustainable Solid Waste Management* (pp. 1–16).

Gorazda, K., Tarko, B., Wzorek, Z., Nowak, A. K., Kulczycka, J., & Henclik, A. (2016). Characteristic of wet method of phosphorus recovery from polish sewage sludge ash with. *Open Chemistry*, *14*(1), 37–45.

Hermann, L., & Schaaf, T. (2019). Outotec (AshDec®) Process for P Fertilizers from Sludge Ash. In *Phosphorus Recovery and Recycling* (pp. 221–233). Singapore: Springer Singapore.

Herzel, H., Krüger, O., Hermann, L., & Adam, C. (2016). Sewage sludge ash - A promising secondary phosphorus source for fertilizer production. *Science of the Total Environment*, *542*, 1136–1143.

Hossain, M. A., Piyatida, P., da Silva, J. A. T., & Fujita, M. (2012). Molecular Mechanism of Heavy Metal Toxicity and Tolerance in Plants: Central Role of Glutathione in Detoxification of Reactive Oxygen Species and Methylglyoxal and in Heavy Metal Chelation. *Journal of Botany*, *2012*, 1–37.

Kabbe, C. (2015). *Sustainable sewage sludge management fostering phosphorus recovery and energy efficiency. Project Final Report*. Berlin, Germany.

Levlin, E., Löwén, M., Stark, K., & Hultman, B. (2002). Effects of phosphorus re-

covery requirements on Swedish sludge management. *Water Science and Technology*, *46*(4–5), 435–440.

Li, J., Chen, Z., Wang, Q., Fang, L., Xue, Q., Cheeseman, C. R., … Poon, C. S. (2018). Change in re-use value of incinerated sewage sludge ash due to chemical extraction of phosphorus. *Waste Management*, *74*, 404–412.

Lynn, C. J., Dhir, R. K., Ghataora, G. S., & West, R. P. (2015). Sewage sludge ash characteristics and potential for use in concrete. *Construction and Building Materials*, *98*, 767–779.

Marani, D., Braguglia, C. M., Mininni, G., & Maccioni, F. (2003). Behaviour of Cd, Cr, Mn, Ni, Pb, and Zn in sewage sludge incineration by fluidised bed furnace. *Waste Management*, *23*(2), 117–124.

Mogollón, J. M., Beusen, A. H. W., van Grinsven, H. J. M., Westhoek, H., & Bouwman, A. F. (2018). Future agricultural phosphorus demand according to the shared socioeconomic pathways. *Global Environmental Change*, *50*(March), 149–163. Retrieved from https://doi.org/10.1016/j.gloenvcha.2018.03.007

Pettersson, A., Åmand, L.-E., & Steenari, B.-M. (2008a). Leaching of ashes from co-combustion of sewage sludge and wood—Part I: Recovery of phosphorus. *Biomass and Bioenergy*, *32*(3), 224–235.

Pettersson, A., Åmand, L.-E., & Steenari, B.-M. (2008b). Leaching of ashes from co-combustion of sewage sludge and wood—Part II: The mobility of metals during phosphorus extraction. *Biomass and Bioenergy*, *32*(3), 236–244.

Scheidig, K., Schaaf, M., & Mallon, J. (2009). *Profitable recovery of phosphorus from sewage sludge and meat & bone meal by the Mephrec process–a new means of thermal sludge and ash treatment* (pp. 5635–566). London: IWA Publishing.

Singh, N., Kumar, D., & Sahu, A. P. (2007). Arsenic in the environment: effects on human health and possible prevention. *Journal of Environmental Biology*, *28*(2), 359–365.

Stark, K., & Hultman, B. (2003). Phosphorus recovery by one or two-step technology with use of acids and bases, 281–288.

Stark, K., Plaza, E., & Hultman, B. (2006). Phosphorus release from ash, dried sludge and sludge residue from supercritical water oxidation by acid or base. *Chemosphere*, *62*(5), 827–832.

Stylianou, M. A., Kollia, D., Haralambous, K. J., Inglezakis, V. J., Moustakas, K. G., & Loizidou, M. D. (2007). Effect of acid treatment on the removal of heavy metals from sewage sludge. *Desalination*, *215*(1–3), 73–81.

TR. (2018). Regulation on Organic, Mineral and Microbial Fertilizers Used in Agriculture. *Republic of Turkey Ministry of Agriculture and Forestry Official Gazette No: 30341, Official Gazette Date: February 23, 2018*.

USGS. (2020). Mineral Commodity Summaries 2020-Phosphate Rock. U.S Geological Survey. Retrieved from https://pubs.usgs.gov/periodicals/mcs2020/mcs2020.pdf

Wang, Q., Li, J. shan, Tang, P., Fang, L., & Poon, C. S. (2018). Sustainable reclamation of phosphorus from incinerated sewage sludge ash as value-added struvite by chemical extraction, purification and crystallization. *Journal of Cleaner Production*, *181*, 717–725.

Xu, H., He, P., Gu, W., Wang, G., & Shao, L. (2012). Recovery of phosphorus as struvite from sewage sludge ash. *Journal of Environmental Sciences (China)*, *24*(8), 1533–1538.

Yu, H., Lu, X., Miki, T., Matsubae, K., Sasaki, Y., & Nagasaka, T. (2022). Sustainable phosphorus supply by phosphorus recovery from steelmaking slag: a critical review. *Resources, Conservation and Recycling*, *180*, 106203.

Zhang, X., Yang, L., Li, Y., Li, H., Wang, W., & Ye, B. (2012). Impacts of lead/zinc mining and smelting on the environment and human health in China. *Environmental Monitoring and Assessment*, *184*(4), 2261–2273.

Chapter 10

ULTRASOUND APPLICATIONS IN FOOD TECHNOLOGY

Ayhan DURAN[1], Emre Cem ERASLAN[2]

1 Aksaray University, Department of Engineering Faculty, Aksaray, Turkey
2 Akdeniz University, Department of Biology, Faculty of Science, Antalya, Turkey

INTRODUCTION

ULTRASOUND

Sound is the mechanical vibrations of particles in an equilibrium state. Sound source for any system that can give sound, movements made by sound sources while making sound are called sound vibrations, one full vibration period in these movements is called the period of sound vibration and the number of revolutions per second is called the frequency of the sound. Sound consists of a vibrational movement. The reverse is not always true. In other words, every vibration movement does not necessarily produce a sound. The human ear can perceive wave energy between 20-20,000 Hz as sound.

Unlike electromagnetic waves, sound cannot be transmitted in a vacuum. Sound waves can only be transmitted in molecular media. The diffusivity of sound is inversely proportional to the compressibility of the medium. Therefore, the speed of sound is slowest in gases and fastest in solids. In addition, the speed of sound increases with temperature in liquids and gases. The average speed of sound in air is 33 m/s (Büyüktanır, 2010).

Sound waves are longitudinal waves that propagate in different media. These waves propagate in any medium at a speed that depends on the properties of the medium. While the sound wave propagates in a medium; Particles of the medium vibrate, producing changes in density and volume along the direction of the waves motion (Halliday & Resnick, 1992). Sound is mechanical energy, and sound production means producing vibrational energy. Vibrating a wire, a membrane or air molecules are methods of producing sound that we know from daily life. All sound production tools work with one of these methods (Gürpınar, 2007).

Sound is listed in four categories; Infrasound frequency is between 0-20 Hz, Audible Sound frequency is between 20-20,000 Hz, Ultrasound frequency is between 20,000 Hz and 1 GHz and Hypersound: It is sound with a frequency above 1 GHz.

Ultrasound is the name given to sound waves with a frequency that is too high for the human ear to hear. Ultrasound is an acoustic wave. (Buyuktanir, 2010). The human ear is sensitive to sounds within the frequency range of 16 Hz to 20000 Hz (20 kHz). Infrasonic waves starting from audible frequencies up to 25 MHz (25.10^6 Hertz) are used for different purposes. Ultrasound is born as a vibrational movement, spreads as a vibrational movement and is perceived as a vibrational movement (Özden, 1981). Ultrasound is expressed as sound power (W), sound intensity (W/m^2), or sound energy density (Ws/m^3) (Yüksel, 2013).

FORMATION OF ULTRASOUND

Although there are many mechanical methods similar to audible sound production methods, such as vibrating a wire or a membrane, piezoelectric phenomena are used in ultrasound production. Ultrasound was first produced by the brothers Piere and Jacques Curies in 1880 with the help of crystals with piezoelectric (pressure electrification) feature. Crystals with piezoelectric properties such as quartz, lithium sulfate, cadmium sulfate, zinc oxide, tourmaline, barium, titanate, lead titanate are used in ultrasound production. The piezoelectric phenomenon simply means the formation of an electrical voltage in some crystal and ceramic materials on which a mechanical pressure is applied. A piezoelectric crystal material is cut in the form of a disc or prism, and its surfaces are covered with a thin conductive metal (gold, silver, aluminum). If mechanical pressure is applied to the lower and upper surfaces of the crystal, polarizations are obtained on these surfaces, and as a result of the opposite application, serial elongation and contraction are obtained depending on the frequency of the constantly changing voltage. These mechanical contractions (vibrations) also give us ultrasound. The piezoelectric effect is bidirectional. Ultrasound is obtained by inverse piezoelectric effect, the system is used as a transmitter. Ultrasound is detected by normal piezoelectric effect, the system uses it as a receiver.

Ultrasound waves are formed by the conversion of electric current or magnetic field into pressure waves by the crystals. Devices that perform this operation are also called transducers. In other words, transducers are devices that can convert energy from one form to another. Industrial applications of ultrasonic waves are grouped into three groups as liquid, solid and air environments. Ultrasound is applied in industry, medicine, marine science and service sector (Büyüktanır, 2010).

USE OF ULTRASOUND WITH DIFFERENT CONSERVATION METHODS

When ultrasound is used in combination with other methods, its effectiveness (especially on microbial and enzymatic activation) increases. With these methods, it is aimed to improve the quality of food by reducing the temperature and pressure of the process, minimizing the negative effects that may occur in the quality of the food. The methods in which ultrasound is used in combination are Thermosonication, Manosonication and Manothermosonication. Thermosonication is a method in which heat and ultrasound are used together. Manosonication is a method in which pressure and ultrasound are used together. Manothermosonication is a method in which pressure, heat and ultrasound processes are used together.

In addition to these generally used combinations, ultrasound and pulsed electric field, pH and antimicrobial chemicals can also be used (Demirdöven & Baysal, 2009). Ultrasound has three basic effects in an environment, namely mechanical vibration effect, acoustic flow and acoustic cavitation. Mechanical vibration and acoustic flow are non-cavitational physical effects. While the mechanical vibration effect is used in cleaning and extraction applications, acoustic flow can accelerate mass transfer, which increases cleaning and extraction efficiency (Askokkumar et al., 2010).

The application of ultrasound technology is more effective in liquid systems and the effect is mainly due to the phenomenon of cavitation (which creates bubbles in liquid food). Production of ultrasound; it's in the form of a compression that continues very rapidly and the oscillation of the waves it produces as it passes through the medium. The sound waves sent into the liquid occur when the molecules in the liquid vibrate and continue this vibration by transferring it to the neighboring molecule. With the transfer of this energy, compression and relaxation occur in the molecules in the environment. While the molecules in the liquid approach each other during compression, bubbles are formed as a result of the attraction between the molecules that start to move away from each other during relaxation. As the molecules move from the moment of divergence to the approach phase, the bubbles that occur as a result of the serial oscillation burst suddenly between the molecules approaching each other. With this explosion, a temperature of up to 5500 ^{0}C and a pressure of 50 MPa are formed around the bubble in a very short time. The sudden burst of these gas bubbles causes a high shear effect and turbulence in the cavitation zone. The heat, pressure and turbulence formed here have various effects. During this energy and density, the viscosity of the medium, surface tension, vapor pressure, released gas concentration, state of the solid particles, temperature, application pressure depend on the size of the cavitation. The amount of energy released by cavitation depends on the effect of bubbles on bubble growth kinetics and collapse. This energy can increase with the surface tension at the interface of the bubbles with the vapor pressure of the liquid. Especially if watery foods have high surface tension, the effect of the environment for cavitation is much higher (Yüksel, 2013).

Ultrasound process is divided into two main groups as low power (power, intensity)-high frequency and high power-low frequency according to the applications. Low-power-high-frequency ultrasound is applied at frequencies of 100 kHz and above and energy density below 1 W/cm^2. In the low-power ultrasound process, the sound waves passing through the medium do not cause significant physical and chemical changes in the material. They are generally used to determine the

composition and physicochemical properties of foodstuffs. The use of low-power ultrasound as a simple, fast, precise, inexpensive and non-destructive analytical method is increasing (Salazar et al., 2010; Award et al., 2012; Chandrapala et al., 2012). The main mechanism of action in high frequency ultrasound is acoustic current (Patist & Bates, 2008; Award et al., 2012). Low power ultrasound process in food products and beverages sugar and alcohol content, meat fat content, characterization of fruits and vegetables, egg quality, mechanical properties of cheese, biscuit texture, milk coagulation, fermentation control in wine, sugar content of melon, fat index and fermentation of dough. (Muthukumarappan et al., 2010; Award et al., 2012; Chandrapala et al., 2012).

High-power-low-frequency ultrasound is used at frequencies in the range of 20-100 kHz and energy density of 10-1000 W/cm^2 (Muthukumarappan et al., 2010; Salazar et al., 2010). High power ultrasound has physical, chemical and biochemical effects and improves the quality of food systems during processing while modifying the physicochemical properties of various foods (Award et al., 2012).

OBJECTIVES OF ULTRASOUND IN FOOD TECHNOLOGY

High power ultrasound in food processing, microbial and enzymatic inactivation, crystallization, filtration, drying, extraction, emulsification, degassing, defoaming, freezing, enzyme activity and protein denaturation, separation, polymerization/depolymerization, cutting, thawing frozen food, processing of meat products and oxidation used in the processes. In general, there are many studies on the procedures in which ultrasound is used, its mechanism of action, its advantages and the products studied (Mason, 1998; Torley & Bhandari, 2007; Patist & Bates, 2008; Salazar et al., 2010; Baysal & Demirdöven, 2011; Chemat et al., 2011) are available.

Sound waves are used in the food industry to accelerate oxidation, inhibit enzyme activity, and perform emulsion, extraction, crystallization, filtration and gas removal processes. In addition, it has been reported that the application of ultrasonic sound waves in foods such as yogurt increases the activity of *Lactobacillus* by 50% and shortens the total production process by up to 40%, and accelerates the germination of seeds when used in herbal production. It can also be used for surface decontamination with liquid disinfectants (Povey & Mason, 1998).

Use in Microbial Inactivation

The investigation of ultrasonic sound wave technology as a microbial inactivation method started in the 1960s. The mechanism of microorganism death is mainly due to thinning of the cell membrane, localization of temperature and formation of free radicals (Butz & Tauscher, 2002). The

theory of the mechanism of inactivation of microorganisms is based on the disintegration of bubbles that occur at the microscopic level under the influence of changing pressure. The micromechanical shocks that occur during this disintegration disrupt the structural and functional compounds of microorganisms. In studies on the subject, there are explanations that ultrasonic sound waves can create a synergistic effect, especially in terms of microbial inactivation, when used with other preservation methods, not alone (Piyasena et al., 2003). Ultrasonic sound wave application in aqueous suspensions of *E. coli*, *S. aureus*, *B. subtilis*, *P. Aeruginosa*, *Trichophyton mentagrophytes* and *Feline herpesvirus* Type 1 (Bayraktaroğlu & Obuz, 2006). The cellular destruction of *E. coli* and *L. rhamnosus* cells was investigated by the application of high-intensity ultrasonic sound waves, and it was shown that the lethal effect of this wave was more resistant to Gram-positive *L. rhamnosus* than Gram-negative *E. coli* (Antana et al., 2005).

Ultrasound has a lethal effect on microorganisms. It has been stated that ultrasound application can destroy *Escherichia coli*, *Staphylococcus aureus*, *Bacillus subtilis* and *Pseudomonas aeruginosa* bacteria, *Trichophyton mentagrophytes* fungi and *Feline herpesvirus* type1 virus in aqueous suspension. The destruction of microorganisms is dependent on time and the power of the ultrasonic application. Increased potency and duration of application resulted in greater microbial destruction. The lethal effect of ultrasound on bacteria is based on the destruction of the cytoplasmic membrane. Because the destruction of the membrane prevents the proliferation of microorganisms (Pohlman, 1994).

Gram-positive cells, on the other hand, are more resistant than gram-negative cells due to their thicker cell walls. Spores are very resistant to ultrasound (Anonymous, 2011). In a study, the inactivation of *Streptococcus faecium* and *Streptococcus durum* was investigated in a 20 kHz/160 W application at temperatures ranging from 5 to 62 °C (Ordoñez et al., 1984). It has been observed that the application of ultrasound with temperature is much more effective. Ultrasound was applied on *Bacillus subtilis* spores in milk at a temperature range of 70-95 °C (Ordoñez et al., 1987). While ultrasound alone did not show any effect, the application of ultrasound with temperature reduced the sports population by 63-73%. In another study, ultrasound method was applied with previous norms for *Staphylococcus aureus* in UHT milk. It has been observed that the heat treatment applied together with ultrasound reduces the D values 43% more than the thermal method alone. It is stated that ultrasound application combined with high pressure and thermal treatments is effective on *L. monocytogenes*. Since dense liquids and solids prevent the propagation of ultrasound waves, this technique is thought to be more useful for sterilization of milk and fruit juices (Bayraktaroğlu & Obuz, 2006).

In the study conducted by Yıldırım and Öksüz (2013), as a result of the application of sound waves at different frequencies to *E. coli* bacteria, the samples taken from the control and experimental groups at different time intervals were sown on solid media and colony counts of the bacteria formed as a result of sowing were made. In the light of these data, the relationship between the frequency of the sound, the duration and the number of colonies was tried to be revealed. Yıldırım and Öksüz (2013) found that sound waves have a reducing effect on the number of bacteria. It was observed that all subsonic and ultrasonic waves in the study reduced the number of bacterial colonies in the solid medium. Subsonic (5 kHz, 11 kHz) waves were found to be more effective in reducing the colony count of bacteria and removing them from the environment than ultrasonic (21 kHz, 25 kHz, 30 kHz, 35 kHz) waves. However, it has been determined that subsonic waves cause discomfort for the human ear in removing bacteria from the environment, while ultrasonic waves are not heard and do not cause discomfort in the environment.

Use in Extraction of Bioactive Components

Treatment with ultrasonic sound waves is a possible innovation for the extraction of bioactive compounds in industry (Virot et al., 2010). Extraction of bioactive components by propagation of ultrasonic sound waves; It is one of the extraction techniques that supports a high level of manufacturability in a short time, is easy to apply, and reduces solvent consumption, temperature and energy input (Chemat et al., 2008). Ultrasonic sound waves; its a non-thermal effective alternative method for extract extraction. Ultrasonic sound wave application breaks down cell walls mechanically and provides material transfer. With the destruction of the cell wall, the liquid extract inside the cell can easily get out of the cell. Since the cell wall is removed with this application, the extraction process with this method is faster than other extraction methods. With this treatment, the surface area between the solid and liquid parts increases as a result of decreasing the particle diameter. The mechanical activity of ultrasonic sound waves accelerates the distribution of the solvent towards the tissues. When the cell wall is mechanically broken down, the intracellular components easily pass into the solvent (Kim & Zayas, 1989). Ultrasonic sound wave application also improves the extraction kinetics and the quality of the extract. As a result of the optimization of the extraction process of phenolic components from wheat bran, it was emphasized that the most suitable process was obtained by ultrasonic extraction with 64% ethanol at 60 °C for 25 minutes (Wang et al., 2008). It has been found that the results obtained in the ultrasonic sound wave assisted extraction system used in the extraction of dill are 1.3-2 times faster than the traditional extraction (Torley & Bhandari, 2007). This practice has also been used

in oil extraction from oilseeds such as rapeseed, soybean and sunflower, and has halved the processing time without changing the extracted oil compositions (Luque-García & Luque de Castro, 2004). Extraction with this treatment creates a "sponge effect" on the solid material. Ultrasonic vibration movements cause mechanical pressure waves, causing the liquid inside the solid to come out and the external liquid to enter the solid, so a more efficient extraction process takes place (Tavman et al., 2009). It has been reported that the sensory quality of tea infusion with ultrasonic sound assisted extraction is much better than tea infusion with traditional extraction (Xia et al., 2006). Hesperidin and total phenolic content from Penggan (*Citrus reticulata*) bark (Ma et al., 2008a). Ultrasonic sound wave assisted extractions have been used recently for the extraction of phenolic acid and chavanone glycoside (Ma et al., 2008b) from Satsuma mandarin (*Citrus unshiu Marc*) bark.

Usage in Homogenization / Emulsification Processes

The process of mixing two immiscible liquids is called emulsion, and the substances added to the environment to mix them are called emulsifiers. A good homogenization/emulsification can be achieved when ultrasound is applied to two immiscible liquids. When the bubbles formed as a result of the cavitation process created by the ultrasound process in the liquids burst between these two liquids, a shock effect occurs and allows these two liquids to mix more homogeneously. High energy ultrasound treatment contributes to the formation of a more stable emulsion compared to the low energy applied ultrasound treatment (Soria & Willamiel, 2010).

It has been observed that ultrasound treatment applied in a mixing process with palm oil and β-lactoglobulin alginate can make the coagulating droplets very small and prepare a suitable environment for emulsion (Pongsawatmanit et al., 2006). Gaikwad and Pandit (2008) investigated the effects of ultrasound on droplet sizes in the dispersed phase, volume and physicochemical properties of the dispersed phase, time and power effects in oil. As a result, it was observed that the droplets obtained by applying the ultrasound process were smaller in size compared to the droplet sizes normally produced. Bermudez-Aguirre et al. (2008) conducted a study on the microstructure of fats in thermosonicated ultrasound treated milk with electron microscopy and concluded that the granular surface and fat globules become smaller due to their interactions with some casein micelles of fat globules, and thus the fat globule membrane in milk is fragmented. It is thought that the use of ultrasound technology in the production of ketchup and mayonnaise will increase the stability of the emulsion (Povey, 1998).

The food industry will benefit greatly from the ultrasound process in the future. In order for this process to have a better effect, while designing the ultrasound equipment, a tool that can affect the entire liquid of the cavitation process should be developed and used for a more effective emulsification process (Soria & Willamiel, 2010). Ultrasound treatment has the potential to be an alternative for the industry, since emulsion processes applied in the industry take a long time, require labor, troubles in finding the emulsifiers to be used, and being a costly method.

Use for Filtration Purposes

The application of ultrasonic sound waves for filtration and imaging processes can benefit the process in a number of ways. These provide vibrational energy to keep particles in suspension, create a frictionless surface area, allow rapid passage of liquid or small particles.

Ultrasound has very important effects in the filtration process. During the filtration process, solid materials leave residue on the surface of the filter membrane, resulting in clogging of the filter pores and interruption of the filtration process. Thanks to the filtration process with ultrasound treatment, cake and polarized substances formed on the surface of the filter membrane are broken and the flow becomes faster. In addition, it has been observed that the application of ultrasound treatment together with the membrane filter gives a more effective result than the application of ultrasound alone (Chemat et al., 2011).

Use in Inactivation of Enzymes

The effectiveness of ultrasound against enzymes found in foods increases with the combination of heat, pressure and other processes with which it is used, as in microorganisms. Along with thermosonication, monosonication and monothermosonication applications, ultrasound is an effective method against enzymes such as lipoxygenase (LOX), polyphenoloxidase (PPO), peroxidase (POD) and lipase and protoase enzymes that are resistant to heat (Lopez & Burgos, 1995; Vercet et al., 1997; O'Donnell et al., 2010). The effectiveness of the ultrasound process can be explained by the energy generated as a result of the explosion of the cavitation bubbles formed in the application, as in the effectiveness with microorganisms.

Coakley et al. (1973) applied ultrasound treatment to alcohol dehydrogenase, catalase and lysozyme at a pressure of 20 kHz and determined that the process had a very good effect against alcohol dehydrogenase and lysozyme enzymes, while its effect was very limited against catalase enzyme. In another ultrasound study against the lysozyme enzyme, it was reported that ambient temperature and atmospheric

pressure are not very effective, and that the desired temperature is 60-70°C and 200 kPa at pressure for successful inactivation (Manas et al., 2006). Kadkhodaee and Povey (2008) applied heat, pressure and ultrasound (thermosonication) treatments on α-amylase together. As a result of the study, they determined that the activation energy of the enzyme was 109 kJ/mol K with only heat treatment, and the activation energy of the enzyme decreased to 19.27 kJ/mol K as a result of the treatment applied with thermosonication. Özbek and Ülgen (2000) stated in their study that the effect of ultrasound on enzymes depends on the amino acid composition of the enzymes. Tiwari et al. (2009) emphasized that ultrasound alone is not sufficient in a study they conducted on pectin methyl esterase (PME). They found that the best treatment on the PME enzyme was 10 minutes at high acoustic energy density (1.05 W/ml), and there was a 62% reduction in the PME enzyme as a result of the treatment.

Cheng et al. (2007) applied a treatment to tropical fruits at low pressures in an ultrasound bath. In this study, they observed that when they applied high-pressure ultrasound to the fruits, they saw that the cell walls of the fruits were broken down and the proteins were denaturated, and therefore they concluded that the low-pressure ultrasound treatment was more appropriate. Lopez et al. (1994) applied the monothermosonication process on PPO in a study and observed a decrease in the D value of the enzyme as a result of the experiment. However, they stated that ultrasound treatment can reduce the resistance of enzymes, but heat application is required for inactivation. Peroxidase enzyme is an enzyme that causes the vegetables to turn white due to its high heat stability. Peroxidase enzyme is an important enzyme due to its presence in fruits and vegetables and the color and taste changes it creates in them. With the thermosonication process, the peroxidase enzyme is inactivated and the time required for the bleaching process is also reduced. For example, for 90% inactivation of peroxidase enzyme, 70 s of heat treatment is required, while this rate is 5 s with thermosonication application for some food samples (Cruz et al., 2006).

The LOX enzyme in soybean oil can be inactivated at a rate of 75-85% with ultrasound treatment (Thakur & Nelson, 1997). The inactivation of the LOX enzyme during the ultrasound process depends on factors such as temperature, application time, pH, and ultrasound frequency range. With daily ultrasound application to milk, pathogenic and spoilage microorganisms in milk can be easily inhibited. However, most of the microorganisms in the environment can reduce the quality and shelf life of milk obtained by UHT by producing extracellular lipase and protease. The monothermosonication process can be more effective than conventional methods when applied against these heat-resistant microorganisms (Lopez

& Burgos, 1995). Villamiel and De Jong (2000a), in a study investigating the effect of ultrasound on enzymes, found that ultrasound alone had no effect without heat. However, when the temperature was increased above 61 °C and sonication was applied, it was observed that the enzymes were inactivated. They found that the inactivation effect of all enzymes in milk was related to the environment properties.

Various processes occurring in the presence of cells or enzymes are activated by ultrasonic sound waves. High-intensity sound waves disrupt cells or denature enzymes. It has been shown that an increase in fermentation rate occurs in beer and wine production when low-intensity sound waves are applied during fermentation (Matsuura et al., 1994). A decrease in the viscosity of maize starch granules with ultrasonic sound waves was detected and it was stated that this effect was related to the partial breaking of glycosidic bridges, which led to a decrease in the molecular weight of starch (Huang et al., 2007), but it was also seen that the opposite of this effect could be possible (Bates et al., 2006). Ultrasonic sound wave treatment allows moisture to move quickly into the fiber web causing viscosity increase in tomato puree. In some studies, structural changes were observed on proteins after this application (Kresic et al., 2008).

USAGE AREAS OF ULTRASOUND IN FOOD TECHNOLOGY

In Ice Cream Technology

Recent studies have shown that ultrasound technology gives promising results on freezing. The benefit of the sound energy produced by the ultrasound technology can be explained by the various effects it makes while passing through the environment. Among the effects caused by sound waves, perhaps the most important is their cavitation effect. The gas bubbles formed with the help of ultrasound are very small in size and the process continues continuously. At this time, ice nuclei (icing) may form and these crystals allow the freezing process to be more efficient. On the other hand, when dense and incompressible materials are subjected to varying acoustic stress, ice crystals break, resulting in the formation of similarly sized ice crystal fragments. This is a targeted situation in the freezing process (Zheng & Sun, 2006).

As a result, the cavitation effect is thought to be beneficial in various freezing processes. If ultrasound technology is applied in the freezing of fresh foods, the freezing process can be done in a shorter time and at the same time, it will lead to the formation of higher quality foods. In addition, if this process is applied to the freezing process together with drying, the size of the ice crystals in the frozen product can be controlled. In addition, the ultrasound process has benefits such as the formation of a

frozen surface in the partially frozen product, the reduction of ice crystals and the prevention of crust formation from the frozen surface. For all these reasons, a freezing process using ultrasound can contribute to the formation of both a high-value food product and a pharmaceutical product (Zheng & Sun, 2006). In a study investigating the effect of ultrasound application on freezing time, it was determined that ultrasound treatment reduces the freezing time of potato slices (Li & Sun, 2002).

In Meat and Products Technology

Along with safety and color, crispness is one of the most important features sought by consumers in meat. While the crispness of meat varies greatly due to biological and technological factors, technological applications are being tried to increase the crispness of the meat and reduce its variability. Among these applications, the application of ultrasound can trigger the mechanical change of the intercellular structure. In a study, muscle samples (~ 50 g) taken from eight cattle were subjected to ultrasound application in both pre-rigor (pre-rigor) and post-rigor (post-rigor) periods. In the pre-firm application, ultrasound caused very little delay in postmortem stiffness (rigor mortis), stretching of the sarcomere, ultra-structural change in the Z-line region, and a sudden increase in calcium secretion in the chitosol region. It has been concluded that there is no definite result. While the application after hardening did not cause any structural change, a slight improvement in the ripening index occurred after 6 days (Got et al., 1999).

Short-term low-frequency high-intensity ultrasound application to a whole meat placed in a degassed mineral salt solution can reduce the firmness of meat that is not placed in simultaneous mineral salt (Smith et al., 1991). Ultrasound applied to cured ham (with 2% salt addition) can increase intermolecular cohesion (Reynolds et al., 1978).

In Dairy and Products Technology

Jambrak et al. (2008) investigated the solubility and foam formation properties of proteins at 20, 40 and 500 kHz at 15 and 30 minutes to determine the properties of serum protein suspensions. While the high frequency did not cause any change in these properties, they reported that the hydrophilic parts of the amino acids were opened towards the water at low frequencies and 15 minutes of application, and the solubility of the protein increased with the change in the structure and conformation. They reported that changes in the tertiary structure of globular proteins with the increase in the number of charged groups with high conductivity may also be effective on the increase in solubility. Thus, they reported that electrostatic forces will increase and more water will bind to protein and protein-water interaction will increase (Jambrak et al., 2008; Kresic et al.,

2008). An increase in foam formation was also detected in a short time and at low frequency. Hydrolysis of serum proteins and local temperature increase during the process increase foam formation. The increase in foaming property has been associated with the homogenization effect of ultrasound (Jambrak et al., 2008; Jambrak et al., 2010). They determined that α-LA was more resistant to ultrasound treatment than β-LG (Jambrak et al., 2008; Chandrapala et al., 2012).

In a study investigating the effect of pH on the recombination of casein micelles at low (35 kHz) and high (130 kHz) frequencies, it was determined that as the pH value increased, the turbidity decreased and the particle size of the samples increased. Expansion of micelles was attributed to electrostatic repulsion between casein molecules and increased serum phase quality. It has been reported that 130 kHz is more effective in increasing interparticle homogeneity and lowers the viscosity more. They attributed this effect to the fact that 130 kHz was more effective in dispersing the micelles than 35 kHz, and that more free radicals were formed in the environment surrounded by the splitting of the bubbles (Madadlou et al., 2009).

Bermudez-Aguire et al. (2009b) investigated the protein, acidity, fat, color and microbiological properties of milk by thermosonication and heat treatment and stored the processed milk at 4 °C for 16 days. It was determined that the protein content and pH of the thermosonicated samples decreased, while the oil content and acidity increased. The decrease in protein was explained by denatured serum proteins and partial modification of the tertiary and quaternary structure of casein, while the increase in fat content was attributed to the cavitation breaking fat globules and the release of triacylglycerol. The decrease in pH value was associated with enzymatic activities resulting from cavitation and the increase in acidity with nitrite, nitrate and hydrogen peroxide formed after lipolysis and sonication. As a result of storage, acidity and pH remained constant. At the end of storage, no more than 2 log increase was observed in the mesophilic bacteria content of the samples that were subjected to ultrasound. This decrease in bacteria increased with the increase of power, which shows that a certain amount of power is required for cell walls to be damaged. Cavitation, which occurs according to the increase in power, creates pores on the cell walls, the cell structure is disintegrated and the cells are broken. In addition, free radicals formed by the sonolysis of water in aqueous media and their combination have a bactericidal effect. When the colors of the ultrasound applied samples were examined, they were found to be whiter (Bermudez-Aguire et al., 2008; Bermudez-Aguire et al., 2009b; Riener et al., 2010).

Shanmugam et al. (2012) reported that the turbidity of the samples decreased, while the viscosity of the samples did not change with the application of ultrasound at 20 kHz, 20 and 41 W energy and at 22 and 30°C for 15, 30, 45 and 60 minutes in pasteurized skim milk. Small reductions in the size of the casein micelles were observed at two power levels, while significant reductions in fat globules were observed. With the increase of sonication time at applied power levels, a decrease in dissolved particles was observed due to the shear effects produced by acoustic cavitation. It is reported that the turbulence that occurs after cavitation causes an increase in the mobility of the particles and supports the formation of aggregates. In the study, they associated the decrease of serum proteins among the soluble particles with denaturing. They reported that denatured/aggregate serum proteins interact with κ-casein and form micellar aggregates, and that these aggregates are formed by the thiol-disulfide exchange reaction.

It has been reported that gram-negative bacteria, which *Pseudomaonas fluorescens* and *Streptococcus thermophilus* can be inactivated by ultrasound, are more sensitive than gram-positive bacteria in milk samples. It has been reported that ultrasound treatment is more effective than the application of ultrasound alone on inactivation with temperature, but they reported that the lethal effect decreases when the temperature rises above 60 °C (Villamiel & De Jong, 2000b). It has been reported that thermosonication provides a 5.3 log reduction on *Listeria innocua* in milk samples. It was observed that the cells weakened and decreased towards the end of the treatment period, where the bacteria remained in a constant period under moderate thermosonication conditions. In the inactivation of bacteria, as a result of cavitation, the cells first weaken and then are destroyed. In the study, it was reported that ultrasound can also inactivate mesophilic bacteria (Bermudez-Aguirre, 2009a). Ultrasound was applied to raw, low heat treated (55 °C/15 h) and pasteurized milk (75 °C-15s) and the samples were stored at 4 °C and changes in the number of viable bacteria and psychrotrophic bacteria were observed. Live bacteria and mesophilic bacteria persisted for 1-2 days as a result of ultrasound application to raw milk, while heat-treated milks lasted 2-5 days, pasteurized milks lasted 8 days (Chouliara et al., 2010).

It was determined that volatile compounds were formed by applying high power ultrasound to milk. They reported that the number of volatile compounds formed increased as the duration of the applied ultrasound, which initially contained acetone, dimethylsulfite, 2-butane and chloroform, increased in the form of a decrease-increasing amount (Riener et al., 2010). In food systems, carbonyl compounds such as hexanal and heptanal are defined as secondary oxidation products. In milk, these compounds are formed by the breakdown of hydroperoxides by photooxidation. Therefore,

volatile compounds are formed by increasing lipid oxidation by sonication (Riener et al., 2009; Chouliara et al., 2010). This undesirable taste and odor in milk has been defined as "rubbery", that is, "rubber-like", and it has been shown that this undesirable aroma can be eliminated by reducing the sonication power (Riener et al., 2009).

Villamiel and De Jong (2000a) reported that ultrasound treatment was insufficient to inactivate alkaline phosphatase, γ-glucomyltranspeptidase, and lactoperoxidase enzymes in fat and skim milk, and when used with heat, it inactivated alkaline phosphatase and γ-glucomyltranspeptidase in milk, while a certain degree of inactivation was achieved in lactoperoxidase. In the same study, they reported that β-LG and α-LA were denatured in fat and skim milk with ultrasound application at 75.5 °C, and denaturation occurred more in skimmed milk. While changes may occur in the tertiary and quaternary structures of caseins, it was determined that ultrasound did not completely wash the casein micelles.

It has been reported that fat globules can be reduced by more than 1 μm by applying ultrasound to milk at 400 W, 24 kHz and 63 °C for 30 minutes. This effect occurs with the destruction of the fat globule membrane as a result of cavitation (Bermudez-Aguirre et al., 2008). Similarly, Villamiel and De Jong (2000a) reported that an 81.5% reduction can be achieved in the fat globules of milk with ultrasound treatment applied with heat and increased application time. They reported that cream formation in milk would not be observed during storage, with the diameter of the fat globules falling below 0.8 μm. Vercent et al. (2002) reported that the diameter of fat globules could be smaller than 0.8 μm by manothermosonication. Ertugay et al. (2004) reported that the fat globule diameter could be reduced by applying ultrasound to milk at different times and strengths. They showed that the fat globule diameter was 0.725 μm at 100% power and 10 min, and when ultrasound was applied at 40% power, the same size reduction could be achieved with conventional homogenization. The best homogenization efficiency (4-6%) was obtained with 100% power and 10 minutes of treatment. In another study, they reported that ultrasound treatment was more effective than conventional homogenization at increasing power levels and increasing durations. They reported that the diameter of fat globules is less than 2 μm and this effect occurs as a result of cavitation (Wu et al., 2001).

Sengul et al. (2009) examined the effect of homogenization with ultrasound on the water holding capacity of yoghurt, and applied 20, 50 and 70 % power and 3 and 6 minutes of treatment. The highest water holding capacity (66.18%) and homogenization efficiency were obtained in the sample with 70% power and 6 minutes of treatment. As a result of the ultrasound process, the diameter of the oil particles decreased and the total

oil membrane surface increased, and the water holding capacity increased at high power levels, since there were many newly bonded hydrophilic caseins on the membrane surface (Ertugay et al., 2004).

Wu et al. (2001) produced yoghurt by applying ultrasound to milk and applying ultrasound for homogenization after the starter addition to milk, and reported that the fermentation time of the samples, which were applied ultrasound after the starter addition, was shortened by 30 minutes. This effect shows that 8 min ultrasound treatment at 40, 60 and 100 powers did not inactivate the yogurt cultures. In addition, the release of intracellular enzymes from yoghurt bacterial cells according to sonication also promotes acid development. The released β-galactosidose shows high intracellular lactose hydrolysis activity and acid production increases.

It was determined that homogenizing the milk with the application of manothermosonication (MTS) increased the water holding capacity of yoghurt. Although the rheological properties of yoghurt prepared by manothermosonication were better, it was reported that they exhibited thixotropic and pseudoplastic behavior in two samples. With MTS application, the initial viscosities of the yoghurts were higher, but the decrease over time was higher. G' values of MTS yoghurts were 50% higher than control yoghurts (Vercent et al., 2002).

Riener et al. (2009) The effect of applying thermosonication (TS) process at 24 kHz frequency at 45 °C for 10 minutes to milk samples with 3 different fat compositions (0.1%, 1.5 and 3.5) on the water holding capacity, particle size and rheological properties of yoghurt produced traditionally. 90 °C-10 min) were determined by comparison. The fat globules of the milk treated with TS at 3 different fat ratios were found to be 2.5 times smaller than the milk treated with the conventional method. The pH values of TS applied yoghurts were higher than the traditional method (Riener et al., 2010). The G' values and water holding capacities of TS applied yoghurts are higher than the traditional method. In their study, they reported that with the traditional method, serum proteins were denatured at a higher rate than TS, but gel hardness decreased at high denaturation. They attributed this effect to the support of the distribution of casein micelles to the subunits during the development of the culture, the formation of a strong network by rearrangement with each other, and the degree of denatured serum proteins. The main reason for the increase in the hardness of yoghurt is the enrichment of fat globules, which are reduced in size with TS, with coagulated proteins. The water holding capacity of yoghurts produced with TS, whose structure is strengthened by protein-protein and protein-fat interaction, has increased with the increase in the ability to bind water in the 3-dimensional network structure (Riener et al., 2009).

Nguyen et al. (2010) compared the properties of acid gel obtained by applying temperature-controlled and uncontrolled ultrasound to skimmed milk with the traditional method (80 °C-30 min). When the temperature is between 20-40 °C, higher G' is obtained compared to the treated sample, while when the temperature rises to 60-70 °C, a G' value close to the conventional heat treatment is obtained. It has been reported that denaturation of α-LA takes longer time than denaturation of β-LG. It has been reported that almost all of the α-LA and β-LG were denatured by ultrasound application at 70 °C for 30 minutes, while denaturation of 70% and 80% occurred at 60 °C. It has been reported that κ-casein level increased as the ultrasound duration increased in the serum phase, and decreased since serum proteins were denatured after 15 minutes of treatment, and then an increase occurred. After applying ultrasound for 15 and 30 minutes at 20 °C, heat treatment was applied to the oil-free samples at 80 °C-30 minutes, and it was reported that the G' value of the acid gels obtained was higher than those that did not undergo heat treatment.

In the study with serum protein solutions, first heat treatment was applied at 80 °C for 1 minute, then ultrasound was applied at 50% power for 5 seconds and 20 minutes, and lastly, heat treatment was applied at 85 °C for 20 minutes. A sample with only two heat treatments and only a final heat treatment was also prepared. It has been reported that while the viscosity increases in the sample where two heat treatments are applied, the viscosity decreases in the samples where the ultrasound treatment is applied due to the physical forces produced by acoustic cavitation. It has been reported that the aggregation of serum proteins by heat treatment is effective in the increase in viscosity with heat treatment (Ashokkumar et al., 2009). In another study, it was reported that while the particle size of serum protein concentrate solutions, which were subjected to two heat treatments, increased with the application of two heat treatments, denatured serum proteins formed aggregates with hydrophobic and disulfide-thiol interactions at temperatures above 65 °C, resulting in an increase in viscosity. It has been reported that as a result of the application of ultrasound, a decrease in particle size and viscosity occurs with the effect of cavitation (Zisu et al., 2010).

Ertugay et al. (2012) prepared ayran samples for yoghurts prepared with the traditional method (95 °C-5 min) with 40% water and 1% salt in the final product. Samples were prepared by applying and not applying ultrasound treatment to these samples at 20 kHz fixed frequency at 40%, 60% and 80% powers (500 W maximum power) for 2 and 4 minutes and they were stored for 15 days. All specimens exhibited pseudoplastic behavior. The apparent viscosity of the samples increased as the applied power and time increased.

Other Area of Usage

The effect of ultrasonic sound wave treatment on the solubility and foaming properties of whey suspensions was investigated. In this study, high-intensity (500 kHz) and low-intensity ultrasonic sound waves (20 kHz probe and 40 kHz water bath) were used and it was determined that pH did not change significantly with these treatments. Ultrasonic sound wave technique with a frequency of 40 kHz has less effect on protein properties and much better results were obtained with 15 minutes of treatment instead of 30 minutes (Jambrak et al., 2008).

These waves are a method developed to prevent possible damages in many process stages such as cutting / shredding / slicing of foods, shaping. Ultrasonic sound breaking is a powerful non-linear percussion process and is used in many industrial applications (Arnold et al., 2009). With this application, cutting/slicing is a fairly new method to be used in the food industry and there are still many deficiencies that need to be studied. The selection of properties used in cheese technology depends on the type of cheese. In particular, composition properties such as total dry matter, fat and protein content of cheese affect the cut-off frequency (Myshkin et al., 2005).

The effect of high-power ultrasonic sound waves on the quality parameters, nutritional and sensory characteristics of the oil was investigated. Oils obtained from sonicated olive pastes showed lower bitterness, while it was stated that they had higher values in terms of tocopherol, chlorophyll and carotenoid content (Jiménez et al., 2007).

It has been shown that unwanted reactions between radicals and food components generated by ultrasonic sound waves can be minimized by selecting low ultrasonic frequencies in food processing. However, high frequency ultrasonic sound waves can be used in food processing, provided that a suitable radical scavenger is present in the solution (Ashokkumar et al., 2008). With the application of ultrasonic sound to liquids, free radicals emerge. It transforms into OH^-, H^+ or hydrogen peroxide. These compounds have significant bactericidal action. The first target of free radicals in the cell is DNA and they break the chain at various points (Earnshaw, 1998). Cavitational density largely reveals the mechanism of inactivation. It has been reported that this density is measured as the production rate of H_2O_2 (O'Donnell et al., 2010).

The application of low frequency high power ultrasonic sound waves (<0.1 MHz, 10-1000 W/cm^2) in the food industry has been widely researched in recent years. Ultrasonic sound waves technique alone or in combination with temperature has no effect on *E. coli* and *L. monocytogenes* (Baumann et al., 2005) found in fluid (Salleh-Mack & Roberts, 2007) and apple juice

(Ugarte-Romero et al., 2006). may have been reported. Inactivation of pathogenic and spoilage microorganisms and enzymes by sonication is mainly caused by physical (cavitation, mechanical effects) and/or chemical (formation of free radicals due to sonochemical reaction) processes. Inactivation of alcohol dehydrogenase, catalase and lysozyme enzymes was investigated by applying a 20 kHz ultrasonic sound wave into a model solution and it was determined that alcohol dehydrogenase and lysozyme enzymes were inactivated very well, but showed very low effects for catalase (Coakley et al., 1973). It has been stated that the inactivation mechanism of this application depends on the conformational mechanism and amino acid composition of the enzymes, and it varies according to the studies conducted (Özbek & Ülgen, 2000). Some enzymes, such as catalase, invertase or pepsin, are resistant to ultrasonic sound wave treatment (Sala et al., 1995). It has been shown that inactivation of the alpha amylase enzyme is achieved by thermosonication (Kadkhodaee & Povey, 2008). When sonication is combined with applications such as low temperature, low pressure and pH, it increases the effectiveness of ultrasonic sound wave technique (Feng, 2010). Generally, low frequencies of ultrasonic sound waves are used in food processing. This situation causes cavitation of sound waves with an intensity of 20-100 kHz and 10-1000 W/cm^2 (Feng & Yang, 2005). The application of these waves on the quality of some fruit juices such as orange (Valero et al., 2007), guava (Cheng et al., 2007) has minimal effect. It has been investigated whether ultrasonic sound wave technology is a potential force for inactivation of various foodborne pathogens (Jiranek et al., 2008).

Recently, the effect of thermosonication on the microstructure of fat globules in milk has been studied by electron microscopy. Treatment with ultrasonic sound wave; it causes small fat globules on the surface due to the interaction of some casein micelles, leading to the breakdown of the globular membrane of milk fat (Bermúdez-Aguirre et al., 2008). Compared to classical homogenization, it was stated that ultrasonic homogenization was more effective on the water holding capacity of yogurt, and the water holding capacity increased as the processing time and power level increased (Şengül et al., 2009).

CONCLUSION

Ultrasound technology has the potential to be a food preservation method that can be used a lot in the future in the food industry due to its features such as not damaging the product it is applied to, being easy to apply and being environmentally friendly. It is a development that the food industry dreams of replacing the thermal processes already applied in food preservation, such as pasteurization and sterilization, to non-thermal technologies such as ultrasound. Because the negativities that occur in

thermal processes can cause both material and moral damage to food businesses. Elimination of damages in such transactions is important in terms of nutrition, as well as in terms of advertising and market share of the business. Experiments show that ultrasound technology alone is not sufficient for the preservation of foods. On the other hand, when ultrasound is used together with heat, pressure or heat + pressure, it has been observed that the process efficiency increases too much. Although it is still widely used in laboratory studies, it has not been fully integrated into the industry stage. It is trying to develop the applications of ultrasound technology in instrument and equipment parts and to shift it to the industrial stage by following this development. However, the food industry prefers not to use this technology due to some problems encountered in applications. If such negativities can be prevented, ultrasound technology will become an application that both science and the food industry will benefit widely in the future.

REFERENCES

1. Ananta, E., Voigt, D., Zenker, M., Heinz, V. & Knorr, D., (2005). Cellular injuries upon exposure of *Escherichia coli and L. rhamnosus* to high-intensity ultrasound, *J Applied Microbiol*, 99, 271-278.

2. Anonymous, 2011. A report of the Institute of Food Technologists for the Food and Drug Administration of the U.S. Department of Health and Human Services. http://www.fda.gov/food/ScienceResearch/ResearchAreas/ Safe Practices for Food Processes/ucm100158.htm.

3. Arnold, G., Leiteritz, L., Zahn, S. & Rohm, H., (2009). Ultrasonic cutting of cheese: Composition affects cutting work reduction and energy demand, *Int Dairy J*, 19, 314–320.

4. Ashokkumar, M., Sunartio, D., Kentish, S., Mawson, R., Simons, L., Vilkhu, K. & Versteeg, C. K., (2008). Modification of food ingredients by ultrasound to improve functionality: A preliminary study on a model system, *Innov Food Sci and Emerg Technol*, 9, 155–160.

5. Ashokkumar, M., Lee, J., Zisu, B., Bhaskarcharya, R., Palmer, M. & Kentish, S., (2009). Hot topic: Sonication increases the heat stability of whey proteins, *Journal Dairy Science*, 92:5353-5356.

6. Ashokkumar, M., Bhaskaracharya, R., Kentish, S., Lee, J., Palmer, M. & Zisu, B. (2010). The ultrasonic processing of dairy products-An overview. *Dairy Science Technology*, 90, 147-168.

7. Award, T. S., Moharram, H. A, Shaltout, O. E., Asker, D. & Youssef, M. M., (2012). Applications of ultrasound in analysis, processing and quality control of food: A review, *Food Research International*, 48, 410–427

8. Bates, D. M., Bagnall, W. A. & Bridges, M. W., (2006). Method of treatment of vegetable matter with ultrasonic energy, US Patent Application, 20060110503.

9. Baumann, A. R., Martin, S. E. & Feng, H., (2005). Power ultrasound treatment of *Listeria monocytogenes* in apple cider, *J of Food Protect*, 68, 2333-2340.

10. Bayraktaroğlu, G. & Obuz, E., (2006). Ultrasound yönteminin ilkeleri ve gıda endüstrisinde kullanımı, Türkiye 9. Gıda Kongresi, Bolu, Bildiriler Kitabı, 57-60.

11. Baysal, T. & Demirdöven, A., (2011). Ultrasound in Food Technology: Handbook on Applications of Ultrasound: Sonochemistry for Sustainability, 163-184. Edited by Ackmez Mudhoo., CRC Press.

12. Bermúdez-Aguirre, D., Corradini, M. G., Mawson, R. & Barbosa-Cánovas, G. V. (2009a). Modeling inactivation of *Listeria innocua* in raw whole milk treated under thermo-sonication. *Innovative Food Science and Emerging Technologies*, 10, 172-178.

13. Bermudez-Aguirre, D., Mawson, R. & Barbosa-Canovas, G. V., (2008).

Microstructure of fat globules in whole milk after thermosonication treatment, *Journal of Food Science*, 73, 325–332.

14. Bermúdez-Aguirre, D., Mawson, R., Versteeg, K. & Barbosa-Cánovas, G. V. (2009b). Composition properties, physicochemical characteristics and shelf life of whole milkafetr thermal and thermo-sonication treatments. *Journal of Food Quality*, 32, 283-802.

15. Butz P. & Tauscher, B., (2002). Emerging technologies: Chemical aspects, *Food Res Int*, 35, (2/3), 279-284.

16. Büyüktanır, A., 2010. Ultrases (Ultrasound), Gazi Üniversitesi Gazi Eğitim Fakültesi Orta Öğretim Fen ve Matematik Alanları Eğitimi Bölümü Fizik Eğitimi Anabilim Balı, Danışman: Mustafa Karadağ, Ankara.

17. Chandrapala, J., Oliver, C., B., Kentish, S. & Ashokkumar, M., (2012). Ultrasonics in food processing, *Ultrasonics Sonochemistry*. 19:5, 975-983.

18. Chemat, F., Huma, Z. & Khan, M. K., (2011). Applications of ultrasound in food technology: processing, preservation and extraction. *Ultrasonic Sonochemistry*, 18, 813-835.

19. Chemat, F., Tomao, V. & Virot, M., (2008). Ultrasound- assisted extraction in food analysis, In: Handbook of Food Analysis Instruments by Semih Ötles, 85–103. Boca Raton, Florida, USA: CRC press.

20. Cheng, L. H., Soh, C. Y., Liew, S. C. & Teh, F. F., (2007). Effects of sonication and carbonation on guava juice quality, *Food Chemistry*, 104, 1396–1401.

21. Chouliara, E., Georgogianni, K. G., Kanellopoulou, N. & Kontominas, M. G. (2010). Effect of ultrasonication on microbiological, chemical and sensory properties of raw, thermized and pasteurized milk. *International Dairy Journal*, 20, 307-313.

22. Coakley, W. T., Brown, R. C. & James, C. J. (1973). The inactivation of enzymes by ultrasonic cavitation at 20 KHz, *Archives of Biochemistry and Biophysics*, 159, 722–729.

23. Cruz, R. M. S., Vieira, M. C. & Silva, C. L. M. (2006). Effect of heat and thermosonication treatments on peroxidase ınactivation kinetics in watercress (*Nasturtium officinale*), *Journal of Food Engineering*, 72, 1, 8–15.

24. Demirdöven, A. & Baysal, T., (2009). The use of ultrasound and combined technologies in food preservations. *Food Reviews International*, 25, 1-11.

25. Earnshaw, R. G., (1998). Ultrasound a new oppurtunity for food preservation. In M. J. W. Povey & TJ Mason (Eds.), Ultrasound In Food Processing, 183-192. London: Blackie Academic & Professional.

26. Ertugay, M. F., Şengül, M. & Şengül, M., (2004). Effect of ultrasound treatment on milk homogenization and particle size distribution of fat, *Turkish Journal of Veterinary and Animal Sciences*, 28, 303-308.

27. Ertugay, M., Başlar, M., Şengül, M. & Sallan, S., (2012). The effect of

acoustic energy on viscosity and serum separation of traditional ayran, a Turkish yogurt drink, *Gıda* 37, 5, 253-257.

28. Feng, H. & Yang, W., (2005). Power ultrasound, In Y. H. Hui (Ed.), Handbook of Food Science, Technology, and Engineering, New York: CRC Press., 3632

29. Feng, H., (2010). Ultrasound technology in food processing and preservation, 1th International Congress on Food Technology, 3-6 Kasım, Antalya, Turkey, 60.

30. Gaikwad, S. G. & Pandit, A. B., (2008). Ultrasound emulsification: effect of ultrasonic and physicochemical properties on dispersed phase volume and droplet size, *Ultrasonics Sonochemistry*, 15, 554–563.

31. Got, F., Culioli, J., Berge, P., Vignon, X., Astruc, T., Quideau, J. M. & Lethiecq. M., (1999). Efects of high-intensity high-frequency ultrasound on ageing rate, ultrastructure and some physico-chemical properties of beef, *Meat Science*, 51, 35–42.

32. Gürpınar, G., (2007). Ses ötesi dalgaların cevher zenginleştirmede kullanılabilirliğinin araştırılması, Doktora Tezi, Osmangazi Üniversitesi Fen Bilimleri Enstitüsü, Maden Mühendisliği Anabilim Dalı, Eskişehir.

33. Halliday, D. & Resnick, R., (1992). FiziğinTemelleri-I, 3. baskı, (Çeviren: Prof. Dr. Cengiz YALÇIN), 368-369.

34. Huang, Q., Li, L. & Fu, X., (2007). Ultrasound effects on the structure and chemical reactivity of cornstarch granules, *Starch* 59, 371-378.

35. Jambrak, A. R., Mason, T. J., Lelas, V., Herceg, Z. & Herceg, I. L., (2008). Effect of ultrasound treatment on solubility and foaming properties of whey protein suspensions. *Journal of Food Engineering*, 86, 281-287.

36. Jiménez, A., Beltrán, G. & Uceda, M., (2007). Highpower ultrasound in olive paste pretreatment, Effect on process yield and virgin olive oil characteristics, *Ultrasonics Sonochem*, 14, 725–731.

37. Jiranek, V., Grbin, P., Yap, A., Barnes, M. & Bates, D., (2008). High power ultrasonics as a novel tool offering new opportunities for managing wine microbiology, *Biotechnol Letters*, 30, 1-6.

38. Kadkhodaee, R. & Povey, M. J. W., (2008). Ultrasonic inactivation of Bacillus a-amylase, I. Effect of gas content and emitting face of probe, *Ultrasonics Sonochem*, 15, 2, 133-142.

39. Kim, S. M. & Zayas, J. F., (1989). Processing parameter of chymosin extraction by ultrasound, *J Food Sci*, 54, 700.

40. Kresic, G., Lelas, V., Jambrak, A. R., Herceg, Z. & Brncic, S. R., (2008). Influence of novel food processing technologies on the rheological and thermophysical properties of whey proteins, *J of Food Engineer*, 87, 64-73.

41. Li, B. & Sun, D. W., (2002). Effect of power ultrasound on freezing rate

during ımmersion freezing, *Journal of Food Engineering*, 55, 3, 277–282.

42. Lopez, P. & Burgos, J., (1995), Lipoxygenase inactivation by manothermosonication: effects of sonication physical parameters, pH, KCl, sugars, glycerol and enzyme concentration, *Journal of Agricultural and Food Chemistry*, 43, 620–625.

43. Lopez, P., Sala, F. J., de la Fuente, J. L., Condon, S., Raso, J. & Burgos, J., (1994). Inactivation of peroxidase, lipoxygenase and polypohenol oxidase by manothermosonication, *Journal of Agricultural and Food Chemistry*, 42, 252–256.

44. Luque de Castro, M. D. & Priego-Capote, F., (2007). Ultrasound assisted crystallization (sonocrystallization), *Ultrasonics Sonochem*, 14, 717-724.

45. Luque-García, J. L. & Luque de Castro, M. D., (2004). Ultrasound-assisted soxhlet extraction: An expeditive approach for solid sample treatment application to the extraction of total fat from oleaginous seeds. *J of Chromatog A*, 1034, 1-2, 237-242.

46. Ma, Y., Chen, J., Liu, D. & Ye, X., (2008a). Effect of ultrasonic treatment on the total phenolic and antioxidant activity of extracts from citrus peel, *J of Food Sci*, 73,115-120.

47. Ma Y, Ye X, Fang Z, Chen J, Xu G. & Liu D. (2008b). Phenolic compounds and antioxidant activity of extracts from ultrasonic treatment of satsuma mandarin (*Citrus unshiu* Marc.) peels, *J of Agric and Food Chem*, 56: 5682-5690.

48. Madadlou, A., Mousavi, M. E., Emam-Djomeh, Z., Ehsani, M. & Sheehan, D., (2009). Comparison of pH-dependent sonodistruption of re-assembled casein micelles bu 35 kHz, and 130 kHz ultrasounds. *Journal of Food Engineering*, 95, 505-509.

49. Manas, P., Munoz, B., Sanz, D. & Condon, S., (2006). Inactivation of lysozyme by ultrasonic waves under pressure at different temperatures, *Enzyme and Microbial Technology*, 39, 6, 1177–1182.

50. Mason, T. J., (1998). Power ultrasound in food processing-the way forward: in Ultrasound in Food Processing, 105-126. Eds. Povey, M. J.W ve Mason, T. J., Blackie Academic& Professional, London.

51. Matsuura, K., Hirotsune, M., Nunokawa, Y., Satoh, M. & Honda, K., (1994). Acceleration of cell growth and ester formation by ultrasonic wave irradiation, *J of Ferment and Bioengineer*, 77, 36-40.

52. Muthukumarappan, K., Tiwari, B. K., O'Donnel, C. P. & Cullen, P. J. (2010). Ultrasound processing: rheological and functional properties of food: in Novel Food Processing, Effects on Rheological and Functional Properties, Sf.. 85-102, Eds. Ahmed, J., Ramaswamy, H. S., Kasapis, S., Boye, J. I., CRC Press, USA.

53. Myshkin, N. K., Petrokovets, M. I. & Kovalev, A.V., (2005). Tribology of

polymers: Adhesion, friction, wear, and mass-transfer. *Tribology Int*, 38, 910–921.

54. Nguyen, N. H. A. & Anema, S. G., (2010). Effect of ultrasonication on the properties of skim milk used in the formation of acid gels, *Innovative Food Science and Emerging Technologies*, 11, 616-622.

55. O'Donnell, C. P., Tiwari, B. K., Bourke, P. & Cullen, P. J., (2010). Effect of ultrasonic processing on food enzymes of industrial importance, *Trends in Food Science and Technology,* 21, 358–367.

56. Ordoñez, J. A., Aguilera, M. A., Garcia, M. L. & Sanz, B., (1987). Effect of combined ultrasonic and heat treatment (thermoultrasonication) on the survival of a strain of *Staphylococcus aureus*. *J Dairy Res.* 54:61-67.

57. Ordoñez, J. A., Sanz, B., Hernandez, P. E. & Lopez-Lorenzo, P., (1984). A note on the effect of combined ultrasonic and heat treatments on the survival of thermoduric streptococci. *J Appl Bacteriol.* 56:175-177.

58. Özbek, B. & Ülgen, K., (2000). The stability of enzymes after sonication, *Process Biochem,* 35, 9, 1037-1043.

59. Özden, N., (1981). Ses ötesi (Ultrasonik) ile Muayene, SEGEM, 48, Ankara, 142.

60. Patist, A. & Bates, D., (2008). Ultrasonic innovations in the food industry: From the laboratory to commercial production, *Innovative Food Science and Emerging Technologies*, 9, 147-154.

61. Piyasena, P., Mohareb, E. & McKellar, R. C., (2003). Inactivation of microbes using ultrasound: A review. *Int J of Food Microbiol,* 87, 207-216.

62. Pohlman, W. F., (1994). Ultrasound uses for cookery, and to improve cooking, textural, sensory, and shelf-life stability properties of beef muscle, Kansas State University, Manhattan, Kansas

63. Pongsawatmanit, R., Harnsilawat, T. & McClements, D. J., (2006). Influence of alginate, ph and ultrasound treatment on palm oil-in-water emulsions stabilized by b-lactoglobulin, colloids and surfaces A. *Physicochemical and Engineering Aspects*, 287, 59–67.

64. Povey, M. J. W. & Mason, T. J., (1998). Ultrasound in Food Processing, Thomson Science, New York.

65. Povey, M. J.W., (1998). Ultrasonic of Food, *Contemporary Physics*, 1998, 39(6), 467–478.

66. Reynolds, J. B., Anderson, D. B., Schmidt, G. R., Theno, D. M. & Siegel. D. G., (1978). Effetcs of ultrasonic treatment on binding strength in curet ham rolls, *Journal of Food Science*, 43, 3, 866–869.

67. Riener, J., Noci, F., Cronin, D. A., Morgan, D. J. & Lyng, J. G., (2009). The effect of thermosonication of milk on selected physicochemical and microstructural properties of yoghurt gels during fermentation. *Food Chemistry*, 114, 905-911.

68. Riener, J., Noci, F., Cronin, D. A., Morgan, D. J. & Lyng, J. G., (2010). A comparison of selected quality characteristics of yoghurts prepared from thermosonicated and conventioanlly heated milks, *Food Chemistry*, 119, 1108-1113.

69. Sala, F. J., Burgos, J., Condon, S., Lopez, P. & Raso, J., (1995). Effect of heat and ultrasounds on microorganisms and enzymes, In G. W. Gould (Ed.), New Methods of Food Preservation, 176-204.

70. Salazar, J., Chávez, J. A., Turó, A. & García-Hernández, M. J., (2010). Effect of ultrasound on food processing: in Novel Food Processing, Effects on Rheological and Functional Properties, 65-84, Eds. Ahmed, J., Ramaswamy, H. S., Kasapis, S., Boye, J. I., CRC Press, USA.

71. Salleh-Mack, S. Z. & Roberts, J, S., (2007). Ultrasound pasteurization: The effects of temperature, soluble solids, organic acids and pH on the inactivation of *Escherichia coli* ATCC 25922, *Ultrasonics Sonochem*, 14, 323-329.

72. Shanmugam, A., Chandrapala, J. & Ashokkumar, M., (2012). The effect of ultrasound on the physical and functional properties of skim milk, *Innovative Food Science and Emerging Technologies*.

73. Smith, N. B., Cannon, J.E., Novakofsky, J.E., MacKeith, F.K. & O'Brien, W. D., (1991). Tenderization of semitendinosus muscle using high ıntensity ultrasound, Ultrasonics Symposium, Lake Beuna Vista, Florida, 2, 1371–1373.

74. Soria, A. C. & Willamiel, M., (2010). Effect of ultrasound on the technological properties and bioactivity of food, *Trends in Food Science & Technology*, 21, 323–331.

75. Şengül, M., Bafllar, M., Erkaya, T. & Ertugay, M. F., (2009). Ultrasonik homojenizasyon işleminin yoğurdun su tutma kapasitesi üzerine etkisi, *Gıda,* 34, 4, 219-222.

76. Tavman, Ş., Kumcuoğlu, S. & Akaya, Z., (2009). Bitkisel ürünlerin atıklarından antioksidan maddelerin ultrason destekli ekstraksiyonu, *Gıda*, 34, 3, 175-182.

77. Thakur, B. R. & Nelson, P. E., (1997). Inactivation of lipoxygenase in whole soy flour suspension by ultrasonic cavitation, *Nahrung*, 41, 5, 299–301. ,

78. Tiwari, B. K., O'Donnell, C. P., Muthukumarappan, K. & Cullen, P. J., (2009). Effect of sonication on orange juice quality parameters during storage, *International Journal of Food Science and Technology*, 44, 3, 586–595.

79. Torley, P. J. & Bhandari, B. R., (2007). Ultrasound in Food Processing and Preservation: in Handbook of Food Preservation., 713-732. Edited by M . Shafiur Rahman, Second Edition, CRC Press.

80. Ugarte-Romero, E., Feng, H., Martin, S. E., Cadwallader, K. R. & Robin-

son, S. J., (2006). Inactivation of *Escherichia coli* with power ultrasound in apple cider, *J of Food Sci*, 71, 102-108.

81. Ulusoy, K. & Karakaya, M., (2011). Gıda endüstrisinde ultrasonik ses dalgalarının kullanımı, *Gıda*, 36, 2, 113-120.

82. Valero, M., Recrosio, N., Saura, D., Munoz, N., Martic. N. & Lizama, V., (2007). Effects of ultrasonic treatments in orange juice processing, *J of Food Engineer*, 80,509-516.

83. Vercet, A., Lopez, P., & Burgos, J., (1997). Inactivation of Heat-Resistant Lipase and Protease from *Pseudomonas fluorescens* by Manothermosonication, *Dairy Science*, 80, 29–36.

84. Vercent, A., Oria, R., Marquina, P., Chelier, S. & Lopez-Buesa, P., (2002). Rheological properties of yoghurt made with milk submitted to manothermosonication, *Journal of Agriculturel and Food Chemisty*, 50, 6165-6171.

85. Villamiel, M. & Jong, P., (2000a). Influence of high-intensity ultrasound and heat treatment in continuous flow on fat, proteins, and native enzymes of milk, *Journal of Agricultural and Food Chemistry*, 48, 472-478.

86. Villamiel, M. & Jong, P., (2000b). Inactivation of *Pseudomonas fluorescens* and *Streptococcus thermophilus* in Trypticase Soy Broth and total bacteria in milk by continuous-flow ultrasonic treatment and conventional heating, Journal of Food Engineering, 45, 171-179.

87. Virot, M., Tomao. V., Le, Bourvellec, C., Renar M. C. G. C. & Chemat, F., (2010). Towards the industrial production of antioxidants from food processing by-products with ultrasound-assisted extraction, *Ultrasonics Sonochem*, 17, 1066-1074.

88. Wang, J., Sun, B., Cao, Y., Tian, Y. & Li, X., (2008). Optimization of ultrasound-assisted extraction of phenolic compounds from wheat bran. *Food Chem*, 106, 804-810.

89. Wang, L. & Weller, C. L., (2006). Recent advances in extraction of nutraceuticals from plants, *Trends in Food Sci & Technol*, 17, 300-312.

90. Wu, H., Hulbert, G. J. & Mount, J. R., (2001). Effect of ultrasound on milk homogenization and fermentation with yogurt starter, *Innovative Food Science&Technologies*, 1, 211-218.

91. Xia, T., Shi, S. & Wan, X., (2006). Impact of ultrasonic-assisted extraction on the chemical and sensory quality of tea infusion, *J of Food Engineer*, 74,557-560.

92. Yıldırım, B. O. & Öksüz M. U., (2013). Bakterilere sesleniyorum!, Amasya Bilim ve Sanat Merkezi.

93. Yüksel, F., (2013). Gıda teknolojisinde ultrases uygulamaları, *Gıda Teknolojileri Elektronik Dergisi*, 8, 2, 29-38.

94. Zheng, L. & Sun, D. W., (2006). Innovative applications of power ultrasound during food freezing processes: A review, *Trends in Food Science*

& Technology, 17, 16–23.

95. Zisu, B., Bhaskarcharya, R., Kentish, S. & Ashokkumar, M., (2010). Ultrasonic processing of dairy systems in large scale reactors, *Ultrasonic Sonochemistry*, 17, 1075-1081.

Chapter 11

VALUE OF ADOPTING A MULTI-PERIOD MODELING APPROACH IN SUPPLY CHAIN NETWORK DESIGN PROBLEMS

Mehmet ALEGÖZ[1]

1 Asst. Prof. Dr. Eskisehir Technical University, Faculty of Engineering, Department of Industrial Engineering, 26555, Eskisehir, Turkey. ORCID: https://orcid.org/0000-0002-6290-0448

E-mail: mehmetalegoz@eskisehir.edu.tr

1. INTRODUCTION

In this study, we investigate the effects of adopting a multi-period modeling approach in supply chain network design (SCND) problems. To this end, we consider a durable product supply chain network including suppliers, production plants, distribution centers and customers and propose two mixed-integer linear programming models, one of which adopts a single-period modeling approach and the other one adopts a multi-period modeling approach. By making a comparison between them using the data of a real-life case, we derive several insights regarding the effects of adopting multi-period modeling approach in SCND problems.

SCND problem is one of the well-known and widely addressed problems in the supply chain management literature. Some researchers deal with this problem by using a single-period modeling approach (i.e., Santoso et al., 2005; Bithandi et al., 2009; Wang et al., 2011; Yildiz et al., 2016; Hasani et al., 2021; Kazancoglu et al., 2022; Vali-Siar et al., 2022; Foroozesh et al., 2022). Among these researchers, some of them propose exact solution approaches such as mixed-integer programming to address this problem, while some other consider the large-size instances of the problem and propose heuristic or metaheuristic approaches such as genetic algorithms.

On the other hand, there are also some other researchers that consider a multi-period modeling approach for the SCND problem (i.e., Alumur et al., 2012, Correia et al., 2013, Keshavarz Ghorabaee et al., 2017, Savadkoohi et al., (2018), Wang et al., 2020; Govindan et al., 2020; Rabbani et al., 2020; Diabat and Jebali, 2021, Döngül et al., 2022; Boskabadi et al., 2022; Wang and Wan, 2022). These researchers use similar techniques or solution approaches with the researchers adopting a single-period modeling approach. However, the complexity of the problem of course increases as a result of the multiple periods considered.

Adopting a single-period modeling approach may be beneficial in terms of simplifying the model and may give an opportunity to focus on other issues that cannot be addressed in multi-period models due to the complexity of those models. Considering the steady-state conditions, adopting a single-period modeling approach may give acceptable results that can be used in real-life cases. On the other hand, researchers adopting a multi-period modeling approach emphasize the importance of considering the dynamic structure of the problem to avoid from misleading results.

Motivating the discussions above, this study presents a comparison between single-period and multi-period modeling approaches. As the literature above shows, both single-period modeling and multi-period modeling approaches are widely used in the SCND problems. However, to

the best of our knowledge effect of adopting a multi-period modeling approach has not yet received enough attention from the researchers. In this regard, main motivation and contribution of this study can be stated as investigating and quantifying the effects of adopting a multi-period modeling approach in SCND problems.

The rest of this chapter is organized as follows. Problem definition is presented in the following section. Section 3 is dedicated to the mathematical models for single-period and multi-period problem cases and section 4 is dedicated to the computational study. Finally, conclusion and some future work suggestions are presented in fifth section.

2. PROBLEM DEFINITION

A durable product supply chain consisting of suppliers, production plants (PPs), distribution centers (DCs) and customers is considered in this study. The product requires different raw materials in the manufacturing process and each raw material is manufactured by a subset of suppliers, i.e., all the suppliers do not manufacture all the raw materials. The raw materials are shipped from the suppliers to PPs and after the necessary operations carried in the PPs, they are shipped to DCs to be kept until a customer demand occurs. Finally, those products are shipped from DCs to customers based on their demands. Demands are assumed to be deterministic. The supply chain network considered in this study is illustrated below in Figure 1.

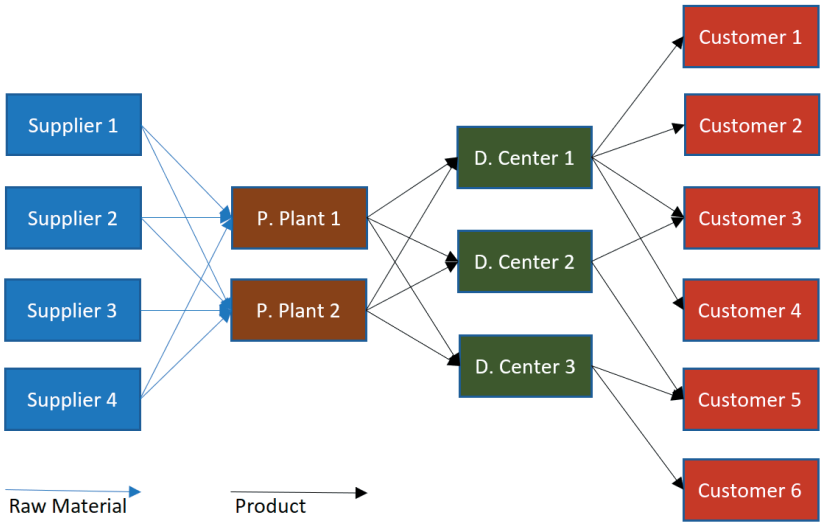

Figure 1: Considered Supply Chain Network

In the supply chain network considered, suppliers and customers have fixed locations, which cannot be changed. However, locations of the PPs and DCs are expected to be determined by the mathematical model. There

are candidate locations for PPs and DCs, each of which has a different fixed cost, i.e., opening a PP or DC yields to a fixed cost for the company charged per unit time. Moreover, minimum and maximum number of DCs that can be opened is also known. In line with these facts, the company aims to determine the PPs and the DCs that should be opened so as to minimize the total cost.

Shipments between the actors in the supply chain can be carried by different types of vehicles. Each shipment yields to a fixed shipment cost independent from the shipment amount and a variable shipment cost depending on the amount of product shipped and distance. In line with these facts the company aims to determine the type of the vehicles that can be used for each of the shipments.

Considering the problem setting above, in this study we focus on two modeling approach, single-period and multi-period. In the single period modeling approach, we consider a 12-month planning period and consider the annual supply capacities of the suppliers, annual demands of the customers and annual capacities of the PPs and DCs. On the other hand, in the multi-period setting, we consider the periodic (monthly) supply capacities of the suppliers, periodic demands of the customers and periodic capacities of the PPs and DCs.

In both single-period and multi-period mathematical models, the models aim to minimize the total supply chain cost including the fixed costs of opening PPs and DCs, variable costs of shipments between the supply chain actors, fixed costs of shipments between the supply chain actors, and finally procurement costs of raw materials procured from different suppliers. In this regard, the model decisions include the amount of raw materials and products shipped between supply chain actors, the number and locations of the PPs opened and the number and locations of the DCs opened. Proposed models are presented in the next section.

3. MATHEMATICAL MODELS

Notation used in the proposed models is presented in Figure 2 below.

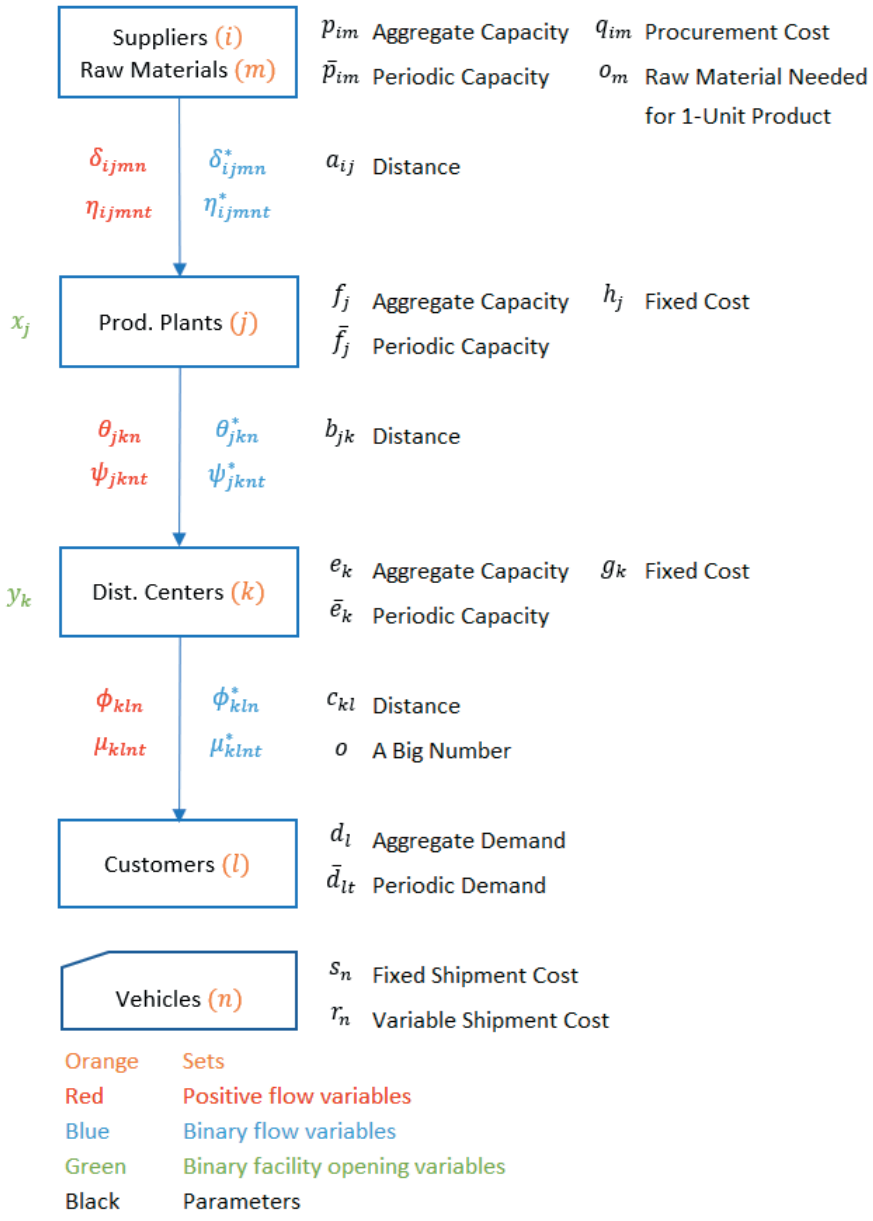

Figure 2: Notation

4.1. Single-Period Model

The objective function of the single-period model can be stated as in equation (1).

$$\begin{aligned}\min z = &\sum_i \sum_j \sum_m \sum_n a_{ij}\delta_{ijmn} r_n + \sum_j \sum_k \sum_n b_{jk}\theta_{jkn} r_n \\ &+ \sum_k \sum_l \sum_n c_{kl}\phi_{kln} r_n \\ &+ \sum_i \sum_j \sum_m \sum_n \delta^*_{ijmn} s_n + \sum_j \sum_k \sum_n \theta^*_{jkn} s_n \\ &+ \sum_k \sum_l \sum_n \phi^*_{kln} s_n + \sum_k g_k y_k + \sum_j h_j y_j \\ &+ \sum_i \sum_j \sum_m \sum_n \delta_{ijmn} q_{im}\end{aligned} \tag{1}$$

The objective of the single-period model is minimization of the total supply chain cost. In equation (1), first term is the shipment cost resulting from the shipments of the raw materials from suppliers to production plants. Second term is the shipment cost resulting from the shipments of products from production plants to distribution centers. Third term is the shipment cost resulting from the shipment of products from distribution centers to customers. Fourth term is the fixed vehicle cost resulting from the shipments between suppliers and production plants. Fifth term is the fixed vehicle cost resulting from the shipments between production plants and distribution centers, sixth term is the fixed vehicle cost resulting from the shipments between distribution centers and customers. Seventh term is the fixed cost of opening production plants in candidate locations and eighth term is the fixed cost of opening distribution centers in candidate locations. Finally, the last term is the cost of acquiring the raw materials from the suppliers.

$$\sum_j \sum_n \delta_{ijmn} \leq p_{im} \quad \forall i, m \tag{2}$$

The constraint above ensures that the amount of raw material shipped from a supplier to all production plants cannot exceed the capacity of the supplier for that raw material.

$$\sum_i \sum_n \delta_{ijmn} \geq v_m \sum_k \sum_n \theta_{jkn} \quad \forall j, m \tag{3}$$

Constraint (3) is the balance constraint for the raw materials and products manufactured in the production plants. It basically ensures that enough amount of raw materials to manufacture the products must be shipped from the suppliers to that production plant.

$$\sum_j \sum_n \theta_{jkn} \geq \sum_l \sum_n \phi_{kln} \quad \forall k \tag{4}$$

The constraint above is the balance constraint for the distribution centers. It ensures that the amount of products shipped from a distribution center to all customers cannot exceed the amount of products received by that distribution center.

$$\sum_{k}\sum_{n}\phi_{kln} = d_l \quad \forall l \tag{5}$$

Constraint (5) is the demand satisfaction constraint ensuring that the amount of products received by a customer will be equal to the demand of that customer.

$$\sum_{k}\sum_{n}\theta_{jkn} \leq x_j f_j \quad \forall j \tag{6}$$

The constraint above is the capacity constraint. It ensures that if a production plant is opened in a candidate location, at most f_j units of products can be manufactured in that production plant. On the other hand, if a production plant is not opened in a candidate location, no manufacturing can be made in that location.

$$\sum_{l}\sum_{n}\phi_{kln} \leq y_k e_k \quad \forall k \tag{7}$$

Similar to the constraint (6), constraint (7) is the capacity constraint for the distribution centers. It ensures that if a distribution center is opened in a candidate location, at most e_k units of products can be kept in that production plant. On the other hand, if a distribution center is not opened in a candidate location, not any product can be kept in that location.

$$\sum_{k} y_k \geq u^- \tag{8}$$

This constraint guarantees that at least u^- of the y_k variables must take the value of 1, which means that at least u^- distribution centers must be opened.

$$\sum_{k} y_k \leq u^+ \tag{9}$$

Constraint (9) ensures that at most u^+ of the y_k variables must take the value of 1, which means that at most u^+ distribution centers must be opened.

$$\delta_{ijmn} \leq o\delta^*_{ijmn} \quad \forall i,j,m,n \tag{10}$$

The constraint above creates a relationship between the binary and continuous variables regarding the shipments between suppliers and production plants. It ensures that, if at least 1 unit of products is shipped from a supplier to a production plant via a vehicle type, then the binary variable, δ^*_{ijmn} must take the value of 1 for those facilities.

$$\theta_{jkn} \leq o\theta^*_{jkn} \quad \forall j,k,n \tag{11}$$

Constraint (11) creates a relationship between the binary and continuous variables regarding the shipments between production plants and distribution centers. It ensures that, if at least 1 unit of products is shipped from a production plant to a distribution center via a vehicle type, then the binary variable, θ^*_{jkn} must take the value of 1 for those facilities.

$$\phi_{kln} \leq o\phi^*_{kln} \quad \forall k,l,n \tag{12}$$

Similar to the previous two constraints, the constraint above creates a relationship between the binary and continuous variables regarding the shipments between distribution centers and customers. It ensures that, if at least 1 unit of products is shipped from a distribution center to a customer via a vehicle type, then the binary variable, ϕ^*_{kln} must take the value of 1 for those facilities.

$$\delta_{ijmn}, \theta_{jkn}, \phi_{kln} \geq 0, \delta^*_{ijmn}, \theta^*_{jkn}, \phi^*_{kln}, x_j, y_k \in \{0,1\} \tag{13}$$

Finally, the last constraint in the model sets the types and signs of the decision variables. It ensures that $\delta_{ijmn}, \theta_{jkn}, \phi_{kln}$ are positive continuous variables, whereas the other variables are binary variables taking the value of either 0 or 1.

4.2. Multi-Period Model

The objective function of the multi-period model can be stated as follows.

$$\begin{aligned}\min z = & \sum_i \sum_j \sum_m \sum_n \sum_t a_{ij}\eta_{ijmnt} r_n \\ & + \sum_j \sum_k \sum_n \sum_t b_{jk}\psi_{jknt} r_n \\ & + \sum_k \sum_l \sum_n \sum_t c_{kl}\mu_{klnt} r_n \\ & + \sum_i \sum_j \sum_m \sum_n \sum_t \eta_{ijmnt} q_{im} \\ & + \sum_i \sum_j \sum_m \sum_n \sum_t \eta^*_{ijmnt} s_n \\ & + \sum_j \sum_k \sum_n \sum_t \psi^*_{jknt} s_n \\ & + \sum_k \sum_l \sum_n \sum_t \mu^*_{klnt} s_n + \sum_k g_k y_k \\ & + \sum_j h_j y_j \end{aligned} \tag{14}$$

The objective of the multi-period model is minimization of the total supply chain cost. In equation (14), the first term is the shipment cost resulting from the shipments of the raw materials from suppliers to production plants. Second term is the shipment cost resulting from the shipments of products from production plants to distribution centers. Third term is the shipment cost resulting from the shipment of products from distribution centers to customers. Fourth term is the cost of acquiring the raw materials from the suppliers. Fifth term is the fixed vehicle cost resulting from the shipments between suppliers and production plants. Sixth term is the fixed vehicle cost resulting from the shipments between production plants and distribution centers, seventh term is the fixed vehicle cost resulting from the shipments between distribution centers and customers. Eighth term is the fixed cost of opening production plants in candidate locations and finally nineth term is the fixed cost of opening distribution centers in candidate locations. It should be noted that here different from the previous model we sum the costs over all periods.

$$\sum_j \sum_n \eta_{ijmnt} \leq p_{im} \quad \forall i, m, t \tag{15}$$

The constraint above ensures that the amount of raw material shipped from a supplier to all production plants cannot exceed the capacity of the supplier for that raw material. Different from the previous model here the

periodic capacity is considered and thus the constraint works for each period.

$$\sum_{i}\sum_{n}\eta_{ijmnt} \geq v_m \sum_{k}\sum_{n}\psi_{jknt} \quad \forall j, m, t \tag{16}$$

The constraint above is the balance constraint for the raw materials and products manufactured in the production plants. It basically ensures that enough amount of raw materials to manufacture the products must be shipped from the suppliers to that production plant. Different from the previous model, in this model periodic shipments are considered. Hence, the constraint works for each period.

$$\sum_{j}\sum_{n}\psi_{jknt} \geq \sum_{l}\sum_{n}\mu_{klnt} \quad \forall k, t \tag{17}$$

Constraint (17) is the balance constraint for the distribution centers. It ensures that the amount of products shipped from a distribution center to all customers cannot exceed the amount of products received by that distribution center. Different from the previous model, in this model periodic shipments are considered. Hence, the constraint works for each period.

$$\sum_{k}\sum_{n}\mu_{klnt} \geq \bar{d}_{lt} \quad \forall l, t \tag{18}$$

Constraint (18) is the demand satisfaction constraint ensuring that the amount of products received by a customer will be equal to the demand of that customer. Different from the previous model, here we consider the periodic demands of the customers. Hence, the constraint works for each period.

$$\sum_{k}\sum_{n}\psi_{jknt} \leq x_j \bar{f}_j \quad \forall j, t \tag{19}$$

The constraint above is the capacity constraint. It ensures that if a production plant is opened in a candidate location, at most f_j units of products can be manufactured in that production plant. On the other hand, if a production plant is not opened in a candidate location, no manufacturing can be made in that location. Different from the previous model, here we consider the periodic capacities of the production plants. For this reason, the constraint works for each period.

$$\sum_{l}\sum_{n}\mu_{klnt} \leq y_k \bar{e}_k \quad \forall k,t \tag{20}$$

Similar to the constraint (19), constraint (20) is the capacity constraint for the distribution centers. It ensures that if a distribution center is opened in a candidate location, at most e_k units of products can be kept in that production plant. On the other hand, if a distribution center is not opened in a candidate location, not any product can be kept in that location. Different from the previous model, here we consider the periodic capacities of the distribution centers. For this reason, the constraint works for each period.

$$\sum_{k} y_k \geq u^- \tag{21}$$

This constraint guarantees that at least u^- of the y_k variables must take the value of 1, which means that at least u^- distribution centers must be opened.

$$\sum_{k} y_k \leq u^+ \tag{22}$$

Constraint (22) above guarantees that at most u^+ of the y_k variables must take the value of 1, which means that at most u^+ distribution centers must be opened. Notice that constraints (21) and (22) are same in both models, i.e., they do not change based on the modeling approach (single-period or multi-period) used.

$$\eta_{ijmnt} \leq o\eta^*_{ijmnt} \quad \forall i,j,m,n \tag{23}$$

The constraint above creates a relationship between the binary and continuous variables regarding the shipments between suppliers and production plants. It ensures that, if at least 1 unit of products is shipped from a supplier to a production plant via a vehicle type, then the binary variable, δ^*_{ijmn} must take the value of 1 for those facilities. It should be emphasized that here we consider the periodic shipments, which constitutes the main difference between constraints (23), (24) and (25) and their single-period counterparts.

$$\psi_{jknt} \leq o\psi^*_{jknt} \quad \forall j,k,n \tag{24}$$

Constraint (24) creates a relationship between the binary and continuous variables regarding the shipments between production plants and distribution centers. It ensures that, if at least 1 unit of products is

shipped from a production plant to a distribution center via a vehicle type, then the binary variable, θ^*_{jkn} must take the value of 1 for those facilities.

$$\mu_{klnt} \leq o\mu^*_{klnt} \quad \forall k, l, n \tag{25}$$

Similar to the previous two constraints, the constraint above creates a relationship between the binary and continuous variables regarding the shipments between distribution centers and customers. It ensures that, if at least 1 unit of products is shipped from a distribution center to a customer via a vehicle type, then the binary variable, ϕ^*_{kln} must take the value of 1 for those facilities.

$$\eta_{ijmnt}, \psi_{jknt}, \mu_{klnt} \geq 0, \eta^*_{ijmnt}, \psi^*_{jknt}, \mu^*_{klnt}, x_j, y_k \in \{0,1\} \tag{26}$$

Finally, the last constraint in the model sets the types and signs of the decision variables. It ensures that $\eta_{ijmnt}, \psi_{jknt}, \mu_{klnt}$ are positive continuous variables, whereas the other variables are binary variables taking the value of either 0 or 1.

4. COMPUTATIONAL RESULTS

In order to test the applicability of the model, we consider a supply chain of a real-life firm selling household goods to its customers. The product we consider includes six components that can be procured from thirteen different suppliers. Seven candidate locations are determined as the locations of production plants and nine candidate locations are determined as the locations of distribution centers. The company serves 20 major customers located in different cities. As the first task, distances between the supply chain members are obtained by using the Google Map. As an example, we present the distances between the distribution centers and customers in Table 1.

Table 1: Distances Between the Distribution Centers and Customers

C\DC	1	2	3	4	5	6	7	8	9
1	8	256	345	328	169	277	343	223	100
2	256	21	597	536	421	385	342	258	311
3	291	543	339	507	122	540	606	322	363
4	345	597	104	296	269	445	573	532	408
5	328	536	296	96	395	151	279	551	228
6	169	421	269	395	113	418	484	314	241
7	277	385	445	151	418	98	132	490	177
8	526	656	452	198	593	271	399	749	426
9	453	452	683	389	594	242	110	662	353
10	326	578	126	176	374	325	453	549	332

11	343	342	573	279	484	132	101	552	243
12	223	258	532	551	314	490	552	142	323
13	100	311	408	228	241	177	243	323	117
14	310	562	155	141	358	290	418	533	316
15	367	619	99	395	241	544	672	554	430
16	306	305	605	311	447	160	37	515	206
17	115	367	273	223	172	308	382	338	139
18	336	369	641	664	419	603	665	119	436
19	339	75	680	619	504	468	420	253	394
20	375	236	674	380	516	229	106	501	275

Moreover, supply capacities of the suppliers for each component are determined as another input of the model. As an example, we present the supply capacities of suppliers for Component 5 in Table 2. Notice that some suppliers do not supply Component 5.

Table 2: Supply Capacities of the Suppliers for Component 5

M\S	1	2	3	4	5	6	7	8	9	10	11
1	3000	0	5000	4000	15000	0	0	1000	5000	4000	2000
2	300	0	5000	4000	15000	0	0	1000	5000	4000	2000
3	300	0	5000	4000	15000	0	0	750	5000	4000	4000
4	300	0	5000	4000	15000	0	0	750	5000	4000	4000
5	300	0	5000	4000	15000	0	0	750	5000	4000	4000
6	300	0	5000	4000	10000	0	0	750	5000	4000	4000
7	300	0	5000	4000	10000	0	0	750	5000	4000	4000
8	300	0	5000	4000	10000	0	0	1000	5000	4000	4000
9	300	0	5000	5000	10000	0	0	1000	5000	4000	4000
10	300	0	5000	5000	15000	0	0	1000	5000	4000	4000
11	300	0	5000	5000	15000	0	0	1000	5000	4000	4000
12	300	0	5000	4000	15000	0	0	1000	5000	4000	4000
Agg.	6300	0	60000	51000	160000	0	0	10750	60000	48000	44000

Finally, by using the data regarding the five previous years, a demand forecast is made and monthly and total demands of customers are obtained as presented in Table 3.

Table 3: Demands of Customers

M\C	1	2	3	4	5
1	5000	8000	10000	8000	7500
2	5000	8000	10000	8000	7500
3	5000	8000	10000	8000	7500
4	5000	8000	10000	8000	7500
5	5000	8000	10000	8000	7500
6	7000	10000	12000	9000	10000
7	7000	10000	12000	9000	10000
8	7000	10000	12000	9000	10000
9	5000	8000	10000	8000	7500
10	5000	8000	10000	8000	7500
11	5000	8000	10000	8000	7500
12	5000	8000	10000	8000	7500
Aggregate	66000	102000	126000	99000	97500

Both single-period and multi-period models are solved with this data by using GAMS optimization software CPLEX solver on a computer including AMD Ryzen 7 processor and 16 GB of RAM. Computational results reveal that the single period model yields to an optimal cost of $718,801.29, while the multi-period model yields to an optimal cost of $791,522,41. This shows that adopting a multi-period model brings about 10% higher cost compared to adopting a single-period model. The reason of this result can be explained with two facts as follows.

In single-period model aggregate demands and aggregate shipments are considered. For instance, if a customer requests 100 units of product in month 1 and 200 units of product in month 2, in single period model, the model considers the aggregate demand of 300 units and assumes that only one shipment is made to the customers to satisfy the demand. As a result, the fixed shipment cost is applied just one time in the single-period model. On the other hand, in multi-period model, 100 units of products are shipped in month 1 and 200 units of products are shipped in month 2. As a result, fixed shipment cost is applied two times. This difference in the fixed shipment costs yields to an increase in the total cost in multi-period modeling approach.

When it comes to real-life practices, it is generally not possible to consolidate the demands of a customer in different periods, firstly because the customers may not want to pay the product that will be needed later and secondly the customers may not have enough space to keep the products that will be needed in future. In those instances, adopting a single-period modeling approach may yield to misleading results, i.e., the costs obtained from model may be lower than that in the real-life.

The second reason of the fact that the multi-period modeling approach yields to a higher cost is the opened facilities. In single-period modeling, aggregate capacities of the facilities are considered, whereas in multi-period modeling monthly capacities are considered. It is obvious that although the aggregate capacity of a set of facility may be enough to satisfy the demand, monthly capacities may not be enough. Due to this fact, in multi-period modeling approach the model decides to open three distribution centers as opposed to two distribution centers in single-period modeling approach.

In the real-life practices where the demands of customers are satisfied with the warehoused products, i.e., in the cases where the company has the ability to keep inventory in the warehouses, considering the aggregate capacities and adopting a single-period modeling approach may be beneficial. However, in the cases where the manufacturing is made in response to demands of customers, adopting a multi-period modeling approach is necessary to avoid from capacity-related infeasibilities.

5. OVERALL DISCUSSIONS AND CONCLUSION

This study investigates the effects of adopting a multi-period modeling approach in the supply chain network design problems and proposes single-period and multi-period mixed-integer linear programming models to make a comparison between them.

Computational results reveal that using a single-period modeling approach may firstly be misleading in some instances, i.e., the total supply chain cost obtained from the single-period mathematical model may be lower than that in the real-life. Moreover, it may also yield to capacity infeasibilities in real-life situations, i.e., the facilities that are suggested by the single-period model may not be enough in real-life instances. At this point, our suggestion to practitioners is that they should understand the underlying assumptions in the single-period modeling approach. If those assumptions are applicable for them in real-life cases, they can avoid from the additional complexity of multi-period modeling approach and can simply use the single-period modeling approach. In other cases, however, using a multi-period modeling approach is essential despite the additional complexity it brings.

This study can be extended in the future in the following ways. First, in this study, we consider a purely deterministic problem environment in which all the parameters such as demands, and supply capacities are assumed to be known. Extension of the models to a case in which some parameters, (especially demand) are uncertain may bring important insights regarding the effects of adopting a multi-period modeling approach in an uncertain environment. Stochastic programming or fuzzy programming may be good candidates for this extension. Second, in this study only the economic aspect of the supply chains is considered. Consideration of the environmental aspect such as greenhouse gas emissions may again yield to significant insights regarding the benefit of multi-period modeling approach in those instances.

REFERENCES

1. Alumur, S. A., Nickel, S., Saldanha-da-Gama, F., & Verter, V. (2012). Multi-period reverse logistics network design. European Journal of Operational Research, 220(1), 67-78.
2. Boskabadi, A., Mirmozaffari, M., Yazdani, R., & Farahani, A. (2022). Design of a distribution network in a multi-product, multi-period green supply chain system under demand uncertainty. *Sustainable Operations and Computers*, 3, 226-237.
3. Bidhandi, H. M., Yusuff, R. M., Ahmad, M. M. H. M., & Bakar, M. R. A. (2009). Development of a new approach for deterministic supply chain network design. *European Journal of Operational Research*, 198(1), 121-128.
4. Correia, I., Melo, T., & Saldanha-da-Gama, F. (2013). Comparing classical performance measures for a multi-period, two-echelon supply chain network design problem with sizing decisions. *Computers & Industrial Engineering*, 64(1), 366-380.
5. Diabat, A., & Jebali, A. (2021). Multi-product and multi-period closed loop supply chain network design under take-back legislation. *International Journal of Production Economics*, 231, 107879.
6. Döngül, E. S., Artantaş, E., & Öztürk, M. B. (2022). Multi-echelon and multi-period supply chain management network design considering different importance for customers management using a novel meta-heuristic algorithm. *International Journal of Information Management Data Insights*, 2(2), 100132.
7. Foroozesh, N., Karimi, B., & Mousavi, S. M. (2022). Green-resilient supply chain network design for perishable products considering route risk and horizontal collaboration under robust interval-valued type-2 fuzzy uncertainty: A case study in food industry. *Journal of Environmental Management*, 307, 114470.
8. Govindan, K., Mina, H., Esmaeili, A., & Gholami-Zanjani, S. M. (2020). An integrated hybrid approach for circular supplier selection and closed loop supply chain network design under uncertainty. *Journal of Cleaner Production*, 242, 118317.
9. Hasani, A., Mokhtari, H., & Fattahi, M. (2021). A multi-objective optimization approach for green and resilient supply chain network design: a real-life case study. *Journal of Cleaner Production*, 278, 123199.
10. Kazancoglu, Y., Yuksel, D., Sezer, M. D., Mangla, S. K., & Hua, L. (2022). A green dual-channel closed-loop supply chain network design model. *Journal of Cleaner Production*, 332, 130062.
11. Keshavarz Ghorabaee, M., Amiri, M., Olfat, L., & Khatami Firouzabadi, S. A. (2017). Designing a multi-product multi-period

supply chain network with reverse logistics and multiple objectives under uncertainty. *Technological and Economic Development of Economy*, 23(3), 520-548.

12. Rabbani, M., Sabbaghnia, A., Mobini, M., & Razmi, J. (2020). A graph theory-based algorithm for a multi-echelon multi-period responsive supply chain network design with lateral-transshipments. *Operational Research*, 20, 2497-2517.
13. Santoso, T., Ahmed, S., Goetschalckx, M., & Shapiro, A. (2005). A stochastic programming approach for supply chain network design under uncertainty. *European Journal of Operational Research*, 167(1), 96-115.
14. Savadkoohi, E., Mousazadeh, M., & Torabi, S. A. (2018). A possibilistic location-inventory model for multi-period perishable pharmaceutical supply chain network design. *Chemical Engineering Research and Design*, 138, 490-505.
15. Vali-Siar, M. M., & Roghanian, E. (2022). Sustainable, resilient and responsive mixed supply chain network design under hybrid uncertainty with considering COVID-19 pandemic disruption. *Sustainable Production and Consumption*, 30, 278-300.
16. Wang, J., Wang, X., & Yu, M. (2020). Multi-period multi-product supply chain network design in the competitive environment. *Mathematical Problems in Engineering*, 2020, 1-15.
17. Wang, F., Lai, X., & Shi, N. (2011). A multi-objective optimization for green supply chain network design. *Decision Support Systems*, 51(2), 262-269.
18. Wang, J., & Wan, Q. (2022). A multi-period multi-product green supply network design problem with price and greenness dependent demands under uncertainty. *Applied Soft Computing*, 114, 108078.
19. Yildiz, H., Yoon, J., Talluri, S., & Ho, W. (2016). Reliable supply chain network design. *Decision Sciences*, 47(4), 661-698.

Chapter 12

COMPUTATION METHODS OF AIR QUALITY INDEX

Mine Tulin ZATEROGLU[1]

1 Dr. Mine Tülin Zateroğlu, Cukurova University, Vocational School of AOSB Technical Sciences, Department of Electrical and Energy, Adana, Turkiye; mtzateroglu@cu.edu.tr; ORCID ID: 0000-0002-1050-6174

Introduction

Air pollution which happens in any urban district is a local environmental problem which is mainly related to industrial emissions and domestic heating. Because the developments in engine and fuel technologies, atmospheric environment in provinces is affected by emissions orginated from traffic. Estimating of the index of air quality is an important environmental topic in evaluating impacts of pollutants on humans and environment in urban regions. Rapid improvement and industrilization, increment in population cause some problems associated with environment i.e., air pollution, land use, deforestation, etc. As the result of anthropogenic activities such as the exhausts of motor vehicles, coal combustion, industrial productions, and power plants, air pollutants which include particulate matter and gaseous release into the atmosphere. These activities lead to adversely impacts such as several diseases on human health, especially on sensitive groups i.e. adult and young (Hu and Guo, 2021; Li et al., 2018a; Shubham et al., 2022; Usmani et al., 2020; Almetwally et al., 2020; Bazyar et al., 2019; Zhang et al., 2021, Wei et al., 2021).

The adversely impacts of pollutants on people wellness are evaluated by the term Air Quality Index (AQI) which is defined by using the monitoring air pollution data that consist of criteria pollutants e.g, particulate matter (PM_{10} and $PM_{2.5}$), ground level ozone (O_3), sulfur dioxide (SO_2), carbon monoxide (CO), and nitrogen dioxide (NO_2). The air quality's present scenario is defined by the AQI tool. An AQI is determined as a communication instrument and a normalized information scale of air pollution utilized to determine the health risk's grade associated with gaseous and particulate air pollution, expressing the ambient air quality in a comprehensible and basic way. High values of AQI indicate that many people's health is affected because of the air pollution. To provide the air quality's information which is real-time and accurate has a significant role in controlling air pollution and protecting the people wellness due to negative impacts of air pollution.

Many factors have influences on air pollutants. Commonly, air pollution is originated from two parameters such as meteorological circumstances and air pollutant emissions. Meteorological circumstances control pollutants in atmospheric periphery over transportation and diffusion of them. The emissions of pollutants, from natural and anthropogenic activities, are the air pollution sources. Climate variables affect the concentrations of air pollutants and play an important role on their fluctuations. The statistical relationships and associations between the pollutants and climate parameters have been demonstrated in many studies (Elminir, 2005; Haddad and Vizakos, 2021; Wang et al., 2015; Bose and

Roy Chowdhury, 2023; Radaideh, 2017; Camalier et al., 2007; Akpinar et al., 2009; Luvsan et al., 2012; Pearce et al., 2011; Tai et al., 2010; Ilten and Selici, 2008; Turalıoglu et al., 2005; Witz and Moore, 1981; Zateroglu, 2021a-d).

There are several techniques e.g., artificial neural network (ANN), different regression models, grey model, autoregressive integrated moving average (ARIMA), hybrid models, weather research and forecasting (WRF) model, and fuzzy models, have been developed to evaluate air pollution. Various methods about air quality estimation have been introduced by many researchers (Baklanov et al., 2016; Byun, 1999; Chan and Hanna, 2004; Chen et al., 2022; Suarez Sanchez et al., 2011; Xu et al., 2021; Dominick et al., 2012; Xu et al., 2023b; Zateroglu, 2022). Additionally, Janarthanan et al. (2021) have used the deep learning technique to forecast the index of air quality (Janarthanan et al., 2021). Al-Alola et al. (2022) have employed the GIS-spatial method and the remote sensing to predict the air quality. To estimate the air pollution, a novel spatiotemporal multigraph convolutional network model has presented by Chen et al. (2023).

As air pollution is globally environmental issue around the world, it is important to analyze and control air pollution. Studies focus on the investigations about the sources, implications, and characteristics of air pollutants in urban atmosphere and also air quality (Cincinelli et al., 2019; Zhu et al., 2020; Hu et al., 2015; Maribelli et al., 2020; Mason et al., 2019; Masiol et al., 2017; Viana et al., 2014; Amato et al., 2014: Bo et al., 2019; Zhan et al., 2018). The endeavurs to advance the quality of urban air are carried out by developing different approaches and techniques (Cairncross et al., 2007; van den Elshout et al., 2008; Cheng et al., 2007; Cogliani, 2001; Ai et al., 2016; Gibergans-Baguena et al., 2020)

There are some AQIs which are used extensively around the world e.g., United States Environmental Protection Agency (USEPA), UK Daily AQI (DAQI), China AQI. The term AQI is a quantitative scale utilized to make uniform reporting on the air quality of dissimilar components in terms of human health. At first, the USEPA has constructed a pollution index value named as Pollutant Standard Index (PSI) to ambient air quality over an interval (0 to 500) depended on National Ambient Air Quality Standards (NAAQS) in 1976. Afterwards, PSI has arranged and called as AQI (Zateroglu, 2022). Furthermore, all AQIs have also some limitations.

Since USEPA AQI formula depends on the only one pollutant with highest sub-index value, and does not take into account the contributions of other pollutants and factors. Additionally, this formula is not sensitive to changes in the pollutants' sub-indexes. So, if any variation happens in

the other pollutants except the pollutant with greatest sub-index, it is not included in the total index (Ott, 1978). To overcome these limitations, some novel or revised methods are developed to build up the AQI. This work demonstrates different AQI methodologies and extended studies around the world (Barjoee et al., 2023; Bishoi et al., 2009; Payus et al., 2022; Mason et al., 2020; Dai et al., 2015; Du et al., 2020; Xu et al., 2017; Li et al., 2017a; Ni et al., 2023; Shen et al., 2023; Huang et al., 2017; Li et al., 2018b; Xu et al., 2023a; Tan et al., 2023). Singh et al. used the satellite data to predict AQI via deep learning methods (2023). Fang et al. utilized the Vanilla Long Short Term Memory (LSTM) model to construct prediction models for AQI (2023). Li et al. (2019) developed a modified AQI by employing an improved least squares Support Vector Machine (SVM) method. Wong et al. (2013) have improved an AQI with health impact, called as AQHI, which is risk-based. Additionally, Li et al. (2017b) built up an AQHI model which is dependent on the relations between air pollution and mortality by oprated time series method. Sowlat et al. (2011) designed a new AQI that is fuzzy-based, referred as FAQI. Wang and Tang (2023) designed a combined model, which consists of fuzzy entropy, LSTM, empirical mode decomposition (EMD), and extreme learning machine method, in estimating AQI. Zhu et al. (2017) proposed a hybrid model which is a combination of support vector regression (SVR), EMD, intrinsic mode functions (IMFs) and seasonal ARIMA (S-ARIMA) to improve the accuracy in predicting AQI. Gupta et al. (2023) have used three machine learning methods viz., catboost regression, random forest regression, and support vector regression to estimate AQI. Additionally, Mustakim et al. (2023) operated several machine learning techniques such as gradient boosted trees, random forest, and decision tree in predicting the concentrations of air pollutants and then computed the air pollution index value.

Methods

AQI Using USEPA Method (AQIEPA)

AQI indicates the pollution indice value of pollutants created by USEPA according to National Ambient Air Quality Standards (NAAQS). The term AQI is dependent on not only wellness impacts but also long period impacts on materials and nature. Sub-indexes are computed for all air pollutants, and then the sub-indice with the biggest result is determined as AQI. The pollution index value for each air pollutant is computed by a mathematical formula shown in Equation 1 (EPA, 1999),

$$I_p = \left[\frac{(I_{Hi} - I_{Lo})}{(BP_{Hi} - BP_{Lo})}\right](C_p - BP_{Lo}) + I_{Lo} \quad (1)$$

where I_p denotes the p^{th} pollutant's sub-indice, C_p indicates the p^{th} pollutant's concentration, BP_{Hi}, determines the breakpoint which is equal to or bigger than C_p, BP_{Lo} demonstrates the breakpoint which is equal to or smaller than C_p, I_{Hi} shows the index value defining to BP_{Hi} in Table 1, and I_{Lo} denotes the index value defining to BP_{Lo} in Table 1. Then, AQI is defined in the following formula (Bishoi et al., 2009),

$$AQI_{EPA} = Max(I_p), \quad p = 1, 2, \ldots, n \tag{2}$$

Table 1. Breakpoints of air pollutants for AQI (EPA, 1999)

Breakpoints							AQI	Category
O_3 (ppm) 8-hour	O_3 (ppm) 1-hour[1]	PM_{10} (μg/m^3)	$PM_{2.5}$ (μg/m^3)	CO (ppm)	SO_2 (ppm)	NO_2 (μg/m^3)		
0.000-0.064	-	0-54	0.0-15.4	0.0-4.4	0.000-0.034	([2])	0-50	Good
0.065-0.084	-	55-154	15.5-40.4	4.5-9.4	0.035-0.144	([2])	51-100	Moderate
0.085-0.104	0.125-0.164	155-254	40.5-65.4	9.5-12.4	0.145-0.224	([2])	101-150	Unhealty for sensitive groups
0.105-0.124	0.165-0.204	255-354	65.5-150.4	12.5-15.4	0.225-0.304	([2])	151-200	Unhealty
0.125-0.374	0.205-0.404	355-424	150.5-250.4	15.5-30.4	0.305-0.604	0.65-1.24	201-300	Very unhealty
([3])	0.405-0.504	425-504	250.5-350.4	30.5-40.4	0.605-0.804	1.25-1.64	301-400	Hazardous
([3])	0.505-0.604	505-604	350.5-500.4	40.5-50.4	0.805-1.004	1.65-2.04	401-500	Hazardous

[1] Commonly, 8-hour ozone values are reported for AQI. But, in several places, the greater of 8-h and 1-h O_3 levels is expressed as the AQI value.

[2] The value of NO_2 does not have short-period NAAQS and produces any AQI while it has value bigger than 200.

[3] The values of 8-h O_3 concentrations cannot describe bigger AQI values (bigger than 301), 1-h O_3 concentrations are more appropirate.

Since AQI_{EPA} formula does not contain the effects of all pollutants and the other factors i.e. spatial effect. Thus, researhers have rearranged the AQI_{EPA} formula and/or built up new models by using some statistical methods as alternative to improve the accuracy.

Zateroglu (2022) presented estimating method for AQI employing a combined model, principal component regression (PCR), which consist of multiple regression model (MLR) and principal component analysis

(PCA). AQI has been estimated via two steps: Firtsly, sub-indexes for each pollutant were computed using USEPA formula. In next step, the value AQI has been statistically estimated for explanatory variables viz., meteorological parameters and appropirate air pollutants via PCR method with varimax and also promax rotation. The findings of USEPA formula were compared with statistical analysis' results. It has been demonstrated that both methods were consistent each other and AQI could be also statistically calculated by using PCR with varimax rotation.

Cheng et al. (2007, 2004) introduced a revision of AQIEPA (RAQIEPA) formula. The entropy fuction is used to reflect the other pollutants' influences expect the pollutant with highest sub-indice. The RAQIEPA is computed by using the formula illustrated below:

$$RAQIEPA = Max(I_1, I_2, \dots I_n) \times \frac{Avg_{daily} \times \sum_{i=1}^{n} I_i}{Avg_{annual} \times \left(\sum_{i=1}^{n} I_i\right)} \times \frac{Avg_{annual}\left[Entropy_{daily} \times Max(I_1, I_2, \dots I_n)\right]}{Entropy_{daily} \times Max(I_1, I_2, \dots I_n)} \quad (3)$$

In revised formula, the novel two terms are added to original formula to simplify in adding the effects of all pollutants indexes. The second part of the formula determines the ratio of daily mean total indexes over annual mean of daily mean total indexes. The third part demonstrates the ratio of annual mean of daily entropy model of indexes over daily entropy model of indexes.

Air Quality Health Index

The term Excess Risk (ER) is used in estimating the value of Air Quality Health Index and determined as the percentage increment in daily mortality for each 10 mikrogram per cubic meter increment in each air pollutant and is computed employing the formula shown below (Stieb et al., 2008):

$$ER_{it} = 100 \times [exp(\beta_i \times x_{it})] - 1 \quad (4)$$

where ER_{it} determines the exceedance deaths percent for pollutant i and day t, β_i denotes the coefficient of regression provided from the time series model of single pollutant, x_{it} indicates the concentration of pollutant i for day t.

To predict the term Air Quality Health Index (AQHI), the formula, that is constructed using the calculation of excess risk (ER), is indicated as follows:

$$AQHI_t = 10 \times \frac{daily\ total\ ER_t}{max(daily\ total\ ER_1, daily\ total\ ER_2, \ldots, daily\ total\ ER_n)} \quad (5)$$

where, daily total ER_t denotes the sum of ER_{it} for pollutant i and day t. For daily AQHI values, a time series model is produced on a numerical scale from 0 to 10 (Stieb et al., 2008).

Common Air Quality Index (CAQI)

This index takes into account the differentiating between province backround and traffic situations. Van den Elshout etal. (2008) have proposed Common Air Quality Index (CAQI) with CITEAIR project. The value CAQI is computed by using a grid shown in a table which includes five categories occured according to EU legislation. The CAQI has suggested to simplify the air quality's comparison in real-time in cities of Europe (Elshout et al., 2014). van den Elshout et al. (2014) have evaluated CAQI by updating with PM2.5 for 27 street station and 31 urban backgorund data in Europe.

Novel Air Quality Index (NAQI)

The Novel Air Quality Index (NAQI) is suggested by Bishoi et al. (2009). This method is operated to interpret the air quality in urban areas regarding all pollutants' effects, but not taking into account spatial situation. The NAQI is constructed by using factor analysis which is depend on the principal components that lead to changes in AQI. These principal factors is constructed as a linear structure to define the any pollutant's concentration. In this method, only three principal components are taken into account because their contributions are approximately percent sixty fort he AQI' variaiton, the other factors are disregarded (Duntemann, 1994). The formula for NAQI is indicated as below:

$$NAQI = \frac{\sum_{i=1}^{n} P_i \times E_i}{\sum_{i=1}^{n} E_i} \quad (6)$$

where P_i demonstrates the principal components, E_i indicates the initial eigenvalues. Lohani (1984) determined the principal components as follows:

$$P_i = \sum_{j=1}^{n} \frac{a_{ji} \times X_j}{\beta_i} \quad (7)$$

where β_i define the eigenvalue related to P_i. X_j expresses the ith pollutant' concentration and is calculated by the formula indicated below:

$$X_j = \sum_{1}^{n} a_{ji} \times P_i \tag{8}$$

Oak Ridge Air Quality Index (ORAQI)

The Oak Ridge National Laboratory improved the term Oak Ridge Quality Index (ORAQI) which has been recommended by Thom and Ott (1975). In urban regions, this technique can be operated to evaluate the air quality disregarding spatial impact, but regarding wellness impacts.

$$ORAQI = \left(a \sum \frac{C_i}{C_s}\right)^b \tag{9}$$

Where C_i denotes the measured/estimated values of i[th] pollutant concentration, C_s defines the value for i[th] pollutant from NAAQS, the terms a and b indicate the contants for pollutants.

Hong Kong Air Quality Index (HKAQI)

Thach et al. (2018) built up a novel model of AQI which estimates health impacts in Hong Kong. In this method, there are three steps to improve the HKAQI: At first, relevant pollutants are chosen; in second step, all chosen pollutants are normalized into related sub-indexes; in final step, all sub-indexes are formed into total AQI, named as HKAQI. The term HKQAI is computed by the following formula:

$$HKAQI = \left(\frac{1}{n}\sum_{i=1}^{n} s_i^p\right)^{\frac{1}{p}} \tag{10}$$

where, p denotes power, n defines number of pollutants, s_i determines the sub-index of i[th] pollutant.

$$s_i = 100 \times \left(\frac{q_i}{Q_i}\right) \tag{11}$$

where, q_i shows the concentration of pollutant i, Q_i indicates the suggested short time value according to Air Quality Guidelines by World Health Organization which depend on the associations between adverse health impacts and air quality. If the value of sub-index becomes higher than the reference value, 100, it demonstrates that the exceedance of the guide value is occured.

Conclusion

Today, air quality that affects people wellness, the environment and the ecosystem is accepted as the main issue in urban regions. So authorities and agencies who work and concern with health and environmental studies commonly need the prediction of pollutants' concentrations. The estimation generally depends on the statistical associations between air pollutants and numerous situations.

The idea in the present work is to introduce various models in forecasting the index of air quality. In prediction, several parameters such as atmospheric elements, that consist of air pollutants and climate variables, and other parameters are used as estimators in methods. To diminish urban pollution, the implementation and specification of modeling technique plays a key role in offering management tactics. It is very important that to gain a reliable and accurate air quality prediction model which helps decision makers take the precautions for air pollution's reduction, and environmental deterioration's solution.

REFERENCES

Ai, Z.T., Mak, C.M., Lee, H.C. (2016). Roadside air quality and implications for control measure: A case study of Hong Kong. Atmospheric Environment, 137, 6-16.

Ahmetwally, A.A., Bin-Jumah, M., Allam, A.A. (2020). Ambient air pollution and its influence on human health and wellfare: an overview. Environmental Science and Pollution Research, 27, 24815-24830.

Akpinar, E.K., Akpinar S., Öztop, H.F. (2009). Statistical analysis of meteorological factors and air pollution at winter months in Elaziğ, Turkey. Journal of Urban and Environmental Engineering, 3(1), 7-16.

Al-Alola, S.S., Alkadi, I.I., Alogayell, H.M., Mohamed, S.A. (2022). Air quality estimation using remote sensing and GIS-spatial Technologies along Al-Shamal train pathway, Al-Qurayyat City in Saudi Arabia. Environmental and Sustainability Indicators, 15, 100184.

Amato, F., Cassee, F.R., Denier van der Gon, H.A.C., Gehrig, R., Gustasson, M., Hafner, W., Harrison, R.M., Jozwicka, M., Kelly, F.J., Moreno, T., Prevot, A.S.H., Schaap, M., Sunyer, J., Querol, X. (2014). Urban air quality: The challenge of non-exhaust emissions. Journal of Hazardous Materials, 275, 31-36.

Baklanov, A., Molina, L.T., Gauss, M., 2016. Megacities, air quality and climate. Atmospheric Environment, 126, 235–249. https://doi.org/10.1016/j.atmosenv.2015.11.059

Barjoee, S.S., Malverdi, E., Kouhkan, M., Alipourfard, I., Rouhani, A., Farokhi, H., Khaledi, A. (2023). Health assessment of industrial ecosystems of Isfahan (Iran) using phytomonitoring: Chemometric, micromorphology, phytoremediation, air pollution tolerance and anticipated performance indices. Urban Climate, 48, 101394.

Bazyar, J., Pourvakhshoori, N., Khankeh, H., Farrokhi, M., Delshad, V., Rajabi, E. (2019). A comprehensive evaluation of the association between air pollution and adverse health outcomes of majör organ systems: a systematic review with a worldwide approach. Environmental Science and Pollution Research, 26, 12648-12661.

Bishoi, B., Prakash, A., Jain, V.K. (2009). A Comparative Study of Air Quality Index Based on Factor Analysis and US-EPA Methods for an Urban Environment. Aerosol and Air Quality Research, 9(1), 1-17.

Bo, X., Xue, X., Xu, J., Du, X., Zhou, B., Tang, L. (2019). Aviation's emissions and contribution to the air quality in China. Atmospheric Environment, 201, 121-131.

Bose, A., Roy Chowdhury, I. (2023). Investigating the association between air pollutants' concentration and meteorological parameters in a rapidly growing urban center of West Bengal, India: a statistical modeling-based approach. Model. Earth Syst. Environ. https://doi.org/10.1007/s40808-022-01670-6

Byun, D.W. (1999). One-atmosphere dynamics description in the Models-3 Community Multi-scale Air Quality (CMAQ) modeling system. In Proceedings of the 7th International Air Pollution Conference, Stanford University, Stanford, CA, USA, 26–28 July 1999; 883–892.

Cairncross, E.K., John, J., Zunckel, M. (2007). A novel air pollution index based on the relative risk of daily mortality associated with short-term exposure to common air pollutants. Atmospheric Environment, 41, 8442-8454.

Camalier, L., Cox, W., Dolwick, P. (2007). The effect of meteorology on ozone in urban areas and their use in assessing ozone trends. Atmospheric Environment, 41, 7127-7137.

Chan, J.C., Hanna, S.R., 2004. Air quality performance evaluation. Meteorology and Atmospheric Physics, 87, 167-196.

Chen, H., Deng, G., Liu, Y. (2022). Monitoring the Influence of Industrialization and Urbanization on Spatiotemporal Variations of AQI and PM2.5 in Three Provinces, China. Atmosphere, 13, 1377.

Chen, J., Yuan, C., Dong, S. et al., 2023. A novel spatiotemporal multigraph convolutional network for air pollution prediction. Appl Intell. https://doi.org/10.1007/s10489-022-04418-y

Cheng, W-L, Chen, Y-S, Zhang, J., Lyons, T.J., Pai, J-L., Chang, S-H. (2007). Comparison of the Revised Air Quality Index with the PSI and AQI indices. Science of the Total Environment, 382, 191-198.

Chen, W.L., Kuo, Y.C., Lin, P.L., Chang, K.H., Chen, Y.S., Lin, T.M., Huang, R. (2004). Revised air quality index derived from an entropy fuction. Atmospheric Environment, 38, 383-391.

Cincinelli, A., Guerranti, C., Martellini, T., Scodellini, R. (2019). Residential wood combustion and its impact on urban air quality in Europe, Current Opinion in Environmental Science and Health, 8, 10-14.

Cogliani, E. (2001). Air pollution forecast in cities by an air pollution index highly correlated with meteorological variables. Atmospheric Environment, 35, 2871-2877.

Dai, J., Chen, R., Meng, X., Yang, C., Zhao, Z., Kan, H. (2015). Ambient air pollution, temperature and out-of-hospital coronary deaths in Shanghai, China. Environmental Pollution, 203, 116-121.

Dominick, D., Juahir, H., Latif, M.T., Zain, S.M., Aris, A.Z., 2012. Spatial Assessment of Air Quality Patterns in Malaysia Using Multivariate Analysis. Atmos. Environ., 60, 172–181.

Du, X., Chen, R., Meng, X., Liu, C., Niu, Y., Wang, W., Li, S., Kan, H., Zhou, M. (2020). The es tablishment of National Air Quality Health Index in China. Environment International, 138, 105594.

Duntemann, G.N., (1994). In Factor Analysis and Related Techniques. Vol.5, Lewis-Beck, M.S. (Ed.), Sage Publications, London, 157.

Elminir, H.K., 2005. Dependence of urban air pollutants on meteorology. The Science of the Total Environment, 350, 225-237.

EPA, (1999). Guideline for Reporting of Daily Air Quality – Air Quality Index (AQI). EPA-454/R-99-010, United States Environmental Protection Agency, Office of Air Quality Planning and Standards Research Triangle Park, NC 27711.

Gupta, N.S., Mohta,Y., Heda, K., Armaan, R., Valarmathi, B., Arulkumaran, G. (2023). Prediction of Air Quality Index Using Machine Learning Techniques: A Comparative Analysis. Journal of Environmental and Public Health, Article ID, 4916267, https://doi.org/10.1155/2023/4916267.

Fang, W., Zhu, R., Lin, J.C.-W. (2023). An air quality prediction model based on improved Vanilla LSTM with multichannel input and multiroute output. Expert Systems With Applications, 211, 118422.

Gibergans-Baguena, J., Hervada-Sala, J., Jarauta-Bragulat, E. (2020). The Quality of Urban Air in Barcelona: A New Approach Applying Compositional Data analysis Methods. Emerging Science Journal, 4(2), 113-121, http://dx.doi.org/10.28991/esj-2020-01215

Haddad, K., Vizakos, N. (2021). Air Quality pollutants and their relationship with meteorological variables in four suburbs of Greater Sydney, Australia. Air Quality, Atmosphere & Health, 14, 55-67.

Hu, F., Guo, Y., (2021). Health impacts of air pollution in China. Front. Environ. Sci. Eng. 15(4), 74.

Hu, J., Ying, Q., Wang, Y., Zhang, H. (2015). Characterizing multi-pollutant air pollution in China: Comparison of three air quality indices, Environment International, 84, 17-25.

Huang, L., Hu, J., Chen, M., Zhang, H. (2017). Impacts of power generation on air quality in China – part I: An overview. Resources, Conservation and Recycling, 121, 103-114.

Ilten, N., Selici, A.T., 2008. Investigating the impact of some meteorological parameters on air pollution in Balikesir, Turkey. Environmental Monitoring Assessment, 140, 267-277.

Janarthanan, R., Partheeban, P., Somasundaram, K., Elamparithi, P.N. (2021). A deep learning approach for prediction of air quality index in a metropolitan city. Sustain. Cities Soc. 67, 102720.

Li, H., Wang, J., Li,R., Lu, H. (2019). Novel analysis–forecast system based on multi-objective optimization fora ir quality index. Journal of Cleaner Production, 208, 1365-1383.

Li, H., You, S., Zhang, H., Zheng, W., Zheng, X., Jia, J., Ye, T., Zou, L. (2017a). Modellinf of AQI related to building space heating energy demand based on big data analytics. Applied Energy, 203, 57-71.

Li, W., Cao, Y., Li, R., Ma, X., Chen, Y., Wu, Z., Xu, Q. (2018a). The spatial variaiton in the effects of air pollution on cardiovascular mortality in Beijing, China. Journal of Exposure Science and Environmental Epidemiology, 28, 297-304.

Li, X., Xiao, J., Lin, H., Liu, T., Qian Z., Zeng, W., Guo, L., Ma, W. (2017b). The construction and validity analysis of AQHI based on mortality risk: A case study in Guangzhou, China. Environmental Pollution, 220, 487-494.

Li, Y., Chiu, Y.-H., Lu, L.C. (2018b). Energy and AQI performance of 31 cities in China. Energy Policy, 122, 194-202.

Lohani, B.N. (1984). Environmental Quality Management, South Asian Publishers, New Delhi.

Luvsan, M.E., Shie, R.H., Purevdorj, T., Badarch, L., Baldorj, B., Chan, C.C. (2012). The influence of emission sources and meteorological conditions on SO2 pollution in Mongolia. Atmospheric Environment, 61, 542-549.

Mason, T.G., Chan, K.P., Schooling, C.M., Sun, S., Yang, A., Yang, Y., Barratt, B., Tian, L. (2019). Air quality changes after Hong Kong shipping emission policy: An accountable study. Chemosphere, 226, 616-624.

Mason, T.G., Schooling, C.M., Rhan, J.J., Chan, K.P., Tian, L. (2020). Does the AQHI reduce cardiovascular hospitalization in Hong Kong's elderly population? Environment International, 135, 105344.

Masiol, M., Squizzato, S., Formenton, G., Harrison, R.M., Agostinelli, C. (2017). Air quality across a European hotspot: Spatial gradients, seasonality, diurnal cycles and trends in the Veneto region, NE Italy. Science of the Total Environment, 576, 210-224.

Mirabelli, M.C., Ebelt, S., Damon, S.A. (2020). Air Quality Index and air quality awareness among adults in the United States. Environmental Research, 183, 109185.

Mustakim, N.A., Ul-Saufie, A.Z., Shaziayani, W.N., Noor, N.M., Mutalib, S. (2023). Prediction of Daily Air Pollutants Concentration and Air Pollutant Index Using Machine Learning Approach. Pertanika J. Sci. & Technol. 31(1), 123-135.

Ni, W., Hu, X., Ju, Y., Wang, Q. (2023). Air pollution and indoor work efficiency: Evidence from Professional basketball players in China. Journal of Cleaner Production, 399, 136644.

Ott, W.R. (1978). Environmental Indices: Theory and Practice. Ann Arbor Science Publishers Inc., Ann Arbor.

Payus, C.M., Nur Syazni, M.S., Sentian, J. (2022). Extended air pollution index (API) as tool of sustainable indicator in the air quality assessment: El-Nino events with climate change driven. Heliyon, 8, e09157.

Pearce, J.L., Beringer, J., Nicholls, N., Hyndman, R.J., Tapper, N.J. (2011). Quantifying the influence of local meteorology on air quality using generalized addictive models. Atmospheric Environment, 45, 1328-1336.

Radaideh, J. (2017). Effect of meteorological variables on air pollutants variation in arid climates. Journal of Environmental & Analytical Toxicology, 7, 1-12.

Shen, L., Lu, X., Huynh, T.L.D., Liang, C. (2023). Air quality index and the Chinese stock market volatility: Evidence from both market and sector indices. International Review of Economics and Finance, 84, 224-239.

Shubham, S., Kumar, M., Sarma, D.K., Kumawat, M., Verma, V., Samartha, R.M., Tiwari, R.R. (2022). Role of air pollution in chronic kidney disease: an update on evidence, mechanisms and mitigation strategies. International Archieves of Occupational and Environmental Health, 95, 897-908.

Stieb, D.M., Burnett, R.T., Smith –Doiron, M., Brion, O.,Shin, H.H., Economou, V.A. (2008). A new multipollutant, no-threshold air quality health index based on short-term associations observed in Daily time series analyses. J Air Waste Manag Assoc., 58, 435-450.

Sowlat, M.H., Gharibi, H., Yunesian, M., Mahmoudi, M.T., Lotfi, S. (2011). A novel, fuzzy-based air quality index (FAQI) for air quality assessment. Atmospheric Environment, 45, 2050-2059.

Suarez Sanchez, A., Garcia Nieto, P.J., Riesgo Fernandez, P., del Coz Diaz, J.J., Iglesias-Rodriguez, F.J. (2011). Application of an SVM-based regression

model to the air quality study at local scale in the Aviles urban area (Spain). Math. Comput. Model. 54, 1453–146.

Tai, A., Loretta, J., Daniel, J. (2010). Correlations between fine particulate matter (PM2.5) and meteorological variables in the United States: Implications for the sensitivity of PM2.5 to climate change. Atmospheric Environment, 44, 3976–3984.

Tan, Y., Han, S., Chen, Y., Wu, Z., Lee, S.-C. (2023). Long-term variation and evaluation of air quality across Hong Kong. Journal of Environmental Sciences, 127, 284-294.

Thach, T.-C., Tsang, H., Cao, P., Ho, L.-M. (2018). A novel method to construct an air quality index based on air pollution profiles. International Journal of Hygiene and Environmental Health, 221, 17-26.

Turalioglu, F.S., Nuhoglu, A., Bayraktar, H. (2005). Impacts of some meteorological parameters on SO2 and TSP concentrations in Erzurum, Turkey. Chemosphere, 59, 1633-1642.

Usmani, R.S.A., Saeed, A., Abdullahi, A.M., Pillai, T.R., Jhanjhi, N.Z., Hashem, I.A.T. (2020). Air pollution and its health impacts in Malaysia: a review. Air Quality, Atmosphere & Health, 13, 1093-1118.

Van den Elshout, S., Leger, K., Nussio, F. (2008). Comparing urban air quality in Europe in real time, A review of existing air quality indices and the proposal of a common alternative. Environment International, 34, 720-726.

Van den Elshout, S., Leger, K, Heich, H. (2014). CAQI Common Air Quality Index – Update with $PM_{2.5}$ and sensitivity analysis. Science of the Total Environment, 488-489, 461-468.

Viana, M., Pey, J., Querol, X., Alastuey, A., de Leeuw, F., Lükewille, A. (2014). Natural sources of atmospheric aerosols influencing air quality across Europe. Science of the Total Environment, 472, 825-833.

Wang, J., Ogawa, S. (2015). Effects of meteorological conditions on PM2.5 concentrations in Nagasaki, Japan. International Journal of Environmental Research and Public Health, 12, 9089-9101.

Wang, W., Tang, Q. (2023). Combined model of air quality index forecasting based on the combination of complementary empirical mode decomposition and sequence reconstruction. Environmental Pollution, 316, 120628.

Wei, W., Wu, B.-J., Tong, Z.-T., Zhong, F., Hu, C.-Y. (2021). Association between lon-term ambient air pollution exposure and the risk of breast cancer: a systematic review and meta-analysis. Environmental Science and Pollution Research, 28, 63278-63296.

Witz, S., Moore, A.B., 1981. Effect of meteorology on the atmospheric concentrations of traffic-related pollutants at a Los Angeles site. JAPCA, 31, 1098-1101.

Wong, T.Z., Tam, W.W.S., Yu, I.T.S., Lau, A.K.H., Pang, S.W., Wong, A.H.S. (2013). Developing a risk-based air quality health index. Atmospheric Environment, 76, 52-58.

Xu, R., Deng, X., Wan, H., Cai, Y., Pan, X. (2021). A deep learning method to repair atmospheric environmental quality data based on Gaussian diffusion. Journal of Cleaner Production, 308.

Xu, Q., Ning, L., Yuan, T, Wu, H. (2023a). Application of data mining combined with power data in assessment and prevention of regional atmospheric pollution. Energy Reports, 9, 3397-3405.

Xu, R., Wang, D., Li, J., Wan, H., Shen, S., Guo, X.A. (2023b). Hybrid Deep Learning Model for Air Quality Prediction Based on the Time–Frequency Domain Relationship. Atmosphere, 14, 405. https://doi.org/10.3390/atmos14020405

Xu, Y., Yang, W., Wang, J. (2017). Air quality early-warming system for cities in China. Atmospheric Environment, 148, 239-257.

Zateroglu, M.T. (2021a). Assessment of the effects of air pollution parameters on sunshine duration in six cities in Turkey. Fresenius Environmental Bulletin, 30(02A), 2251-2269.

Zateroglu, M.T. (2021b). The Role of Climate Factors on Air Pollutants (PM10 and SO2). Fresenius Environmental Bulletin, 30(11), 12029-12036.

Zateroglu, M.T. (2021c). Evaluating the Sunshine Duration Characteristics in Association with Other Climate Variables. European Journal of Science and Technology, 29, 200-207, https://doi.org/10.31590/ejosat.1022639.

Zateroglu, M.T. (2021d). Statistical Models For Sunshine Duration Related To Precipitation and Relative Humidity. European Journal of Science and Technology, 29, 208-213. https://doi.org/10. 31590/ejosat.1022962.

Zateroglu, M.T. (2022). Modelling The Air Quality Index For Bolu, Turkey. Carpathian Journal of Earth and Environmental Sciences, 17(1), 119–130. https://doi.org/10.26471/cjees/2022/017/206.

Zhan, D., Kwan, M.-P., Zhang, W., Yu, X., Meng, B., Liu, Q. (2018). The driving factors of air quality index in China. Journal of Cleaner Production, 197, 1342-1351.

Zhang, X., Fung, J.C.H., Lau, A.K.H., Hossain, M.S., Louie, P.K.K., Huang, W. (2021). Air quality and synergistic health effects of ozone and nitrogen

oxides in response to China's integrated air quality control policies during 2015-2019. Chemosphere, 268, 129385.

Zhu, C., Fan, R., Sun, J., Luo, M., Zhang, Y. (2020). Exploring the fluctuant transmission characteristics of Air Quality Index based on time series network model. Ecological Indicators, 108, 105681.

Zhu, S., Lian, X., Liu, H., Hu, J., Wang, Y., Che, J. (2017). Daily air quality index forecasting with hybrid models: A case in China. Environmental Pollution, 231, 1232-1244.

Chapter 13

CONTACT NETWORKS IN EPIDEMIC DISEASE SPREAD

Amera Al-Amery[1]

Zeynep Ertem[2]

1 Systems Science and Industrial Engineering Department, Binghamton University, State University of New York

2 Systems Science and Industrial Engineering Department, Binghamton University, State University of New York, ORCID 0000-0003-0632-0905

Modeling the spread of disease, different mathematical models have been used in the literature like mathematical modeling using ordinary differential equations (ODEs) to multi-agent systems with high computational demand (Bajer, Martinović, and Brest, 2016). ODEs models (compartment models) were limited by the idea that individuals in different stages of disease should be well mixed and homogeneously distributed throughout the space (Roy and Pascual, 2006). A mass-action assumption is made in ODEs assumes that all susceptible individuals have the same likelihood to be infected. If this assumption is violated, inaccurate estimates may result or estimates that do not apply to the whole population. There is considerable variation in the spread of some infectious diseases, where in some cases a small number of individuals may be responsible for a large percentage of transmission. Consider the following two situations: a community where each entity has a relatively equal number of contacts compared with communities where a few individuals have a large number of contacts while the rest have only one or a few contacts. The resulting epidemiology will differ significantly for both communities, although some basic epidemiological characteristics (e.g., reproduction number) can be the same. Mathematical epidemiologists have developed several methods in case spatial factors are important or contact patterns are heterogeneous including contact network epidemiological (Albert and Barabási, 2002)

The contact networks consist of nodes that represent individuals or locations and edges that represent the appropriate connection among them, Definition 1.1.1. Using a set of nodes and edges, a contact network can capture the interaction patterns that cause disease transmission. A contact network can be more complex, it may contain multiple types of nodes or edges, and nodes or edges may have a variety of properties, numerical or otherwise. When considering a social network of people, for example, the nodes may be men or women, individuals with different characteristics. The edges of a graph may represent friendship, but they may also represent sexual behavior, business relationship, or proximity to a location (Schimit PHT, 2017). A network normally has undirected and unweighted edges, although directed networks are sometimes required to model certain asymmetrical structures, it can be defined as adjacency matrix $A = (a_{u,v})$, where $a_{u,v} = 1$ if there is a link from v to u and 0 otherwise.

Definition 1.1.1 $G = (V, E)$ is a network. V is the set of nodes and E is the set of edges. $\forall e \in E$, if e joins $u, v \in V$, we write $e = \langle u, v \rangle$. Nodes u and v in this case are considered adjacent. Edge e is incident with vertices u and v, respectively

The main topological parameters used to identify the properties of the network are:

- Density: It is defined as the ratio between the number of edges in a network and its potential number of edges, Equation 1.1. A network with a density of one indicates that all potential connections have been established (PINTO et al., 2020).

$$d = \frac{\sum_{i=1}^{N} \sum_{j=1}^{N} (a_{i,j})}{N(N_{-1})}$$

where $a_{i,j}$ are the elements of the adjacency matrix A.

- Degree: It is the number of edges that connect a node to another node. For undirected, unweighted networks it can be expressed as (PINTO et al., 2020):

$$K_i = \sum_{i=1}^{N} (a_{i,j}) = \sum_{j=1}^{N} (a_{j,i}),$$

and the average degree can be computed as:

$$\langle K \rangle = \frac{\sum_{i=1}^{N} k_i}{N}$$

- Clustering Coefficient: It measures the degree of interconnection which may exist between nodes (PINTO et al., 2020).

$$CC_i = \frac{\sum_{i \neq j} \sum_{h \neq i,j} (a_{i,j})(a_{i,h})(a_{j,h})}{\frac{1}{2} k_i (k_i - 1)},$$

the global clustering coefficient CC represents the overall clustering level, which can be computed as the average of the local clustering coefficients of all the nodes.

- Average Shortest Path (L) : it is defined as the average number of steps along the shortest paths for all possible pairs of network nodes, with a small L ensuring that information is easily distributed throughout the network. It can be computed as follows (PINTO et al., 2020):

$$L = \frac{1}{N(N-1)} \sum_{i \neq j} d(i,j),$$

where N is the number of nodes in the graph and $d(i,j)$ is the shortest path length between nodes i and j respectively.

Many epidemiological studies have begun to utilize complex networks as an effective way of modeling the population (Albert and Barabási, 2002) (Boccaletti et al., 2006). Studies of this type have developed networks with different complex connection structures, such as small-world and scale-free models.

Contact Network Models

In order to replicate the connections found in real networks, several contact network models have been proposed. The simplest form of the contact network is the undirected network represented in Figure 1a, considering that two individuals are connected, then both individual has the same probability to infect each other. The other form is semi-directed networks, Figure 1 b. This form of contact network can capture situations where an individual may infect another individual, but the converse is not true.

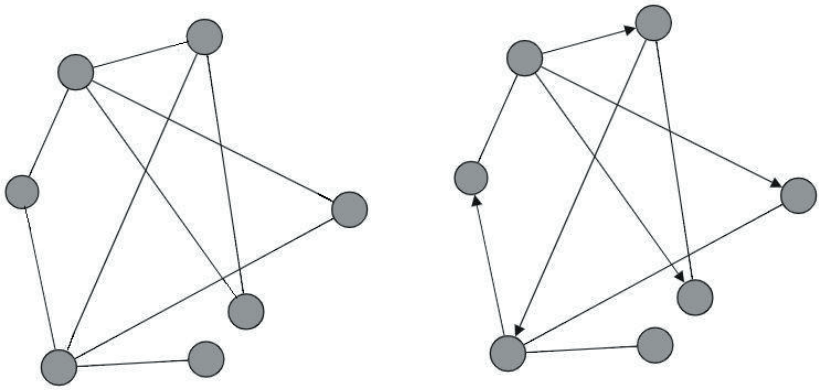

(a) (b)

Figure 1: Contact networks. (a) Undirected network; (b) Semi-directed network

It is important to note that realistic contact networks do not necessarily fall into one of these families. More complex contact network models can be as follows:

Small World Networks

A small-world network is a network in which the majority of nodes do not have neighbors, but are reached via a limited number of links from one node to another. Two characteristics distinguish a small-world network from other networks. Firstly, it has a high clustering coefficient, and secondly, it has short path lengths, which are also characteristic of random networks. Small values of short paths ensure that information or resources are easily dispersed throughout the network. In order to construct a small world network, a random rewiring procedure is applied to the regular network. The procedure begins with a ring topology consisting of n nodes and k edges per node. Nodes are randomly selected and the edges that connect them to their nearest neighbors are connected to one of their other neighbors with probability p. This process is repeated over all the network nodes until all edges are rewired, Figure 2. As a result of this process, the graph can be tuned between regularity ($p = 0$) and totally random ($p = 1$) (Watts and Strogatz, 1998).

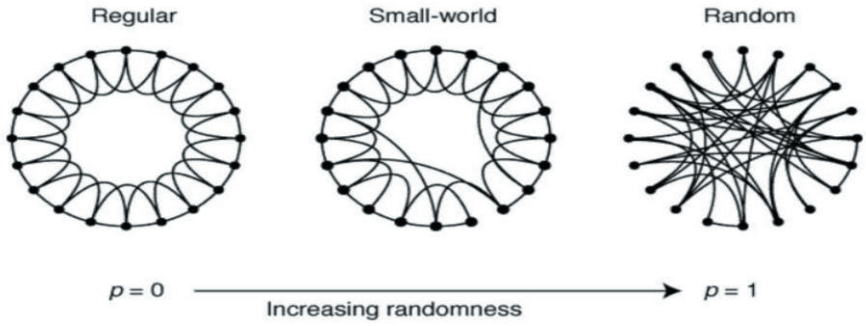

Figure 2: Random rewiring procedure (Watts and Strogatz, 1998)

Scale-Free Networks (SF)

The scale-free network was first proposed by Barabasi and Albert (Barabási and Albert, 1999), based on random networks. Based on the mapping of connections between World Wide Web pages, they found that only a few nodes in the network, termed hub points, have a high number of connections, while most nodes have a smaller number of connections. In particular, links to highly connected nodes have a greater probability of being established in succession, Figure 3. As a general rule, on the Internet and other social networking sites, it is more likely that new individuals will establish connections with individuals who are already well-known and highly connected.

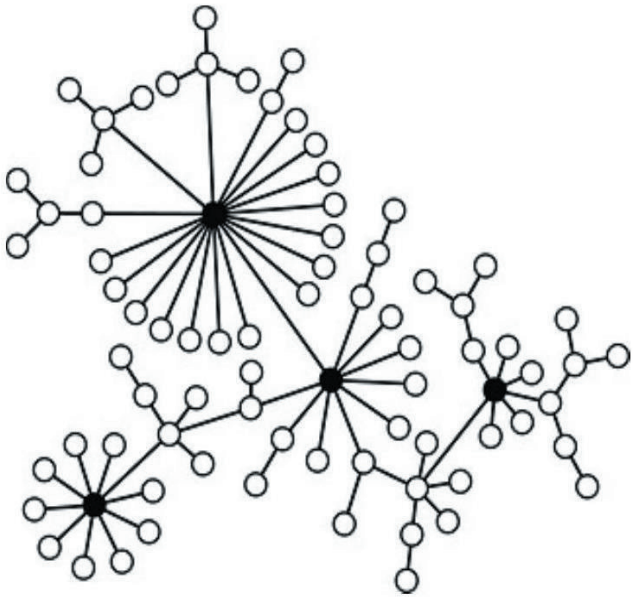

Figure 3: Representation of a scale-free network. Black nodes represent "hubs", (Schneider et al., 2014)

Contact Networks in Epidemiology

Diseases and networks are closely interconnected. The contact networks of two diseases with different modes of transmission may be extremely different within the same population. A highly transmitted disease involving coughing and sneezing transmission is expected to have a dense contact network structure because the network will have a large number of connections in which any pair of individuals (such as in transportation) will create a link between each other. For non-highly transmissible diseases in which close contact is required, fewer people are connected by links, resulting in a sparser contact network.

The use of contact networks in epidemiology involves three steps. First, construct a realistic network model of the contact patterns. The second step involves the use of mathematical epidemic models (e.g., SIR, SEIR) in order to predict the spread of disease through populations based on the underlying characteristics of the disease and the structural characteristics of the network. The third step involves manipulating the network in order to model containment strategies and analyzing their epidemiological impact (David and Jon, 2010).

The mathematical epidemic models can be applied to any contact network model, by considering the compartmental SIR model (Kermack,

McKendrick, and Walker, 1927), there are three possible states for a node in the contact network: susceptible, infectious, and recovered. The susceptible individuals are at risk of getting infected by the disease; infectious individuals have the disease and can transmit it to other susceptible individuals by close contact; recovered individuals are cured of the disease. A model for epidemics on the contact networks can be developed by utilizing the three-stage described above. If there is an edge between u and v in the network, the disease has the potential to spread directly to v with a probability of β_{uv} if u becomes infected at some point. In order to represent a symmetric contact, individuals can be potentially infected in either direction. The transmission of the disease in the contact network can be summarized as follows:

- A set of random nodes will be in the I state while all remaining nodes will be in S

- Nodes in I state remain infected for a period of time τ

- During infected time τ, nodes can transmit the disease to their S neighbors with probability β

- After spending τ nodes will transmit to state R, which can not receive or transmit the disease

In statistical physics, this process is known as percolation models and has been developed into a framework to predict infectious diseases in contact networks (Newman, 2002). The transmissibility T of the disease is computed by:

$$T = 1 - (1 - \beta)^{\tau}$$

which is an indicator of disease severity, i.e., the likelihood that the disease will spread across any given edge.

The percolation process is controlled by the probability of disease transmission β, length of infected period τ, and network structure are three factors that control the spread of the disease in the network (David and Jon, 2010).

The Basic Reproductive Number

The basic reproduction number R_0 is crucial to understanding the dynamics of epidemics. It is defined as the average number of cases of an infectious disease caused by transmission from a single individual. In contact networks, R_0 is computed as follows (Meyers, 2007):

$$R_0 = T\left(\frac{\langle k^2\rangle - \langle k\rangle}{\langle k\rangle}\right)$$

where T represents the transmissibility of disease, $\langle k\rangle$ and $\langle k^2\rangle$ are the mean degree and mean square degree respectively. It is worth mentioning that R_0 is highly dependent on the structure of the network represented by $\langle k\rangle$ and $\langle k^2\rangle$. Consequently, two different structured populations may experience different transmission dynamics for the same disease. In case of two populations have the same $\langle k\rangle$, the population with a greater degree variance $\langle k^2\rangle - \langle k\rangle$ will be more vulnerable to disease transmission. The R_0 value is considered to be a critical epidemiological value. The disease will spread through the population if $R_0 > 1$, which indicates that each infected individual will transmit the disease to at least one other susceptible individual at some point during the infection period. If $R_0 < 1$, the disease is expected to disappear before affecting a large portion of the population.

Percolation can be used to predict the size of an outbreak, namely the number of nodes that are reached because of disease transmission along the edges of the network. There is generally an epidemic threshold (T_c) in fixed contact networks below which there will be only small outbreaks, and above which there may be large outbreaks relative to the size of the entire network (Meyers, 2007).

$$T_c = \frac{\langle k\rangle}{\langle k^2\rangle - \langle k\rangle}$$

When the transmissibility of a disease reaches the epidemic threshold ($T = Tc$), then $R_0 = 1$

Disease Containment Strategies in Contact Networks

Healthcare systems face numerous challenges in controlling the spread of epidemics and preventing the overburden of the health system. A set of pharmaceutical and non-pharmaceuticals can be implemented to contain the spread of the disease through the population by reducing the prevalence of the disease from levels above an epidemic threshold to levels below that threshold ($T \leq T_c$). Vaccination, contact reduction, and transmission reduction are three commonly used interventions used for this purpose (Pourbohloul et al., 2005).

Vaccination is one of the most used pharmaceutical interventions which refers to the vaccination of a large proportion of the population. A

wide variety of vaccination strategies can be used (e.g., random, targeted population, age groups, and ring). Vaccination strategies can be modeled in the contact network by removing all vaccinated nodes or moving them directly to the recovery state.

Contact reduction intervention includes reducing the number of contacts between infected and susceptible individuals in the population (e.g., quarantine, school closure, business closure). To model this intervention the contact networks, a set of edges that represent contact between targeted nodes can be removed.

Transmission reduction intervention can be implemented by a set of procedures that aim to introduce physical barriers between individuals in the community (e.g., face masking). In contact networks, this intervention can be studied by reducing the transmissibility of the disease for the contact between node u and node v. A set of epidemiologically relevant objectives can be used to evaluate the containment interventions. As an example, the time and size of an outbreak can be identified after modeling an intervention and used as an indicator of the effectiveness of the intervention (Meyers, 2007).

Agent-Based Modeling

Agent-based simulation models (ABM) are commonly used in place of equation-based models when many scenarios need to be implemented and the assumption of homogenous populations has to be violated. Agent-based models enable individuals to interact with the environment through predefined rules. In epidemiology, it is often used to model the progression of the disease when experiments cannot be conducted. It is possible for individuals in ABM to behave differently and make different decisions, which adds flexibility to the model and enables realistic modeling at the global, national, and community levels. ABMS does not have a universal definition of the term "agent"; agents may be human, or organizational, characterized by diverse and dynamic attributes and behaviors, and having the following properties (Hunter, Mac Namee, and Kelleher, 2017):

- An agent is self-directed: The agent can interact with its environment and with other agents independently.

- Agents are self-contained: An agent is a distinct, recognizable individual possessing a particular set of characteristics and attributes, as well as the ability to behave, make decisions, and, in some cases, learn from its experiences and adapt their behaviors accordingly.

- An agent is social, interacting with other agents according to protocols or mechanisms which describe how they interact.

There are three steps involved in ABM: identification of agents, specifying their behaviors accurately, and representing their interactions appropriately.

Agent-Based in Epidemiology

ABMs have become increasingly significant in the epidemiology of infectious diseases, as they capture both the dynamics of disease transmission and the heterogeneous mixing of agents. For an ABM to be useful in real-world situations, it must represent both the characteristics of the disease (such as infection rates), as well as the characteristics of the agents and their environment, all at a sufficient level of detail. The SIR model is commonly used in ABMs addressing infectious disease transmission, which incorporate extensions in order to represent individual heterogeneity and more complex network interactions within these compartmental models, providing valuable insight into the transmission of infectious diseases in real-life settings, it is possible to categorize infectious disease ABM into those that simulate a specific disease or specific outbreak, and those that simulate general disease dynamics (Tracy and Keyes, 2018). An epidemiological agent-based model of four main components must be considered: disease, society, transportation, and the environment. In modeling the disease two main parts should be determined: between host transmission and within-host progression; between host transmission determines how the infectious disease is transmitted between agents while the within-host progression determines how the disease progresses in an infected agent.

A society's structure can have an impact on the development of an outbreak. A simulation of a specific society requires consideration of the number of agents, household structure, as well as many other factors.

The process of modeling transportation involves determining the movement of agents between different locations. A model of the environment is an important part of an agent-based model, since it represents the environment in which agents move and interact, and its complexity will depend on the model's needs and the dynamics of disease transmission (Hunter, Mac Namee, and Kelleher, 2017).

In designing any model, validation is a crucial part, as a model that has not been validated cannot be fully trusted if any unexpected results occur. To date, there is no exact definition or methodology for testing the validity of agent-based models. Epidemiological models can be used to

simulate historical outbreaks of infectious diseases. As a result of this, validation can be performed by comparing the simulation outbreak to the real outbreak, which allows the researcher to assume that the model will accurately simulate future outbreaks, providing insight into the behavior of the disease. However, if the model is not simulating a past outbreak or epidemic cross validation can be used as an alternative in which the agent-based model results can be compared to another widely used model such as an equation-based SIR model (Hunter, Mac Namee, and Kelleher, 2017).

REFERENCES

1. Albert, Réka and Albert-László Barabási (2002). "Statistical mechanics of complex networks". In: Rev. Mod. Phys. 74 (1), pp. 47-97. Dor: 10 . 1103/RevModPhys . 74 . 47. URL: https: / /link.aps.org/doi/10.1103/RevModPhys . 74 .47.
2. Bajer, Dražen, Goran Martinović, and Janez Brest (2016). "A population initialization method for evolutionary algorithms based on clustering and Cauchy deviates". In: Expert Systems with Applications 60, pp. 294-310. ISSN: 0957-4174. Dor: https:// doi .org/10.1016/j . eswa.2016.05.009. URL: https://www . sciencedirect .com/science/article/pii/s0957417416302287. Barabási, Albert-László and Réka Albert (1999). "Emergence of Scaling in Random Networks". In: Science 286.5439 , pp. 509-512. DoI: 10.1126 /science. 286.5439 . 509. URL: https: / / www . science .org/doi / abs / 10.1126/ science . 286 .5439 .509$.
3. Boccaletti, S. et al. (2006). "Complex networks: Structure and dynamics". In: Physics Reports 424.4, pp. 175-308. IssN: 0370-1573. DoI: https://doi .org/10.1016/ j .physrep .2005 .10.009. URL: https://www . sciencedirect.com/science/ article/pii/s037015730500462X.
4. David, Easley and Kleinberg Jon (2010). Networks, Crowds, and Markets: Reasoning About a Highly Connected World. USA: Cambridge University Press. IsBn: 0521195330.
5. Hunter, Elizabeth, Brian Mac Namee, and John D. Kelleher (2017). "A Taxonomy for Agent-Based Models in Human Infectious Disease Epidemiology". In: Journal of Artificial Societies and Social Simulation 20.3 , p. 2. ISSN: 1460-7425. Dor: 10 . 18564/ jasss. 3414. URL: http://jasss. soc. surrey.ac.uk/20/3/2 .html.
6. Kermack, William Ogilvy, A. G. McKendrick, and Gilbert Thomas Walker (1927). "A contribution to the mathematical theory of epidemics". In: Proceedings of the Royal Society of London. Series A, Containing Papers of a Mathematical and Physical Character 115.772, pp. 700-721. Dor: 10.1098/rspa.1927.0118. eprint: https: //royalsocietypublishing.org/doi/pdf/10 .1098/rspa .1927 . 0118. URL: https: / / royalsocietypublishing .org / doi / abs / 10.1098 / rspa . 1927 .0118.
7. Meyers, Lauren (Feb. 2007). "Contact network epidemiology: Bond percolation applied to infectious disease prediction and control". In: BULLETIN (New Series) OF THE AMERICAN MATHEMATICAL SOCIETY 44. DoI: 10.1090/ S0273-0979-06 −01148 − 7.
8. Newman, M. E. J. (2002). "Spread of epidemic disease on networks". In: Phys. Rev. E 66 (1), p. 016128 . DoI: 10.1103 /PhysRevE.66.016128. URL: https://link.aps .org/doi/10.1103/PhysRevE.66.016128.
9. PINTO et al. (Apr. 2020). "Impact of network topology on the spread of infectious diseases". In: TEMA 21, pp. 95-115. Dor: 10.5540/tema.2020.021.01.0095.
10. Pourbohloul et al. (2005). "Modeling control strategies of respiratory pathogens". In: Emerg Infect Dis 11, pp. 1249-1256. Dor: doi : 10.3201/eid1108.040449.

11. Roy, Manojit and Mercedes Pascual (2006). "On representing network heterogeneities in the incidence rate of simple epidemic models". In: Ecological Complexity 3.1, pp. 80-90. IssN: 1476-945X. DoI: https : / /doi .org/10 .1016/ j . ecocom . 2005 .09 .001. URL: https://www .sciencedirect. com/science/article/pii/ S1476945X05000814.
12. Schimit PHT, Pereira FH (2017). "Disease spreading in complex networks: A numerical study with Principal Component Analysis". In: Expert Systems with Applications 97, pp. 294-310. IsSN: 41-50. doI: doi:10.1016/j . eswa. 2017.12 .021$.
13. Tracy Melissa, Magdalena and Katherine M. Keyes (2018). "Agent-Based Modeling in Public Health: Current Applications and Future Directions". In: Annual Review of Public Health 39.1. PMID: 29328870, pp. 77-94. DoI: 10.1146/ annurev -publhealth-040617-014317. eprint: https://doi .org/10.1146/annurev -publhealth-040617-014317. uRL: https : / / doi .org / 10.1146 / annurev -publhealth-040617-014317.

Chapter 14

ECG DATA ANOMALIES DETECTION WITH STACKED AUTOENCODER ON LOW-POWER AND LOW-MEMORY MICROCONTROLLERS

Hatice Vildan DÜDÜKÇÜ[1]
Murat TAŞKIRAN[2]

1 Research Assistant, Yildiz Technical University, 0000-0002-0314-6262
2 Lecturer PhD, Yildiz Technical University, 0000-0002-6436-6963

1. Introduction

Electrocardiography (ECG) is defined as the recording of electrical activities in the heart muscle for the purpose of examining and interpreting. The data obtained from the ECG signals are recorded as a time series and it is possible to diagnose many diseases by examining and interpreting these recorded data. For the correct diagnosis of the disease, the examination and interpretation of ECG signals should be performed by specialist doctors. However, with the rapid developments in the field of artificial intelligence in recent years, it allows the interpretation of this data to be done by a machine. Although artificial intelligence models created in current studies are used to give an idea to doctors for the diagnosis of diseases, the opinion that it will be the definitive decision mechanism for the diagnosis of diseases in the near future is quite common among researchers.

In recent years, the use of machine learning methods is very common in the detection of anomalies in data in ecg signals, as it has been used in solving many problems in the literature (Chakraborty et. al, 2018; Chauhan and Vig, 2015; Chauhan et. al, 2019; Kumar and Chakrapani, 2022; Li and Boulanger, 2020; Noor et. al, 2021; Serhal et. al, 2022; Sun et. al, 2020; Wang et. al, 2020). In the study carried out by Chauhan and Vig in 2015, a method using the Long-Short Term Memory (LSTM) model was proposed to detect anomalies in ECG signals. The reason for choosing the LSTM network in the study is that preprocessing is not required before the ECG signal is given to the model, and it is shown that the parts with high errors can be detected as anomalies in the predictions made with an LSTM model trained with healthy ECG data (Chauhan and Vig, 2015). The results of the study showed that the predictions made by the LSTM model are sufficient to detect ECG anomalies. In another study conducted by Chauhan and Vig, the LSTM model trained with ECG signals of 1 minute length was used to detect 7 different ECG anomalies (Chauhan et. al, 2019). Besides, in stage 2, Multilayer Perceptron (MLP), Support Vector Machine (SVM) and Logistic Regression (LR) are used for the same anomaly detection. The results obtained as a result of the study, in which the advantages and disadvantages of these four methods for ECG anomaly detection are examined, are promising for real-time ECG anomaly detection. In the method proposed by Chakraborty et al. in 2018, in order to detect abnormalities in semi-periodic signals such as ECG signal, firstly to create a "Mother Signal" based on the average data obtained from normal ECG data, and then to compare the data obtained from the sensors with this mother signal. Regions with deviations higher than the threshold value determined as a result of the comparison were determined as anomalies (Chakraborty et. al, 2018).

In the survey study carried out by Li and Boulanger in 2020, the methods found in the literature were investigated in detail on the detection of anomalies using the Ambulatory Electrocardiogram (Li and Boulanger, 2020). In the survey, general information is given about the common methods used for noise removal, feature extraction and classification, which are important steps of ECG signal processing studies, and the results obtained with the MIT-BIH Database (Goldberger et. al, 2000; Moody and Mark, 2001) in simulation studies using these methods are given. In the study performed by Noor et al, classification of ECG signals as normal, abnormal and risky was performed using recurrent neural networks (Noor et. al, 2021). In the study using 5000 ECG data, it was shown in the loss charts that normal ECG data can be predicted much more successfully, and it was determined that there was a connection between the risk of depression and ECG signals. Kumar and Chakrapani used Fast Fourier Transform (FFT) for feature extraction and AlexNet for classification process in their study to classify ECG signals (Kumar and Chakrapani, 2022). The simulation results showed that the proposed method in the detection of 4 different types of ECG anomalies performed 20% higher deviation detection compared to traditional methods.

Sun et al. carried out a study using stacked LSTM architecture to predict Atrial fibrillation (AF), one of the ECG anomalies (Sun et. al, 2020). The aim of the developed architecture is to prevent the gradient exploitation problem experienced in traditional RNN networks. The prediction performance of 92% obtained in the simulation studies using the long-term AF database (Li et. al, 2017) and the AF terminal challenge database showed that the proposed method provides sufficient performance for the prediction of Atrial fibrillation (AF). Another study that performed Arrhythmia prediction using DNN from ECG data was carried out by Wang et al. In the study, the method called ECG Anomaly Prediction DNN (EAPD) classified the type of ECG segment before the heartbeat, instead of classifying the heartbeat itself, to predict the types of heartbeats that have not yet occurred (Wang et. al, 2020). In order for researchers to learn about studies that perform atrial fibrillation prediction, classification and detection from ECG signals, A detailed review of the studies of the last 10 years was carried out by Serhal et. al (Serhal et. al, 2022).

Within the scope of this study, an autoencoder architecture that classifies ECG data as normal and abnormal was proposed and after the training of the proposed architecture was completed, it was embedded in a low-power and low-memory microcontroller. In the sections below, detailed information about the method used in the study is given under the title of "Methodology", in the next section "Experimental Setup" both information about the data set used in the training of the proposed method

and the test process, as well as the test results and graphics obtained are given respectively. In the last section, "Conclusion and Discussion", the simulation results obtained were interpreted and brief information about future studies was given.

2. Methodology

The block diagram in which the main steps of the processes within the scope of the study are given is given in Figure 1.

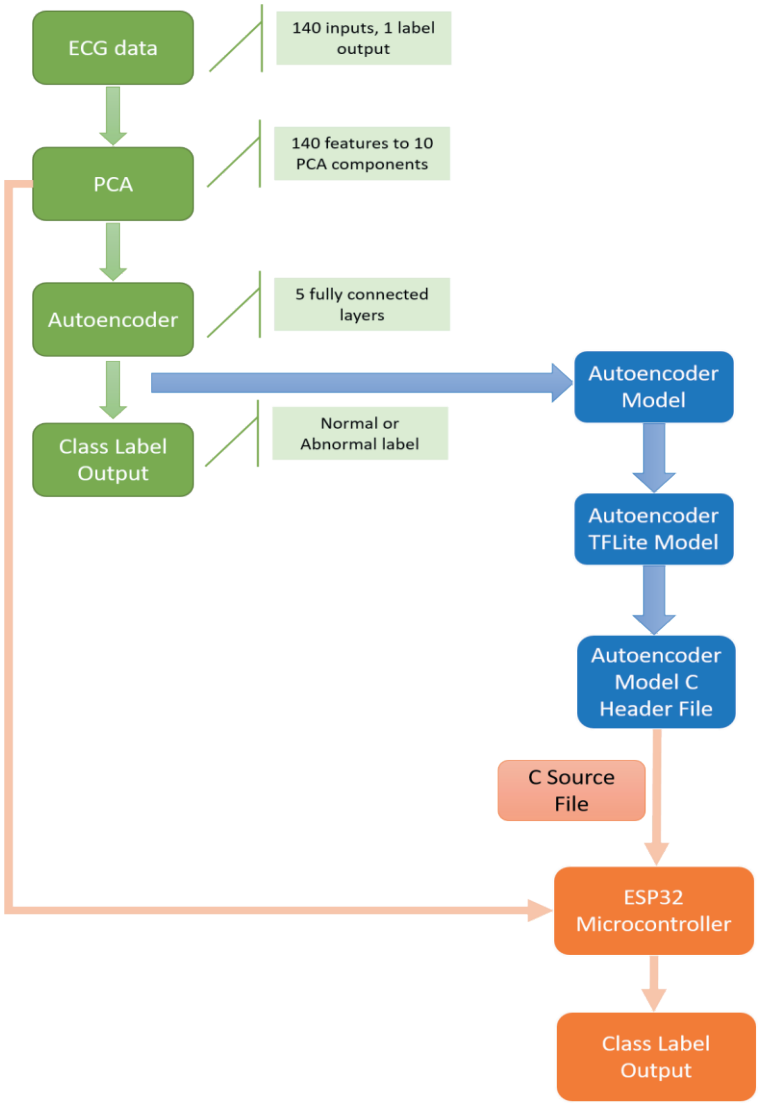

Figure 1. The block diagram of the proposed method

In the proposed method, firstly, the data editing process was carried out. In the data set used, there are ECG data, each consisting of 140 dimensional time series and labeled as "normal" and "abnormal" in binary. Before using this data in the training of the network, feature reduction was performed using the Principal Component Analysis (PCA) algorithm (Wold et. al, 1987). The purpose of this process is to ensure that the computational cost is as low as possible by giving less data as input for the trained model deployed to the microcontroller. After the feature reduction process, the training of the model was carried out and the obtained model was tested using data that was not used in the training before, and the ECG classification performance of model was measured. After it was determined that the model achieved sufficient performance, the process of deploying the model to the microcontroller was carried out and the performance of the model in the microcontroller was tested.

2.1. Principal Component Analysis (PCA)

Principal Component Analysis (PCA) method is one of the commonly used methods for feature reduction in signal processing problems (Wold et. al, 1987). The main purpose of the method is to detect and store features that carry more information in data represented in multidimensional space, and to create a new representation that does not contain features that carry less information. Although there is usually data loss in the use of the PCA algorithm, the main purpose is to reduce the computational cost as much as possible while keeping this data loss as minimal as possible.

Within the scope of this study, the PCA algorithm was used to avoid computational cost of the data to be sent to the microcontroller. ECG data, each of which is represented by a 140-dimensional time series in the data set, has been reduced to 10 dimensions. The 10-dimensional vector obtained as a result of reduction contains 93.33% of the information in the whole data. The computational cost gain obtained is at an acceptable level when compared to 6.66% lost data.

2.2. Stacked Autoencoder

Autoencoder(AE) structures are one of the unsupervised neural network structures that were proposed in the late 1980s and whose basic structure consists of 3 layers (input layer, hidden layer and output layer) (Rumelhart et. al, 1986; Baldi and Hornik, 1989). The structure of auto encoders basically consists of two different parts; Decoder and encoder. While the input layer and hidden layer inside the structure create the decoder structure, the hidden layer and output layer create the encoder

structure (Zhang et. al, 2020). The reason why autoencoder structures are widely used in the literature is their success in extracting non-linear features. In addition, autoencoder structures are also widely used in the denoising process. After the first proposed basic AE structure in the late 1980s, many different AE variations have been proposed in the literature over the years to solve different problems; Stacked AE, Denoising AE, Stack denoising AE, Variational AE etc. The Autoencoder structure that will be used in this study is the Stacked AE structure. Stacked AE is defined as having more than one hidden layer inside an autoencoder structure. The Stacked AE structure used in this study consists of 5 layers. Stacked AE architecture used in this study is given in Figure 2.

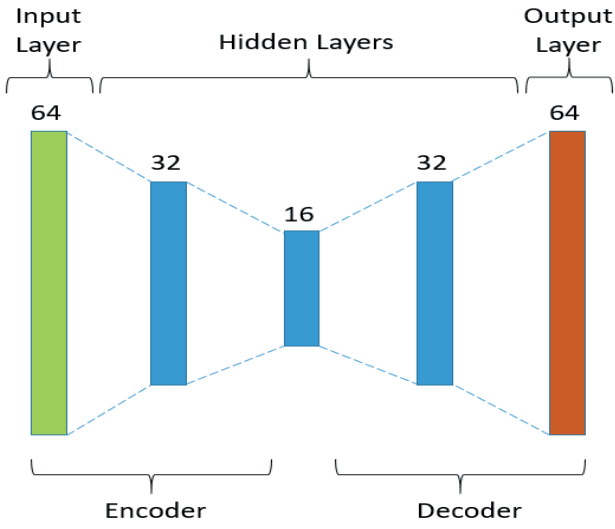

Figure 2. Stacked AE architecture used in the proposed method

3. Experimental Setup

After deciding on the methods for this study, first of all, the process of organizing the data for the training of the model was carried out. After the data set was separated as test and train, the training process of the stacked AE architecture was carried out. In order to examine the classification performance of the model after the training process, model performence tests was carried out for various evaluation metrics. Afterwards, the model, which achieved sufficient test performance, was deployed to ESP32 microcontroller using various tinyML libraries. After model deployement, the results for the AE model and the deployed model were shared with the researchers in the following subsections.

3.1. Dataset

The ECG data that will be used for the training of the Stacked Autoencoder architecture in the study were obtained from the BIDMC Congestive Heart Failure Database in PhysioNet (Baim et. al,1986; Goldberger et. al, 2000). The ECG5000 dataset in the BIDMC Congestive Heart Failure Database was used for training and testing the model in this study. There are time series obtained from approximately 5000 ECG signals in the ECG5000 data set. Each ECG signal consists of 140 steps and these data are labeled as "normal" and "abnormal". The ECG data for normal and abnormal labels are can be seen in Figure 3. While 3498 out of 4998 data in the data set were used for training and validation of the model, 1500 data were reserved as test data. 20% of 3498 data is also reserved as validation data. As a result of these processes, the ratios of training, validation and test data in the data set were 56%, 14% and 30%, respectively.

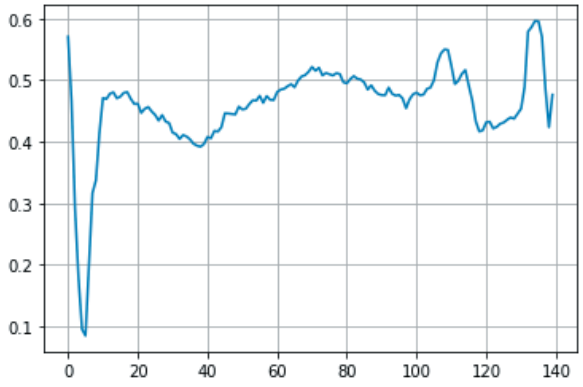

(a)

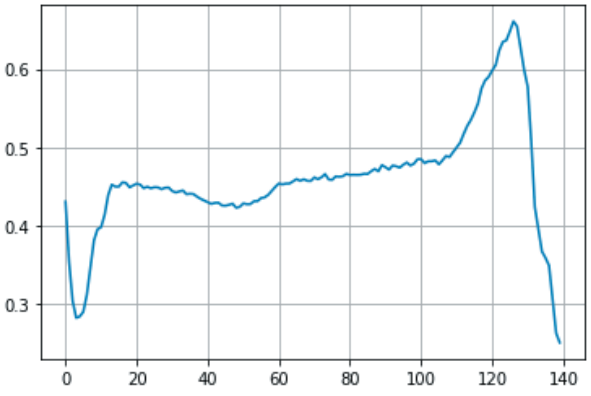

(b)

Figure 3. ECG data. (a) normal ECG, (b) anomalous ECG.

Within the scope of the study, it is aimed to represent the ECG data with a smaller size feature vector in order to reduce the computational cost on the microcontroller. Since the model whose training is completed will be embedded in the ESP32, the PCA algorithm is used to reduce the feature dimension. After the features in the whole data set were normalized between 0 and 1, the representation of each ECG data was reduced from 140 dimensions to 10 by PCA algorithm. The reason for obtaining a 10-dimensional vector as a result of this feature reduction process is that this 10-dimensional vector contains 93.33% of whole data information. Thus, a great gain from computational cost has been achieved without a great loss of data.

3.2. Experimental Results

After editing the data and completing the feature reduction process, the training process of the 5-layer Stacked Autoencoder architecture was carried out. During the training of the model, a single dense neuron was used with the sigmoid activation function as the Output neuron. The threshold value used for the separation of classes in the binary classification training was chosen as 0.5. During the training, the "Adam" algorithm was used as the optimizer and "binary cross-entropy" was used as the loss function. For training, epoch number was selected as 100, the batch size was determined as 512 and patience was determined as 25 to avoid overfitting during model training.

A confusion matrix was used to examine the classification performance of the trained model, and various evaluation metrics were obtained by using this matrix. Calculations of the evaluation metrics used in the classification performance of the model from Equation 1 to Equation 4.

$$Accuracy = \frac{TP + TN}{TP + FP + TN + FN} \qquad (Eq.1)$$

$$Precision = \frac{TP}{TP + FP} \qquad (Eq.2)$$

$$Recall = \frac{TP}{TP + FN} \qquad (Eq.3)$$

$$F1_{Score} = 2\,x\,\frac{Precision\ x\ Recall}{Precision + Recall} \qquad (Eq.4)$$

Below, in Figure 4, the graph showing the change of the model's loss during training according to epochs, the confusion matrix obtained in Table 1 and the values of the evaluation metrics obtained in Table 2 are given respectively.

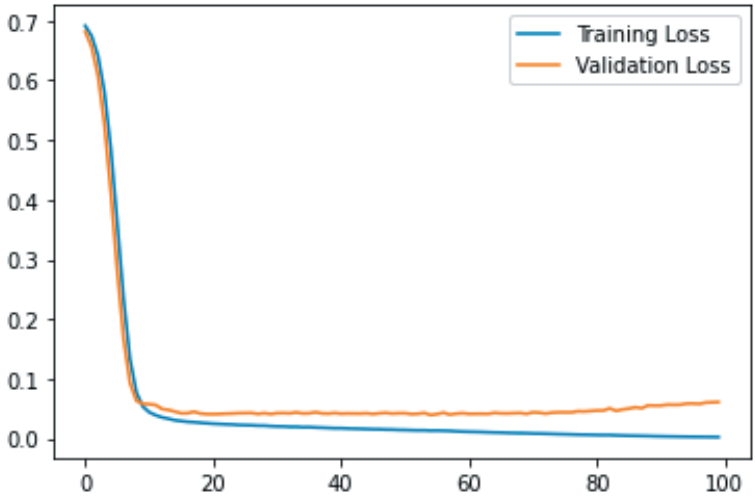

Figure 4. The change graph of the loss values obtained during the training process according to the number of epochs.

Table 1. Confusion matrix of trained stacked AE model

		Predicted Label	
		Abnormal	**Normal**
Actual Label	**Abnormal**	633	7
	Normal	6	854

Table 2. Evaluation metric values obtained from stacked AE model tests

Evaluation Metric	Results
Accuracy	99.13%
Precision	99.19%
Recall	99.30%
F1-Score	99.24%
AUC (Area Under Curve)	99.10%

After observing that the model has achieved sufficient classification success, it is first converted to TFLite model and the same tests are performed in the Python environment.

Confusion matrix and evaluation metrics obtained from the model that was converted to TFLite are given in Table 3 and Table 4, respectively.

Table 3. Confusion matrix of TFLite model

		Predicted Label	
		Abnormal	**Normal**
Actual Label	**Abnormal**	633	7
	Normal	6	854

Table 4. Evaluation metric values obtained from TFLite model tests

Evaluation Metric	**Results**
Accuracy	99.13%
Precision	99.19%
Recall	99.30%
F1-Score	99.24%
AUC	99.10%

The TFLite model, which was found to be successful after the tests carried out in the Python environment, was then deployed to an ESP32 microcontroller. ESP32 is a microcontroller unit (MCU) that can be used for wide variety of applications. ESP32 is a small size MCU with ultra-low power consumption, and due to these features, it is widely preferred especially for mobile and IoT applications.

The stacked AE model, whose training is completed in the Python environment, is converted to the TFLite model before being deployed into ESP32 (Esspressif Systems, 2023). The model obtained after this conversion was converted to a HEX file to be used as a C header file in order to run on the microcontroller. After the conversion was carried out in the Python environment, the source code was prepared using the Arduino IDE (Fezari and Al Dahoud, 2018) environment, which could call the header file containing the model and obtained the output label from the input data with the model inference. After the prepared source code is loaded into ESP32 with the header file, the classification performance of the deployed AE model was then tested on ESP32 board and the results for these performance tests are given in Table 5 and Table 6, respectively.

Table 5. Confusion Matrix of the model deployed to microcontroller

		Predicted Label	
		Abnormal	**Normal**
Actual Label	**Abnormal**	633	7
	Normal	6	854

Table 6. Evaluation metric values obtained from the model deployed to microcontroller

Evaluation Metric	Results
Accuracy	99.13%
Precision	99.19%
Recall	99.30%
F1-Score	99.24%
AUC	99.10%

4. Conclusion and Discussion

This study is aimed to train a stacked AE architecture that classifies ECG signals as normal and abnormal, and then deploy the trained model to the ESP32 microcontroller to create a system that consumes low power and low memory. Stacked AE, which was trained with the data in the ECG5000 data set, was tested with the ECG signals in the same data set and this process confirmed that model is ready to be deployed to the ESP32 microcontroller. After the completed model was deployed to ESP32, tests were carried out to measure the classification performance and it was observed that the model performed the classification with the same performance in ESP32. The accuracy value of 99.13%, obtained both in the simulation environment and in the tests performed with microcontrollers, clearly showed that the system performs classification with high performance. In addition, the number of incorrectly classified data from each class was shared with the researchers, along with the confusion matrix created according to the obtained test results. Thus, the aim of creating a system in which abnormalities in ECG signals can be detected with the help of a microcontroller with low power consumption and low memory, which was aimed at the beginning of the study, was achieved.

Today, the trend of wearable health technologies and telemedicine applications using IoTs are rapidly becoming widespread. In addition, the rapid development of artificial intelligence applications in the field of medicine has created a need for a new research field to combine these two disciplines. The future aim of this new research field is to develop systems

that perform real-time self-diagnosis with wearable sensors. The most vital part of these systems is artificial intelligence models that run on microcontrollers with ultra-low power, low response time, low memory and have small size. As demonstrated within this study, health data obtained from sensors as sequential data such as ECG can be instantly diagnosed and classified on the MCU.

In future studies, in addition to the instant diagnosis of health data and the detection of abnormal conditions with wearable sensors, the main goals of the researchers will be to create warning systems to prevent fatal consequences by informing the patient himself, patient relatives or emergency teams about the abnormalities in the patient's vital signs.

REFERENCES

Baim, D. S., Colucci, W. S., Monrad, E. S., Smith, H. S., Wright, R. F., Lanoue, A., ... & Braunwald, E. (1986). Survival of patients with severe congestive heart failure treated with oral milrinone. Journal of the American College of Cardiology, 7(3), 661-670.

Baldi, P., & Hornik, K. (1989). Neural networks and principal component analysis: Learning from examples without local minima. Neural networks, 2(1), 53-58.

Chakraborty, G., Kamiyama, T., Takahashi, H., & Kinoshita, T. (2018). An efficient anomaly detection in quasi-periodic time series data—A case study with ECG. In Time Series Analysis and Forecasting: Selected Contributions from ITISE 2017 (pp. 147-157). Springer International Publishing.

Chauhan, S., & Vig, L. (2015, October). Anomaly detection in ECG time signals via deep long short-term memory networks. In 2015 IEEE international conference on data science and advanced analytics (DSAA) (pp. 1-7). IEEE.

Chauhan, S., Vig, L., & Ahmad, S. (2019). ECG anomaly class identification using LSTM and error profile modeling. Computers in biology and medicine, 109, 14-21.

Esspressif Systems. (2023). ESP32 Series Datasheet Version 4.2.

Fezari, M., & Al Dahoud, A. (2018). Integrated development environment "IDE" for Arduino. WSN applications, 1-12.

Goldberger, A.L.; Amaral, L.A.N.; Glass, L.; Hausdorff, J.M.; Ivanov, P.C.; Mark, R.G.; Mietus, J.E.; Moody, G.B.; Peng, C.K.; Stanley, H.E. PhysioBank, PhysioToolkit, and PhysioNet: Components of a New Research Resource for Complex Physiologic Signals. Circulation 2000, 101, e215–e220

Kumar M, A., & Chakrapani, A. (2022). Classification of ECG signal using FFT based improved Alexnet classifier. Plos one, 17(9), e0274225.

Li, H., & Boulanger, P. (2020). A survey of heart anomaly detection using ambulatory Electrocardiogram (ECG). Sensors, 20(5), 1461.

Li H, Wang Y, Wang H, Zhou B. Multi-window based ensemble learning for classification of imbalanced streaming data. World Wide Web. 2017;20(6):1507–25.

Noor, S. T., Asad, S. T., Khan, M. M., Gaba, G. S., Al-Amri, J. F., & Masud, M. (2021). Predicting the risk of depression based on ECG using RNN. Computational intelligence and neuroscience, 2021.

Rumelhart, D. E., Hinton, G. E., & Williams, R. J. (1986). Learning representations by back-propagating errors. nature, 323(6088), 533-536.

Serhal, H., Abdallah, N., Marion, J. M., Chauvet, P., Oueidat, M., & Humeau-Heurtier, A. (2022). Overview on prediction, detection, and classification of

atrial fibrillation using wavelets and AI on ECG. Computers in Biology and Medicine, 105168.

Sun, L., Wang, Y., He, J., Li, H., Peng, D., & Wang, Y. (2020). A stacked LSTM for atrial fibrillation prediction based on multivariate ECGs. Health information science and systems, 8, 1-7.

Wang, Y., Sun, L., Wang, H., Shklovskiy-Kordi, N., Xu, J., Lu, Y., & Yuan, K. (2020, October). A DNN for arrhythmia prediction based on ECG. In Health Information Science: 9th International Conference, HIS 2020, Amsterdam, The Netherlands, October 20–23, 2020, Proceedings (pp. 146-153). Cham: Springer International Publishing.

Wold, S., Esbensen, K., & Geladi, P. (1987). Principal component analysis. Chemometrics and intelligent laboratory systems, 2(1-3), 37-52. Moody, G.B.; Mark, R.G. The impact of the MIT-BIH arrhythmia database. IEEE Eng. Med. Biol. Mag. 2001, 20, 45–50.

Zhang, G., Liu, Y., & Jin, X. (2020). A survey of autoencoder-based recommender systems. Frontiers of Computer Science, 14, 430-450.

Chapter 15

CONTENT-BASED IMAGE RETRIEVAL BASED ON BLOCK TRUNCATION CODE USING FUZZY-C-MEANS QUANTIZATION AND EDGE DETECTION

Mürsel Ozan İNCETAŞ[1]

1 Asst. Prof. Dr., Alanya Alaaddin Keykubat University, ALTSO Vocational School of Higher Education, ozan.incetas@alanya.edu.tr, ORCID ID: 0000-0002-1016-1655

With the substantial developments in imaging and communication technologies in recent years, the number of digital images continues to increase. Because users and online smart devices frequently need images, it becomes difficult to find a searched image in large databases. This situation increases the importance of image retrieval, and a new approach is added every day to existing Content-Based Image Retrieval (CBIR) (Flickner et al., 1995; Pentland et al., 1994; Smith & Chang, 1997) approaches developed to find a searched image in databases using various features.

CBIR systems try to identify the images that are the most similar to the query image in a database. To determine similarity, feature vectors of both the images in the database and the query image are created, and these vectors are compared. The representation of various features obtained from the image with vector sizes renders the dimensions of the images unimportant. Thus, comparison operations are performed at the vector level, not at the pixel level, and images of different sizes can be compared to each other. Additionally, the comparison process is made faster, and the computational cost is reduced.

The main subject of CBIR studies, which have been popular for a long time, is the extraction of features that enable the objects in the image to be distinguished. While one of the features (Hejazi & Ho, 2007; Kiliçaslan et al., 2020; Liu & Yang, 2013; Murala et al., 2012; Plataniotis & Venetsanopoulos, 2000; Singha & Hemachandran, 2012), such as color, texture, pattern, or shape of the image, used to be employed in the first CBIR approaches, these features have been used together (Dey et al., 2016; Liu, 2016; Verma et al., 2015) in the following years. Additionally, it is striking that techniques such as local binary patterns (LBP) (Ojala et al., 2002), Gist (Oliva & Torralba, 2001), scale-invariant feature transform (SIFT) (Lowe, 2004), and Speeded Up Robust Features (SURF) (Bay et al., 2008), which are local, replaced the Histogram (Swain & Ballard, 1991) and Color Moments (Stricker & Orengo, 1995) methods, which used to be global features in the early days. It is also seen that studies in which color information and edge information obtained from the image have been used together have achieved successful results.

In 2018, Ashraf et al. (Ashraf et al., 2018) developed a new CBIR approach using the Canny edge detection and Discrete Wavelet Transform (DWT) methods in the YCbCr color space. In their study, after the Y channel was replaced with the results of the Canny edge operator, the YCbCr space was converted back to RGB, and DWT was applied to the histogram of each color channel. Thus, a total of 128 bins were obtained, including 64 for the R channel and 32 for each of the G and B channels. Results were obtained by testing with the Corel-1k dataset. In another

study in 2018, Nazir et al. (Nazir et al., 2018) presented an approach in which they obtained a feature vector of 310 bins using the Edge Histogram Descriptor (EHD) (Park et al., 2000) and DWT in the HSV color space. While 150 and 32 features were obtained from the RGB space with EHD and DWT, respectively, 128 features were obtained through HSV quantization. The Corel-1k dataset was also used in their study. Moreover, in 2018, Singh et al. obtained a feature vector of 542 bins consisting of LBP and color histograms for CBIR (Singh et al., 2018).

In 2019, Raza et al. developed a new feature descriptor called Square Texton Histogram (STH) developed a new feature descriptor called Square Texton Histogram (STH) (Raza et al., 2019) for image retrieval by using the Sobel edge operator in the RGB color space. While horizontal, vertical, and diagonal edges were obtained with the Sobel operator, a total of 172 features were used, including features obtained by quantizing the RGB color space. In 2019, Hua et al. developed a new feature descriptor for CBIR in the HSV color space, which they named the color volume histogram (Hua et al., 2019). They tested their technique, which included 104 features, respectively 72 and 32 features for color information and edge information, on the Corel-1k dataset. Thusnavis Bella and Vasuki performed a CBIR operation with the help of a 49-bin vector they obtained using color moments in the HSV color space and texture and shape features in the RGB color space (Thusnavis Bella & Vasuki, 2019).

In 2020, Chen et al. developed a new CBIR approach using the edge-based quantization (EQBTC) technique and the Canny edge operator in the RGB color space (Chen et al., 2020). The number of features of the technique was not fixed, and it varied based on the local block size selected. In the tests performed using the Corel-1k dataset, it was observed that the highest results were achieved when the selected block size was 4×4, while the level of success decreased considerably in 32x32 blocks. Bhunia et al. obtained a feature vector of 348 bins by combining the quantized histograms of the H and S channels in the HSV color space with the gray-level co-occurrence matrix (GLCM) (Haralick et al., 1973) obtained from the V channel and used it for CBIR (Bhunia et al., 2020). Furthermore, in 2020, Yuan and Liu developed a new feature extraction approach for CBIR in the HSV color space, which they named gradient-structures histogram (GSH), which is also the basis of this study. By quantizing the horizontal, vertical, and diagonal edge information obtained using the Sobel edge operator, a vector of 130 features was obtained for CBIR (Yuan & Liu, 2020).

In 2021, Singhal et al. proposed a CBIR approach (DLTCoP-CH) using histogram features that also contained local ternary patterns and color information in the HSV color space (Singhal et al., 2021). The study

using a feature vector of 4864 bins achieved a very high CBIR performance.

The most important common point of these studies, in which various local features have been used in different color spaces, is that they have used the edges obtained from the image. While obtaining edges, techniques that generate gray-level edges, such as the Sobel or derivative operators, or those that generate binary edge maps, such as the Canny edge detector, have been utilized. It is seen that the common dataset in which all aforementioned CBIR approaches have been tested is Corel-1k.

In this study, a new CBIR method is proposed to increase retrieval success. The proposed method performs the retrieval operation with the help of relatively few features, using both edge and color information. In addition to the HSV color space, the Sobel edge detection approach and the color features quantized by FCM are used by coding with the help of Block Truncation Code (BTC). The proposed method was compared with the techniques in the literature using the Corel-1k database and similar features. The remainder of this article is as follows: The proposed CBIR method is presented in Chapter 2. Chapter 3 includes the detailed experimental results of the proposed method and performance comparisons. The last section contains conclusions.

2. Proposed method

In this study, edge and color features are used together in the feature extraction process for CBIR, similar to many studies in the literature. The proposed feature extraction method, whose block diagram is shown in Figure 1, uses the HSV color space and Gray Level values obtained from the RGB color space. From the images converted to HSV color space, five images were randomly selected from each of the ten categories in the Corel-1k database, and these images were clustered with FCM (64 clusters). All images in the Corel-1k database are then quantized so that their pixel values are closest to the centers of 64 clusters. After the quantization process, all images are subjected to the color consistency process, which is explained in detail in section 2.2.

On the other hand, the edges of gray-level images are determined by the Sobel edge detector. Sobel edge results obtained as gray-level are first quantized uniformly (Liu & Yang, 2013; Yuan & Liu, 2020). In the next step, the consistent edges are determined by analyzing the directions of the quantized edge images. Then, the edges of the edge consistency image quantized with the Sobel edge detector are detected again. Edge and Color Consistency Histogram is determined by combining color and color consistency information.

In another step, the Sobel edge images, obtained from gray-level images, are converted to binary images to obtain a binary edge map. An edge code book is created by reducing the edge patterns obtained from 4×4 blocks of 50 randomly selected images to 64 with FCM. All images are divided into 4×4 blocks, and each block is assigned the closest value in this codebook. A histogram of these values is created and added to the feature vector.

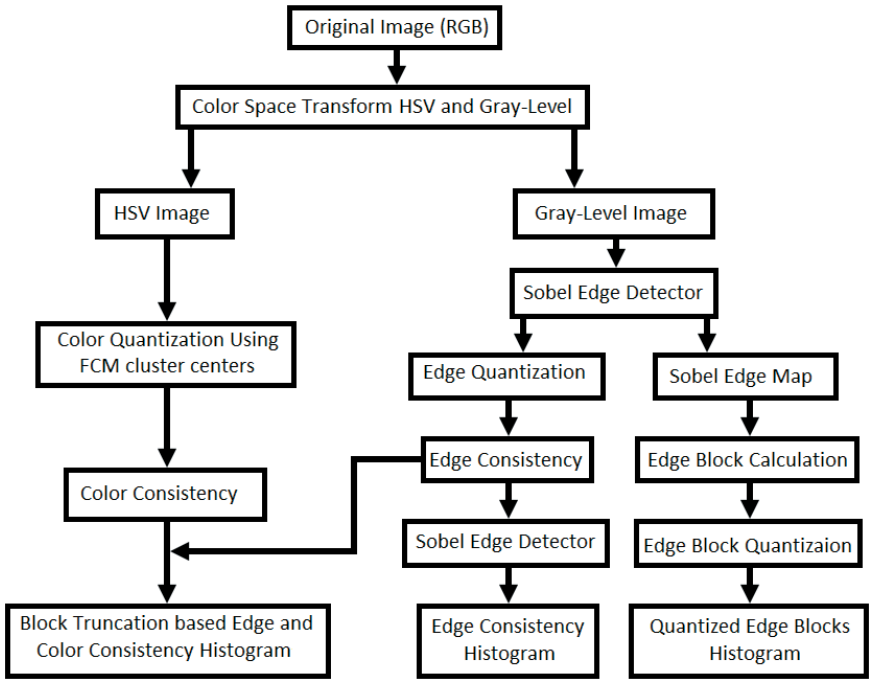

Figure 1. Block diagram of the proposed method.

2.1. Quantization and Edge detection

HSV color space and gray-level values are used in the proposed feature extraction method. First, all images are converted to HSV color space. In addition, 50 images, 5 for each category, are reduced to 64 colors with FCM, and cluster centers are determined for each cluster. Then, all 1000 images in the Corel-1k dataset are quantized by assigning the cluster number of the color closest to these cluster values. Thus, the color quantization process is completed. Quantized images are expressed as $Q_C(x, y) = q$, with $q \in \{0, 1, 2, \ldots, 62, 63\}$.

The edge detection process is performed with the Sobel operator on gray-level images. Each edge image has a gray level value between 0-255. As seen in Figure 2(c), prominent edge pixels have gray level values close to 255, and non-edge pixels have gray level values close to 0. The

edge images are then uniformly reduced to 16 different values. Hence, the quantized edge matrices can be expressed as $Q_E(x, y) = p$, with $p \in \{0, 1, 2, \ldots, 14, 15\}$. Also, the binary map is obtained for all edge images obtained with the Sobel operator. For this process, the edge function in the Matlab program is used. A binary edge image example is shown in Figure 2(d).

Figure 2. Edge detection results of an image in Corel-1k dataset. (a) Original image, (b) Gray-level image, (c) Sobel result, (d) Sobel Edge Map result

2.2. Edge and color consistency

Consistency can be expressed as pixels with the same gray level value as the center pixel in a certain direction in an image patch (Yuan & Liu, 2020). In this study, consistency control was performed on 3×3 patches of quantized edge and color matrices, including vertical, horizontal, left diagonal, and right diagonal. Examples of 4-way consistency control seen in Figure 3(a) are given in Figures 3(b) and 3(c). It is seen that the pixels have the same value in the right diagonal angle shown with orange in Figure 3(b). In this case, the consistency value for the corresponded patch is used as 9. In Figure 3(c), there is no consistency status and the consistency value of this patch is 0.

$$C_E(x,y)=\begin{cases} Q_E(x,y) & \text{if consistency=true} \\ 0 & \text{if consistency=false} \end{cases} \quad (1)$$

Edge consistency matrix C_E is calculated for the edge matrix Q_E, together with the consistency control. With the help of Equation 1, the C_E matrix is obtained by controlling the consistency of the Q_E matrix patches. Color consistency control is also provided for the quantized color matrix Q_C. For quantized color matrix, color consistency matric C_C is obtained with the help of Equation 1 in accordance with the structure given in Figure 3.

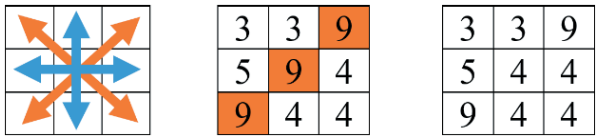

Figure 3. Edge consistency control, (a) Consistency directions for 3×3 image patch, (b) An example patch with result 9, (c) An example patch with result 0.

2.3. Edge and color consistency histograms

Consistency histograms are created using edge consistency (C_E) and color consistency (C_C) matrices. First, the consistency is checked in the vertical, horizontal, and left-right diagonal directions of each 3×3 patch of the Q_C matrix. Hence, a control as in Figure 3 is used again, but this time the value of each patch can be 0 or 1. For example, the L_C value indicating the presence of color consistency for a patch in the C_C matrix will be 1 for a patch as in Figure 3(b) and 0 for a patch as in Figure 3(c). Histograms are created by checking the color consistency in 3×3 patches for all pixels. Equations 2, 3, and 4 are used when calculating the consistency histogram H_C for the quantized image.

$$H_C(C_C(x,y))=\sum_{x}^{X}\sum_{y}^{Y}(1-e^{-\frac{C_E(x,y)}{avg}})L_C(x,y) \quad (2)$$

$$L_C(x,y)=\begin{cases} 1 & \text{if consistency=true for } C_C(x,y) \\ 0 & \text{if consistency=false for } C_C(x,y) \end{cases} \quad (3)$$

$$avg=mean(C_E) \quad (4)$$

In the quantized color values of an image of X×Y size, the color consistency control value L_R in 3×3 patches for all pixels and the average edge consistency value *avg* are calculated, and the consistency histogram

H_C with 64 bins is created. In addition, the H_C histogram with 16 bins is calculated with the help of the edge image obtained from the C_E with the Sobel operator.

2.4. Edge block quantization

Finally, binary edge maps obtained from gray-level images are determined. Edge patterns obtained from 4×4 blocks are created for 50 previously selected images. Also, the pattern value $P(i, j)$ is calculated for each block. For an image of mxn size, i=1, 2, … m/4 and j=1, 2, …, n/4, each block is denoted by $B(i, j)$. For $e_p \in B(i, j)$ ($p \in \{0, 1, 2, \ldots, 14, 15\}$) elements in a 4×4 block, the block's pattern value $P(i, j)$ is calculated by Equation 5.

$$P = e_p \times 2^p \tag{5}$$

0_0	0_1	0_2	0_3
0_4	0_5	0_6	0_7
0_8	0_9	0_{10}	0_{11}
0_{12}	0_{13}	0_{14}	0_{15}

(a)

1_0	1_1	1_2	1_3
1_4	1_5	1_6	1_7
1_8	1_9	1_{10}	1_{11}
1_{12}	1_{13}	1_{14}	1_{15}

(b)

1_0	0_1	1_2	0_3
0_4	0_5	0_6	0_7
0_8	0_9	0_{10}	0_{11}
0_{12}	0_{13}	0_{14}	0_{15}

(c)

Figure 4. Example of edge blocks, (a) all of the pixels are non-edge, (b) all of the pixels are edge, (c) two of the pixels are edge.

Since an ep value in a block is binary, it can take only 0 or 1. As can be seen in Figures 4(a) and 4(b), for a block with no edges, $P(i, j)$=0, and for a block with all 16 pixels as edges, $P(i, j)$=65535. For the block in Figure 4(c), $P(i, j)$=5.

The $P(i, j)$ values calculated for each 4×4 block in the previously selected 50 images are quantized to 64 by FCM. By determining the closest cluster for each $P(i, j)$ in all 1000 images in the dataset, quantized blocks are expressed as $Q_P(i, j) = q$, with $q \in \{0, 1, 2, \ldots, 62, 63\}$ using BTC. The histogram of the quantized pattern values is created H_P and added to the feature vector.

3. Experimental results and discussion

The success of the proposed method was measured with different metrics and compared with various techniques. The tests and comparisons were performed on Corel-1k, which is the most frequently used dataset in image retrieval. All 1000 images in the Corel-1k dataset, which includes

10 categories with 100 images in each, consist of 384×256 (or 256×384) pixels.

Precision and Recall performance metrics were used to measure the success of the proposed method and to compare it with other methods. Precision and Recall metrics are the most commonly used metrics in CBIR studies in the literature and are common to all studies. Precision and Recall values were calculated with the help of Equations 6 and 7 (Kayhan & Fekri-Ershad, 2021).

$$Precision = \frac{N_R}{N_T} \tag{6}$$

$$Precision = \frac{N_R}{N_C} \tag{7}$$

where N_R is the number of images in the same category as the query image among the retrieved images. N_T shows the total number of images retrieved in the query. N_C shows the total number of images in a category.

The retrieval results are obtained using the Canberra metric. To compare the results correctly, the Canberra metric is used as the distance metric in this study. The Canberra metric, which is used commonly in almost all CBIR studies developed in recent years, is also used as the distance metric in this study.

Table 1. Comparing Precision and Recall Results (%) of CBIR methods on Corel-1k dataset for top 10 images

Method	(Verma et al., 2015)	(Dey et al., 2016)	(Hua et al., 2019)	(Chen et al., 2020)	(Singh et al., 2018)	(Bhunia et al., 2020)	(Yuan & Liu, 2020)	(Kayhan & Fekri-Ershad, 2021)	(Singh al et al., 2021)	Proposed
Precision(%)	77.86	80.20	79.89	79.42	74.39	80.56	82.80	82.50	85.51	86.41
Recall(%)	7.79	8.02	7.99	7.94	7.44	8.06	8.28	8.25	8.55	8.64

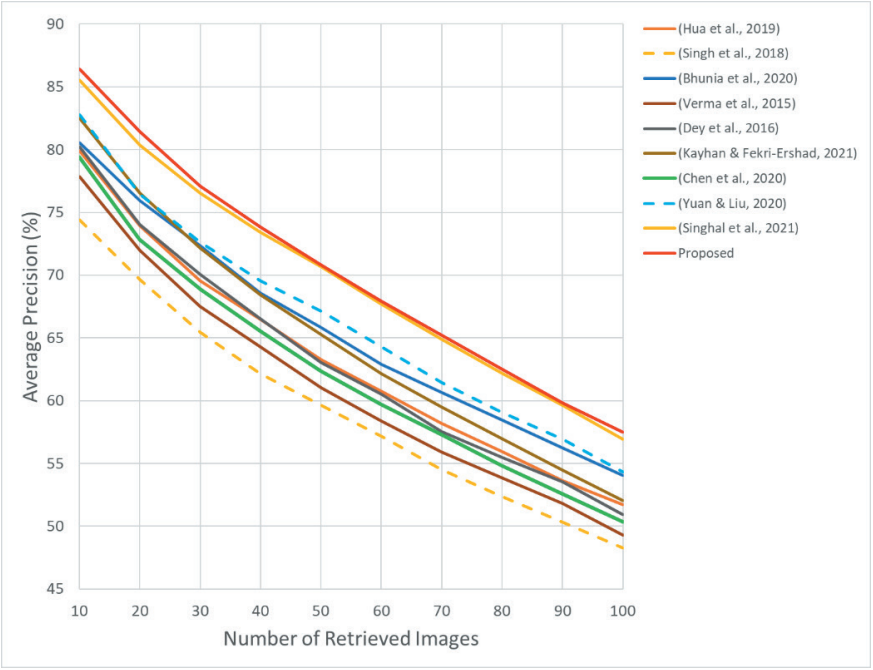

Figure 5. Average precision (%) performances for Corel-1k dataset

Precision and recall performances are given in Table 1 for N=10 (the number of retrieved images). It is seen that the proposed method is more successful than other techniques. The success of the proposed method continues when more images are retrieved. It is clear from the graph in Figure 5 that the success of the techniques in the literature drops dramatically as the number of retrieved images N increases. However, the success of the proposed method is significantly high compared to other techniques. The closest results to the proposed method are obtained with the technique (Singhal et al., 2021).

The images taken for some query images in the Corel-1k dataset are given in Figure 6. As can be seen from the results, not only the color but also the edge information significantly affects the retrieval results. For example, in 2nd row where the blue bus image is queried, the first image taken is in pink, white, and red colors but has almost the same edge angles. Similarly, the first image taken for the query image in row 3 is a dinosaur standing at a similar angle.

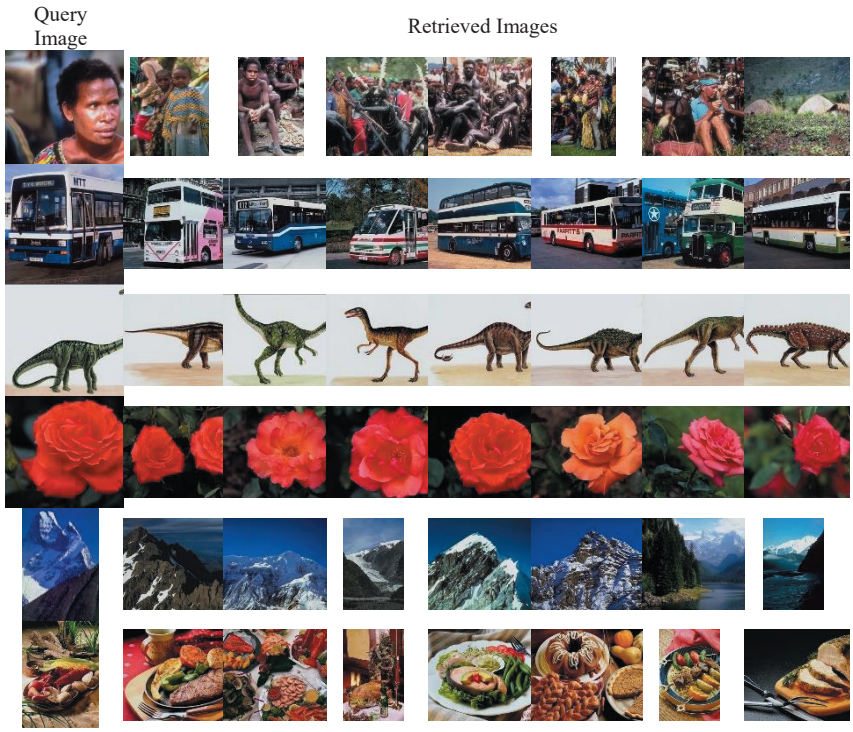

Figure 6. Examples of query images and retrieved images for Corel-1k.

In the CBIR process, the number of features used is also very important, as well as the success. Of course, considering all pixels individually to express the image will increase success, but reducing various information with approaches such as quantization is very considerable for the usability of a CBIR technique. In addition to the successful retrieval performance of the proposed method, an important advantage is that the number of features used is quite low compared to the techniques in the literature. As seen in Table 2, achieving an effective retrieval success with 144 bins, which can be considered quite low, especially compared to other techniques with similar results (Singhal et al., 2021), also shows the usefulness of the proposed method.

Table 2. Feature vector size of some CBIR techniques

Method	(Hua et al., 2019)	(Chen et al., 2020)	(Singh et al., 2018)	(Bhunia et al., 2020)	(Yuan & Liu, 2020)	(Kayhan & Fekri-Ershad, 2021)	(Singhal et al., 2021)	Proposed
Bins	104	58	542	348	130	104	4064	144

Another important advantage of the proposed method is that it does not require any parameter selection. Thus, the user does not need to select parameters. For example, selecting different parameters in (Kayhan &

Fekri-Ershad, 2021) causes significant changes in the results. However, linear measurement of these features with the help of relatively simple metrics is seen as an important obstacle to achieving higher success. Improving retrieval performance of the proposed method using machine learning techniques will be studied in the future.

4. Conclusions

In this study, a new CBIR approach is proposed in which FCM quantization and edge detection are used together. In the tests, quite successful retrieval results were obtained with very few features extracted from both color channels and edge detection. Compared to many state-art techniques, the proposed method is very successful on images containing general scenes, showing that it can be used in many different imaging fields. The fact that the number of features used is quite low compared to many techniques in the literature also emerges as one of the advantages of the proposed method. In the future, it is planned to use the features extracted by the proposed method, together with machine learning and especially deep learning techniques, in studies on classification as well as CBIR.

REFERENCES

Ashraf, R., Ahmed, M., Jabbar, S., Khalid, S., Ahmad, A., Din, S., & Jeon, G. (2018). Content Based Image Retrieval by Using Color Descriptor and Discrete Wavelet Transform. *Journal of Medical Systems*, *42*(3), 1–12.

Bay, H., Ess, A., Tuytelaars, T., & Van Gool, L. (2008). Speeded-Up Robust Features (SURF). *Computer Vision and Image Understanding*, *110*(3), 346–359.

Bhunia, A. K., Bhattacharyya, A., Banerjee, P., Roy, P. P., & Murala, S. (2020). A novel feature descriptor for image retrieval by combining modified color histogram and diagonally symmetric co-occurrence texture pattern. *Pattern Analysis and Applications*, *23*(2), 703–723.

Chen, Y. H., Chang, C. C., & Hsu, C. Y. (2020). Content-based image retrieval using block truncation coding based on edge quantization. *Connection Science*, *32*(4), 431–448.

Dey, M., Raman, B., & Verma, M. (2016). A novel colour- and texture-based image retrieval technique using multi-resolution local extrema peak valley pattern and RGB colour histogram. *Pattern Analysis and Applications*, *19*(4), 1159–1179.

Flickner, M., Sawhney, H., Niblack, W., Ashley, J., Huang, Q., Dom, B., Gorkani, M., Hafner, J., Lee, D., Petkovic, D., Steele, D., & Yanker, P. (1995). Query by Image and Video Content: The QBIC System. *Computer*, *28*(9), 23–32.

Haralick, R. M., Dinstein, I., & Shanmugam, K. (1973). Textural Features for Image Classification. *IEEE Transactions on Systems, Man and Cybernetics*, *SMC-3*(6), 610–621.

Hejazi, M. R., & Ho, Y. S. (2007). An efficient approach to texture-based image retrieval. *International Journal of Imaging Systems and Technology*, *17*(5), 295–302.

Hua, J. Z., Liu, G. H., & Song, S. X. (2019). Content-Based Image Retrieval Using Color Volume Histograms. *International Journal of Pattern Recognition and Artificial Intelligence*, *33*(11).

Kayhan, N., & Fekri-Ershad, S. (2021). Content based image retrieval based on weighted fusion of texture and color features derived from modified local binary patterns and local neighborhood difference patterns. *Multimedia Tools and Applications*, *80*(21–23), 32763–32790.

Kiliçaslan, M., Tanyeri, U., & Demirci, R. (2020). Image Retrieval using One-Dimensional Color Histogram Created with Entropy. *ADVANCES IN ELECTRICAL AND COMPUTER ENGINEERING*, *20*(2), 79–88.

Koteswara Rao, L., Rohini, P., & Pratap Reddy, L. (2019). Local color oppugnant quantized extrema patterns for image retrieval.

Multidimensional Systems and Signal Processing, *30*(3), 1413–1435.

Liu, G. H. (2016). Content-based image retrieval based on cauchy density function histogram. *12th International Conference on Natural Computation, Fuzzy Systems and Knowledge Discovery*, 506–510.

Liu, G. H., & Yang, J. Y. (2013). Content-based image retrieval using color difference histogram. *Pattern Recognition*, *46*(1), 188–198.

Lowe, D. G. (2004). Distinctive Image Features from Scale-Invariant Keypoints. *International Journal of Computer Vision 2004 60:2*, *60*(2), 91–110.

Murala, S., Maheshwari, R. P., & Balasubramanian, R. (2012). Directional local extrema patterns: a new descriptor for content based image retrieval. *International Journal of Multimedia Information Retrieval*, *1*(3), 191–203.

Nazir, A., Ashraf, R., Hamdani, T., & Ali, N. (2018). Content based image retrieval system by using HSV color histogram, discrete wavelet transform and edge histogram descriptor. *2018 International Conference on Computing, Mathematics and Engineering Technologies: Invent, Innovate and Integrate for Socioeconomic Development, ICoMET 2018 - Proceedings*, *2018-January*, 1–6.

Ojala, T., Pietikäinen, M., & Mäenpää, T. (2002). Multiresolution gray-scale and rotation invariant texture classification with local binary patterns. *IEEE Transactions on Pattern Analysis and Machine Intelligence*, *24*(7), 971–987.

Oliva, A., & Torralba, A. (2001). Modeling the Shape of the Scene: A Holistic Representation of the Spatial Envelope. *International Journal of Computer Vision 2001 42:3*, *42*(3), 145–175.

Park, D. K., Jeon, Y. S., & Won, C. S. (2000). Efficient use of local edge histogram descriptor. *Proceedings of the ACM Multimedia*, 51–54.

Pentland, A. P., Picard, R. W., & Scarloff, S. (1994). Photobook: tools for content-based manipulation of image databases. *SPIE on Storage and Retrieval for Image and Video Databases II*, *2185*, 34–47.

Plataniotis, K. N., & Venetsanopoulos, A. N. (2000). *Color Image Processing and Applications*. Springer Berlin Heidelberg.

Raza, A., Nawaz, T., Dawood, H., & Dawood, H. (2019). Square texton histogram features for image retrieval. *Multimedia Tools and Applications*, *78*(3), 2719–2746.

Shih, J. L., & Chen, L. H. (2002). Colour image retrieval based on primitives of colour moments. *IEE Proceedings: Vision, Image and Signal Processing*, *149*(6), 370–374.

Singh, C., Walia, E., & Kaur, K. P. (2018). Color texture description with novel local binary patterns for effective image retrieval. *Pattern Recognition*, *76*, 50–68.

Singha, M., & Hemachandran, K. (2012). Content Based Image Retrieval using Color and Texture. *Signal & Image Processing : An International Journal*, *3*(1), 39–57.

Singhal, A., Agarwal, M., & Pachori, R. B. (2021). Directional local ternary co-occurrence pattern for natural image retrieval. *Multimedia Tools and Applications*, *80*(10), 15901–15920.

Smith, J. R., & Chang, S. F. (1997). VisualSEEk: A fully automated content-based image query system. *Proceedings of the 4th ACM International Conference on Multimedia, MULTIMEDIA*, 87–98.

Stricker, M. A., & Orengo, M. (1995). Similarity of color images. *Proceeding of Storage and Retrieval for Image and Video Databases III*, *2420*, 381–392.

Swain, M. J., & Ballard, D. H. (1991). Color indexing. *International Journal of Computer Vision 1991 7:1*, *7*(1), 11–32.

Thusnavis Bella, M. I., & Vasuki, A. (2019). An efficient image retrieval framework using fused information feature. *Computers & Electrical Engineering*, *75*, 46–60.

Verma, M., Raman, B., & Murala, S. (2015). Local extrema co-occurrence pattern for color and texture image retrieval. *Neurocomputing*, *165*, 255–269.

Yuan, B. H., & Liu, G. H. (2020). Image retrieval based on gradient-structures histogram. *Neural Computing and Applications*, *32*(15), 11717–11727.

Chapter 16

THE ANALYSIS OF THE REFRIGERATION SYSTEM OF FRIGORIFIC VEHICLES USED IN ROAD TRANSPORT

Arzu KEVEN[1], Canan CIMŞIT[2]

1 Kocaeli University, Golcuk Vocational School, Golcuk-Kocaeli, Turkey, (ORCID: 0000-0003-0040-9167) arzu.keven@kocaeli.edu.tr
2 Kocaeli University, Golcuk Vocational School, Golcuk-Kocaeli, Turkey, (ORCID: 0000-0002-3222-1735) ccimsit@kocaeli.edu.tr

1. Introduction

Road transport is the most widely used mode of transport among the transport types. The road transport has many advantages compared to other means of the transport. Some of the advantages of the road transport are: loading and unloading operations can be done more easily than other transportation types, almost all types of cargo can be transported, the initial investment cost is lower than other transportation modes. The reasons such as traffic congestion, capacity limitation of the volume to be loaded, bad weather conditions and being affected by environmental factors are the disadvantages of road transport (Ozceylan, 2021).

All food prepared for meal distribution must be transported in vehicles suitable for its purpose. For this purpose, frigorific vehicles with insulated refrigeration units are used (Tas and Gunduz, 2021). The process of transporting foodstuffs from processing centers to retail outlets by refrigeration or freezing according to the product characteristics is considered a cold chain. Many frigorific vehicles (FV) are used in cold chain logistics. These are; frigorific ships, frigorific trucks and frigorific urban distribution vehicles. The development of international trade between countries located far from each other and the increase in the variety of products traded accelerated the development of the frigorific transportation market. Thanks to specially equipped frigorific vehicles, the properties of the products do not change during transportation. Thus, damage and loss of property are prevented. This type of transport is in great demand in the food, cosmetic, chemical, pharmaceutical industry, agriculture and some other industries. The walls, ceiling, floor and doors of the section reserved for product transport are insulated to minimize the heat transfer between the indoor and outdoor environment, and this section is equipped with a device that has a vapour compression mechanical refrigeration cycle with heat absorption capability (MEGEP, 2013).

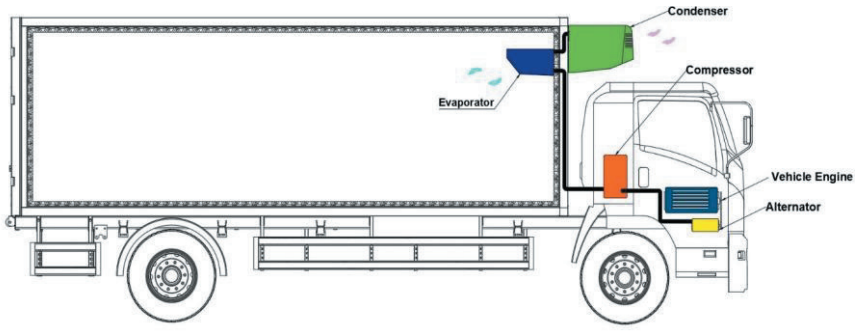

Figure 1. Frigorific vehicle

A wide variety of frigorific vehicles (2-60 m^3) have been developed according to product type, quantity, transportation temperature, and transportation time. For example, in the frigorific boxes with a frame length of 5 m to 13.60 m, the refrigeration compressors of these devices are driven by the diesel engine of the refrigeration system itself (Figure 1). Environmentally friendly refrigerants R-134A and R-404A are used in the refrigeration system. In Figure 2, the refrigeration capacity values are given for the corresponding unit volume (1m^3) to the desired transport temperatures for a standard frigorific vehicle. By using these values, the required refrigeration device can be selected for various products (MEGEP, 2013).

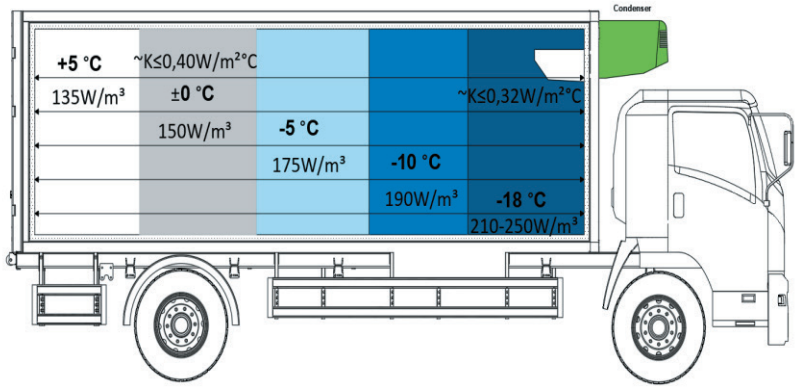

Figure 2. Required capacity values for the unit volume at different temperatures in the frigorific vehicle

The lift system should be used in the frigorific vehicles to save time and reduce the need for loading and unloading ramps. Another important

issue is the necessity of having side doors in addition to the rear door for product loading and unloading. The frigorific vehicles with a "double deck" system are also used to transport different products with each other without odor and heat transfer. On the other hand, air and plastic curtain systems are also used in the frigorific vehicles to minimize heat loss during loading and unloading. Some vehicles may also have more than one compartment. It is very common, especially in products that have to be shipped at different temperature levels and at the same time. In case of need, products that do not harm each other physiologically or that are close to the required temperatures can be preferred. The insulated container is used to transport sensitive products that need to be transported within a certain temperature range without deterioration in the cold chain. For thermal insulation performance, the inside of the case is covered with homogeneous polyurethane material and foam is placed inside the case walls. It is used for frozen foods or cargo and frozen foods produced at a certain temperature and must be transported at the same temperature (Ozceylan, 2021).

One of the most important features of the frigorific vehicles used in the cold chain is that they are designed in such a way that repair and service services are carried out on-site, quickly and easily. For this, steel or copper pipes prepared in flexible standard design are used in a significant part of the refrigeration circuit (MEGEP, 2013).

2. Analysis of energy reduction methods in the refrigeration system of the frigorific vehicles

The vapor compression mechanical refrigeration systems are used in the frigorific vehicles. One of the energy reduction methods in the refrigeration system of these vehicles is the selection of refrigerants with high performance and the possibility of refrigeration without damaging the ozone layer for the refrigeration system. In another method, it can be said that refrigeration systems that can be an alternative to the mechanical refrigeration system should be preferred. After determining the appropriate fluid and refrigeration system, analyzes should be made to improve the cycle by determining exactly where the real losses are and how they can be reduced in order to increase efficiency. In this context, the thermodynamic analysis of the system elements of the mechanical refrigeration system has been carried out at different condenser temperatures depending on the outdoor temperatures. In the study, R-407C, R-600, R-600A, R-423A, R-1234zd(E) and R-1234yf refrigerants, which can be alternatives to R-134-A and R-410A refrigerants used in the frigorific vehicles, have been selected. Also, detailed exergy analysis of the system elements of the mechanical refrigeration system has been

made according to different condenser temperatures. The working conditions accepted for analysis; T_{eva}= 253 K and refrigeration capacity 10 kW. 50 m^3 can be taken for the vehicle body volume of 190 W/m^3.

The mechanical refrigeration systems of the frigorific vehicles consist of two parts (Figure 3). In the vapor compression mechanical refrigeration system, the refrigerant coming out of the evaporator as saturated vapor is compressed to high pressure in the compressor and sent to the condenser in the superheated vapor phase. The refrigerant condensed in the condenser comes to the evaporator by being throttled in the throttling valve. In the evaporator, the refrigerant enters the saturated vapor phase with the heat it receives from the cooling medium and is absorbed by the compressor and the cycle is completed (Yamankaradeniz et al., 2022).

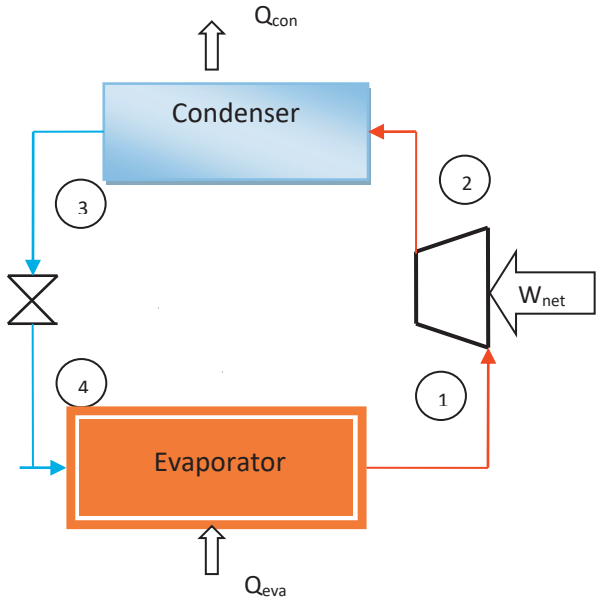

Figure 3. The vapour compression mechanical refrigeration system

Equations used in the thermodynamic analysis:

Energy and mass balance equations and the coefficients of the performance for the vapour compression refrigeration cycle can be written as follows:

$$\sum \dot{m}_{in} = \sum \dot{m}_{out} \quad (1)$$

$$\sum \dot{Q} - \sum \dot{W} = \sum H_{out} - \sum H_{in} \quad (2)$$

$$COP_{vapour-comp} = Q_{eva}/W_{comp} \quad (3)$$

The exergy balance, applied to a fixed control volume is given as a general rule by the following equation (Bejan et al., 1996):

$$\sum m_{in}\, e_{in} - \sum m_{out}\, e_{out} + \sum Q(1 - T/T_0 - \sum W - E_D = 0 \quad (4)$$

specific exergy (e) is stated as:

$$e = (h - h_0) - T_0(s - s_0) \quad (5)$$

The exergy efficiency of the vapour compression refrigeration cycle:

$$\eta_{ex} = Exergy\ in\ product/Exergy\ of\ fuel \quad (6)$$

2.1. Analysis of alternative refrigerants in the mechanical refrigeration system of the frigorific vehicles

In the study carried out according to different condenser temperatures, it has been concluded that as the condenser temperature increased, the COP value decreased (Keven and Karaali, 2022). While the highest COP value belonged to R-1233zd(E) fluid among the analyzed fluids, it is seen that the lowest COP value belonged to R-407C fluid (Figure 4).

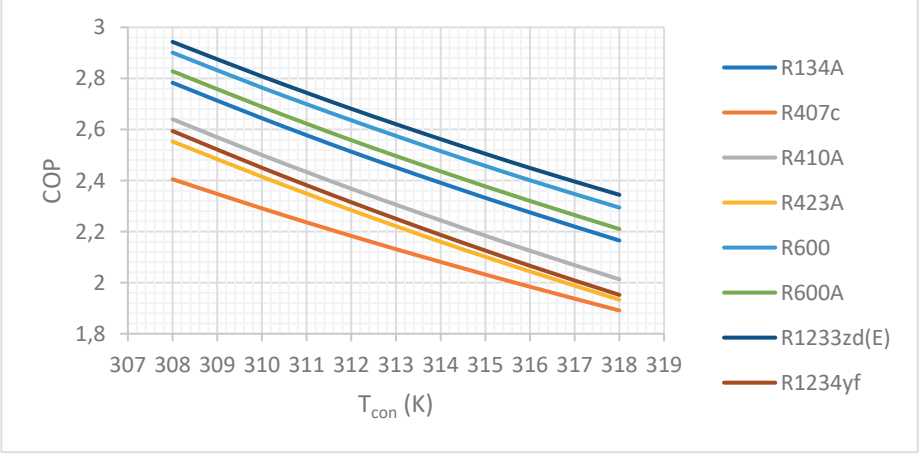

Figure 4. COP variation with condenser temperatures of refrigerants

Figure 5 illustrates how mass flow rate ratio behaves due to increased condenser temperature. The highest and lowest mass flow rate ratios throughout the rising condenser temperature range occur when R-423A and R-600 are used.

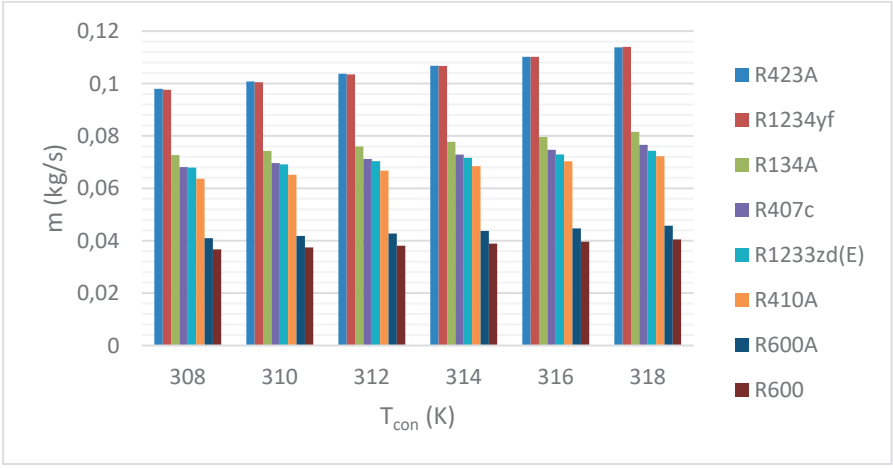

Figure 5. Exchange of refrigerants with mass flow rate ratio

The detailed exergy analysis has been made according to different condenser temperatures in the use of different refrigerants in the mechanical refrigeration system. In Figure 6, the second law efficiency of R-134A, R-410A, R-407C, R-600, R-600A, R-423A, R-1234yf and R-1233zd(E) refrigerants according to different condenser temperatures is given. It has been seen that the second highest efficiency value belonged to the R-1233zd(E) fluid, while the lowest efficiency value belonged to the R-407C fluid.

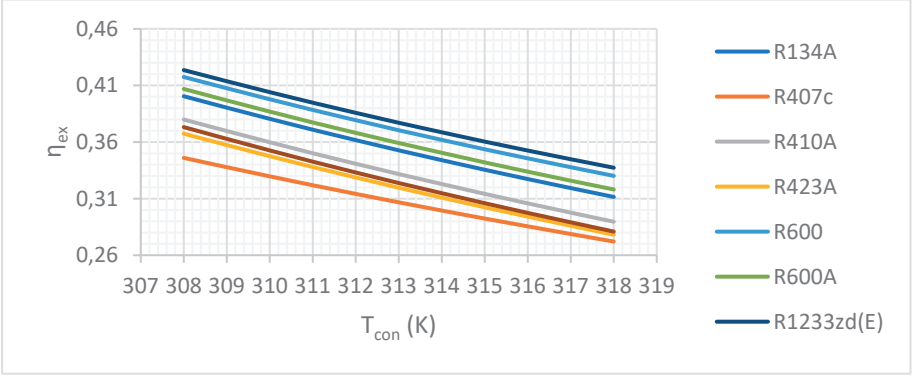

Figure 6. ηex change of refrigerants with condenser temperatures

The total exergy destruction value of system in the analysis performed at different condenser temperatures has been shown in Figure 7. Accordingly, while the highest exergy destruction values belonged to R-407C, the lowest values have been obtained for R-1233zd(E).

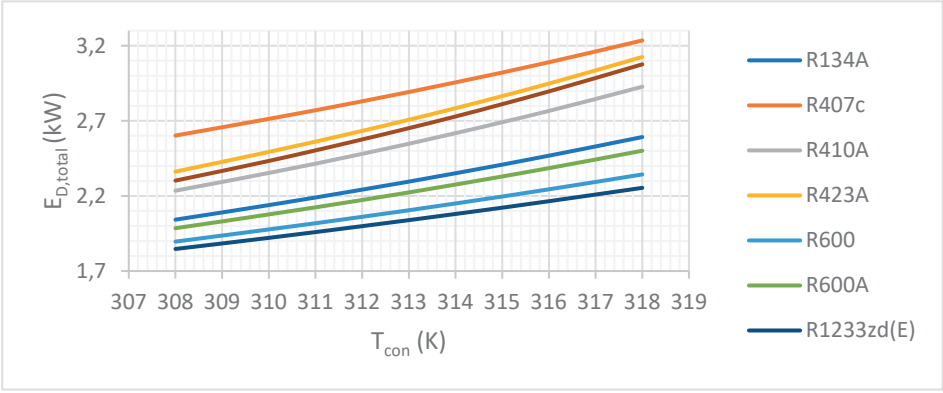

Figure 7. Total the exergy destruction according to the condenser temperatures of the refrigerants

In the analysis, the total exergy destruction value of each system element performed at different condenser temperatures has been shown in from Figure 8 to Fig. 11. The highest exergy destruction values belonged to R-407C, the lowest values have been obtained for R-134A in the evaporator (Figure 8).

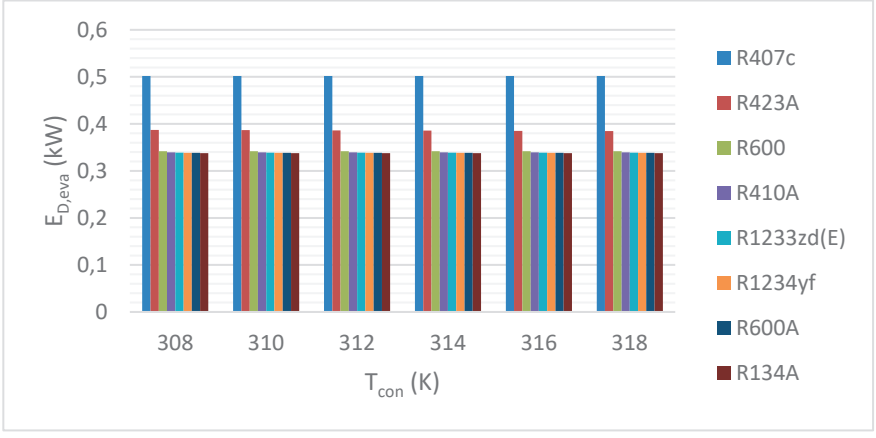

Figure 8. Total the exergy destruction according to the condenser temperatures of the refrigerants in the evaporator

Figure 9 shows that the highest exergy and lowest destruction values in the condenser belong to R-407C and R-600, respectively. The highest exergy destruction values belonged to R-423A, while the lowest values have been obtained for R-1233zd(E) in the compressor (Figure 10).

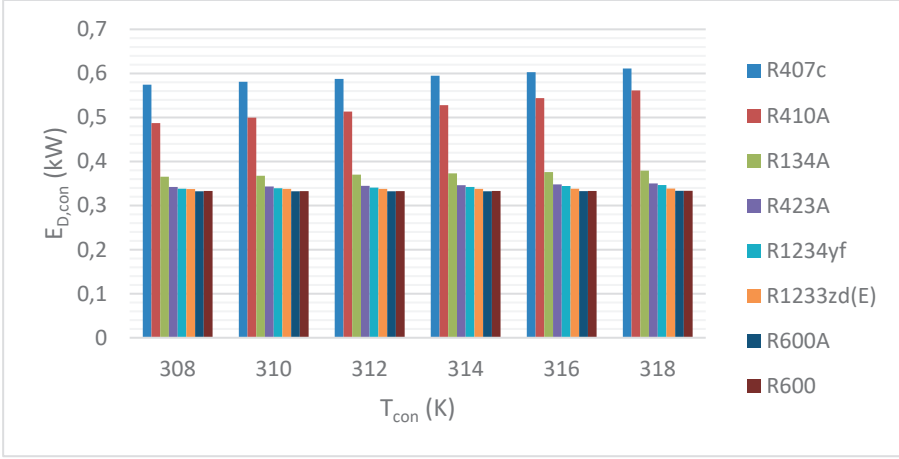

Figure 9. Total the exergy destruction according to the condenser temperatures of the refrigerants in the condenser

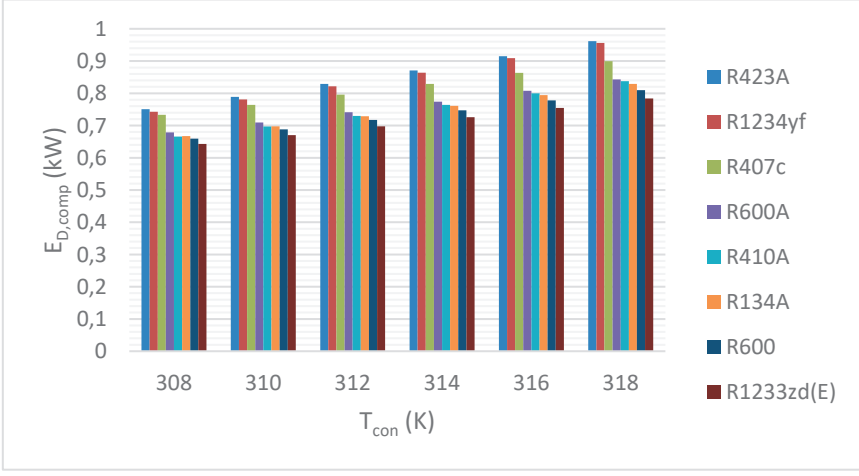

Figure 10. Total the exergy destruction according to the condenser temperatures of the refrigerants in the compressor

Figure 11 shows that the highest and lowest exergy destruction values have been obtained at R-1234yf and R-1233zd(E), respectively in

the valve. It is seen that the highest exergy destruction values belong to R-423A and R-407C fluid after R-1234yf.

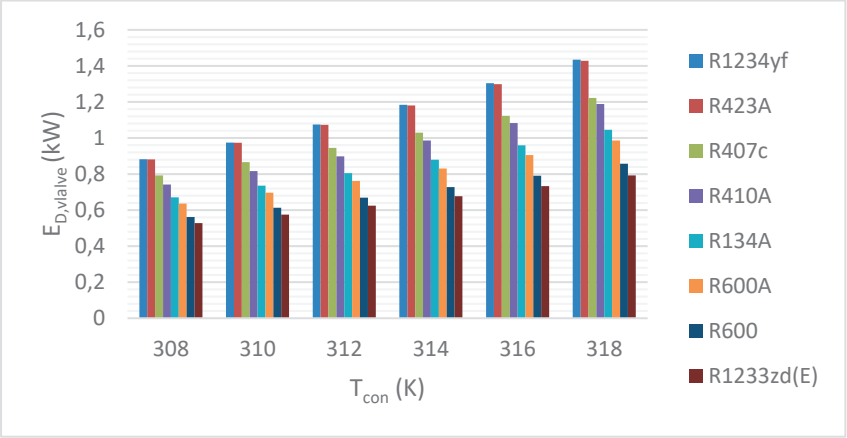

Figure 11. Total the exergy destruction according to the condenser temperatures of the refrigerants in the valve

2.2. Alternative Refrigeration Technologies for the Frigorific Vehicles

The frigorific vehicles, in which vapor compression refrigeration systems are used, operate their refrigeration systems with the power they receive from their own engine. For bigger refrigeration capacities, an extra diesel engine system is used.

There are also systems in which different technologies are used for the transportation of agricultural-food products. One of them is the eutectic-FDM (phase change material) based transport refrigeration units that have been used in the frigorific vehicles for about 50 years (Ozceylan, 2021).

Figure 12. Eutectic plate transport cooling unit

In this section, alternative refrigeration technologies have been presented to reduce energy dependency in the frigorific vehicles. As an alternative to mechanical refrigeration, cryogenic freezing/chilling systems are available that use cryogenic liquids such as liquid nitrogen or carbon dioxide. This system uses a large refillable, vacuum-insulated tank with a capacity ranging from 420-700 kg, mounted under the trailer, to store LN_2 or LCO_2. In addition to the alternative refrigeration system mentioned above, solar and hydrogen fuel refrigeration systems are also available. In solar-powered photovoltaic transport refrigeration systems, silicone solar photovoltaic (PV) panels can be mounted on the trailer's roof to capture solar irradiation and convert it to direct current (DC) electricity. The DC can then be converted to alternating current (AC) using an inverter to power the refrigeration unit. An on-board battery is used to store the additional power generated from the PV for use by the refrigeration unit during hours of low or no solar radiation. The hydrogen-fuel-cell powered TRUs are currently in the demonstration phase of commercialization. The current system design includes electric standby option that allows the compressor to run either on a diesel auxiliary engine or with an external 80V or 460 V AC motor powered using hydrogen fuel cells (Rai and Tassou, 2017).

Also, as an alternative to the refrigeration systems used in the frigorific vehicles, absorption and absorption-vapor compression cascade refrigeration cycles can be considered. In these systems, the thermal energy required for the generator of the system can be obtained from the exhaust of the diesel engine. Thus, with these systems, both energy savings will be achieved and the exhaust gas temperature at high temperatures will be reduced and it will be prevented from being discharged to the environment.

3. Conclusions

Many frigorific vehicles are used in the process of transporting foodstuffs from processing centers to retail outlets by refrigeration or freezing. This type of transport is in great demand in the food, cosmetic, chemical, pharmaceutical industry, agriculture and some other industries. In the frigorific vehicles, the compressor is driven by the vehicle engine. This process both affects engine performance and increases fuel consumption.

In this study, different refrigerants that may be suitable for vapour compression refrigeration systems used in the frigorific vehicles have been analyzed. These refrigerants are R-407C, R-600, R-600A, R-423A, R-1234zd(E) and R-1234yf, which can be alternatives to R-134-A and R-410A refrigerants. The detailed exergy analysis of the system elements of the mechanical refrigeration system has been made according to different condenser temperatures. The aim of the detailed exergy analysis in the frigorific vehicles in this study is to improve the cycle by finding exactly where the actual losses occur and how these losses can be reduced. As the total exergy destruction values increase at increasing condenser temperatures, the second law efficiency values of the system also decrease. It has been concluded that the highest second law efficiency values belong to the refrigerant R-1234zd(E). In contrast, the lowest second law efficiency values belong to the R-407C refrigerant. Also, alternative refrigeration technologies have been presented to reduce energy dependency in the frigorific vehicles.

Selection of high-performance refrigerants in the vapor compression refrigeration system, determination of suitable alternative refrigeration systems, and improvement of the cycle by determining exactly where the actual losses are and how they can be reduced can be listed as energy reduction methods in the frigorific vehicles. The application of energy reduction methods in the frigorific vehicles will make these vehicles even more advantageous.

REFERENCES

1. Ozceylan, A., (2021). Transportation in the Agri-Food Supply Chain, Agri-Food Supply Chain Management with Interdisciplinary Approaches-Featured Articles, Nobel Academic Scientific.
2. Tas, A., Gunduz, M., (2021). Analysıs Of Crıterıa Affectıng The Food Transportıon Industry, Journal of Erciyes University Faculty of Economics and Administrative Sciences, Issue: 58.
3. MEGEP, (2013). Installation Technology And Air Condıtıonıng, Selection Of Frigorific Vehicle.
4. Yamankaradeniz, R., Horuz, İ., Çoşkun, S., (2002). Refrigeration Technique and Applications, Vipaş A.Ş., Uludağ University Empowerment Foundation, Bursa.
5. Bejan, A., Tsatsaronis, G., Moran, M., (1996). Thermal design and optimization, New York: John Wiley and Sons Inc.
6. Keven, A., Karaali, R., (2022). Performance Analyses Of Newly Manufactured Refrıgerants For Vapor Compressıon Refrıgeratıon Cycles, ANADOLU 11 th International Conference on Applied Science, Diyarbakır, December 29- 30.
7. Rai, A. (2019). Energy demand and environmental ımpacts of food transport refrigeration and energy reduction methods during temperature-controlled distribution. Doctoral Thesis, Brunel University, Department of Mechanical and Aerospace Engineering College of Engineering, Design and Physical Sciences, London.

Chapter 17

CUSTOMER UTILITY-BASED MODELS FOR THE PRICING AND PRODUCTION DECISIONS BEFORE AND AFTER THE NEW PRODUCT LAUNCH

Mehmet ALEGOZ[1]

1 Corresponding author: Asst. Prof. Dr. Eskisehir Technical University, Faculty of Engineering, Department of Industrial Engineering, 26555, Eskisehir, Turkey. ORCID: https://orcid.org/0000-0002-6290-0448

E-mail: mehmetalegoz@eskisehir.edu.tr

1. INTRODUCTION

In this study we consider a manufacturer manufacturing a product such as household goods, technological devices etc. There is a base market and a demand for this product depending on the utilities of the customers derived from this product and selling price the manufacturer sets.

In Phase 1, the manufacturer manufactures and sells these products to the customers. In Phase 2, another manufacturer starts to manufacture and sell Product 2, a similar product to Product 1. Hence, a competition occurs between Product 1 and Product 2. Due to this competition, both the manufacturers of Product 1 and Product 2 determine new prices and production quantities for their own products and reach to an equilibrium.

In this problem environment, this study proposes customer utility-based models for one-product case (the case observed before the launch of Product 2) and two-product case (the case observed after the launch of Product 2). By making a comparison between them under various parameter settings, the study presents several managerial insights that are valuable both from the theoretical and practical points of view.

New product development and launch is widely addressed in the existing literature. Di Benedetto (1999) focus on the determination of the critical success factors in new product launch and state that the timing of the launch and the logistics operations need the specicial attentions of the managers. Lee et al. (2003) discuss the new product launch strategies for the products that yields to network effects. Ernst et al. (2010) focus on the cooperation between various departments in the new product development phase and indicate that existing literature generally focuses on the cooperation between the marketing department and Research and Development (R&D) department. Through a systematic analysis they state that cooperation between sales and R&D, and sales, and sales and marketing are also very important for the success of new product development. Chang and Taylor (2016) investigate the effect of customer participation in the idea and launch phases of new product development process and indicate that the participations of customers has a positive impact n the financial performance of the new product. Cooper (2019) focus on the critical success factors in new product development. Through an extensive review of the existing literature, he determine several factors such as innovation strategy and R&D investment decisions.

Moreover, competition between the products is also received the attentions of numerous researchers. Hafezalkotob (2015) consider the

competition of two green supply chains under the government tariffs and report that there are boundaries for the government tariffs to ensure the stable competition in the market. Zhu and He (2017) focus on the effect of green product design on the competition between actors and report that the greenness competition in fact negatively affect the greenness levels of the actors in equilibrium. Li et al. (2020) focus on the sourcing decisions under a quality competition between the products manufactured by different manufacturers and develop game theory-based models to obtain the equilibrium decisions considering different sourcing cases. Chai et al. (2020) propose mathematical models to investigate the effect of carbon cap-and-trade policy on the product competition and report that if the allocated carbon cap to the original equipment manufacturer is less, the carbon cap-and-trade policy significantly affects the original equipment manufacturer in this competition.

In this study, different from the studies above, we focus on the pricing and production decisions before and after the launch of a competing product and compare them with each other. The rest of the chapter is organized as follows. In section 2, we derive the demand functions for one-product and two-product cases. Section 3 is dedicated to the models and equilibrium results, and section 4 is dedicated to the computational study and discussions. Finally, we conclude the study in Section 5.

2. DERIVATION OF DEMAND FUNCTIONS

Before the launch of the product there will be only one-product in the market and that product will have a demand function as follows (Huang et al., 2013). Here, the first term is the base market, and the second term is leaving customers depending on the price of the product.

$$d_1(p_1) = q_1 - a_1 p_1 \tag{1}$$

On the other hand, when there are two competing products in the market, demand functions will be as presented below. Different from one-product case here, the price of the competing product has also an effect on the demand.

$$\begin{aligned} d_1(p_1, p_2) &= q_1 - a_1 p_1 + a_2 p_2 \\ d_2(p_1, p_2) &= q_2 - a_1 p_2 + a_2 p_1 \end{aligned} \tag{2}$$

It should be noted that the q_1 values in one-product case and two-product case might not be the same, i.e., some of the base customers may prefer to buy Product 2 instead of Product 1 due to low price of Product 2. Moreover, some new customers, which cannot buy the Product 1 due to its

high price, may buy the Product 2. Similarly, the a_1 values in one-product case and two-product case may also be different, i.e., the demand function may be more price sensitive based on the intensity of the competition.

Briefly, it is important to determine the demand parameters carefully in one-product case and two-product case to create the correct relationships between them. In this section, by using an analytical model, we determine the values of these parameters. In their study, Huang et al. (2013) present a demand model where two firms compete in a market, and each produces a differentiated good. Parameters for this model can be presented as follows.

Table 1: Notation for the Utility Model

$\psi_1, \psi_2, \phi_1, \phi_2$	Impact of the price of Product 1 and Product 2 on the demands of these products
η	The substitutability measure for products
δ_1, δ_2	Quantities purchased by a representative consumer.
$u(\delta_1, \delta_2)$	Consumers' utility function

Based on the notation in Table 1, consumer's utility function can be presented as in equation (3)

$$u(\delta_1, \delta_2) = \psi_1\delta_1 + \psi_2\delta_2 - \frac{\phi_1{\delta_1}^2 + 2\eta\delta_1\delta_2 + \phi_2{\delta_2}^2}{2} \tag{3}$$

Here both $\psi_i, \phi_i > 0$ and $\psi_i\phi_j - \eta\psi_i > 0$ for $i = 1, 2$ and $i \neq j$. To ensure the strict concavity of the utility function, the parameters must also satisfy $\phi_1\phi_2 - \eta^2 > 0$. In order to determine the δ values, we will use the following problem

$$\max_{\delta} \wedge(\boldsymbol{\delta}) \equiv u(\boldsymbol{\delta}) - \boldsymbol{p}^T\boldsymbol{\delta} \tag{4}$$

where $u(\boldsymbol{\delta})$ is a representative consumer's utility, which is smooth and strictly concave. If there is only one-product the function will be as follows;

$$\max_{\delta_1} = \psi_1\delta_1 - \frac{\phi_1{\delta_1}^2}{2} - p_1\delta_1 \tag{5}$$

As a result, optimal value of δ_1 can be obtained as follows.

$$\delta_1 = \frac{\psi_1}{\phi_1} - \frac{1}{\phi_1}p_1 \tag{6}$$

If there are two competitive products the function will be as follows.

$$\max_{\delta_1,\delta_2} = \psi_1\delta_1 + \psi_2\delta_2 - \frac{\phi_1{\delta_1}^2 + 2\eta\delta_1\delta_2 + \phi_2{\delta_2}^2}{2} - p_1\delta_1 - p_2\delta_2 \tag{7}$$

As a result, optimal values of δ_1 and δ_2 can be obtained as follows.

$$\begin{aligned}\delta_1 &= \frac{\psi_1\phi_2 - \psi_2\eta}{\phi_1\phi_2 - \eta^2} - \frac{\phi_2}{\phi_1\phi_2 - \eta^2}p_1 + \frac{\eta}{\phi_1\phi_2 - \eta^2}p_2 \\ \delta_2 &= \frac{\psi_2\phi_1 - \psi_1\eta}{\phi_1\phi_2 - \eta^2} - \frac{\phi_1}{\phi_1\phi_2 - \eta^2}p_2 + \frac{\eta}{\phi_1\phi_2 - \eta^2}p_1\end{aligned} \tag{8}$$

In order to simplify the above functions, if we assume $\phi_1 = \phi_2$, the functions can be written as follows for one-product.

$$\delta_1 = \frac{\psi_1}{\phi} - \frac{1}{\phi}p_1 \tag{9}$$

Moreover, the function can be presented as in equation (10)

$$\begin{aligned}\delta_1 &= \frac{\psi_1\phi - \psi_2\eta}{\phi^2 - \eta^2} - \frac{\phi}{\phi^2 - \eta^2}p_1 + \frac{\eta}{\phi^2 - \eta^2}p_2 \\ \delta_2 &= \frac{\psi_2\phi - \psi_1\eta}{\phi^2 - \eta^2} - \frac{b}{\phi^2 - \eta^2}p_2 + \frac{\eta}{\phi^2 - \eta^2}p_1\end{aligned} \tag{10}$$

Note that in one-product case, the demand function is denoted as; $d_1 = q_1 - a_1p_1$. Since for one-product $\delta_1 = \frac{\psi_1}{\phi} - \frac{1}{\phi}p_1$, we assume that $q_1 = \frac{\psi_1}{\phi}$ and $a_1 = \frac{1}{\phi}$.

Moreover, in two-product case, the demand function for Product 1 is denoted as $d_1 = q_1 - a_1p_1 + a_2p_2$ and the demand function for Product 2 is denoted as $d_2 = q_2 - a_1p_2 + a_2p_1$. By considering δ_1 and δ_2 above, $q_1 = \frac{\psi_1\phi - \psi_2\eta}{\phi^2 - \eta^2}$, $q_2 = \frac{\psi_2\phi - \psi_1\eta}{\phi^2 - \eta^2}$, $a_1 = \frac{\phi}{\phi^2 - \eta^2}$ and $a_2 = \frac{\eta}{\phi^2 - \eta^2}$ can be obtained. Based on these discussions, demand functions can be presented as in Table 2.

Table 2: Derived Demand Functions

	Demand
Product 1 in One-Product Case	$d_m = \frac{\psi_1}{\phi} - \frac{1}{\phi} p_1$
Product 1 in Two-Product Case	$d_1 = \frac{\psi_1 \phi - \psi_2 \eta}{\phi^2 - \eta^2} - \frac{\phi}{\phi^2 - \eta^2} p_1 + \frac{\eta}{\phi^2 - \eta^2} p_2$
Product 2 in Two-Product Case	$d_2 = \frac{\psi_2 \phi - \psi_1 \eta}{\phi^2 - \eta^2} - \frac{\phi}{\phi^2 - \eta^2} p_2 + \frac{\eta}{\phi^2 - \eta^2} p_1$

3. EQUILIBRIUM DECISIONS

For one-product case demand function of the manufacturer can be presented as in equation (11).

$$\Pi_1 = p_1(q_1 - a_1 p_1) \tag{11}$$

In the above model, the first term is the selling price of the manufacturer, and the second term is the demand depending on the selling price. First derivative of this function with respect to p can be obtained as follows.

$$\Pi_1{}' = q_1 - 2a_1 p_1 \tag{12}$$

Moreover, second derivative of the function with respect to p_1 can be obtained as follows.

$$\Pi_1{}'' = -2a_1 \tag{13}$$

Since the second derivative is negative, the function is concave in p_1. As a result, the profit maximizing selling price can be determined by solving the following equation.

$$q_1 - 2a_1 p_1 = 0 \tag{14}$$

As a result, optimal selling price can be obtained as $p_1 = \frac{q_1}{2a_1}$. Since in the previous section we have found $q_1 = \frac{\psi_1}{\phi}$ and $a_1 = \frac{1}{\phi}$, all in all the selling price can be presented as in equation (15) for the one-product case.

$$p_1 = \frac{\psi_1 \phi}{2\phi} = \frac{\psi_1}{2} \tag{15}$$

Finally, by using the equilibrium value of the selling price, equilibrium demand for Product 1 in the one-product case can be presented as in equation (16).

$$d_m = \frac{\psi_1}{\phi} - \frac{1}{\phi}\left(\frac{\psi_1}{2}\right) \tag{16}$$

We next focus on the two-product case. Profit function for the Product 1 can be stated as follows.

$$\Pi_1 = p_1(q_1 - a_1 p_1 + a_2 p_2) \tag{17}$$

In the above model, first term is the selling price, and second term is the demand depending on the prices of the competing products. First derivative of this function can be obtained as in eq. 7.

$$\Pi'_1 = q_1 - 2a_1 p_1 + a_2 p_2 \tag{18}$$

Moreover, second derivative of this function can be obtained as in equation (19).

$$\Pi'_1 = -2a_1 \tag{19}$$

Since second derivative is negative, the function is concave in its own selling price. Hence, we can find the optimal selling price by using the equation below.

$$q_1 - 2a_1 p_1 + a_2 p_2 = 0 \tag{20}$$

As a result, optimal selling price for Product 1 can be obtained as $\frac{q_1 + a_2 p_2}{2a_1}$.

Moreover, profit function for the Product 2 can be presented as follows.

$$\Pi_1 = p_2(q_2 - a_1 p_2 + a_2 p_1) \tag{21}$$

In the above model, first term is the selling price, and second term is the demand depending on the prices of the competing products. First derivative of this function can be obtained as in equation (22).

$$\Pi'_1 = q_2 - 2a_1 p_2 + a_2 p_1 \tag{22}$$

Moreover, second derivative of this function can be obtained as presented in equation (23).

$$\Pi'_1 = -2a_1 \tag{23}$$

Since second derivative is negative, the function is concave in its own selling price. Hence, we can find the optimal selling price by using the equation below.

$$q_2 - 2a_1 p_2 + a_2 p_1 = 0 \tag{24}$$

By solving the equation above, optimal selling price for Product 2 can be obtained as $\frac{q_2 + a_2 p_1}{2a_1}$.

Notice that optimal selling price for Product 1 includes the selling price of Product 2. Similarly, optimal selling price for Product 2 includes the selling price of Product 1. In this regard, we can obtain the equilibrium prices by jointly solving the following two equations.

$$\begin{aligned} p_1 &= \frac{q_1 + a_2 p_2}{2a_1} \\ p_2 &= \frac{q_2 + a_2 p_1}{2a_1} \end{aligned} \tag{25}$$

Solving the above equations yields to the following values for the selling prices.

$$\begin{aligned} p_1 &= \frac{2a_1 q_1 + a_2 q_2}{4a_1^2 - a_2^2} \\ p_2 &= \frac{2a_1 q_2 + a_2 q_1}{4a_1^2 - a_2^2} \end{aligned} \tag{26}$$

Since in the previous section we have found $q_1 = \frac{\psi_1\phi - \psi_2\eta}{\phi^2 - \eta^2}$, $q_2 = \frac{\psi_2\phi - \psi_1\eta}{\phi^2 - \eta^2}$, $a_1 = \frac{\phi}{\phi^2 - \eta^2}$ and $a_2 = \frac{\eta}{\phi^2 - \eta^2}$, we can rearrange the prices as presented in equation (27).

$$\begin{aligned} p_1 &= \frac{2\left(\frac{\phi}{\phi^2 - \eta^2}\right)\left(\frac{\psi_1\phi - \psi_2\eta}{\phi^2 - \eta^2}\right) + \left(\frac{\eta}{\phi^2 - \eta^2}\right)\left(\frac{\psi_2\phi - \psi_1\eta}{\phi^2 - \eta^2}\right)}{4\left(\frac{\phi}{\phi^2 - \eta^2}\right)^2 - \left(\frac{\eta}{\phi^2 - \eta^2}\right)^2} \\ p_2 &= \frac{2\left(\frac{\phi}{\phi^2 - \eta^2}\right)\left(\frac{\psi_2\phi - \psi_1\eta}{\phi^2 - \eta^2}\right) + \left(\frac{\eta}{\phi^2 - \eta^2}\right)\frac{\psi_1\phi - \psi_2\eta}{\phi^2 - \eta^2}}{4\left(\frac{\phi}{\phi^2 - \eta^2}\right)^2 - \left(\frac{\eta}{\phi^2 - \eta^2}\right)^2} \end{aligned} \tag{27}$$

By using these equilibrium values for selling prices, demand of Product 1 in the equilibrium can be stated as follows.

$$
\begin{aligned}
& d_1 \\
& = \frac{\psi_1\phi - \psi_2\eta}{\phi^2 - \eta^2} \\
& - \frac{\phi}{\phi^2 - \eta^2}\left(\frac{2\left(\frac{\phi}{\phi^2 - \eta^2}\right)\left(\frac{\psi_1\phi - \psi_2\eta}{\phi^2 - \eta^2}\right) + \left(\frac{\eta}{\phi^2 - \eta^2}\right)\left(\frac{\psi_2\phi - \psi_1\eta}{\phi^2 - \eta^2}\right)}{4\left(\frac{\phi}{\phi^2 - \eta^2}\right)^2 - \left(\frac{\eta}{\phi^2 - \eta^2}\right)^2}\right) \\
& + \frac{\eta}{\phi^2 - \eta^2}\left(\frac{2\left(\frac{\phi}{\phi^2 - \eta^2}\right)\left(\frac{\psi_2\phi - \psi_1\eta}{\phi^2 - \eta^2}\right) + \left(\frac{\eta}{\phi^2 - \eta^2}\right)\frac{\psi_1\phi - \psi_2\eta}{\phi^2 - \eta^2}}{4\left(\frac{\phi}{\phi^2 - \eta^2}\right)^2 - \left(\frac{\eta}{\phi^2 - \eta^2}\right)^2}\right)
\end{aligned}
\tag{28}
$$

Similarly, demand of Product 2 in the equilibrium can be obtained as in equation (29).below by using the equilibrium values of the selling prices.

$$
\begin{aligned}
& d_2 \\
& = \frac{\psi_2\phi - \psi_1\eta}{\phi^2 - \eta^2} \\
& - \frac{\phi}{\phi^2 - \eta^2}\left(\frac{2\left(\frac{\phi}{\phi^2 - \eta^2}\right)\left(\frac{\psi_2\phi - \psi_1\eta}{\phi^2 - \eta^2}\right) + \left(\frac{\eta}{\phi^2 - \eta^2}\right)\frac{\psi_1\phi - \psi_2\eta}{\phi^2 - \eta^2}}{4\left(\frac{\phi}{\phi^2 - \eta^2}\right)^2 - \left(\frac{\eta}{\phi^2 - \eta^2}\right)^2}\right) \\
& + \frac{\eta}{\phi^2 - \eta^2}\left(\frac{2\left(\frac{\phi}{\phi^2 - \eta^2}\right)\left(\frac{\psi_1\phi - \psi_2\eta}{\phi^2 - \eta^2}\right) + \left(\frac{\eta}{\phi^2 - \eta^2}\right)\left(\frac{\psi_2\phi - \psi_1\eta}{\phi^2 - \eta^2}\right)}{4\left(\frac{\phi}{\phi^2 - \eta^2}\right)^2 - \left(\frac{\eta}{\phi^2 - \eta^2}\right)^2}\right)
\end{aligned}
\tag{29}
$$

4. COMPUTATIONAL STUDY

In this section, we present a computational study to test the models and derive managerial insights regarding the one-product case and two-product case. Utility parameters of the base case problem is determined as in Table 3.

Table 3: Base Case Utility Parameters

ψ_1	ψ_2	ϕ	η
90	80	2	1

Computational results corresponding to this base case instance is presented in Table 4 below.

Table 4: Computational Results Corresponding to Base Case

q_1	p_1	d_1	Π_1	q_1	q_2	p_1	p_2	d_1	d_2	Π_1	Π_2	Total
45.0	45.0	22.5	1012	33.3	23.3	31.3	25.3	20.9	16.9	654.5	427.9	1082.4

Table 2 shows that as the Product 2 starts to be sold by the competing firm, market size of the Product 1 decreased from 45 to about 33, which means that 12 people that normally plans to purchase Product 1 started to purchase Product 2 after the launch of Product 2. Moreover, the table reveals that after the launch of Product 2, manufacturer of Product 1 decreased the price of Product 1 due to the competition Product 2 created. By decreasing the price, the manufacturer of Product 1 becomes able to keep the decrease in demand very limited, i.e., decreased from 22.5 to 20.9. Third, we observe from the computational results that the profit of the manufacturer substantially decreases as a result of the launch of Product 2. In this base case instance, this decrease is about 35%. Finally, the total supply chain profit in the market increased from 1012.5 to 1082.4 as a result of the launch of Product 2. This is mainly a result of the attendance of new people to the market as a result of the competition obtained after the launch of Product 2.

It should be noted that the results above are based on the specific parameters we consider. In order see the effects of parameters and test the models in different parameter settings, we also made a sensitivity analysis. First, we focus on the change in the market size as a result of the launch of Product and present the computational results in Table 5.

Table 5: Sensitivity Analysis on the Market Sizes

	ψ_1	ψ_2	ϕ	η	q_1	q_1	q_2
0	90	80	2	1	45.0	33.3	23.3
1	95	80	2	1	47.5	36.7	21.7
2	100	80	2	1	50.0	40.0	20.0
3	105	80	2	1	52.5	43.3	18.3
4	110	80	2	1	55.0	46.7	16.7
5	115	80	2	1	57.5	50.0	15.0
6	120	80	2	1	60.0	53.3	13.3
7	125	80	2	1	62.5	56.7	11.7
8	130	80	2	1	65.0	60.0	10.0
9	90	50	2	1	45.0	43.3	3.3
10	90	55	2	1	45.0	41.7	6.7
11	90	60	2	1	45.0	40.0	10.0
12	90	65	2	1	45.0	38.3	13.3

13	90	70	2	1	45.0	36.7	16.7
14	90	75	2	1	45.0	35.0	20.0
15	90	80	2	1	45.0	33.3	23.3
16	90	85	2	1	45.0	31.7	26.7
17	90	80	1.25	1	72.0	57.8	17.8
18	90	80	1.5	1	60.0	44.0	24.0
19	90	80	1.75	1	51.4	37.6	24.2
20	90	80	2	1	45.0	33.3	23.3
21	90	80	2.25	1	40.0	30.2	22.2
22	90	80	2.5	1	36.0	27.6	21.0
23	90	80	2.75	1	32.7	25.5	19.8
24	90	80	3	1	30.0	23.8	18.8
25	90	80	2	0.2	45.0	41.4	35.9
26	90	80	2	0.4	45.0	38.5	32.3
27	90	80	2	0.6	45.0	36.3	29.1
28	90	80	2	0.8	45.0	34.5	26.2
29	90	80	2	1	45.0	33.3	23.3
30	90	80	2	1.2	45.0	32.8	20.3
31	90	80	2	1.4	45.0	33.3	16.7
32	90	80	2	1.6	45.0	36.1	11.1

Table x reveals that, in all the instances considered, the launch of the Product 2 brings a decrease in the market size of Product 1. However, the numerical results reveal that in higher values of ψ_1 and lower values of ψ_2, the decrease in the market size of Product 1 is pretty limited compared to other cases. This happens because in higher values of ψ_1, or in lower values of ψ_2, the customers derive a substaintially higher utility from Product 1 as opposed to Product 2. Hence, in those instances, most of them do not leave the Product 1 after the launch of Product. On the other hand, when ψ_1 is low but ψ_2 is high, the customers derive similar utilities from Product 1 and Product 2. Thus, in those instances, they prefer to shift from the expensive one to a cheaper one, i.e., from Product 1 to Product 2. Hence, the market size of Product 1 substantially decreases.

Moreover, when we focus on the market size of Product 2, we observe that Product 2 attains the highest market size when ψ_1 is low or ψ_2 is high or η is high. As explained before, when ψ_1 is low but ψ_2 is high, customers derive similar utilities from Product 1 and Product 2, and thus they shift from Product 1 to Product 2 which increases the market size of Product 2. Moreover, when η is high, the preferences or valuations of customers for Product 2 increases and thus the market size of Product 2 increases

accordingly. Next, we focus on the selling price differences in one-product and two-product models and present the computational results in Table 6.

Table 6: Sensitivity Analysis on the Selling Prices

	ψ_1	ψ_2	ϕ	η	p_1	p_1	p_2
0	90	80	2	1	45.0	31.3	25.3
1	95	80	2	1	47.5	33.7	24.7
2	100	80	2	1	50.0	36.0	24.0
3	105	80	2	1	52.5	38.3	23.3
4	110	80	2	1	55.0	40.7	22.7
5	115	80	2	1	57.5	43.0	22.0
6	120	80	2	1	60.0	45.3	21.3
7	125	80	2	1	62.5	47.7	20.7
8	130	80	2	1	65.0	50.0	20.0
9	90	50	2	1	45.0	35.3	11.3
10	90	55	2	1	45.0	34.7	13.7
11	90	60	2	1	45.0	34.0	16.0
12	90	65	2	1	45.0	33.3	18.3
13	90	70	2	1	45.0	32.7	20.7
14	90	75	2	1	45.0	32.0	23.0
15	90	80	2	1	45.0	31.3	25.3
16	90	85	2	1	45.0	30.7	27.7
17	90	80	1.25	1	45.0	17.4	11.0
18	90	80	1.5	1	45.0	24.4	18.1
19	90	80	1.75	1	45.0	28.6	22.4
20	90	80	2	1	45.0	31.3	25.3
21	90	80	2.25	1	45.0	33.3	27.4
22	90	80	2.5	1	45.0	34.8	29.0
23	90	80	2.75	1	45.0	35.9	30.2
24	90	80	3	1	45.0	36.9	31.1
25	90	80	2	0.2	45.0	42.9	37.6
26	90	80	2	0.4	45.0	40.5	35.1
27	90	80	2	0.6	45.0	37.8	32.2
28	90	80	2	0.8	45.0	34.8	29.0
29	90	80	2	1	45.0	31.3	25.3
30	90	80	2	1.2	45.0	27.4	21.2
31	90	80	2	1.4	45.0	22.8	16.5
32	90	80	2	1.6	45.0	17.4	11.0

Table x shows that launch of Product 2 substantially decreases the price of Product 1, due to the competition created by Product 2. As the utility of the customers derived from Product 1, ψ_1, increases, manufacturer of Product 1 increases the selling price of Product 1 in both one-product and two-product cases. Similarly, as the utility of the customers derived from Product 2, ψ_2, increases the manufacturer of Product 2 increases the selling price of Product 2 to derive higher profits.

At this point, another interesting result is that as the valuations of customers for Product 2 compared to Product 1 increases, both the manufacturer of Product 1 and Product 2 decrease the selling prices. This happens since as the valuations of customers for Product 2 compared to Product 1 increases, the intensity of competition between Product 1 and Product 2 also increases. As a result, both manufacturers decrease the selling prices to obtain more customers from the market. As a result, both manufacturers profits significantly decrease in those instances. After analyzing the selling prices in on-product and two-product cases, we next focus on the demand in one-product and two-product models and present the computational results in Table 7.

Table 7: Sensitivity Analysis on the Demands

	ψ_1	ψ_2	ϕ	η	d_1	d_1	d_2
0	90	80	2	1	22.5	20.9	16.9
1	95	80	2	1	23.8	22.4	16.4
2	100	80	2	1	25.0	24.0	16.0
3	105	80	2	1	26.3	25.6	15.6
4	110	80	2	1	27.5	27.1	15.1
5	115	80	2	1	28.8	28.7	14.7
6	120	80	2	1	30.0	30.2	14.2
7	125	80	2	1	31.3	31.8	13.8
8	130	80	2	1	32.5	33.3	13.3
9	90	50	2	1	22.5	23.6	7.6
10	90	55	2	1	22.5	23.1	9.1
11	90	60	2	1	22.5	22.7	10.7
12	90	65	2	1	22.5	22.2	12.2
13	90	70	2	1	22.5	21.8	13.8
14	90	75	2	1	22.5	21.3	15.3
15	90	80	2	1	22.5	20.9	16.9
16	90	85	2	1	22.5	20.4	18.4
17	90	80	1.25	1	36.0	38.6	24.3
18	90	80	1.5	1	30.0	29.3	21.8

19	90	80	1.75	1	25.7	24.2	19.0
20	90	80	2	1	22.5	20.9	16.9
21	90	80	2.25	1	20.0	18.4	15.2
22	90	80	2.5	1	18.0	16.6	13.8
23	90	80	2.75	1	16.4	15.1	12.6
24	90	80	3	1	15.0	13.8	11.7
25	90	80	2	0.2	22.5	21.7	19.0
26	90	80	2	0.4	22.5	21.1	18.3
27	90	80	2	0.6	22.5	20.8	17.7
28	90	80	2	0.8	22.5	20.7	17.2
29	90	80	2	1	22.5	20.9	16.9
30	90	80	2	1.2	22.5	21.4	16.6
31	90	80	2	1.4	22.5	22.3	16.1
32	90	80	2	1.6	22.5	24.1	15.2

Following inferences can be made for the demand change in one-product and two-product cases. First, the table reveals that demand for Product 1 prominently decreases as a result of the launch of Product 2 mainly due to the competition between Product 1 and Product 2. Highest demand for Product 1 is observed when the utility of customers derived from Product 1 is high. Moreover, although an increase in the utility of customers from Product 2 decreases the demand for Product 1 in two-product case, this decrease is pretty limited, i.e., Product 1 is less sensitive to the utility of the competing product compared to its own utility.

When it comes to Product 2, computational results reveal that highest demand for Product 2 is observed when the utility of customers for Product 1 is low or when the utility of customers for Product 2 is high. In both cases, the customers derive similar utilities from Product 1 and Product 2, an thus some of the customers that normally purchase Product 1 shifts to Product 2, which increases the demand for Product 2. After analyzing the demand change, we next focus on profits of the actors in one-product and two-product models. Computational results are presented in Table 8.

Table 8: Sensitivity Analysis on the Profits

	ψ_1	ψ_2	ϕ	η	Π_1	Π_1	Π_2	$\Pi_1 + \Pi_2$
0	90	80	2	1	1012.5	654.5	427.9	1082.4
1	95	80	2	1	1128.1	755.6	405.6	1161.3
2	100	80	2	1	1250.0	864.0	384.0	1248.0
3	105	80	2	1	1378.1	979.6	363.0	1342.6
4	110	80	2	1	1512.5	1102.5	342.5	1445.0

5	115	80	2	1	1653.1	1232.7	322.7	1555.3
6	120	80	2	1	1800.0	1370.1	303.4	1673.5
7	125	80	2	1	1953.1	1514.7	284.7	1799.5
8	130	80	2	1	2112.5	1666.7	266.7	1933.3
9	90	50	2	1	1012.5	832.3	85.6	917.9
10	90	55	2	1	1012.5	801.2	124.5	925.7
11	90	60	2	1	1012.5	770.7	170.7	941.3
12	90	65	2	1	1012.5	740.7	224.1	964.8
13	90	70	2	1	1012.5	711.4	284.7	996.1
14	90	75	2	1	1012.5	682.7	352.7	1035.3
15	90	80	2	1	1012.5	654.5	427.9	1082.4
16	90	85	2	1	1012.5	627.0	510.3	1137.3
17	90	80	1.25	1	1620.0	671.3	266.6	937.9
18	90	80	1.5	1	1350.0	713.0	394.2	1107.2
19	90	80	1.75	1	1157.1	691.9	427.4	1119.3
20	90	80	2	1	1012.5	654.5	427.9	1082.4
21	90	80	2.25	1	900.0	614.6	415.9	1030.5
22	90	80	2.5	1	810.0	576.4	399.3	975.7
23	90	80	2.75	1	736.4	541.3	381.5	922.7
24	90	80	3	1	675.0	509.4	363.7	873.1
25	90	80	2	0.2	1012.5	928.7	715.7	1644.4
26	90	80	2	0.4	1012.5	854.5	639.9	1494.4
27	90	80	2	0.6	1012.5	786.2	568.8	1354.9
28	90	80	2	0.8	1012.5	720.5	499.2	1219.7
29	90	80	2	1	1012.5	654.5	427.9	1082.4
30	90	80	2	1.2	1012.5	584.9	351.4	936.3
31	90	80	2	1.4	1012.5	508.0	265.9	773.9
32	90	80	2	1.6	1012.5	419.6	166.6	586.2

Table x reveals that the manufacturer of Product 1 obtains the highest profit when the utility of the customers derived from Product 1 is high or the utility of customers derived from Product 2 is low or the valuations of customers for Product 2 compared to Product 1 is low. Particularly, in those instances the number of customers preferring Product 1 becomes higher and thus the manufacturer derives a higher profit. On the other hand, the manufacturer of Product 2 derives a higher profit when the utilities of the customers derived from Product 2 is high, when the utilities of customers derived from Product 1 is low, or when the valuations of customers for Product 2 compared to Product 1 is high. In those instances, the customers

basically see the Product 1 and Product 2 almost identical and thus a strong competition occurs between them, which yields to a decrease in the profit of Product 1 manufacturer and an increase in the profit of Product 2 manufacturer.

At this point, a discussion regarding the total supply chain profit may also be beneficial. Computational results show that there are instances in which the supply chain profit increases or decreases as a result of the launch of Product 2. Particularly, when the utility of customers derived from Product 1 is high or when the utility of customers derived from Product 2 is low, total supply chain profit decreases as a result of the launch of Product 2. On the other hand, when the utility of customers derived from Product 1 is low, when the utility of customers derived from Product 2 is high, or when the valuations of customers for Product 2 compared to Product 1 is low, total supply chain profit increases as a result of the launch of Product 2. The reason of all above outcomes can be explained with the intensify of the competition between Product 1 and Product 2 and resulting selling price decisions of the actors. Next, we focus on the selling price differences in one-product and two-product models and present the computational results in Table 9.

Table 9: Sensitivity Analysis on the Price Sensitivities

	ψ_1	ψ_2	ϕ	η	a_1	a_1	a_2
0	90	80	2	1	0.5	0.7	0.3
1	95	80	2	1	0.5	0.7	0.3
2	100	80	2	1	0.5	0.7	0.3
3	105	80	2	1	0.5	0.7	0.3
4	110	80	2	1	0.5	0.7	0.3
5	115	80	2	1	0.5	0.7	0.3
6	120	80	2	1	0.5	0.7	0.3
7	125	80	2	1	0.5	0.7	0.3
8	130	80	2	1	0.5	0.7	0.3
9	90	50	2	1	0.5	0.7	0.3
10	90	55	2	1	0.5	0.7	0.3
11	90	60	2	1	0.5	0.7	0.3
12	90	65	2	1	0.5	0.7	0.3
13	90	70	2	1	0.5	0.7	0.3
14	90	75	2	1	0.5	0.7	0.3
15	90	80	2	1	0.5	0.7	0.3
16	90	85	2	1	0.5	0.7	0.3
17	90	80	1.25	1	0.8	2.2	1.8
18	90	80	1.5	1	0.7	1.2	0.8

19	90	80	1.75	1	0.6	0.8	0.5
20	90	80	2	1	0.5	0.7	0.3
21	90	80	2.25	1	0.4	0.6	0.2
22	90	80	2.5	1	0.4	0.5	0.2
23	90	80	2.75	1	0.4	0.4	0.2
24	90	80	3	1	0.3	0.4	0.1
25	90	80	2	0.2	0.5	0.5	0.1
26	90	80	2	0.4	0.5	0.5	0.1
27	90	80	2	0.6	0.5	0.5	0.2
28	90	80	2	0.8	0.5	0.6	0.2
29	90	80	2	1	0.5	0.7	0.3
30	90	80	2	1.2	0.5	0.8	0.5
31	90	80	2	1.4	0.5	1.0	0.7
32	90	80	2	1.6	0.5	1.4	1.1

Table x shows that the price sensitivity in both one-product and two-product cases is independent from the utility of the customers derived from Product 1 and Product 2. This is actually a result we have analytically shown before. As shown in equation (9), the price sensitivity in single-product case depends only on the ϕ, i.e., negative utility of the customers and the price sensitivities in two-product case depends only on two parameters, ϕ and η, i.e., the negative utility and valuation.

The results reveal that as the valuations of customers increases, demand becomes much more sensitive to the product's own price and competing product's price. Main reason of this fact is that as this parameter increases, the intensity of the competition between the Product 1 and Product 2 also increases. Hence, in those instances, the customers become much more sensitive to the prices of the products.

5. CONCLUSION

In this study, we propose customer-utility based models to obtain the pricing and production decisions of the manufacturers before and after a new competing product launch. By making a comprehensive sensitivity analysis, we derive several managerial insights as follows.

Customer behavior and attuite plays a crucial role on the effect of pricing and production decisions of the manufacturers before and after the product launch. Particularly, in the cases where the customers derive similar utilities from the old product and newly launched product, launch of the new product yields to a substantial decrease in the profit of the Product 1 manufacturer. This happens due to the strong competition between Product 1 and Product 2 in those instances. On the other hand, in the cases where

the customers derive a significantly higher utility from Product 1 compared to Product 2, launch of Product 2 has a very limited effect on Product 1. In fact, this case corresponds to the case in which Product 2 is not exactly as beneficial as Product 2 for the customers. In such a case, shift from Product 1 to Product 2 becomes very limited.

This study can be extended in various ways in the future. First, in this study we consider a single-tier supply chain to clearly observe the effect of the new product launch. Consideration of a multi-tier supply chain may bring important insights regarding the effects of this launch to each actor. Another issue can be considering the uncertainties in the system. However, such a consideration may yield to complex newsvendor models that are difficult to solve and additional assumptions regarding the system may be needed.

REFERENCES

1. Chai, Q., Xiao, Z., & Zhou, G. (2020). Competitive strategies for original equipment manufacturers considering carbon cap and trade. *Transportation Research Part D: Transport and Environment*, 78, 102193.
2. Chang, W., & Taylor, S. A. (2016). The effectiveness of customer participation in new product development: A meta-analysis. *Journal of Marketing*, 80(1), 47-64.
3. Cooper, R. G. (2019). The drivers of success in new-product development. *Industrial Marketing Management*, 76, 36-47.
4. Di Benedetto, C. A. (1999). Identifying the key success factors in new product launch. *Journal of Product Innovation Management: An International Publication of The Product Development & Management Association*, 16(6), 530-544.
5. Ernst, H., Hoyer, W. D., & Rübsaamen, C. (2010). Sales, marketing, and research-and-development cooperation across new product development stages: implications for success. *Journal of Marketing*, 74(5), 80-92.
6. Huang, J., Leng, M., & Parlar, M. (2013). Demand functions in decision modeling: A comprehensive survey and research directions. Decision Sciences, 44(3), 557-609.
7. Lee, Y., & O'Connor, G. C. (2003). New product launch strategy for network effects products. *Journal of the Academy of Marketing Science*, 31(3), 241-255.
8. Li, W., Chen, J., & Chen, B. (2020). Sourcing strategy of original equipment manufacturer with quality competition. *Decision Sciences*, 51(5), 1110-1130.
9. Zhu, W., & He, Y. (2017). Green product design in supply chains under competition. *European Journal of Operational Research*, 258(1), 165-180.